An instrument for monitoring number and mass of ambient particles in coarse, fine and ultrafine size ranges

Thomas Kuhn

A thesis submitted in partial fulfilment of the requirements of the University of Hertfordshire for the degree of PhD

The programme of research was carried out in the Departments of Physical Sciences and Environmental Sciences, Faculty of Natural Sciences, University of Hertfordshire in collaboration with Casella CEL Ltd

August 2003

Meinem Vater, den ich sehr vermisse.

To my father, who I greatly miss.

A Consuelo, per il suo sostegno e amore.

To Consuelo for her support and love.

Abstract

Airborne particulate matter is today recognized as an important category of air pollutants. Current air quality standards, and hence most particle instruments, are based on particle mass concentration—the European standard, for example, on the PM10 fraction. For other metrics, such as number concentration, there is currently a lack of suitable instrumentation for monitoring purposes. A novel real-time particle-counting instrument has been developed in an attempt to fill this gap.

The new instrument is capable of detecting and counting particles from about 10 nm to 10 μm particle diameter. This instrument, aimed at monitoring ambient air quality, uses a parallel combination of optical particle counting for larger particles plus condensation particle counting for the smallest particles. The particles are classified into several size fractions, which allows discrimination between ultrafine, fine, and coarse particles. The instrument also enables gravimetric measurement of PM_{10} or $PM_{2.5}$ providing the possibility of comparing the measured number concentrations with the mass concentration standards. Furthermore, a conversion of the number concentration data into PM_{10}, $PM_{2.5}$, and also PM_1 mass concentration is possible. The new instrument is unique in offering number and mass information over the complete size range of interest in urban air quality monitoring.

The design of the instrument and the development and construction of first prototypes are described as well as calibration and performance results. The performance tests included side-by-side comparisons of two identical prototypes and comparison studies with traditional instrumentation in an urban field environment at a monitoring station in Birmingham (UK). Here, very good correlation was observed between the ultrafine particle concentration indicated by the new instrument and the total number concentration measured by a CPC (TSI model 3022A). Number-to-mass conversion results correlated well with mass concentration measured by TEOM.

Possibilities for a further size fractionation in the ultrafine particle size range were investigated and selected techniques tested. Size separation using diffusion devices was identified as a suitable technique to be implemented in the new instrument for ultrafine fractionation. Other future possibilities for further developments are also discussed.

Acknowledgement

I thank my supervisors, Paul Kaye, Edwin Hirst, and Ranjeet Sokhi of the University of Hertfordshire, as well as my industrial supervisor Steve Tearle of Casella CEL Ltd for the stimulating discussions and support. I also thank my colleagues at the ASRG and the STRC as well as at Casella CEL Ltd for their help and support. Department of Trade and Industry, NERC, and Casella CEL Ltd are acknowledged for their financial support of this work through the TCS programme. Casella CEL Ltd is also acknowledged for their technical support during construction of prototype instruments. I thank netcen (operating division of AEA Technology, Abingdon, UK), for offering their facilities, and Emma Payne, who helped during the laboratory studies at netcen. I also thank Casella Stanger and Birmingham City Council for their support at the Birmingham Centre site. Peter Holloway and Srinivas T. G. Srimath are thanked for their help during the field tests.

Contents

Nomenclature

α	Size parameter, see equation (3.1)
β_i	Eigenvalues in solution of Graetz problem
η	Air viscosity
η_T	Transmission efficiency for particles through a sampling device
γ	Angle used to calculate inertial deposition losses in a bend, see equation (3.31)
λ	Wavelength of light
ν	Mean number of particles in the sensing volume
ϕ	Azimuthal angle, page 16
ψ_i	Function of $\hat{r}$ in solution of Graetz problem
ρ_g	Air density
ρ_l	Density of condensing liquid
σ	Surface tension of condensing liquid
σ_N	Relative statistical counting error, see equation (3.33)
τ	Minimum time difference between two particles that can be detected separately, page 27
θ	Scattering angle, page 16
ξ	Dimensionless parameter for calculation of diffusive losses
a	Thermal diffusivity of air
a_i	Coefficients in solution of Graetz problem, see equation (3.20)
$\bar{c}$	Mean molecular speed, page 137
C_{2n}	Coefficients in solution of Graetz problem, see equation (3.19)
C_C	Slip correction factor, see equation (3.28)
c_p	Specific heat capacity
D	Particle diffusion coefficient, see equation (3.27)
d_d	Droplet diameter
d_K	Kelvin diameter, see equation (3.5)
d_{min}	Minimum detectable particle diameter in CPC, see equation (3.7)

d_p Particle diameter
d_t Tube diameter
D_v Vapour diffusivity in air
E Electric field
f Focal length of cylindrical lens
$f(\mathrm{Kn})$ Fuchs correction factor, see equation (3.23)
H Height of rectangular thin channel
I_i Incident light intensity
I_s Scattered light intensity
k Boltzmann constant ($k = 1.3807 \cdot 10^{-23}\ \mathrm{J \cdot K^{-1}}$)
k Wave number, page 17
k_g Thermal conductivity of air
k_p Particle thermal conductivity
L Molar latent heat of vaporization
L Length
l Mean free path of air molecules
M Molar mass
m Molecular mass
m Refractive index (or relative refractive index), page 16
N Number of sampled particles
$N(d_p)$ Cumulative log-normal distribution function, see equation (5.2)
n_i Measured number concentration of particles as indicated by the instrument, see equation (3.34)
n_p Number concentration of particles
p_0 Saturation vapour pressure at temperature T_0, see equation (3.21)
p_d Vapour pressure at droplet surface
p_s Saturation vapour pressure
p_v Vapour pressure
$\hat{p}_v$ Dimensionless vapour pressure, page 21
$p_{v,i}$ Vapour pressure at CPC condenser inlet
$p_{v,w}$ Vapour pressure at CPC condenser wall
p_∞ Vapour pressure away from droplet surface
q Volumetric sample flow rate
R Universal gas constant ($R = 8.3143\ \mathrm{J \cdot K^{-1} \cdot mol^{-1}}$)
r Radial coordinate

$\hat{r}$	Dimensionless radial coordinate, see equation (3.11)
R_c	Radius of cylindrical condenser tube
s	Stop distance of particle, page 25
S_{11}, S_{12}	Scattering matrix elements
S_R	Saturation ratio, see equation (3.6)
T	Temperature
$\hat{T}$	Dimensionless temperature, page 20
T_d	Temperature at droplet surface
T_i	Temperature at CPC condenser inlet
t_s	Sampling time
T_w	Wall temperature of CPC condenser
T_∞	Temperature away from droplet surface
v	Velocity of air flow or of a particle
v_m	Mean air velocity
$v_{m,duct}$	Mean air velocity in round duct
$v_{m,sample}$	Mean air velocity in sampling inlet
V_s	Sensing volume
v_{th}	Thermophoretic velocity, see equation (6.5)
W	Width of rectangular thin channel
W	Width of collimated laser beam
W_t	Characteristic width of tube
Z	Electrical mobility, see equation (6.1)
z	Axial coordinate
$\hat{z}$	Dimensionless axial coordinate, see equation (3.12)
Kn	Knudsen number, page 137
Pe	Péclet number, page 19
Re	Reynolds number
Stk	Stokes number, see equation (3.32)

List of Figures

List of Tables

1 Introduction

1.1 Background Information

1.1.1 Particulate Matter

An assembly of particles suspended in air (or gas) is called an *aerosol*. The size of aerosol particles ranges from approximately 1 nm to 100 µm. Airborne particles or particulate matter are other terms referring to an aerosol. Usually, aerosol particles are classified as *coarse particles* or *fine particles* (Whitby, 1978). Coarse particles have sizes larger than about 2 µm, whereas fine particles are usually defined as particles with size less than about 2 µm. Particles in the fine and coarse size ranges are substantially different due to different sources and particle formation processes, as will be explained below.

Besides this size classification, ambient aerosol is often described with a trimodal model consisting of a *nuclei, accumulation, and coarse mode*. Whitby (1978) reviewed size distribution data and found that a model consisting of three additive log-normal distributions fitted the data well. Figure 1.1 shows such a fitted size distribution using parameters found by Whitby (ibid.) for averaged urban distribution data visualizing the three modes. Whitby (ibid.) associated this structure with different sources contributing to the different modes. Road traffic and industry are sources of primary particles (particles emitted directly in the atmosphere) which contribute to the nuclei mode. Secondary particles (particles formed in the atmosphere) are generated in the nuclei mode by nucleation from the gas phase, involving mainly sulphur dioxide, oxides of nitrogen and volatile organic compounds. The nuclei mode is also referred to as *nucleation mode*, particles in this mode are referred to as *ultrafine particles* or *nanoparticles*. Coagulation of particles from the nuclei mode and condensation of gas on particles lead to a rapid growth of the particles into the the accumulation mode be-

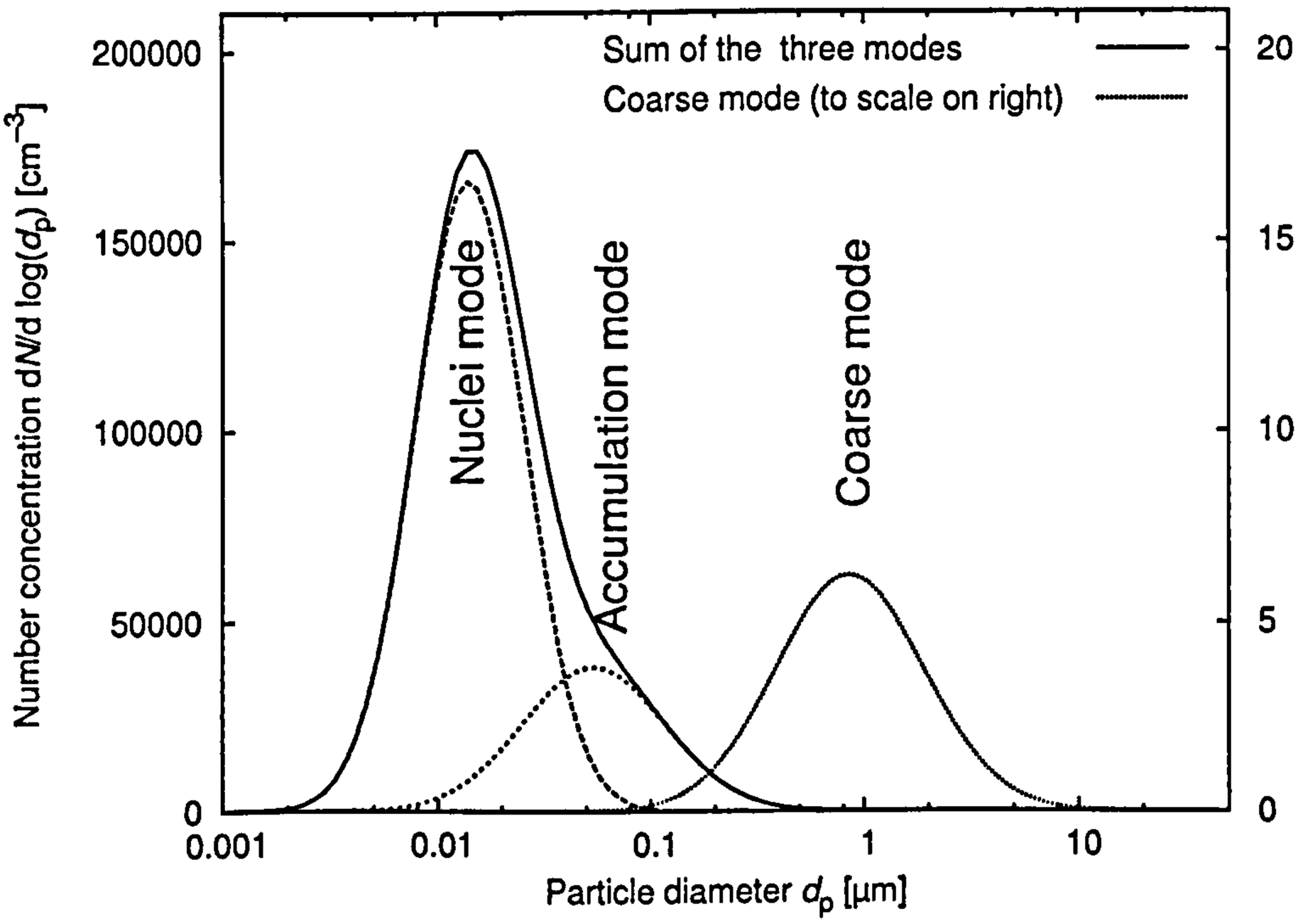

Figure 1.1: Ambient aerosol particle size distribution showing nuclei, accumulation, and coarse modes. (Average urban aerosol data as presented by Whitby, 1978)

tween about 100 nm and 2 µm. In the accumulation mode particles grow to a certain upper limit of around 2 µm where further growth would result in unstable particles. The coarse mode is associated with different generation processes, mostly mechanical, and contains particles such as resuspended surface soils, particles from construction activities, and sea spray. The sources of particulate matter in the UK are described in a report of the Airborne Particles Expert Group (APEG, 1999).

1.1.2 Air Quality Standards

Ambient particles affect visibility and are today recognized as one of the major air pollutants affecting human health. Particles larger than about 10 µm are, however, often not of special interest, as they remain suspended only for relative short periods before settling and do not pose health risks because they do not penetrate deep into the human respiratory system. Particles below 10 µm size, on the other hand, receive special attention. This fraction of aerosol particles is called PM_{10}, where PM_{10} refers to particulate matter consisting of particles with an aerodynamic diameter of less or equal

than 10 µm (for a definition of aerodynamic diameter see section 3.1). In the same manner one can define $PM_{2.5}$ and PM_1 as the fractions of particles with diameter less or equal than 2.5 µm or 1 µm respectively. While these definitions remain vague, for the legal air quality standards PM_{10} is defined as the fraction of particulate matter sampled with specified sampling efficiency at various aerodynamic particle diameters below and above 10 µm, where the efficiency at 10 µm is close to 50% (defined, for example, by EN12341, 1998).

Current ambient particulate matter standards are mass based and most standards use PM_{10} mass concentration (EU Council Directive 1999/30/EC Stage 1; US EPA 40 CFR Part 50). In the USA an air quality standard for $PM_{2.5}$ mass concentration has been added to the PM_{10} standard, reflecting the increasing concern about health effects of fine particles. The European standard specifies a 24 h and an annual limit value of 50 $\mu g \cdot m^{-3}$ and 40 $\mu g \cdot m^{-3}$ respectively, the 24 h limit value not to be exceeded on more than 35 days. The limit values are to be met by 1 January 2005. The reference method to be used for measuring PM_{10} mass concentrations is based on gravimetric measurement as specified in EN12341 (1998) or an equivalent method. The standard will be reviewed when Stage 2 comes in force on 1 January 2005 based on experience with the current Stage 1.

1.2 Health Effects of Particulate Matter

In the 1950's smog episodes killed many people. At that time, it was believed that black smoke, mainly carbonaceous soot from fossil fuel combustion in home heating and industry, was the cause of these health effects. Several studies demonstrated a relationship between black smoke concentration and variations in morbidity and mortality and the prevalence of respiratory illness (for example Schwartz and Marcus, 1990). Due to the use of different fuels and better filtration of particles, the particle composition in the second half of the 20th century changed, black smoke becoming less important. Nevertheless, an increasing number of studies shows the relationship between particles and health effects such as increased morbidity and mortality in people with respiratory and cardiac disease and increased respiratory morbidity in asthmatic people (Dockery et al., 1993; Pope III et al., 1995; Seaton et al., 1995, 1999; Osunsanya et al., 1999; Wong et al., 2001).

Discussions about the health effects of particulate matter are often concerned with the size of particles. While coarse particles are not considered particular harmful in general, as they do not penetrate deep into the lung, fine particles receive more attention today. Since the 1990's there has been increasing evidence of the importance of fine and especially ultrafine particles affecting health (for example Pope III et al., 1995). Several hypotheses and experimental studies explained the toxic effects of ultrafine particles and possible mechanisms of causing respiratory and cardiovascular diseases (Oberdörster et al., 1995; Seaton et al., 1995, 1999; Donaldson et al., 1998). There are now epidemiological studies which consider ultrafine particles, mainly by measuring the total number concentration alongside PM_{10} and $PM_{2.5}$ mass concentration. Such studies conclude that the ultrafine particles should not be dismissed when looking at the health effects of particulate matter. Studied symptoms of the health effects often correlate better or equally well with ultrafine number concentration as compared to correlation with, for example, $PM_{2.5}$ mass concentration (Peters et al., 1997; Pekkanen et al., 1997; Penttinen et al., 2001; Ibald-Mulli et al., 2002). However, some studies did not find evidence for the ultrafine particles being correlated with health problems (for example Osunsanya et al., 2001).

Although there is a clear correlation between particulate pollution episodes and increased morbidity and mortality, the causal mechanism of these health effects is not yet clear. It is not known which component of airborne particulate matter best represents the effects on human health (Harrison and Yin, 2000). The toxicity of the single components is not well known. Toxic components of particles, their combination in ambient air, and physical properties such as size distribution and mass will all influence how particles affect health. The Expert Panel on Air Quality Standards (EPAQS) addressed this issue, but could not give clear guidance and instead recommended a future review and suggested that metrics other than PM_{10}, such as count or surface area, should be included in future epidemiological studies to collect more data (EPAQS, 2001).

1.3 Monitoring Needs

Most monitoring instruments are mass-based to satisfy monitoring needs arising from the air quality standards. The tapered element oscillating microbalance (TEOM) (Rupprecht & Patashnick Co, Albany NY, USA; described on page 10) has been used in the UK for PM_{10} measurements for a number of years. There is, however, an ongoing discussion on how to compare the results of PM_{10} mass concentration measurements from TEOM and gravimetric instruments, as the TEOM is suspected to suffer from losses of semi-volatile particles. Green et al. (2001) give a short review of some of the studies and suggestions of correction factors to the TEOM measurements.

Given the potential health effects of ultrafine particles and since the mass of ultrafine particles is negligible (the mass decreasing with the third power of particle size) in comparison to fine and coarse particle mass concentrations, metrics other than mass concentration alone should be monitored. Morawska et al. (1999b) determined that while in most cases there is a distinct nuclei mode in the number size distribution representing the high number concentration of ultrafine particles, this does not translate to a nuclei mode in the volume size distribution, and thus does not contribute significantly to the mass concentration. Furthermore, while many of the number size distributions were different, the volume distributions were similar. Mass-based air quality standards will therefore reveal little information about the ultrafine number concentration. A number of other studies have confirmed a poor correlation between number and mass concentration of particles (for example Tuch et al., 1997; Harrison et al., 1999b; Greig, 2000). Consequently many studies suggest that the particle number concentration provides a more appropriate indication of possible effects on human health than particle mass (Oberdörster et al., 1994; Seaton et al., 1995; Figler et al., 1996; Harrison et al., 1999a; Morawska et al., 1999a).

Until there is a better understanding of what causes health effects, simultaneous measurements of more than one metric can be of great value. However, despite this need, there are currently very few commercial instruments which measure more than a single metric (such as mass concentration or particle count). In particular, to the knowledge of the author no instrument is available for the measurement of both mass concentration and size-

segregated number concentration, including the ultrafine and coarse size ranges. In fact, the uncertainties about the health effects are partly due to the difficulties of measuring particles and particle properties. Most measurements are complicated by the fact that the properties of single particles such as size, shape, refractive index, or density are usually unknown. On the other hand, many instruments are not suited for routine measurements and thus are not widely used in epidemiological studies. These instruments are often limited in the size range of the particles measured. Moreover, such instruments are often also sophisticated and either too expensive for routine measurements or in the form of laboratory prototype systems not suited for monitoring ambient air.

1.4 Aim and Objectives

Section 1.3 highlighted on the one hand the necessity and on the other hand the lack of instrumentation for routine urban air quality monitoring that provides multiple metrics. Such instrumentation would be very useful also in providing more data, necessary for revised or new legal standards. The aim of the work was therefore to:

> *Develop an instrument for simultaneously measuring particle number concentration, size distribution, and mass concentration in ambient air.*

The project involves combining existing technologies coupled with implementing novel design ideas and theoretical modelling. The overall aim would be achieved through the following objectives:

1. Identify technologies to be used and design a new instrument integrating these technologies.
2. Build prototype modules for testing single stages of the new instrument and compare their performance with results from theoretical modelling.
3. Build a complete prototype instrument.
4. Test the performance of the new instrument in the laboratory.

5. Compare the new instrument in field trials with current instrument standards.

The work is described in the following chapters. In chapter 2 a brief overview of currently used measurement methods for monitoring of ambient particulate matter is given. Chapter 3 provides a theoretical background for the topics covered in the subsequent chapters. Chapter 4 describes the development of the instrument. The design is presented in section 4.1. The implementation of components of the design in two prototype modules is described in sections 4.2 and 4.3. Section 4.4 shows details of the construction of a complete prototype instrument. Chapter 5 reports results of tests showing the performance of the prototype instrument. Calibration results are discussed in section 5.1. While section 5.2 describes a test of the prototype instrument with high ultrafine number concentrations to illustrate the possibility of coincidence corrections, section 5.3 reports on tests during a field trial comparing the prototype instrument with traditional instrumentation. Section 5.4 investigates three different conversion algorithms from particle number concentration data to mass concentration using data from the comparison tests described in section 5.3. Section 5.5 reports on side-by-side comparisons of two identical prototype instruments. The performance tests with the new instrument are summarized in section 5.6. Chapter 6 studies possibilities of a further size fractionation in the ultrafine size range and shows results of tests with selected technologies. Chapter 7 concludes summarizing the achievements and outlines further work requirements.

2 Particle Measurement Methods

There are several different methods of measuring particle number and mass concentrations and other particle properties such as particle surface area. Lehtimäki and Willeke (1993), Baron (1994), and McMurry (2000) give a detailed overview. In the following sections an overview of the methods currently used in air quality monitoring instrumentation that measures particle number concentration, mass concentration and size distribution is given to highlight their limitations relevant to this work.

2.1 Commercial Instruments

Counting Instruments

OPC The optical particle counter (OPC) measures the amount of light (usually from a laser diode) scattered by single particles. Scattered light from a particle is collected on a photodetector and converted to an electronic pulse whose amplitude gives information on the size of the detected particles as the scattering intensity depends mainly on the particle diameter (see section 3.2). According to the height of the pulses, the counted particles are classified in several size fractions, usually within a range from a lower limit of around 300 nm to 500 nm up to a upper limit typically around 10 µm. OPCs can theoretically have a lower detection limit of around 50 nm and it is not possible to extend this further due to limitations by scattering of air molecules (Knollenberg, 1985). The OPC therefore normally consists of a focused light source, a sensing volume (volume in which particles are detected) illuminated by the light source, collecting optics which collect scattered light, a photodetector receiving the scattered light, and signal-processing electronics. OPCs are calibrated using particles of known size.

APS The aerodynamic particle sizer (APS) counts single particles and measures their aerodynamic diameter (see section 3.1). The particles—together with the carrier gas (usually air)—are accelerated through a nozzle. The larger particles, having more inertia, accelerate more slowly than the smaller particles or the carrier gas and, therefore, have a lower velocity at the exit of the nozzle. The velocity of a particle after exiting the nozzle is therefore a measure of its inertia, and hence of its aerodynamic diameter. The velocity of the particles is measured as the time of flight between two laser beams (or the two intensity maxima of one double-crested laser beam) which are crossed perpendicularly by the particles close to the exit of the nozzle. The APS is limited for smaller particle sizes as these will follow the acceleration of the carrier gas more closely resulting in times of flight essentially independent of size. A typical lower limit of APSs is at about 0.5 µm, below which particles might still be counted but not sized. The lower detection limit for counting particles is similar to that of an OPC, as both instruments use light scattering.

CPC A condensation particle counter (CPC), also called condensation nucleus counter (CNC), measures the total number concentration of particles. CPCs grow particles by condensation of vapour onto the particle surface until the particles become droplets which are large enough to be detected. The detection is achieved by light scattering as in a conventional OPC. A CPC has a very low detection limit of a few nanometres as opposed to hundreds of nanometres for an OPC. Particle size cannot be measured as all particles are grown to droplets of similar size.

DMPS, ELPI Particle size distributions can be measured with instruments like the differential mobility particle sizer (DMPS) or the electrical-low pressure impactor (ELPI). The DMPS uses electrical mobility to size-classify previously charged particles in a differential mobility analyser (DMA), which is combined with a CPC or an electrostatic filter stage to detect the size-selected particles. It is difficult to use a DMPS for particles larger than a micrometre and also deconvolution of the data to get the size distribution can be problematic. More information on the DMPS can be found in McMurry (2000). The ELPI is a near real-time size analyser for particles in the size

range from 30 nm to 10 µm consisting of an aerosol charger and a cascade impactor. The use of impaction technique results in difficulties to extend the size range below 30 nm. The electrical detection of particles yields a lower detection limit for number concentration which is relatively high for typical ambient concentrations, for example 4 cm^{-3} in the size fraction 0.38 µm to 0.61 µm or 0.4 cm^{-3} between 4 µm and 6.7 µm (Marjamäki et al., 2000).

Mass-Based Instruments

Filter Sampling This is the most common analysis method for particles in ambient air. The particles are collected on a filter substrate and can be analysed gravimetrically and chemically after a sufficient amount of particles is collected. The method requires long sampling times and manual handling of the filter samples. High-volume samplers are used to reduce sampling time. The measured mass concentration is integrated over time and the filter does not provide any size information of the aerosol collected.

Beta Gauge In a beta gauge, the mass concentration is determined using the beta attenuation technique, in which the attenuation of beta rays from a radioactive source by the mass collected on a filter is measured. Automated instruments exist which provide near-real time measurement of mass concentration. The beta attenuation technique measures total mass concentration without information on the particle size distribution.

TEOM The TEOM is used to measure the particle mass concentration in real time. It determines the uptake of mass on a filter which is fixed on a tapered oscillating element. The oscillation frequency of the element depends, besides other properties of the element itself, on the mass of the filter such that the change in oscillation frequency of the element is proportional to the collected mass during the observed change in frequency. As for the filter method and the beta gauge, the TEOM does not provide any size information other than that given by the size-selective sampling inlet with either PM_{10} or $PM_{2.5}$ size cut.

Nephelometer, Photometer The integrating nephelometer measures the total amount of light scattered by particles in the gas volume examined. The

light scattering coefficient is so determined. The photometer measures the scattered light of the population of particles in the sensing volume. It covers scattering angles in a solid angle dependent on the design of the instrument. Both instruments can be used as an indication of the mass concentration.

OPC The size-segregated particle number concentration measured by an OPC can be used to calculate the particle mass concentration. Several assumptions are required for this number-to-mass conversion, such as for example the density of particles, their shape, and their size distribution within the size fractions of the OPC. This can result in discrepancies in quality of conversion for different locations or different conditions at the same location due to changing aerosol properties. It is, therefore, important to choose assumptions and conversion algorithms carefully. Some commercial OPCs, such as the GRIMM Dust Monitor Model 1.105 (GRIMM Aerosol Technik GmbH & Co KG, Ainring, Germany), provide calculated mass concentration. The manufacturers, however, do not tell the user which algorithm they use and the user cannot control conversion other than by means of one calibration factor. The mentioned instrument, for example, can collect the sampled particles on a filter for weighing the collected mass and determining a calibration factor as the ratio of actual mass to calculated mass.

Cascade Impactor Impactors are used to classify particles according to their aerodynamic diameter. A cascade impactor has several impactor stages in series, each of which collects particles in a certain size range by inertial deposition. After sufficient sampling time, the size-segregated particles can then be analysed gravimetrically and also chemically. To achieve low size cuts either low pressure (low pressure impactor) or small nozzle diameters (micro-orifice impactor) are used (Marple et al., 2001). Such cascade impactors are typically limited to the size range above approximately 50 nm due to difficulties in using this inertial technique for smaller particles. To measure a size distribution in this size range sampling times in the order of a few days are necessary to collect sufficient particles on each stage to be weighed. The resulting size distribution is integrated over time.

2.2 Particle Size Distribution Measurements

Besides DMPS, ELPI, and cascade impactors with their limitations mentioned above, there have been some attempts to design instruments for the measurement of ambient air particle size distribution. There are only a few systems, however, that measure the particle size distribution for the whole size range of interest including ultrafine and coarse size ranges. An example is the differential mobility and optical particle size spectrometer, using a DMA, OPC, and CPC (Stolzenburg et al., 1998). The instrument is a combination of separate systems and can be operated in two modes, with the OPC and CPC sampling in parallel either directly polydisperse ambient air, or monodisperse particles size-selected by the DMA. The latter is used for size calibration of the OPC with ambient air. Other examples are the mobile aerosol spectrometer using a DMA together with an OPC (Tuch et al., 2000) to measure the size distribution in the size range 10 nm to 2.5 µm and the electrical aerosol spectrometer combining two DMAs working in different particle size ranges (Tammet et al., 2002). The mobile aerosol spectrometer combines again separate systems, whereas the electrical aerosol spectrometer combines two DMAs designed for this instrument to cover the size range from 10 nm to 10 µm. These two aerosol spectrometers were compared in a field study (Tuch et al., 2000), showing good agreement of the size distribution of submicrometre particles, while there were differences in number concentrations above 1 µm (electrical aerosol spectrometer reading more than ten times higher). Tammet et al. (2002) aimed the electrical aerosol spectrometer at continuous monitoring of atmospheric aerosol and built an instrument that measures the number concentration in 12 size fractions. The low size resolution, as compared to typical DMPS systems, allows high time-resolution. Their instrument, however, weighs 70 kg and has dimensions of 0.44 m by 0.49 m by 0.9 m, and hence is relatively bulky. Peters et al. (1993) tested two systems to measure size distribution, combining data from an APS with either data from a DMPS or an electrical aerosol analyser. They compared these systems in a laboratory study with a low pressure impactor giving mass concentration as a function of aerodynamic size in 11 impactor stages between 30 nm and 30 µm. Although they showed that the systems were able to determine particle mass distribution as function of

aerodynamic size, they evaluated the combinations of instruments only for a unimodal sodium chloride test aerosol and the results would need to be confirmed for ambient aerosol. They also found that phantom particles (incidents registered as particles of a certain size but not corresponding to real particles of that size) counted by the APS in the coarse particle size range, although not significant in the number size distribution, resulted in significant, but false contribution to particle mass concentration.

2.3 Observations

The short overview given above shows the lack of suitable instrumentation for field monitoring ambient aerosol using more than one metric. The identified shortcomings of current instrumentation justifies the aim of this work. For example, the few systems reported in literature which count and size particles across the whole PM_{10} size range down to nanometre size, usually combine separate instrumentation and are not always suited for ambient monitoring. Very few instruments give number and mass concentrations in one instrument, as for example an OPC with an implemented number-to-mass conversion algorithm. However, this approach has the limitation in its size range mentioned earlier and difficulties with the conversion algorithm that, for commercial instruments, is usually not published. To the knowledge of the author, there is no instrument that can measure particle mass concentration and, at the same time measure the particle number concentration as size distribution in several size fractions that cover the fine particle size range—including ultrafine particles down to at least 10 nm particle diameter—and coarse particle size range up to 10 µm. Such an instrument, suited for monitoring ambient aerosol, would be very useful to fill the gap in instrumentation currently available. The instrument described in this thesis represents an attempt to meet this requirement.

3 Theoretical Background

3.1 Particle Properties

One of the most important properties of airborne particles is their size, on which many other properties depend. However, the different shapes and morphologies of particles make an exact definition of geometrical size difficult. Depending on which other property, as for example settling velocity, light scattering, or electrical mobility, is used to determine particle size, there are several *equivalent particle sizes*, defined as the size of a spherical particle having the same property as the particle whose size shall be described. Two often-used equivalent sizes are aerodynamic and optical size, defined with settling velocity and intensity of light scattering respectively. These equivalent sizes may depend also on other properties; aerodynamic size of a particle, for example, on its density and shape or the optical size on the refractive index of the particle. The *aerodynamic diameter* is therefore defined as the diameter of a spherical particle with a density of 1 000 $kg \cdot m^{-3}$ having the same gravitational settling velocity as the particle under consideration. The *optical diameter* is defined as the diameter of a spherical particle with a specified refractive index (usually that of the reference material used for calibration of the instrument measuring the optical size) scattering as much light as the particle whose size is to be measured.

Particle mass depends on density and volume, where the volume depends on size and shape, and the density on its morphology. Morphology is important also for the relationship between size and surface area of particles, which together with morphology determines the reactivity of a particle with surrounding gas.

While it is already difficult to characterize single particles using their properties such as size, shape, and mass, the great variety of properties and interdependencies between them make it even more difficult to describe ensembles of many particles, and consequently often integral properties such

as the mass and number concentrations are used, sometimes surface-area and volume concentration. The size distribution is also of interest for characterization of particles and is usually expressed in terms of normalized particle number concentration as a function of particle size. For ambient air the size distribution is often classified in nucleation, accumulation, and coarse modes as mentioned in section 1.1.1; these modes typically appear in many environments as distinct peaks in the number and volume size distributions (Whitby, 1972; Morawska et al., 1999b). Source apportionment derived from averaged chemical composition of particles gives additional information. A source apportionment for the UK is given by APEG (1999).

3.2 Light Scattering

The light scattering of particles is used in many instruments, as for example the OPC, nephelometer, and photometer, and as means for detection also in CPC and APS. There are many publications describing instrumentation that uses light scattering: Gebhart (2001) and Rader and O'Hern (2001) describe direct-reading techniques using the principles of light scattering; Baron et al. (2001) report on techniques using optical detection; Gebhart et al. (1984) characterize OPCs; Knollenberg (1985) explains the theoretical and practical limitations of OPCs; Umhauer (1983) and Hochrainer (2000) describe an OPC with an optically defined sensing volume.

Light scattering by particles with size comparable to the wavelength of the light is often referred to as *Mie scattering*. Gustav Mie published his general theory of particle light scattering in 1908 (Mie, 1908); it is exact for spherical, homogeneous particles which scatter light elastically. For large particles (diameter $>$ 100 µm for visible light) Mie's theory can be approximated well by geometric optics; for small particles ($<$50 nm) Mie's theory converges to Rayleigh scattering (Gebhart, 2001). For particles in the size range between these limits (from around 0.1 µm to 50 µm) Mie's theory has to be used for spherical particles to describe light scattering accurately. A derivation of his theory can, for example, be found in Bohren and Huffman (1983).

The scattered intensity I_s from an illuminated particle depends on the particle's refractive index m and on its size, or more precisely on its size

parameter α. The size parameter is defined as

$$\alpha = \frac{\pi d_p}{\lambda} \tag{3.1}$$

where d_p is the diameter of the particle and λ the wavelength of the incident light. The refractive index m of the particle is expressed as a complex number whose real part is the absolute refractive index and the imaginary part is related to the absorption coefficient. In Mie's theory, the relative refractive index is used, which is given by the ratio of m to the refractive index of the surrounding medium. In most cases the surrounding medium is air so that the relative refractive index is, to a very good approximation, equal to m. I_s is also a function of the *scattering angle* θ , which is the angle between the directions of incident light and scattered light, as shown in figure 3.1. These two directions define the *scattering plane*, whose orientation in space

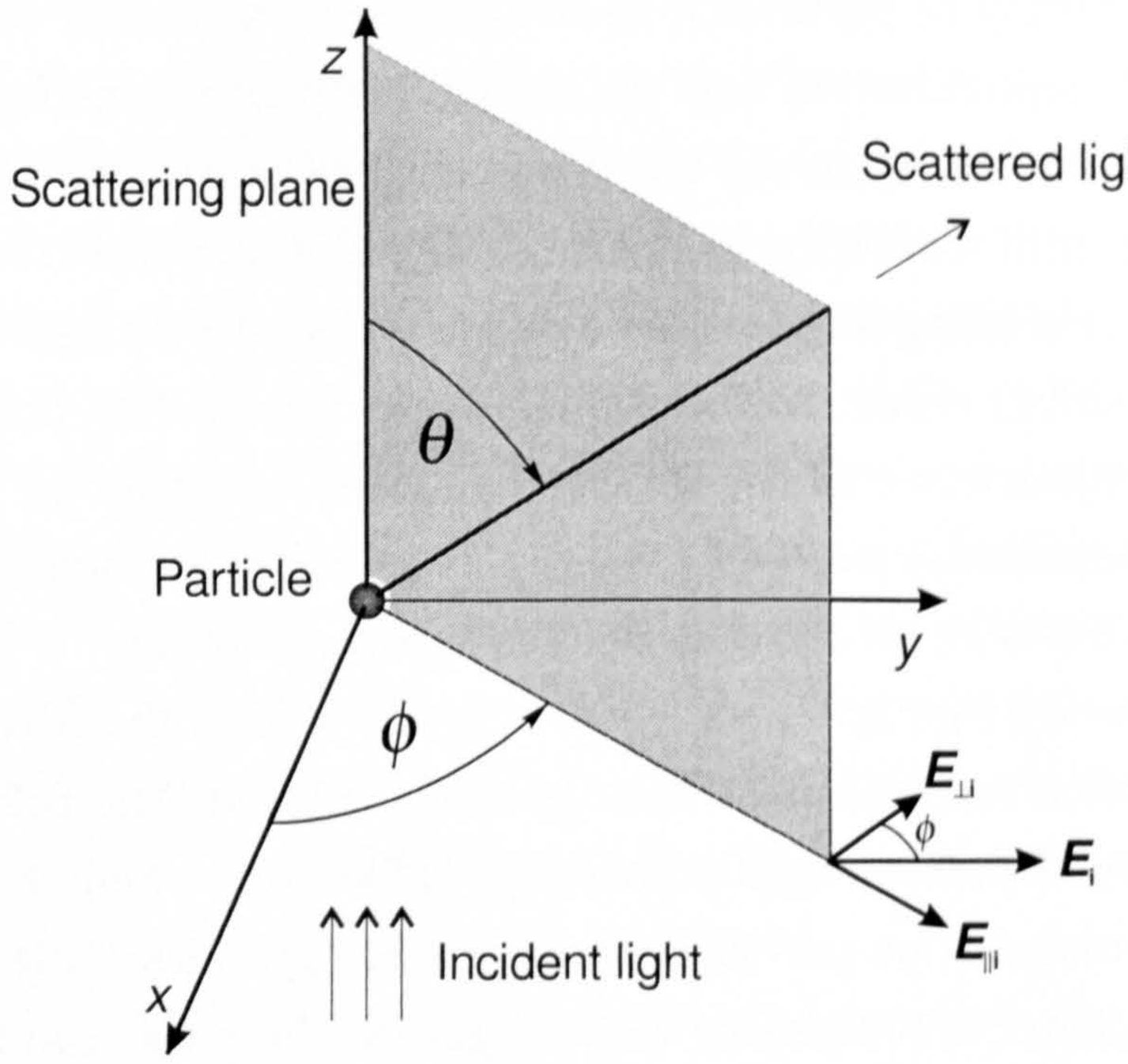

Figure 3.1: Light scattering by a particle at the origin of the coordinate system. The direction of incident light defines the z-axis. The scattering angle θ is the angle between z-axis and direction of scattering. The scattering plane is defined by the z-axis and the direction of scattering. The azimuthal angle ϕ is the angle between the scattering plane and x-axis. Linear polarization is indicated by the direction of the electric field vector ($\boldsymbol{E}_i$), parallel to the y-axis in this case. Its two components parallel ($\boldsymbol{E}_{\parallel i}$) and perpendicular ($\boldsymbol{E}_{\perp i}$) to the scattering plane are also shown.

is defined by the *azimuthal angle* ϕ (angle between the scattering plane and a

plane defined by the direction of incident light and an arbitrarily fixed direction perpendicular to the incident light, the x-axis in configuration shown in figure 3.1).

The angular pattern of scattered intensity depends again on the particle's refractive index m and on its size. For spherical particles, I_s does depend on θ, but as a consequence of the symmetry not directly on the azimuthal angle ϕ. However, in case of polarized incident light, I_s will depend on ϕ as the polarization of the incident light with respect to the scattering plane changes with ϕ.

To calculate the power of scattered light collected by an instrument, I_s needs to be integrated for a given particle diameter d_p, over θ and ϕ within the solid angle covered by the collecting optics of the instrument. The response curve of an instrument shows the scattered power as a function of the particle diameter d_p. Figure 4.3 depicts a response curve calculated using a computer program from Bohren and Huffman (1983), which was modified to include the integration of the scattering intensity (see section 4.2.1) for the OPC described later in section 4.2. It can be noted that the scattered power decreases dramatically as particles become small compared to the wavelength (with the sixth power of the particle size if $\alpha \ll 1$, Knollenberg, 1985). This rapidly decreasing scattered light power limits the OPC to particles larger than the lower detection limit given by the noise of the detector signal. The noise is in most cases mainly electronic noise or stray light from optical surfaces. If these two noise sources can be reduced sufficiently the OPC is ultimately limited by noise created from the light scattered by the air molecules in the sensing volume (volume of the illuminating beam seen by the detector). With red laser light this limits the detectable particle sizes to larger than about 50 nm (Knollenberg, 1985).

The scattered intensity is calculated from the scattering matrix elements S_{11} and S_{12} (Bohren and Huffman, 1983), and for unpolarized incident light with intensity I_i is

$$I_s = \frac{1}{k^2 r^2} S_{11} I_i \tag{3.2}$$

The term $\frac{1}{k^2 r^2}$ accounts for decreasing intensity with increasing distance r from the scatterer, $k = {}^{2\pi}/_{\lambda}$ is the wave number. If a laser diode is used as the light source then the incident light is linearly polarized and it can be split in the two components parallel and perpendicular to the scattering plane. If

polarization is parallel to the scattering plane then the scattered intensity is

$$I_s = \frac{1}{k^2 r^2}(S_{11} + S_{12})I_i \tag{3.3}$$

If incident light is polarized perpendicular to the scattering plane then the scattered intensity is

$$I_s = \frac{1}{k^2 r^2}(S_{11} - S_{12})I_i \tag{3.4}$$

The matrix elements S_{11} and S_{12} depend on the scattering angle θ, the relative refractive index m and the size parameter α, and can be calculated using Mie theory (Bohren and Huffman, 1983).

3.3 Condensational Growth

This section describes the process of condensation on particles as it takes place in the condenser of a CPC. Whether condensation or evaporation takes place on an existing droplet or particle is determined by the Kelvin equation which describes the saturation ratio S_R of the vapour in equilibrium with a droplet of diameter d_K:

$$S_R = \exp \frac{4\sigma M}{\rho_l R T d_K} \tag{3.5}$$

The saturation ratio is defined as

$$S_R = \frac{p_v}{p_s(T)} \tag{3.6}$$

where p_v is the vapour pressure and $p_s(T)$ is the saturation vapour pressure at temperature T. R is the universal gas constant, M is the molar mass, ρ_l and σ are the density and surface tension of the liquid forming the droplet respectively. At the saturation ratio S_R, given by equation (3.5), no net condensation or evaporation occurs on a droplet of diameter d_K. If S_R is larger then condensation dominates over evaporation yielding growth of the droplet. If, on the other hand, S_R is smaller than given by equation (3.5), then evaporation dominates condensation on the droplet surface. For a given S_R the minimum detectable particle diameter that can start condensation is therefore

$$d_{min} = d_K = \frac{4\sigma M}{\rho_l R T \ln S_R} \tag{3.7}$$

The temperature and vapour pressure inside the condenser must be calculated if one wants to know the minimum detectable particle diameter of a CPC. Temperature can be calculated solving the Fourier–Poisson equation of steady state heat conduction in a cylindrical tube. In cylindrical coordinates the equation has the form (Brown, 1960)

$$\frac{v}{a}\frac{\partial T}{\partial z} = \left[\frac{\partial^2}{\partial r^2} + \frac{1}{r}\frac{\partial}{\partial r} + \frac{\partial^2}{\partial z^2}\right] T \tag{3.8}$$

where v is the velocity of the air flow in the condenser, a the thermal diffusivity of air, r the radial coordinate, z the axial coordinate, and T the temperature. The term $\frac{\partial^2}{\partial z^2}T$, describing the axial heat conduction in the flow, can be neglected as it is usually much smaller than the other terms (Brown, 1960). This is the case when heat transfer by thermal diffusion (conduction) is small compared to thermal convection, a condition given by a Péclet number $\mathrm{Pe} > 60$ (Schiesser and Silebi, 1997), where Pe is defined by $\mathrm{Pe} = \frac{2v_\mathrm{m}R_\mathrm{c}}{a}$ using the mean air velocity v_m and the radius of the cylindrical condenser tube R_c. A Péclet number of 60 is given, for example, by a flow rate of 300 ml·min^{-1} through a tube with a diameter of 5 mm. To get T as a function of r and z one needs to solve this equation, which is also known as *Graetz problem* because a solution was first published by Graetz (1883). A derivation of the solution as described below can be found, for example, in Baehr and Stephan (1998).

The vapour pressure p_v of the liquid used in the CPC (usually an alcohol) inside the cylindrical CPC condenser tube is, for steady state conditions, the solution of the equation

$$\frac{v}{D_\mathrm{v}}\frac{\partial p_\mathrm{v}}{\partial z} = \left[\frac{\partial^2}{\partial r^2} + \frac{1}{r}\frac{\partial}{\partial r}\right] p_\mathrm{v} \tag{3.9}$$

where D_v is the vapour diffusivity in air. Due to the similarity to equation (3.8) the problem is the same if the thermal diffusivity of air a is substituted with the vapour diffusivity D_v of alcohol in air.

From the local temperature the saturation vapour pressure p_s can be calculated, which together with the vapour pressure p_v yields the saturation ratio S_R using equation (3.6). Equation (3.7) gives then the minimum particle diameter to act as a nucleus for condensation.

To solve the Fourier–Poisson equation (3.8) the velocity v is expressed as a function of r, which for fully developed laminar flow (Hagen–Poiseuille

velocity profile) is a parabolic profile

$$v = v(r) = 2v_m\left(1 - \left(\frac{r}{R_c}\right)^2\right) \tag{3.10}$$

where v_m is the mean velocity in the cylindrical tube and R_c its radius. Going to dimensionless coordinates $\hat{r}$ and $\hat{z}$ with the substitutions

$$\hat{r} = \frac{r}{R_c} \tag{3.11}$$

$$\hat{z} = \frac{z}{2R_c\mathrm{Pe}} \tag{3.12}$$

equation (3.8) becomes

$$\frac{1}{2}(1-\hat{r}^2)\frac{\partial T}{\partial \hat{z}} = \left[\frac{\partial^2}{\partial \hat{r}^2} + \frac{1}{\hat{r}}\frac{\partial}{\partial \hat{r}}\right]T \tag{3.13}$$

Substituting also $\hat{T} = \frac{T-T_w}{T_i-T_w}$ where T_w is the constant wall temperature and T_i the temperature of air at the tube inlet, equation (3.13) becomes

$$\left[\frac{\partial^2}{\partial \hat{r}^2} + \frac{1}{\hat{r}}\frac{\partial}{\partial \hat{r}} - \frac{1}{2}(1-\hat{r}^2)\frac{\partial}{\partial \hat{z}}\right]\hat{T} = 0 \tag{3.14}$$

Equation (3.14) must be solved for the following boundary conditions:

$$\hat{T}(\hat{r},\hat{z}) = 0 \quad \text{for} \quad \hat{r} = 1, \quad \hat{z} \geq 0 \tag{3.15}$$

$$\hat{T}(\hat{r},\hat{z}) = 1 \quad \text{for} \quad 0 \leq \hat{r} < 1, \quad \hat{z} = 0 \tag{3.16}$$

The constant temperature at the wall ($T = T_w$) is given by equation (3.15), whereas the uniform temperature at the tube inlet ($T = T_i$) by (3.16). With separation $\hat{T}(\hat{r},\hat{z}) = \varphi(\hat{z})\psi(\hat{r})$ and these two boundary conditions one gets the general solution of the differential equation (3.14) (Graetz, 1883)

$$\hat{T} = \sum_{i=1}^{\infty} a_i \exp(-2\beta_i\hat{z})\psi_i(\hat{r}) \tag{3.17}$$

The function ψ_i is defined as

$$\psi_i(\hat{r}) = \sum_{n=0}^{\infty} C_{2n}\hat{r}^{2n} \tag{3.18}$$

where the coefficients C_{2n} are defined for every eigenvalue β_i with the recursive formula

$$C_{2n} = \frac{\beta_i^2}{(2n)^2}(C_{2n-4} - C_{2n-2}) \quad \text{for} \quad n \geq 2 \tag{3.19}$$

$$C_2 = -\frac{\beta_i^2}{4}, \qquad C_0 = 1$$

The coefficients a_i are derived from boundary condition (3.16) as

$$a_i = \frac{\int_0^1 \psi_i(\hat{r})\,(1-\hat{r}^2)\,\hat{r}\,\mathrm{d}\hat{r}}{\int_0^1 \psi_i^2(\hat{r})\,(1-\hat{r}^2)\,\hat{r}\,\mathrm{d}\hat{r}} \tag{3.20}$$

The eigenvalues β_i are found as solutions of a power series derived from equation (3.18) for the boundary condition (3.15) and using the recursive definition (3.19) of the coefficients C_{2n}.

Equation (3.9) can be solved in an analogue way by substituting thermal diffusivity with vapour diffusivity and temperature with vapour pressure, as mentioned above, and assuming that the air entering the condenser is saturated with vapour at the temperature T_i. The dimensionless axial coordinate $\hat{z}$ is then consequently defined with D_v as $\hat{z} = \frac{zD_\mathrm{v}}{4R_\mathrm{c}^2 v_\mathrm{m}}$. The dimensionless temperature $\hat{T}$ is substituted by the dimensionless vapour pressure $\hat{p}_\mathrm{v} = \frac{p_\mathrm{v}-p_\mathrm{v,w}}{p_\mathrm{v,i}-p_\mathrm{v,w}}$, where $p_\mathrm{v,w}$ is the vapour pressure at the condenser wall given by the saturation vapour pressure at T_w and $p_\mathrm{v,i}$ is the vapour pressures at the condenser inlet given by the saturation vapour pressure at T_i, assuming that the vapour is saturated before it flows into the condenser. The saturation vapour pressure at a given temperature is calculated using the Clausius–Clapeyron equation linking heat of vaporization with the saturation vapour pressure

$$p_\mathrm{s} = p_0 \exp\left(\frac{L}{R}\left(\frac{1}{T_0}-\frac{1}{T}\right)\right) \tag{3.21}$$

where p_0 is the saturation vapour pressure at T_0 and L the molar latent heat of vaporization of the alcohol at T_0. As L depends on the temperature, the equation approximates the saturation vapour pressure close to T_0. Supersaturation is then calculated from equation (3.6) and the lowest particle diameter acting as condensation nucleus (d_min) from equation (3.7).

After a particle has activated condensation, it forms a droplet which grows at a rate which is given by the rate of arrival of vapour molecules on the droplet surface, and hence the growth rate depends on vapour diffusivity and vapour pressure. The growth rate of the droplet diameter d_d is given by the equation (Hinds, 1999)

$$\frac{\mathrm{d}d_\mathrm{d}}{\mathrm{d}t} = \frac{4D_\mathrm{v}M}{R\rho_\mathrm{l}d_\mathrm{d}}\left(\frac{p_\infty}{T_\infty}-\frac{p_\mathrm{d}}{T_\mathrm{d}}\right) f(\mathrm{Kn}) \tag{3.22}$$

In the equation $f(\mathrm{Kn})$ is the Fuchs correction factor which accounts for the fact that close to the droplet surface vapour diffusion does not describe correctly the mass transfer of vapour molecules to the droplet. It is given by (Ahn and Liu, 1990)

$$f(\mathrm{Kn}) = \frac{1+\mathrm{Kn}}{1+1.7104\mathrm{Kn}+{}^4/_3\,\mathrm{Kn}^2} \tag{3.23}$$

where $\mathrm{Kn} = \frac{2l}{d_\mathrm{d}}$ is the *Knudsen number* of the droplet, l is the mean free path of air molecules. T_d and p_d are the temperature and vapour pressure at the droplet surface, while T_∞ and p_∞ are the temperature and vapour pressure in the surrounding air away from the droplet surface. T_∞ and p_∞ are therefore given by the local temperature T and the local vapour pressure p_v resulting from the calculations described above. The vapour pressure p_d at the droplet surface is given by the equilibrium vapour pressure given by equations (3.5) and (3.6) as

$$p_\mathrm{d} = p_\mathrm{s}(T_\mathrm{d}) \exp \frac{4\sigma M}{\rho_\mathrm{l} R T_\mathrm{d} d_\mathrm{d}} \tag{3.24}$$

If the droplet growth is slow ($S_\mathrm{R} \approx 1$) then $T_\mathrm{d} \approx T_\infty$. Here, the growth will be fast due to the elevated saturation ratio S_R, so that T_d will be higher than T_∞ due to the heat released during condensation. The temperature elevation $T_\mathrm{d} - T_\infty$ is given by (Hinds, 1999)

$$T_\mathrm{d} - T_\infty = \frac{D_\mathrm{v} L}{R k_\mathrm{g}} \left(\frac{p_\infty}{T_\infty} - \frac{p_\mathrm{d}}{T_\mathrm{d}} \right) \tag{3.25}$$

where k_g is the thermal conductivity of the air (connected to thermal diffusivity of air a by $a = {}^{k_\mathrm{g}}/_{\rho_\mathrm{g} c_p}$ where ρ_g is the density of air and c_p its specific heat capacity). The temperature elevation cannot be calculated directly so that either numerical solution (Ahn and Liu, 1990) or the use of an empirical approximation (Hinds, 1999) is required. The diameter of the droplet leaving the condenser can be calculated by integration of equation (3.22) over the time a particle needs to travel through the condenser.

3.4 Sampling Efficiency

Instruments sampling aerosol may suffer from losses, such as for example inertial deposition of particles in flow constrictions in the inlet and sample

In the equation $f(\mathrm{Kn})$ is the Fuchs correction factor which accounts for the fact that close to the droplet surface vapour diffusion does not describe correctly the mass transfer of vapour molecules to the droplet. It is given by (Ahn and Liu, 1990)

$$f(\mathrm{Kn}) = \frac{1+\mathrm{Kn}}{1+1.7104\mathrm{Kn}+{}^{4}/_{3}\,\mathrm{Kn}^{2}} \tag{3.23}$$

where $\mathrm{Kn} = \frac{2l}{d_\mathrm{d}}$ is the *Knudsen number* of the droplet, l is the mean free path of air molecules. T_d and p_d are the temperature and vapour pressure at the droplet surface, while T_∞ and p_∞ are the temperature and vapour pressure in the surrounding air away from the droplet surface. T_∞ and p_∞ are therefore given by the local temperature T and the local vapour pressure p_v resulting from the calculations described above. The vapour pressure p_d at the droplet surface is given by the equilibrium vapour pressure given by equations (3.5) and (3.6) as

$$p_\mathrm{d} = p_\mathrm{s}(T_\mathrm{d}) \exp \frac{4\sigma M}{\rho_\mathrm{l} R T_\mathrm{d} d_\mathrm{d}} \tag{3.24}$$

If the droplet growth is slow ($S_\mathrm{R} \approx 1$) then $T_\mathrm{d} \approx T_\infty$. Here, the growth will be fast due to the elevated saturation ratio S_R, so that T_d will be higher than T_∞ due to the heat released during condensation. The temperature elevation $T_\mathrm{d} - T_\infty$ is given by (Hinds, 1999)

$$T_\mathrm{d} - T_\infty = \frac{D_\mathrm{v} L}{R k_\mathrm{g}} \left(\frac{p_\infty}{T_\infty} - \frac{p_\mathrm{d}}{T_\mathrm{d}} \right) \tag{3.25}$$

where k_g is the thermal conductivity of the air (connected to thermal diffusivity of air a by $a = {}^{k_\mathrm{g}}/_{\rho_\mathrm{g} c_p}$ where ρ_g is the density of air and c_p its specific heat capacity). The temperature elevation cannot be calculated directly so that either numerical solution (Ahn and Liu, 1990) or the use of an empirical approximation (Hinds, 1999) is required. The diameter of the droplet leaving the condenser can be calculated by integration of equation (3.22) over the time a particle needs to travel through the condenser.

3.4 Sampling Efficiency

Instruments sampling aerosol may suffer from losses, such as for example inertial deposition of particles in flow constrictions in the inlet and sample

delivery system, before the sample is analysed. Such losses would not only reduce the sampling efficiency—the ratio of the concentration of particles that reach the analysis system to the concentration of particles in the air—but, because they are typically size dependent, would also distort the measured size distribution.

The following section describes various mechanisms of particle losses commonly encountered in sampling systems. For a detailed description of sampling losses see also Brockmann (2001); general guidelines on sampling aerosol are given by Booker et al. (1998).

Sampling from Calm Air Sampling from ambient air is not easy when one wants to take a representative sample with original concentration and size distribution. Particle losses at sampling inlets depend on inlet geometry, the sample flow rate, and wind speed and direction. Large particles may not follow sudden changes in the flow direction due to their inertia.

When sampling from calm air the inlet geometry and sampling flow rate must be chosen within a certain range which is limited by two conditions: the upper limit allows large particles, with their high inertia, to follow the flow into the inlet, whereas the lower limit ensures that the sampling-flow velocity is much higher than the settling velocity of the particles (Brockmann, 2001).

Isokinetic Sampling In moving air, sampling errors are avoided only if the directions and velocities of the ambient air stream and sample flow are matched. Under these conditions sampling is said to be isokinetic. More precisely, sampling is said to be isokinetic when it is isoaxial (same direction) and the mean sample flow velocity through the face of the inlet is equal to the air flow velocity.

This applies to laminar flow in the ambient free stream. However, it can be used in similar conditions as well. If isokinetic sampling takes place in a round duct using a sampling inlet small compared to the duct diameter, the aligned inlet must satisfy the following equation if placed in the centre of the duct

$$v_{\mathrm{m,sample}} = 2v_{\mathrm{m,duct}} \tag{3.26}$$

where $v_{\mathrm{m,sample}}$ and $v_{\mathrm{m,duct}}$ are the mean velocities in the sampling inlet and

in the duct respectively, and $2v_{\mathrm{m,duct}}$ is the local stream velocity in the centre of the round duct for fully developed laminar flow (see equation (3.10) for Hagen–Poiseuille flow).

Diffusive Losses Brownian diffusion of particles is a mechanism by which particles are lost to the wall of a sampling tube. When particle transport is slow compared to diffusion, diffusive losses become significant. The smaller the particles the higher is their diffusivity; the smallest particles are therefore affected most by these losses. The *diffusion coefficient* (or *diffusivity*) D of the particle is given by the equation (Baron and Willeke, 2001)

$$D = \frac{kTC_{\mathrm{C}}}{3\pi\eta d_{\mathrm{p}}} \tag{3.27}$$

In the formula k is the Boltzmann constant, η is the viscosity of air and C_{C} is the *slip correction factor*, which is given for solid particles by the equation (Hinds, 1999)

$$C_{\mathrm{C}} = 1 + \frac{l}{d_{\mathrm{p}}}\left(2.34 + 1.05\exp\left(-0.39\frac{d_{\mathrm{p}}}{l}\right)\right) \tag{3.28}$$

Besides the particle diffusivity, the losses depend on the length of the tube and the flow rate in the tube. In a straight circular tube the diameter does not affect the losses. To minimize diffusive losses it is best to make sampling tubes as short as possible (and at least as short as necessary for the selected sample flow rate).

For describing the losses in laminar flow the dimensionless *diffusion parameter* ξ is introduced as

$$\xi = \frac{\text{transport time}}{\text{diffusion time}} = \frac{L/v_{\mathrm{m}}}{W_{\mathrm{t}}^2/D}$$

where L is the length of the tube, v_{m} the mean velocity of the flow, and W_{t} a characteristic width of the tube. For a circular tube W_{t} is the radius and ξ can be expressed as

$$\xi = \frac{\pi LD}{q} \tag{3.29}$$

For high values of ξ, when particle transport is slow compared to diffusion, the losses become significant. The losses are characterized using the *transmission efficiency* η_{T}, which is defined as the ratio of the number of particles

transmitted through a given device to the total number of particles introduced. The transmission efficiency for particles through a circular tube can be expressed as (Gormley and Kennedy, 1949)

$$\eta_T = \begin{cases} 1 - 2.564\xi^{2/3} + 1.2\xi + 0.1770\xi^{4/3} & \text{for } \xi \leq 0.03 \\ 0.8191e^{-3.655\xi} + 0.0975e^{-22.3\xi} + 0.0325e^{-57\xi} & \text{for } \xi > 0.03 \end{cases} \quad (3.30)$$

The transmission efficiency decreases for increasing ξ, and hence for decreasing particle size. Only particles larger than a certain size are therefore transmitted efficiently through a sampling tube and the sampling delivery path needs to be designed accordingly to avoid losses of ultrafine particles.

Inertial Deposition in a Bend In a sample delivery path containing bends, larger particles will be lost if they cannot follow the flow because of their higher inertia. Such particles get deposited on the wall of the bend as they get carried out of the flow. These deposition losses depend on the diameter of the particles, on the flow rate, and the dimension of the flow path, usually the diameter of a round tube. Although a smaller bend radius yields a faster drift of particles towards the wall, particles also spend less time in a smaller bend and, effectively, the losses do not depend on the radius of the bend. To minimize deposition losses it is advisable to keep the transmission lines as straight as possible and introduce only absolutely necessary bends.

The situation can be assessed using the stop distance s of the particle, which is the distance travelled by a particle until it stops in absence of any forces except the drag force in the gas surrounding the particle. A particle drifts by $\pi s/2$ towards the wall of a circular tube while travelling through a 90° bend. If this distance is larger than the tube diameter d_t, all particles with that stop distance are carried out of the flow and η_T equals zero. For smaller particles with their smaller stop distances, and hence smaller drifts, the transmission efficiency η_T approaches unity. From geometrical considerations one gets the following equation for η_T (Booker et al., 1998)

$$\begin{aligned} \eta_T &= \frac{1}{\pi}(\gamma + \sin\gamma) \quad (3.31) \\ \gamma &= 2\cos^{-1}\left(\frac{\pi s}{2d_t}\right) \end{aligned}$$

The stop distance s can be calculated using the Stokes number $\mathrm{Stk} = s/d_t$

which can be given as (Baron and Willeke, 2001)

$$\mathrm{Stk} = \frac{v_\mathrm{m} d_\mathrm{p}^2 \rho_\mathrm{p} C_\mathrm{C}}{18\eta} \tag{3.32}$$

where ρ_p is the particle density.

3.5 Counting Efficiency

Apart from the potential losses affecting the sampling efficiency, there are other errors that affect the analysis of the sample directly. Two, namely statistical and coincidence errors, are briefly discussed in this section.

Statistical Counting Error The measurement of small particle number concentrations is limited by the increased statistical error $\sqrt{N}$ associated with low numbers N of particles sampled. The relative statistical counting error σ_N is therefore $\sqrt{N}/N$. The number of particles sampled during a given sampling time t_s is $N = n_\mathrm{p} q t_\mathrm{s}$, where n_p is the number concentration of particles, so that $n_\mathrm{p} q$ is the number of particles sampled divided by time, as q is the volumetric flow rate. The relative statistical error is then

$$\sigma_N = \frac{1}{\sqrt{n_\mathrm{p} q t_\mathrm{s}}} \tag{3.33}$$

To keep this error small one must take a large sample, which, for a given sample flow rate, means measuring the average number concentration over a sufficiently long sampling time t_s. Alternatively the sample flow rate q may be chosen high enough to ensure a small error σ_N.

Coincidence Error When more than one particle is present in the sensing volume of an OPC (or any particle counter) at the same time, the particles are registered as one particle only. This coincidence error yields a systematic under-reading that becomes significant for high number concentrations. The coincidence error depends on the probability of having more than one particle in the sensing volume, which is given by the Poisson distribution and depends only on the mean number of particles in the sensing volume. That means that for a given number concentration the coincidence error depends only on the size of the sensing volume; making the sensing volume as

small as possible therefore minimizes coincidence errors. If an OPC suffers from coincidence losses, then every coincident event of two or more particles will also result in a sizing error, as the coincident signal has usually a higher amplitude, and hence is interpreted as a larger particle than the single particles producing the signal. This error cannot be easily corrected, whereas it is possible to correct the total particle number concentration measured for coincidence losses. The following equation describes the relation between the concentration n_i indicated by the instrument and the real concentration n_p (Pisani and Thomson, 1971):

$$n_\mathrm{i} = n_\mathrm{p} \mathrm{e}^{-n_\mathrm{p} q \tau} \tag{3.34}$$

In this equation τ is the minimum time difference between two particles that can be detected separately. The product $q\tau$ can be interpreted as an effective sensing volume resulting from signal width and dead time of the electronics. The mean number of particles in that volume is given by $\nu = n_\mathrm{p} q \tau$ and the factor $e^{-n_\mathrm{p} q \tau}$ representing the under-reading is equal to the probability of finding the effective sensing volume free of particles (according to the Poisson distribution), which is the condition for the counter to be ready for counting the next particle. The coincidence error for a given number concentration can therefore ultimately only be reduced by reducing the sensing volume given by $q\tau$.

The indicated concentration n_i assumes a maximum at $\nu = 1$ and decreases again for increasing ν and hence n_p. When measuring high number concentrations, equation (3.34) can be used to correct the indicated number concentration n_i for coincidence losses to get the true number concentration n_p if $\nu < 1$:

$$n_\mathrm{p} = n_\mathrm{i} \mathrm{e}^{q \tau n_\mathrm{p}} \tag{3.35}$$

Unfortunately, this relation cannot be used directly as n_p depends on both the measured n_i and on itself. A recursive approximation, however, can be used to calculate n_p. For this purpose, on the right side of equation (3.35) n_p is approximated by the complete term on the right side substituting n_p now with n_i, which yields $n_\mathrm{p} = n_\mathrm{i} \mathrm{e}^{q \tau n_\mathrm{i} \mathrm{e}^{q \tau n_\mathrm{i}}}$. Instead of substituting n_p with n_i at this stage, this procedure can be repeated several times before eventually using n_i in place of n_p stopping in this way the recursions of the approxi-

mation. Three recursions yield for example

$$n_p = n_i e^{q\tau n_i e^{q\tau n_i e^{q\tau n_i e^{q\tau n_i}}}} \tag{3.36}$$

This can readily be calculated if sample flow rate q and minimum time difference τ between two particles that can be detected separately are known.

3.6 Summary

All these aspects of particle measurement had to be taken into account in the design of the prototype instrument described in the following chapter. The theoretical background given in sections 3.2 and 3.3 was later used for calculations that would predict instrument performance and enable certain design decisions and verifications. Potential sample loss mechanisms and error sources relevant to the instrument design, as outlined in sections 3.4 and 3.5, needed to be considered for avoiding or minimizing such errors.

4 Instrument Development

4.1 Instrument Design

4.1.1 Requirement Specifications

The range of existing commercial instruments suitable for use in air quality monitoring was reviewed in chapter 2; their respective advantages and shortcomings were identified. The customer requirements arising from legislative regulations are focused on instruments providing mass concentration rather than other metrics, such as number concentration. However, the ongoing discussion about health effects of particulate matter (see section 1.2) resulted in the need for monitoring other metrics (see section 1.3). Most of the current customers of particle counting systems can be found in industry and research. Their requirements range from simple monitoring purposes to sophisticated research studies. The users usually need real-time or near real-time instruments in order to perform time resolved studies or to satisfy the needs of industrial processes.

All these observations justified the aim of this work and, together with the theoretical considerations of particle measurement in chapter 3, led to the following requirement specifications for the prototype instrument. Such an instrument, being aimed for monitoring ambient air, would suit both routine monitoring of air quality parameters and monitoring for scientific purposes, as for example for epidemiological studies or air quality modelling.

Size Range and Size Fractions The total size range of the instrument would be required to extend from 10 nm to 2.5 µm or 10 µm. Within these limits several size cuts would subdivide the range into size fractions, wherein the particles would be counted.

A lower limit of 10 nm was considered appropriate since it encompassed

the nucleation mode which for urban environments typically is in the region from 20 nm to 40 nm (Morawska et al., 1999b; Shi et al., 1999). Number concentration of particles below 10 nm would not be required, this information would only be of interest when studying particle formation processes.

Number Concentration The instrument should measure number concentration between 0.01 cm^{-3} and 500 000 cm^{-3}. Typical number concentrations encountered in ambient coarse, fine, and ultrafine size ranges are within these limits.

The lower concentration limit is relevant only for the coarse particle range. Here the concentrations are usually very low, whereas the contribution to the particle mass concentration is significant. The lower concentration limit must allow monitoring aerosols with fairly low mass concentrations. The selected limit of 0.01 cm^{-3}, is equivalent, for example, to a mass concentration of 1 $\mu g \cdot m^{-3}$ for a monodisperse aerosol consisting of 5 µm spheres with a density of 1 600 $kg \cdot m^{-3}$.

The upper concentration limit has relevance only for the ultrafine particles. Near busy roads the average concentrations for ultrafine particles reach ~ 100 000 cm^{-3} (Harrison et al., 1999a). On a short timescale concentrations can go up to 500 000 cm^{-3}.

Mass Concentration Either $PM_{2.5}$ or PM_{10} mass concentrations should be measured by the instrument as daily or weekly averages.

Data Logging The instrument should offer the possibility of data logging and download logged data to a computer.

Operating Conditions The operating conditions should be from −10°C to 50°C in a noncondensing environment, and the instrument should be suitable for outdoor use. Ambient temperature and relative humidity should be logged.

4.1.2 Design Overview

In order to meet the requirements the instrument was to be implemented as shown in figure 4.1. The overall design features are described in this and

the following section. The ambient air would be introduced into the system through a sampling inlet head with a predefined size cut using the PM_{10} convention. An alternative sampling inlet with a $PM_{2.5}$ size cut would allow measuring either PM_{10} or $PM_{2.5}$ mass concentration, according to which inlet was used. The sample air was to be transported to three different sample analysing systems where representative parts of the sample air could be analysed. The sample analysing systems were to be an OPC, a CPC, which for further ultrafine fractionation could be preceded with means of size discrimination, and a filter for gravimetric sampling.

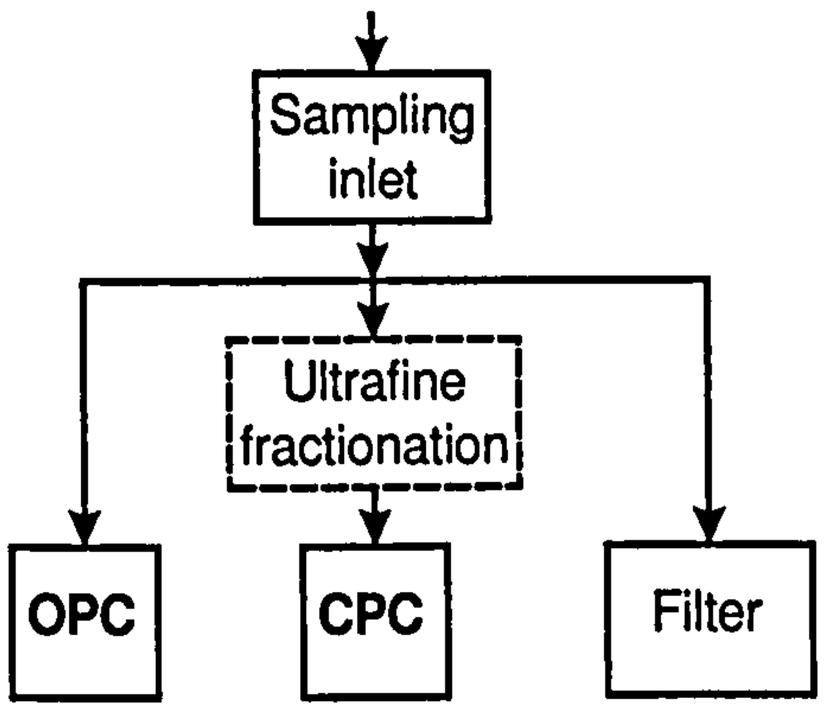

Figure 4.1: This block diagram shows the proposed particle counting system with the different technologies.

The OPC would allow counting and sizing of particles larger than its selected lower detection limit of ~250 nm. The CPC would allow counting of particles larger than its selected lower detection limit of about 10 nm. Particle sizing, however, would not be possible with the CPC, as mentioned in section 2.1. Combining the results of OPC and CPC would allow, indirectly, counting particles in the size fraction between their lower limits of 250 nm and 10 nm. The number concentration of this size fraction (10 nm to 250 nm) would be calculated by subtraction of the sum of the number concentrations of the OPC size fractions, representing particles with diameters larger than 250 nm, from the total number concentration measured with the CPC, representing the particles with diameters larger than 10 nm. A size fractionation technique prior to the CPC would ultimately provide the possibility of subdividing this size fraction in two or three ultrafine size fractions.

The filter would collect the particles for a gravimetric analysis resulting in the mass concentration of particles smaller than the size cut defined by the

inlet. The particle mass concentration would be averaged over the sampling time required for collecting a measurable filter load.

A number-to-mass conversion method would complement the measured mass concentration. The method would give real-time or near real-time, size-segregated mass concentration.

4.1.3 Sample Analysis

Size Fractions The size cuts that divide the total size range in individual size fractions would be provided by different techniques. Three or four size fractions would be defined by the OPC. These size fractions would subdivide the range between the lower detection limit of the OPC and the upper limit of the instrument. They would be given by signal thresholds used to trigger different counters according to the amplitude of the signal, which were related to the particle size (see section 3.2). The different counters would give the numbers of particles found in the different size fractions.

The size range between the lower detection limit of the OPC and the lower detection limit of the instrument, defined by the CPC, would be ultimately subdivided in two or three size fractions using an ultrafine fractionation technique. With the use of the OPC and CPC in parallel only the total count in this size range could be given, and this size range would represent the lowest size fraction of the instrument—the ultrafine size fraction.

Number Concentration The measurement of small particle number concentrations is limited by the increased statistical error (see section 3.5) associated with low numbers of counted particles. To keep this error small one must take a large sample using long sampling times t_s. The lower concentration limit of the instrument would therefore be valid only for long sampling times. While the accuracy is decreasing towards very low concentrations, the instrument should still provide a good indication of such concentration levels.

The upper concentration limit would be given by the coincidence error (see section 3.5). Should this limit be too low then the use of photometric mode of the OPC detecting the droplets in the CPC (operating mode in which not single pulses of light but the DC level of the detector is used as a measure of higher particle concentrations) could extend the concentration

range to the required level. Alternatively, dilution of the sample air in the CPC could also be used.

Mass Concentration The instrument would collect the sample air drawn through the duct on a filter so that average PM_{10} or $PM_{2.5}$ mass concentrations, according to the sampling inlet used, can be determined. This gravimetric sampling would provide daily or weekly averages. A flow rate of 5 $l \cdot min^{-1}$ would be sufficiently high to allow for taking gravimetric samples. The pump necessary for this flow would be fairly small.

PM_1 mass concentration would be derived from the sub-micrometre particle counts. Theoretical investigation and experimental tests would be required to show the accuracy of such a number-to-mass conversion (see section 5.4).

4.2 Optical Particle Counter

4.2.1 Implementation

Configuration of Optical System

Figure 4.2 shows the configuration used by the OPC. To maximize the sensitivity of the OPC and achieve the lowest detectable particle limit possible, particle irradiance and collection efficiency of the scattered light are primary factors. These factors can also be used to classify OPCs in instruments using a *white* or *monochromatic light* source and in instruments collecting scattered light in *near-forward* scattering direction or over a *wide solid angle*. Besides sensitivity, another important design feature of an OPC is its response characteristic, which ideally should be a monotonic function of particle size. For this ideal response an OPC should use white light irradiance and wide solid angle collection (McMurry, 2000). Laser light irradiance, however, is several orders of magnitude higher than what is usually possible with white light sources and consequently most currently available OPCs use a laser light source and also for this work a laser would be used. More considerations about the light source are reported in the next subsection.

Both optical configurations, near-forward scattering and wide solid angle, when used with laser light, exhibit a non-monotonic dependence of re-

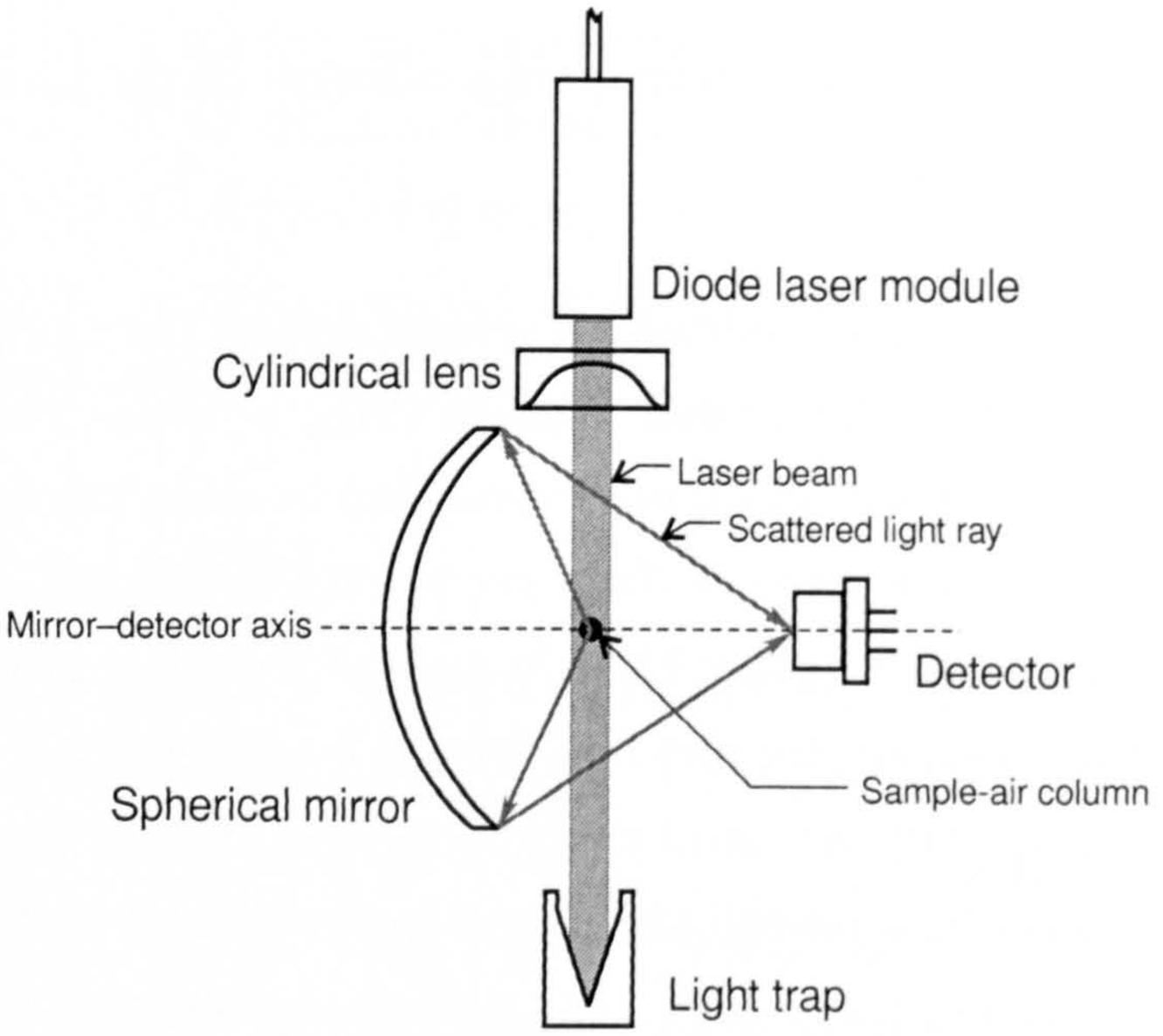

Figure 4.2: The figure shows the main components of the OPC. The sensing volume is defined by the intersection of the laser beam and the sample-air column which is perpendicular to the section shown.

sponse on size which is oscillating for particles larger than about the wavelength of the laser light. This might prohibit particle sizing in a certain size range. It can, however, be acceptable for the size resolution required for the OPC that was to be designed. The selected design should be confirmed by theoretical modelling as described in section 3.2. This was done for the design described in the following and showed that while sizing between about 1 μm and 2 μm would not be accurate (due to the non-monotonic dependence of the scattered power on particle size in this range), size cuts at 1 μm and 2.5 μm would be possible (as can be seen in figure 4.3), which would satisfy the requirement specifications.

Although a near-forward scattering configuration can have a higher sensitivity due to more intense scattering in the forward direction, a wide solid angle scattering configuration was selected because such a configuration, if not extending close to forward direction, is less prone to increased stray-light background, as optical components do not need to be placed close to the laser beam. Such an increased stray-light background could adversely affect the sensitivity of the OPC, compromising the advantage of the near-forward configuration. Wide solid angle collection of scattered light is usually achieved using a mirror which allows a compact design. Here, a spher-

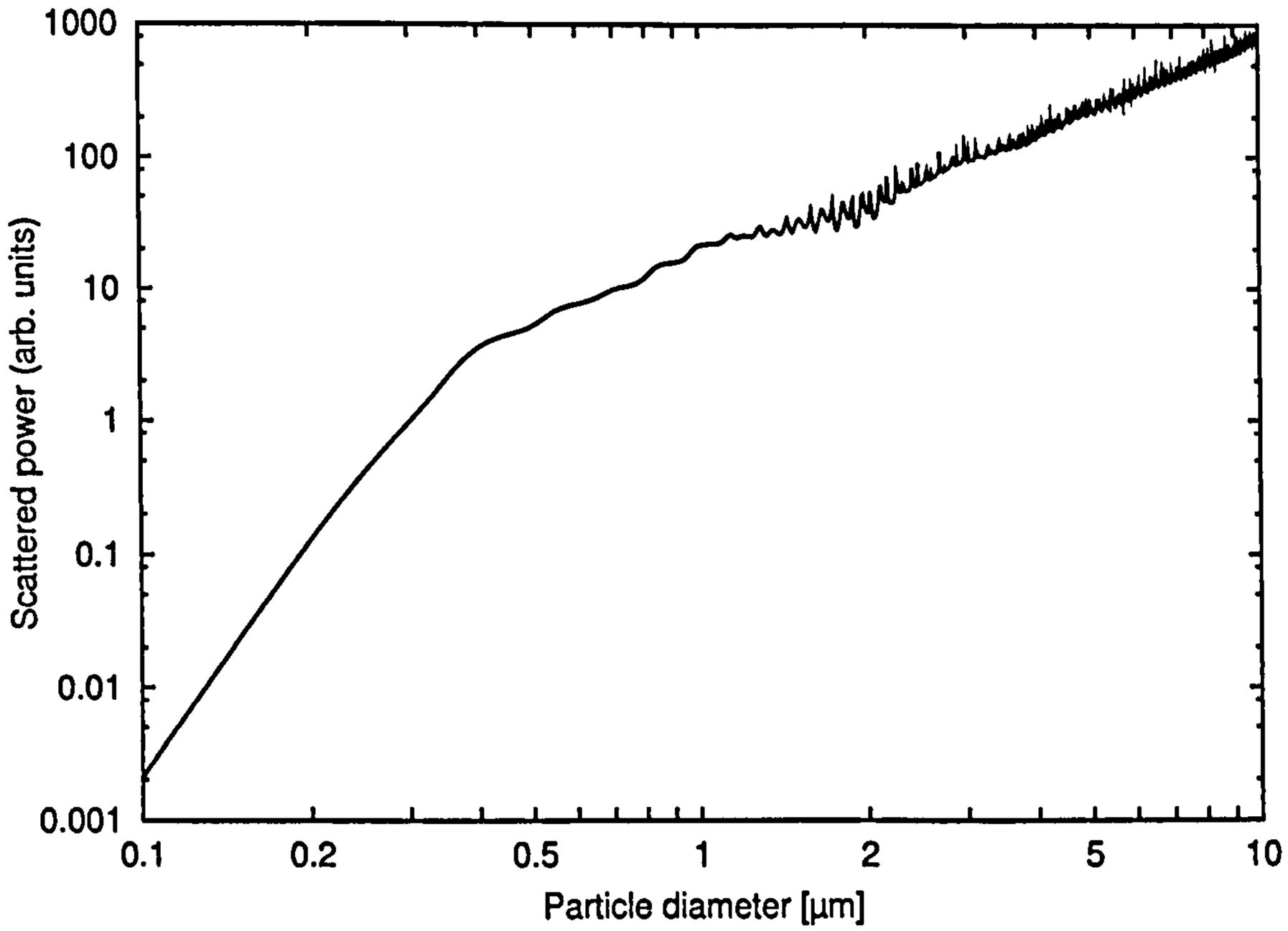

Figure 4.3: OPC response curve for polystyrene latex (PSL) particles (refractive index $m = 1.59$) at a wavelength $\lambda = 650$ nm. The calculated scattering power (in arbitrary units) is plotted against the particle diameter in the range from 100 nm to 10 µm.

ical mirror was selected in a configuration at 90° to the laser beam as depicted in figure 4.2. In this configuration the mirror is not close to the laser beam thus avoiding the stray-light problems which could arise when using other mirror designs, as for example an ellipsoidal mirror design where the laser beam is taken out of the OPC chamber through a hole in the mirror (Gebhart, 2001). Although maximizing the sensitivity of the OPC to achieve a low detectable particle limit was the primary aim, the OPC configuration was also selected for its simplicity, so that it could be developed quickly and a prototype module built and tested early in the presented work. The selected design should also be used as the detector for the CPC, so that the design was desired to be compact, flexible, and robust as well.

The volume in which particles can be detected—called the *sensing volume* or *scattering volume*—and the detector for the scattered light, are arranged on the axis through the centre of the mirror and the centre of the sphere defining the mirror surface. This optical axis of the mirror—called mirror-detector axis in the following—is at an angle of 90° to the laser beam, as given by the configuration. The laser beam and the optical axis are both

perpendicular to the sample-air column. In this configuration, the sensing volume is defined as the intersection between the laser beam and the sample-air column. The scattered light from single particles in the sensing volume is collected by the mirror and focused to the sensitive area of the detector. The dimensions and distances (see table A.2) have been selected to assure that all the scattered light reflected by the mirror would fall completely on the detector independent of the position of the particle in the sensing volume. The image of the sensing volume is therefore completely encompassed by the sensing area of the detector. In this way the solid angle in which scattered light is measured is the same for all detected particles, so that the detected part of the scattered power and hence the amplitude of the detector signal depends on the particle size and not its position when detected. As a consequence, there are no partly detected particles which would result in undersizing. The required dimensions were determined using a ray-tracing program (ZEMAX) and selecting a configuration in which the sensing volume would create an image of approximately 1 mm in diameter on the detector.

Light Source

For the OPC a red diode laser in the visible range of 630 nm to 670 nm was selected to illuminate the sensing volume. Visible red and near infrared diodes are widely available. The reasons for choosing the visible red instead of near infrared are an easier adjustment with a visible laser and higher intensity of the scattered light especially for particles below 500 nm (for small particles the scattered power is proportional to λ^{-4}, Knollenberg, 1985). This effect outweighs the lower efficiency of most photon detectors at visible red as compared to the near infrared. The OPC uses a diode laser module with collimating lens and laser-power control. The power is fixed by the manufacturer at a value close to the nominal maximum of the diode laser of about 30 mW, its power in the collimated beam was measured to be around 25 mW. Predicting scattered power of particles (with refractive index $m = 1.59$, the value of test particles that would be used later for calibration) indicated that this power level would be sufficient to provide detectable scattering from particles down to $\sim$250 nm. At this particle size a photodiode current of 0.3 nA was estimated, which would yield a sig-

nal of 3 mV with an amplifier feedback resistor of 10 MΩ. The incident laser intensity was estimated for a laser beam at the sensing volume having a width of 1.5 mm (dimension of the collimated beam), and a depth of 0.1 mm (as focused by cylindrical lens), a value selected for reasons explained below. The scattering from spherical particles was calculated with Mie theory (Mie, 1908). As outlined in section 3.2, the scattered power depends on the polarization of the incident light. Although the light from the laser diode is linearly polarized, it was not taken into account at this stage, as the effect is only secondary and affects mainly measurements of particles smaller than about 500 nm. The scattered power is integrated over the solid angle of the mirror as seen from the sensing volume. For all scattering angles θ within this solid angle the scattered intensity is calculated using equation (3.2), where I_i and k are not considered, so that the calculated values need to be scaled with I_i/k^2 in order to get the absolute scattered power. This integration was added to the Mie Fortran program from Bohren and Huffman (1983), which was then used to calculate the scattered power as depicted in the response curve in figure 4.3 for this OPC design, with its mirror–detector axis at 90° to direction of incident light and a mirror half angle of 52°, as seen from the sensing volume.

Table 4.1 shows these estimates, listing all design parameters and calculated quantities. The absolute scattered power for a single particle detected by the photodiode was calculated using the unitless calculated power (as in figure 4.3) scaled by the power $I_i/k^2 = I_i\lambda^2/4\pi^2$.

Sensing Volume

To achieve maximum sensitivity required the use of a laser which should also be focused to further enhance the particle irradiance. To guarantee a proper response characteristic required avoiding partially detected particles. In addition to the correct positioning of mirror and detector with respect to the sensing volume, this also requires that the laser beam illuminates uniformly the complete cross section of the sample-air column, so that all particles in the sample experience the same irradiance. The laser beam was therefore focused by a cylindrical lens only in one direction in a thin layer perpendicular to the direction of the sample air flow.

Besides sensitivity and response characteristic, a low coincidence error is

Design parameters		Derived quantities	
Power	25 mW	Laser intensity I_i	167 kW·m^{-2}
Wavelength λ	650 nm	Size parameter α	1.21
Width of laser beam w	1.5 mm	Part. veloc. in sens. v.	5.31 m·s^{-1}
Focal depth	0.1 mm	Width of signal	18.85 µs
Particle diameter d_p	250 nm	Required bandwidth	63.7 kHz
Particle refr. index m	1.59	Sensing volume V_s	$3.14 \cdot 10^{-12}$ m^3
Number conc. n_p	1 000 cm^{-3}	Under-reading factor	0.997
Sample-air col.	0.2 mm	Detected power	0.735 nW
Sample flow rate q	10 ml·min^{-1}	Photodiode current	0.294 nA
Photodiode sensitiv.	0.4 A·W^{-1}	Output amplitude	2.9 mV
Feedback resistor R_F	10 MΩ		

Table 4.1: Design parameters used for the OPC prototype module. Estimates for laser irradiance and sample flow dimension are used to predict the response to particles with sizes close to the required lower detection limit.

another important design issue. An ideally low coincidence error requiring a small sensing volume as described in section 3.5 involves again design considerations regarding laser beam and sample-air column. The sensing volume is, as mentioned above, the intersection between the laser beam and the sample-air column and is given by the focal depth of the laser beam and the diameter of the sample-air column. The laser focal depth was estimated as 0.1 mm, which was considered as an upper limit for possible focusing and hence a worst case for minimizing the sensing volume. A focal depth of less than 0.1 mm should be achievable given the theoretical lower limit of around 3.4 µm (or slightly larger for a non-gaussian beam profile) arising from the formula for the focal depth $\frac{\lambda f}{\pi w}$ where λ is the wavelength of the laser, f the focal length, and w the width of the collimated beam (here $w \approx$ 1.5 mm and $f = 25$ mm). Since the maximum particle size is 10 µm, the laser beam should not be focused close to this lower limit, even if it should be possible, to avoid partially illuminated particles.

To guarantee an under-reading due to coincidence errors of less than 1% at a particle concentration n_p of 1 000 cm^{-3} and of around 10% at $n_p =$ 50 000 cm^{-3} and around 20% at $n_p = 100\,000$ cm^{-3}, the required sensing volume would be $2 \cdot 10^{-12}$ m^3. Table 4.2 shows indicated number concentrations n_i and under-reading factors for several particle number concentrations n_p using this volume and equation (3.34) in the form $n_i = n_p e^{-\nu}$ where ν is the mean number of particles in the sensing volume V_s calculated by

$\nu = n_p V_s$.

n_p	$\nu = n_p V_s$	n_i	Under-reading
1 cm^{-3}	0.000 002	1.000 cm^{-3}	0.999 998
1 000 cm^{-3}	0.002	998 cm^{-3}	0.998
50 000 cm^{-3}	0.1	45 242 cm^{-3}	0.90
100 000 cm^{-3}	0.2	81 873 cm^{-3}	0.82
500 000 cm^{-3}	1	183 940 cm^{-3}	0.37

Table 4.2: Coincidence error of a sensing volume of $V_s = 2 \cdot 10^{-12}$ m^3, as required for the described OPC. Various number concentrations n_p are shown with the corresponding mean number ν of particles in the sensing volume V_s, concentration n_i indicated by the measurement, and a factor representing the under-reading of the OPC.

For the OPC, where ambient particle number concentrations in the size range 250 nm to 10 µm rarely exceed 1 000 cm^{-3} (Harrison et al., 1999a; Hughes, 1999; Shi et al., 1999), the coincidence errors can be neglected using such a sensing volume. For the CPC, which would use the OPC to detect and count the alcohol droplets, these errors would be acceptable too. If a better focus could be achieved, the sensing volume, and therefore the coincidence error would be smaller; otherwise a correction such as proposed in equation (3.36) could be used for the higher number concentrations.

For achieving this sensing volume one would need to focus the sample-air column to a diameter of ~0.16 mm. Considering that a laser focus better than 0.1 mm should be achievable, the sample-air column was selected to have a diameter of around 0.2 mm. This can more easily be achieved if the sample flow rate is low, which would also avoid a high sample velocity through the sensing volume. A high velocity would otherwise cause short signals needing a fast amplifier, which could compromise the gain of the amplifier and hence the sensitivity of the OPC. The flow rate of the sample air into the OPC was consequently fixed to a low value of 10 ml·min^{-1}. Such a low flow rate is conveniently sampled with a capillary tube.

The focusing of the sample-air flow, apart from reducing the sensing volume, would have another advantage. It would constrict the flow to the central part of the laser beam which has a more uniform intensity. The focusing was designed to be achieved using a layer of clean air surrounding the sample-air flow, as shown in figure 4.4. This layer of clean air, usually called

sheath air, would be focused through a nozzle. The capillary end would be placed in the centre of this focusing nozzle, at the position of the starting taper. Dimensions and sheath-air flow were selected so that the two flows,

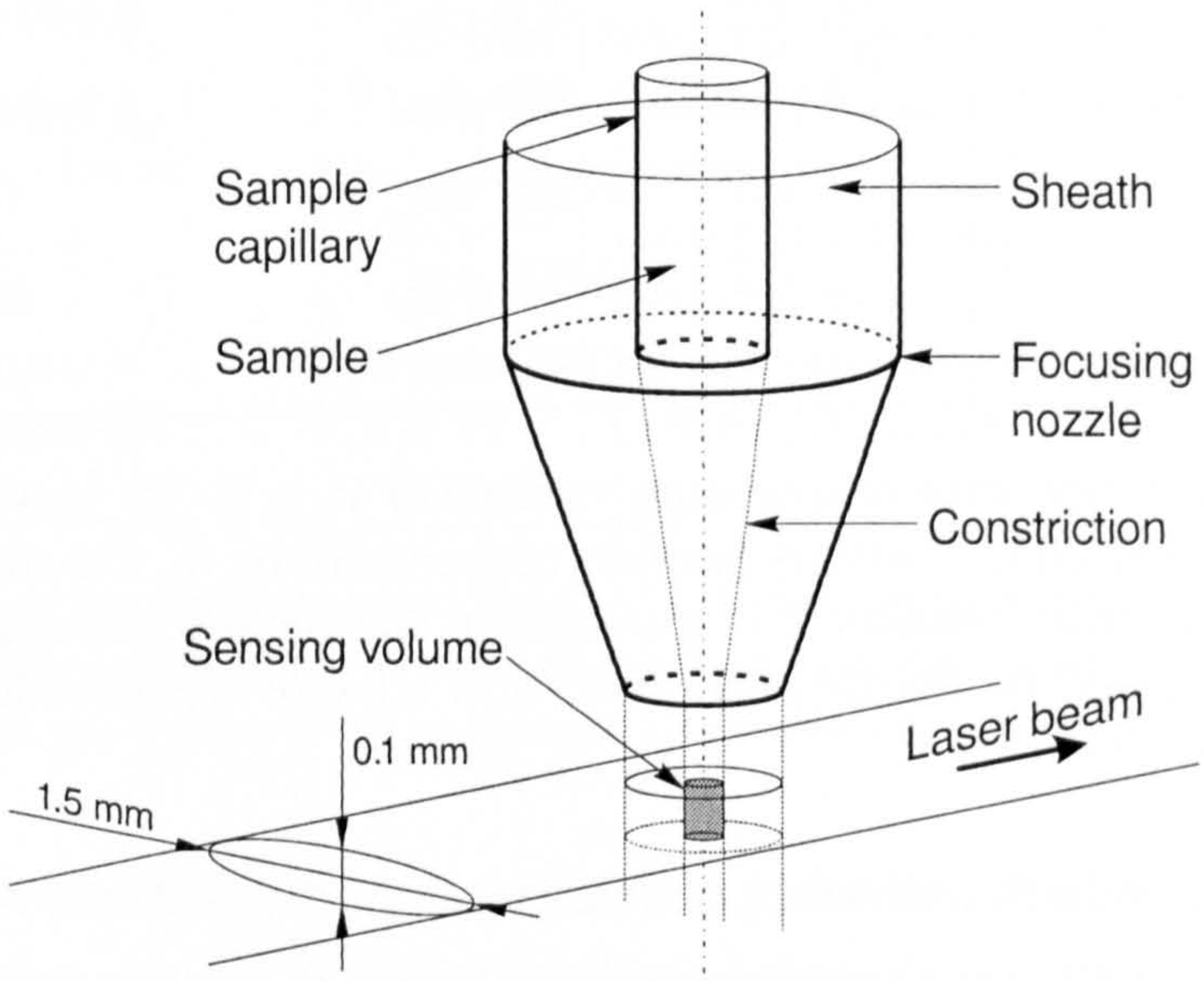

Figure 4.4: Focusing of the sample-air flow. The sample is introduced in the centre of the sheath air. The sheath air is focused through a nozzle, also constricting the sample air. The laser beam and the sensing volume (greyed) are also indicated.

sample air and sheath air, would have similar mean velocity when they join in the nozzle and the sample flow diameter would reduce to approximately 0.2 mm. Non-compressible flow was assumed (given by the velocities being much smaller than sonic velocity) so that the cross-sectional area occupied by sample air flow contracts at the ratio given by nozzle contraction. A nozzle contracting from a diameter of 5.0 mm to a diameter of 1.0 mm was selected in combination with a capillary tube with an inner diameter of 0.76 mm and an outer diameter of 1.59 mm and a sheath-air flow rate of approximately 0.4 $l \cdot min^{-1}$.

Detector

The detector used is a reversed biased photodiode. Reverse biasing reduces the capacitance of the diode and therefore improves the response time of the detector (see, for example Graeme, 1995). The signal is amplified with a transimpedance amplifier using a high-bandwidth and low-noise operational amplifier (see figure A.1 in appendix A.2 for the circuit diagram of the amplifier). The required bandwidth of the transimpedance amplifier is de-

termined by the width of the pulses of scattered light, which depends on the velocity of particles and the depth of the laser beam in the sensing volume. A volumetric sample flow rate of 10 $ml \cdot min^{-1}$ with a diameter of 0.2 mm gives a particle velocity of 5.3 $m \cdot s^{-1}$; a depth of the laser beam of 0.1 mm then results in a pulse width of 19 µs, requiring a detection bandwidth of about 100 kHz. To maximize the gain of the amplifier a high feedback resistor of 9.4 MΩ was selected, similar to the value of 10 MΩ used to estimate the response of the OPC (see table 4.1).

Signal Processing

To measure the particle number concentration in the different size fractions the output signal of the amplifier is further processed in a peak detector, which, having different threshold levels, triggers different counters according to the height of the signal amplitude. Every counter therefore counts particles scattering as much or more light than that corresponding to the respective threshold level. Thus particles with size corresponding to the amplitude given by the threshold level or larger are counted. To count particles in four size fractions the peak detector needs four threshold levels corresponding to the four lower size limits of these size fractions. This assumes that the upper size limit of the size fraction with the largest sizes is given by the size cut of the sampling inlet. While this is not true for the OPC prototype described here as it does not use a sampling inlet, it will be the case for the prototype instrument, as described later in section 4.4. The peak detector measures the signal amplitude relative to the base level corresponding to no particle scattering—the DC level of the amplifier output. This is important as laser stray light in the scattering chamber falling on the photodiode produces a constant output level and the particle scattering signals are relative to this stray-light level. Although it is compensated for, the stray light should be reduced to a minimum in order to reduce the noise of the output signal.

The peak detector also includes a further signal amplification which has to be adjusted through calibration in order to get all threshold levels within the operating range of the electronics of the peak detector. Figure A.3 shows the circuit diagram of the peak detector.

Flow Arrangement

Apart from the clean sheath air, the design includes an additional stream of clean air directly into the OPC chamber. This clean-air flow is called *bleed air* and helps maintain the chamber free of contamination by particles. Most of the air extracted from the OPC chamber is recycled and—after filtration—returned as clean air comprising the two components of sheath and bleed air (see, for example Knollenberg, 1985). Figure 4.5 shows the arrangement of chamber, pump, filters, and valve for adjusting the sample flow rate. The

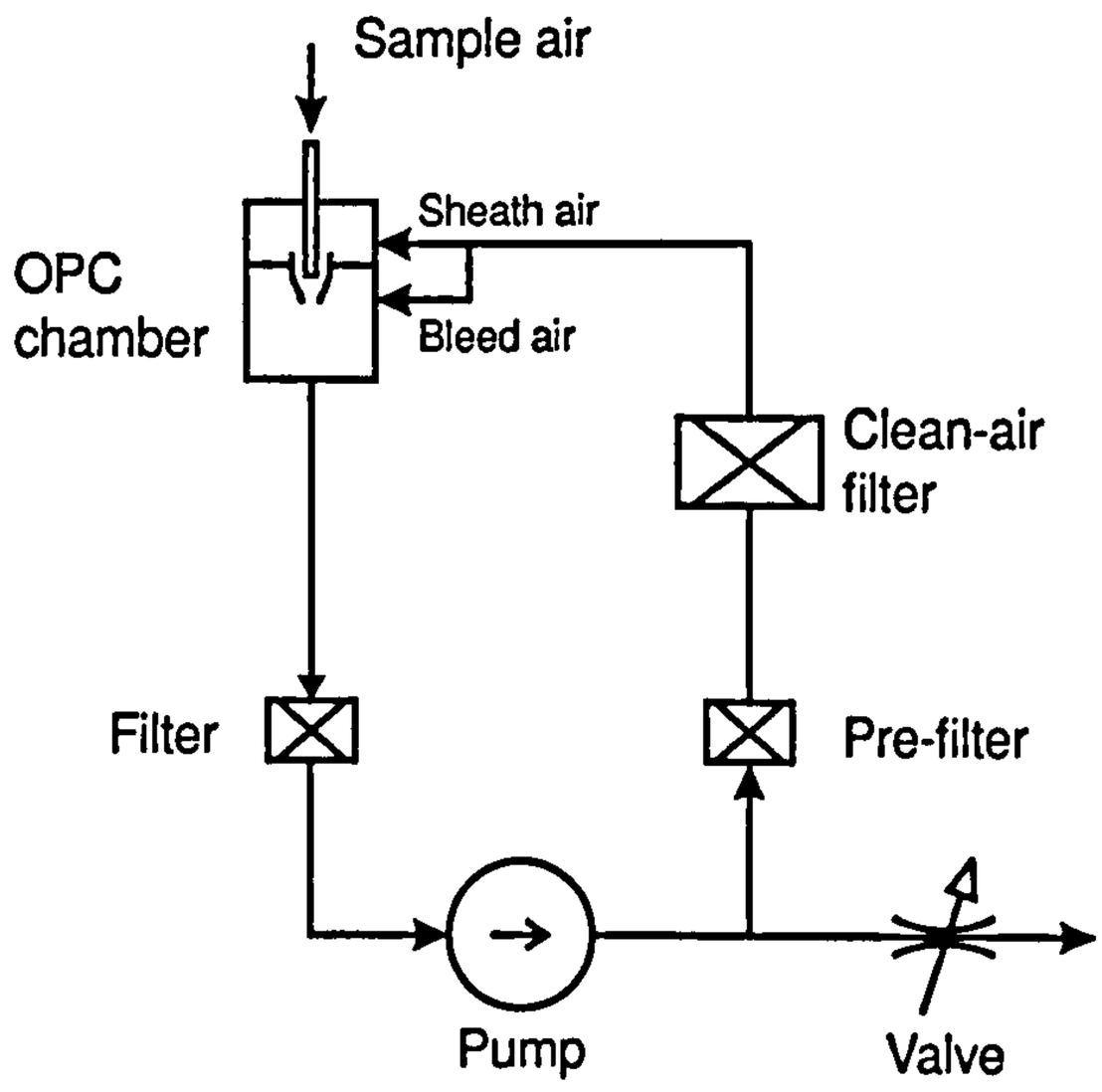

Figure 4.5: Flow arrangement of OPC.

pump load is adjusted to give approximately the desired sample flow rate of 10 ml·min^{-1}. The sample flow rate can then be adjusted more precisely using a valve which releases a small amount of air equal to the amount drawn in as sample air through the capillary tube (sample flow rate). The valve is placed in the part of the flow circuit that has a pressure above ambient. In this way the very low sample flow rate of about 10 ml·min^{-1} can be regulated without directly measuring it (a procedure that would be difficult without adversely affecting the sampling efficiency). A further advantage of this arrangement is the extended lifetime of the filters which are effectively contaminated only at the low sample flow rate, although the flow through the filters is much higher. This flow design makes it necessary to keep the OPC chamber airtight, as any leakage would result in a sample flow rate different from the flow rate of the air released through the adjustable valve.

The amount of clean air in this arrangement depends mainly on the pump load, the pre-filter, and the clean-air filter. The selected pump load creates pressure drops over these two filters and the valve which are very similar (valve releasing directly to ambient air; filters connected to OPC chamber which is at approximately ambient pressure). The valve is adjusted to release the 10 ml·min^{-1} sample air flow at this pressure drop. The pre- and clean-air filters were selected to give a clean-air flow rate of 0.8 l·min^{-1} at a pressure drop of around 0.5 kPa, a value conveniently suited for using a small needle valve. A Whatman Polycap TF(75) (pore size 0.2 µm) was used as clean-air filter. It has a very low pressure drop, while the pre-filter creates most of the pressure drop over these two filters. Whatman Minifilters were used as pre-filter and filter between the OPC extractor nozzle and pump.

The clean air is divided in the sheath and bleed air. The ratio of these two flow rates is, for a given focusing nozzle of the OPC, defined by the inner diameter of the bleed-air nozzle, which was selected to be ~1.2 mm reflecting the dimension of the focusing nozzle to yield approximately equal parts of sheath and bleed air. This might be further adjusted with an additional valve (not shown in figure 4.5) either restricting bleed air or sheath air in case tests with this flow arrangement should indicate the need for such further adjustment.

4.2.2 Construction and Set-Up

Assembly

The assembled scattering chamber of the OPC consists of the main body, laser module holder with laser module and cylindrical lens, mirror with its holder and adjustment flange, photodiode and its holder, light trap, focusing nozzle, inlet chamber cap with capillary tube, extractor nozzle, and sheath- and bleed-air nozzles. Figure 4.6 shows two sections of the OPC scattering chamber. The dimensions and operating parameters of the OPC, as used during calibration (see section 4.2.3), are shown in tables A.1, A.2, A.3, and A.4 in the appendix.

The mirror adjustment flange is screwed to the main body. The laser module, mirror, and photodiode holders are secured using adjustable screw settings (see below). All the nozzles for air inlet and outlet are fixed perma-

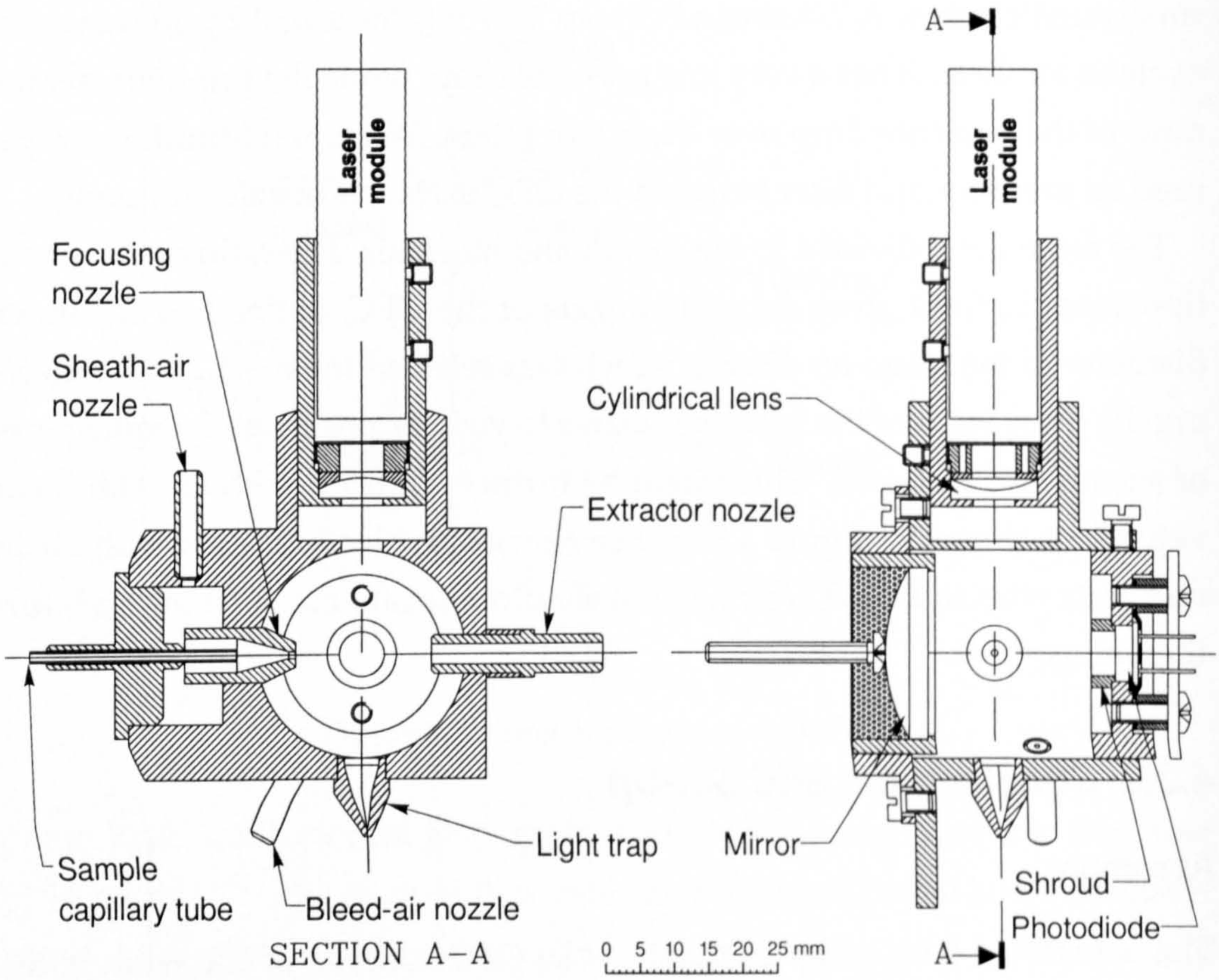

Figure 4.6: Sections of the assembled scattering chamber of the OPC.

nently to the chamber. Silicone grease is used to seal all moveable parts, thus keeping the scattering chamber airtight whilst still allowing the necessary adjustments for alignment.

Alignment

The design allows the mirror holder to slide in the mirror adjustment flange, and the laser module holder and the photodiode holder to slide in the main body, hence changing their distance to the sensing volume. Polyamide screws are used for securing the mirror, laser module, and photodiode holders (screw securing mirror holder not shown in figure 4.6) to prevent the aluminium surfaces from being dented or damaged which could make future adjustments difficult. Additionally, two sets of three polyamide screws allow the laser module (and thus the beam output direction) to be aligned. The mirror can be moved in the plane perpendicular to the mirror–detector axis by sliding the mirror adjustment flange on the main body prior to fixing it with screws (for this purpose the circular holes in the flange are wider than the screws).

The spatial position of the sample air flow is given by the fixed focusing and extractor nozzles. By the above described movements of the laser beam, mirror, and photodiode the optical system can be aligned so that the resulting sensing volume is imaged on the photodiode. The laser beam should be focused on the sample-air column which should cross the laser beam in its centre. The mirror and the photodiode should be aligned with the sensing volume and their distances adjusted to get the best image possible. To aid alignment, smoke was introduced into the sample air thus rendering the sensing volume visible to the naked eye (see figures 4.7 and 4.8). A more detailed description of the alignment procedure is given in section B.1 in the appendix.

4.2.3 Performance Evaluation

Laminar Flow Conditions

The stable, laminar-flow conditions of sample and sheath air between the focusing and extractor nozzles have been verified by introducing smoke into the air flows and observing the flow lines. Smoke in the sample air stays in

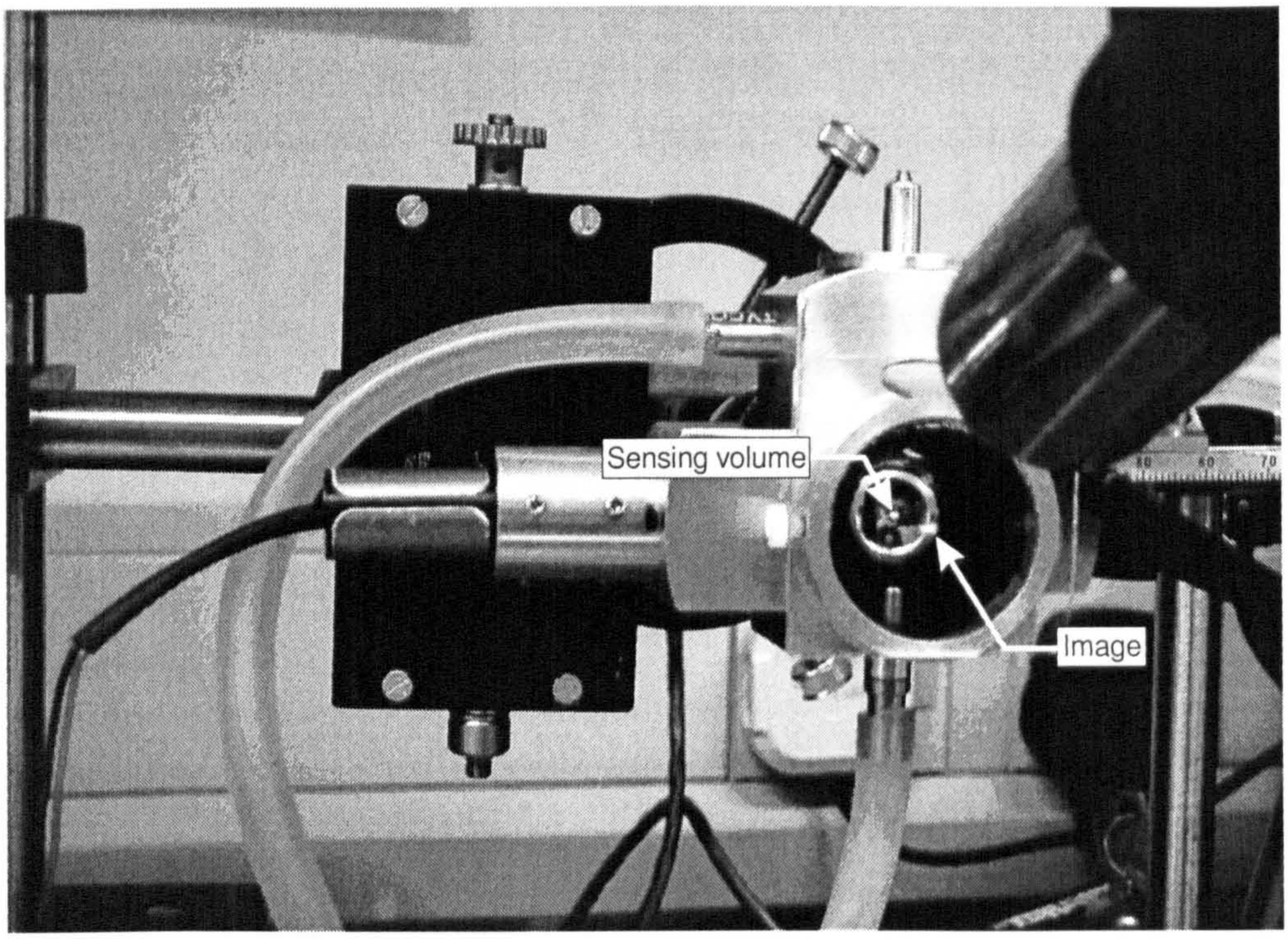

Figure 4.7: Set-up of smoke visualization of air flow through the scattering chamber of the OPC. Scattering in the sensing volume and the image of it produced by the mirror can be seen (indicated by arrows). For this photograph smoke was introduced in the sheath air so that the sensing volume appeared larger (intersection of laser beam and sheath-air column).

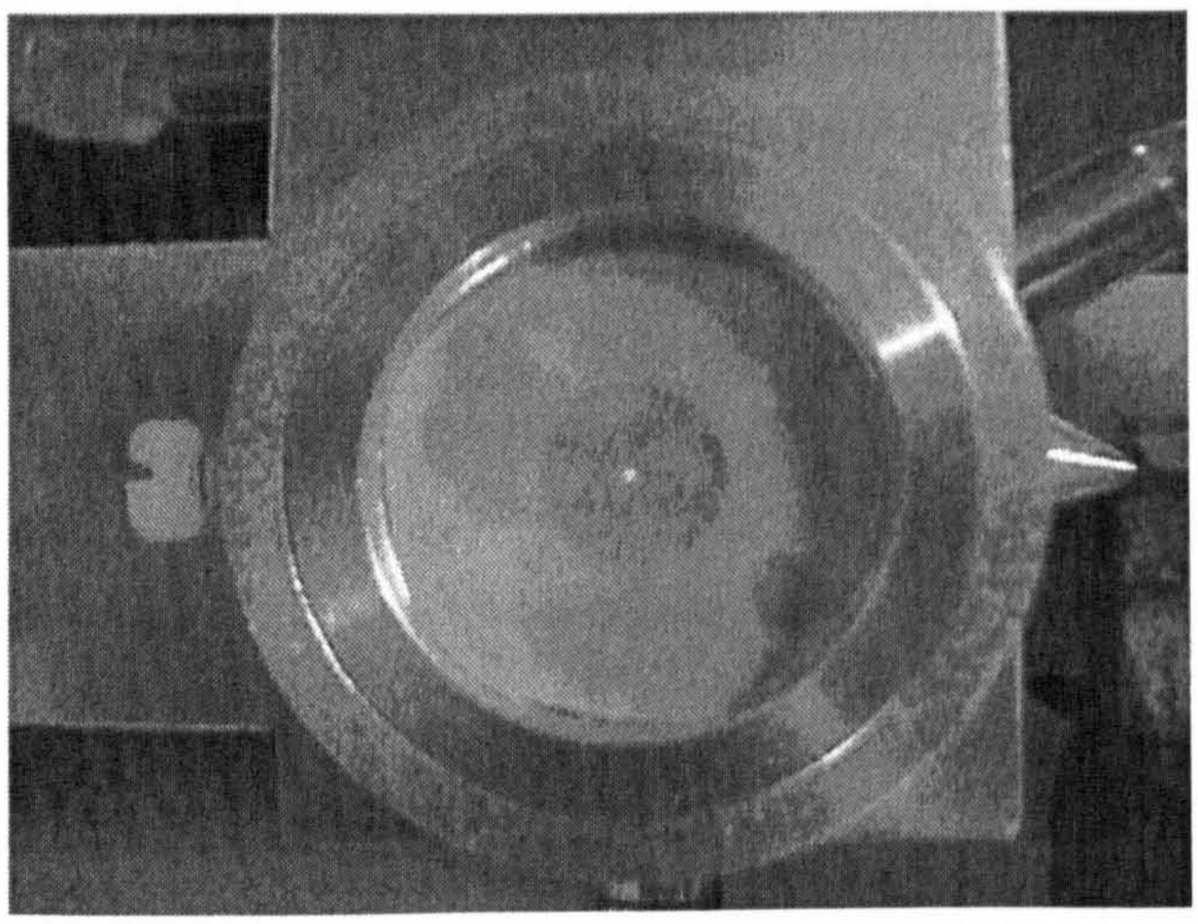

Figure 4.8: OPC alignment with the help of smoke visualization: the photodiode holder was mounted with a screen replacing the photodiode. The mirror produces an image of the scattering in the sensing volume, best alignment is achieved when image is sharp and centred on the screen as seen in the centre of the picture.

a thin column throughout the whole scattering chamber and is completely removed through the extractor nozzle. The sample-air column can easily be seen by probing it with a separate, hand-guided, laser beam because of the high concentration of the smoke particles scattering the light of the probe beam, whereas no smoke particles could be observed outside the sample-air column. The sheath air remains in a column of constant diameter too, as could be seen when adding smoke to the sheath air. In this case it could be observed that the sheath air was removed almost completely through the extractor nozzle and only little contamination with smoke was introduced into the chamber showing that the bleed air process was functioning correctly. The diameter of sample- and sheath-air columns could be measured as 0.16 mm ±0.01 mm and ~ 1.1 mm respectively by using a travelling microscope with micrometer adjustment. These values were close to values predicted from the design of the focusing nozzle, the diameter of the sample-air column being slightly better focused than the estimated 0.2 mm (see page 40).

Signal Detection with Photodiode

Different photodiodes were tested in the amplifier circuit which is shown in figure A.1, using two amplifier prototype boards identical in all respects but the photodiode used. The amplifier showed very similar performance with photodiodes having an active area of 1 mm^2 or 5 mm^2 respectively. With its intrinsic capacitance, the high feedback resistor ($R_F = 9.4\ M\Omega$) was found to be the limiting device for speed rather than the photodiode. Therefore the larger active area photodiode (OSD5-5T, Centronic) was used together with a high-bandwidth, unity-gain-stable, FET-input operational amplifier (OPA655P, Burr-Brown). The bandwidth of the amplifier with the photodiode fitted was tested measuring the rise time (signal increasing from 10% to 90% of full amplitude) of its output for an optical signal with a step change in intensity. The rise time measured was ~ (4 to 5) µs, which was sufficient for detecting the pulses produced by particles with the estimated width of 19 µs. The noise of the output of the amplifier was measured as ~ (1 to 2) mV (peak–peak) by feeding the signal through a low-noise pre-amplifier and observing it then with an oscilloscope. Here, the reported values have been measured with the transimpedance amplifier which has

been used later for the calibration of the OPC. The output noise governs the lower detection limit of the OPC. Low output noise is therefore important besides a high bandwidth and a high gain. These three quantities cannot be optimized independently and compromises are necessary.

The stray-light level in the scattering chamber was relatively high; the resulting constant output level of the amplifier being approximately −80 mV. Such an output level corresponds to the amplitude expected for a particle with diameter of around 800 nm (using parameters as shown in table 4.1). The bias of the amplifier output, as measured when the laser is switched off, is ∼ −10 mV. An attempt was made to reduce the stray light by masking the main part of the front face of the laser module, leaving only a cross section with the dimensions of the laser beam. This was not successful in reducing the stray-light level as detected by the photodiode. Observation of the beam profile at different distances from the laser module showed that the main part of the stray light (visible to the naked eye) left the laser module through the opening of the masks at various angles to the axis of the laser beam. It is believed that reflections from the edge of the collimating lens in the module would create a considerable amount of this stray light. Although masking the stray light from the laser beam at a second position could reduce the stray light, this was not tested, as it could make alignment more difficult (masks would need to be moved during alignment of the laser beam). Efficient reduction was instead achieved by shrouding the photodiode to reduce the half angle of the accepted light rays to 30°, so that the photodiode detects light only coming from the mirror and other areas such as the light trap are blocked (the shroud is shown in figure 4.6). The output level of the amplifier was reduced to ∼ −13 mV, nearly as low as the level when the laser is switched off.

Calibration

The aim of the calibration of the sizing capabilities of the OPC was to verify the calculated response curve (see figure 4.3) and to determine the magnitude of the response. Before calibration, the flow visualization tests were repeated confirming a sample-air column of 0.16 mm ±0.01 mm, which was measured again with the travelling microscope. It was also attempted to measure the laser focus by filling the chamber with smoke and using the

vernier adjustment of the travelling microscope to determine beam depth. When best focused, the laser beam showed a depth of $\sim$ 0.03 mm, which was at the measurement limit of the vernier of the travelling microscope (one division corresponds to 0.01 mm). Since this was smaller than the estimated upper limit of achievable laser focus of 0.1 mm mentioned above (see page 38), showing that a better focus can be achieved indeed, the pulse width of the OPC signals was also shorter than estimated—too short for the amplifier. In order to increase the pulse width, the laser beam was slightly defocused by withdrawing the laser module by a distance of around 2 mm so that the focus was not in the sensing volume but 2 mm away from it. The laser beam depth at the sensing volume was then measured as 0.10 mm $\pm$0.01 mm.

The OPC calibration was performed using polystyrene latex (PSL) spheres (refractive index of 1.59) of known sizes. The PSL spheres were aerosolized from a suspension in water using a nebulizer (TSI TRI-JET Aerosol Generator). The generated particles were collected in a ballast chamber ($\sim$ 20 l) from which the OPC sample was drawn. The set-up is shown in figure 4.9.

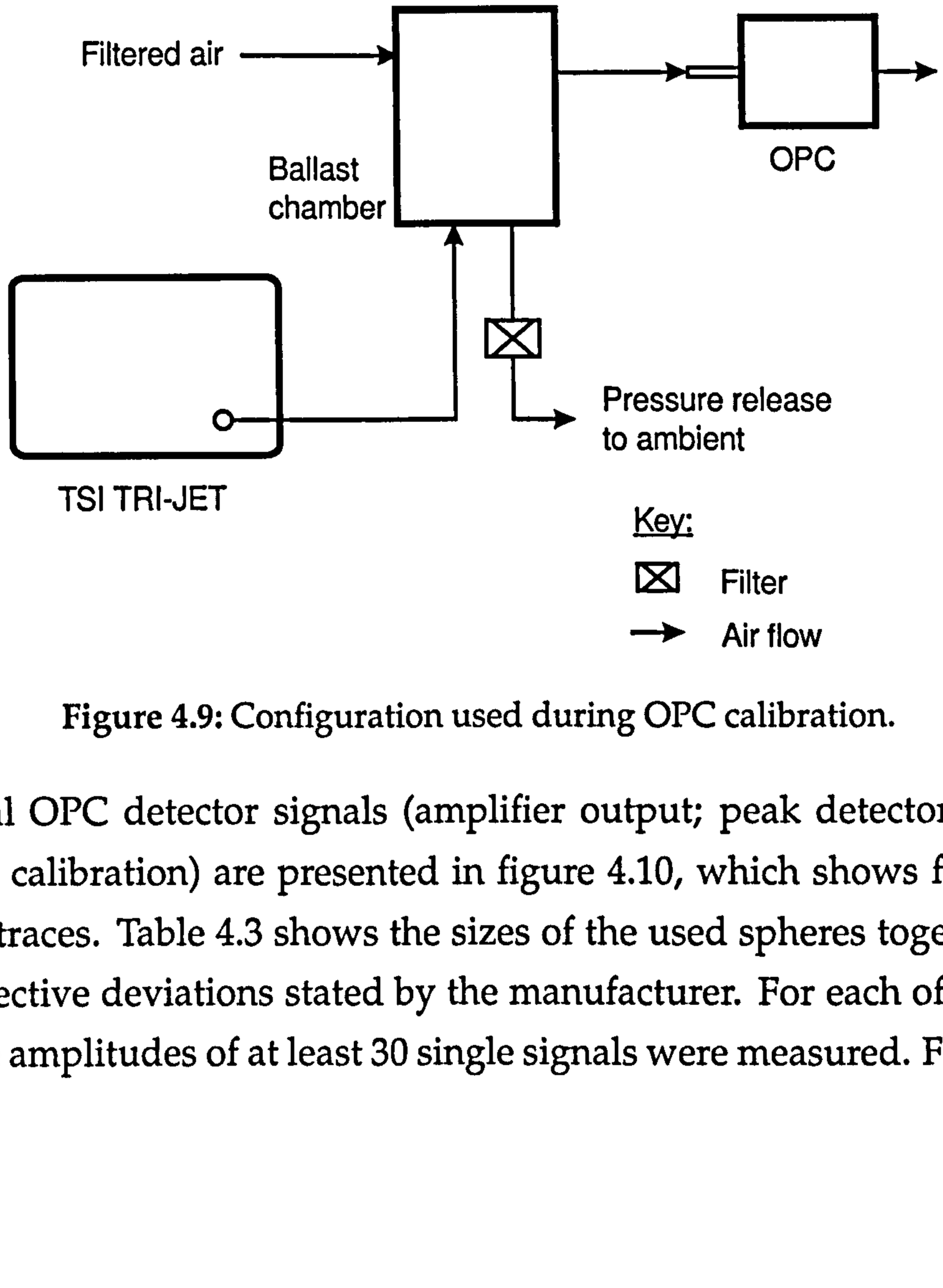

Figure 4.9: Configuration used during OPC calibration.

Typical OPC detector signals (amplifier output; peak detector was not used for calibration) are presented in figure 4.10, which shows four oscilloscope traces. Table 4.3 shows the sizes of the used spheres together with the respective deviations stated by the manufacturer. For each of the three sizes the amplitudes of at least 30 single signals were measured. Figure 4.11

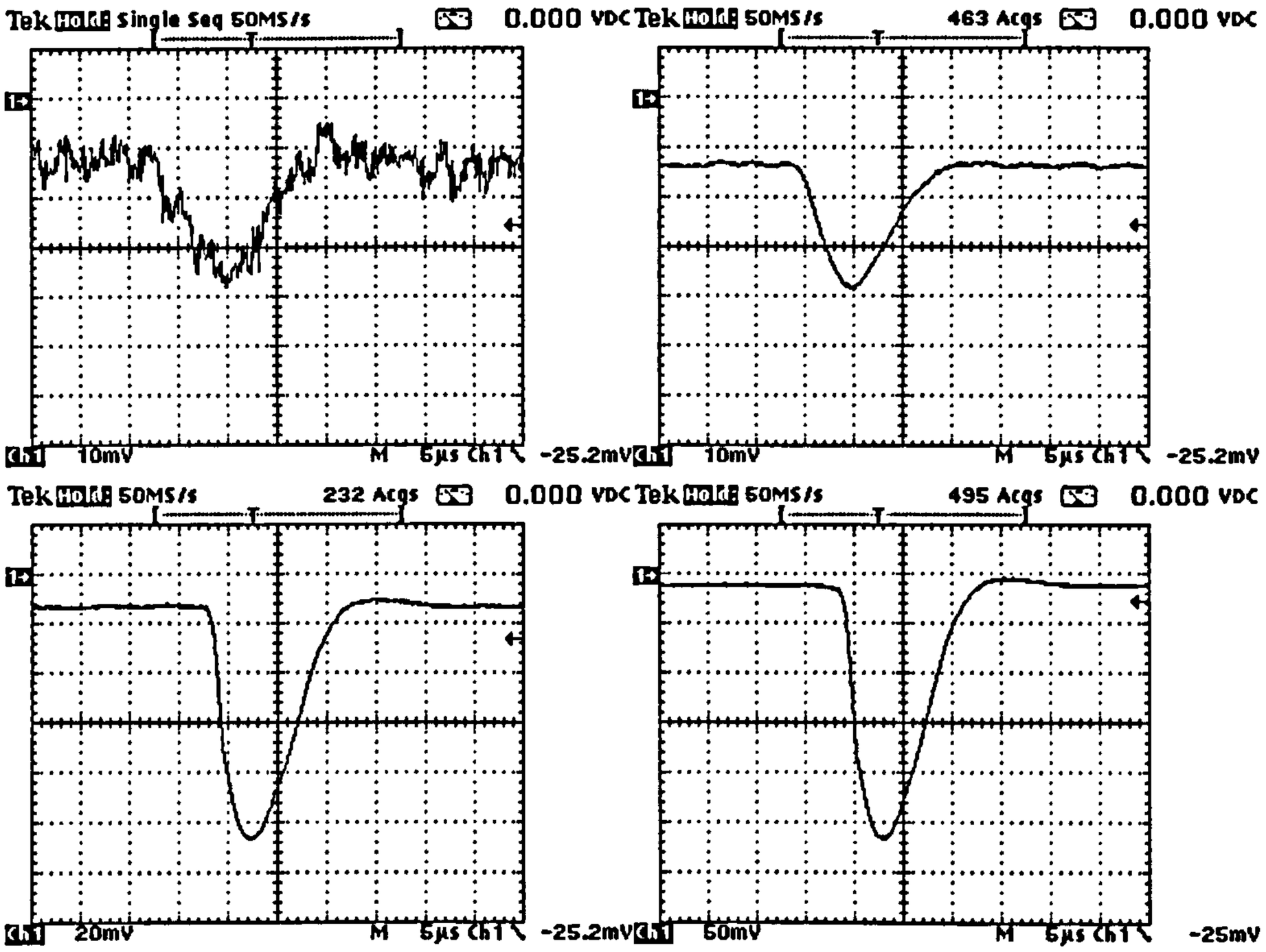

Figure 4.10: Typical OPC detector signals, captured on an oscilloscope. The upper two oscilloscope traces are from 0.356 µm PSL spheres, the left depicts a signal of a single particle, the right is the average of 64 signals. The lower two traces are the averages of 64 signals of 0.548 µm (left) and of 64 signals of 1.053 µm particles (right).

PSL spheres	Response	Fit
(0.356 ± 0.014) µm	(25.4 ± 3.6) mV	24.4 mV
(0.548 ± 0.016) µm	(94 ± 9) mV	93.9 mV
(1.053 ± 0.016) µm	(304 ± 16) mV	315 mV

Table 4.3: PSL spheres used for calibration and the respective results of calibration and theoretical calculation.

shows the measured amplitudes in a histogram. For every particle size,

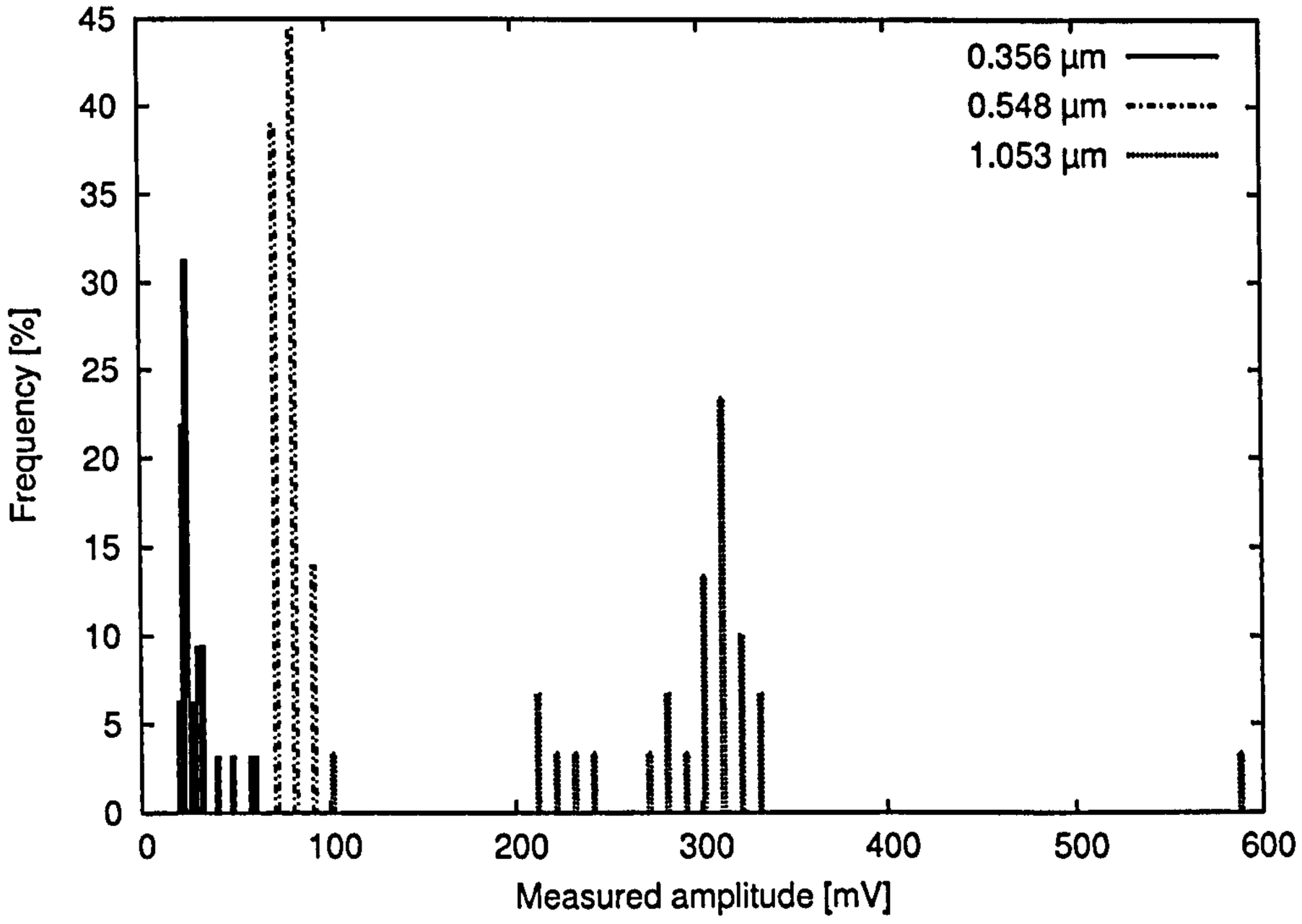

Figure 4.11: The histogram shows the measured amplitudes of the responses to the three different sizes of PSL spheres used during calibration. For each size about 30 scattering signals were examined.

most measured signals were grouped at a certain amplitude, however a few signals were observed at different amplitudes. This suggests that there could be contaminant particles, especially when sampling the 356 nm and 1.053 µm particles. These might result from residual particles in either the tubes of the nebulizer or the ballast chamber. Care was taken to reduce such residual particles when changing the generated particle size by flushing the ballast chamber and the connected tubes with clean air. Tests where less care was taken, indicated such residual particles, showing signals with amplitudes expected for both the newly generated particles as well as for the last generated particles. The resulting response values, which are also shown in table 4.3, are averages with standard deviations calculated excluding these contaminant particles. While for 356 nm particles 4 out of 32 signals (> 49 mV) and for 1.053 µm particles 10 out of 30 signals (< 255 mV and > 550 mV) were excluded, for 548 nm particles all 36 measured signals were considered. The calculated response curve can be fitted to these average values applying a constant factor to the normalized calculated values. The results of this fit (least squares of logarithmic differences) are presented

in table 4.3. The results of the calibration, also represented in figure 4.12 as a response curve, demonstrate the very good agreement between the measured response and Mie theory. Looking at the typical signals as seen on the oscilloscope (see figure 4.10), it can be seen that a signal with an amplitude of around 10 mV (at signal-to-noise ratio of approximately 1:1) should be detectable, corresponding to a lower detection limit of the OPC for PSL particles of about 280 nm, close to the required lower detection limit of 250 nm.

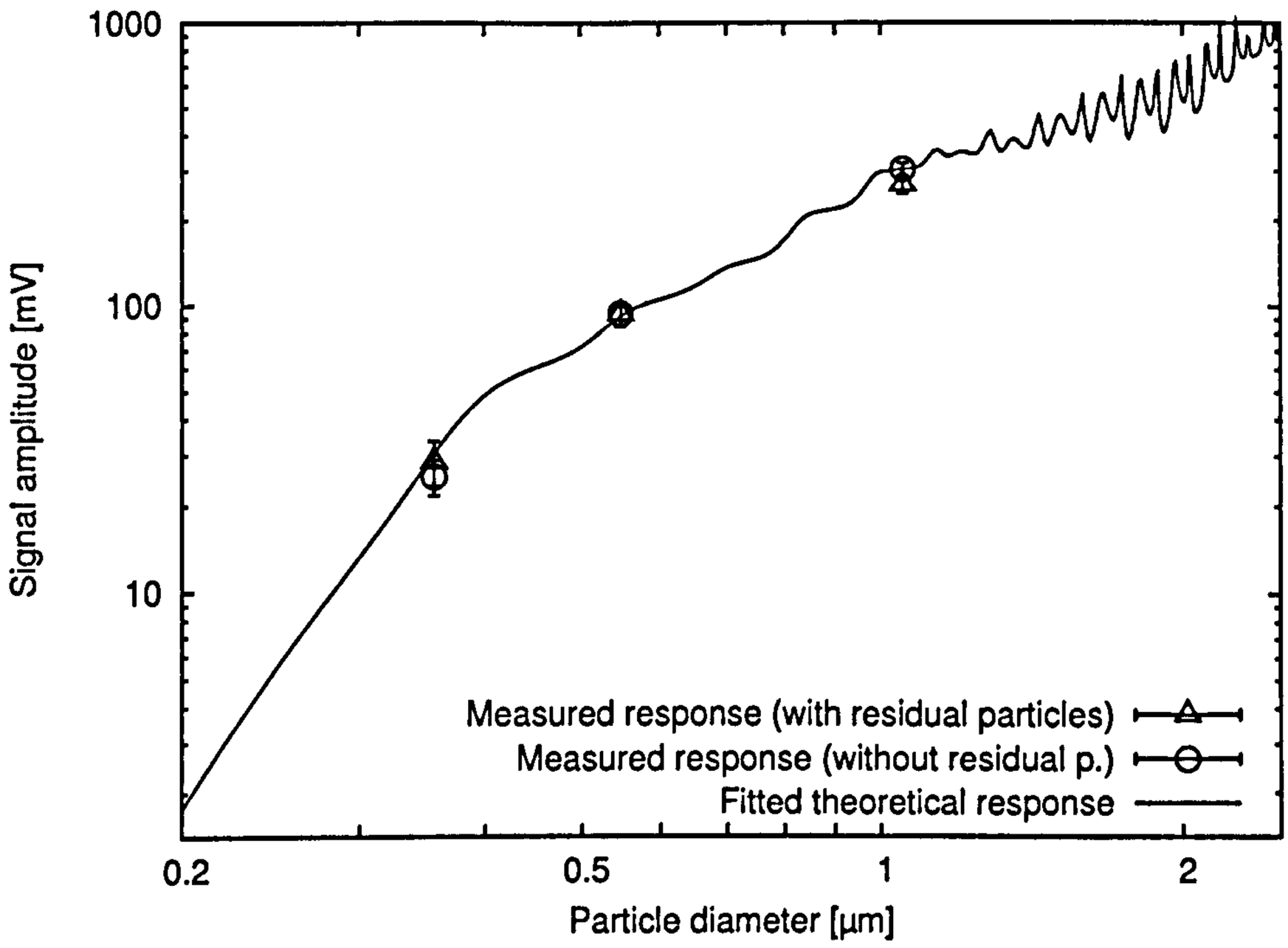

Figure 4.12: The measured response to PSL spheres of the three different sizes is shown together with the calculated response curve which was scaled to best fit the measured data. The values indicated are the averaged amplitudes of about 30 signals. The amplitude of detector signal is plotted against the particle diameter in the range from 200 nm to 2.5 µm.

Preliminary tests were also caried out with the peak detector, proving its operational principles. The gain of the further signal amplification of the peak detector was adjusted to 2.4 so that a threshold at around 2.5 V corresponded to a size cut at 2.5 µm for the calibrated size response of the OPC. The following four thresholds were calculated from the theoretical response to PSL spheres using the scaling factor found at calibration to fit the measured response and the gain of the peak detector: 13.6 mV for size cut at 250 nm; 172 mV for size cut at 500 nm; 715 mV for size cut at 1.0 µm; 2.37 V for size cut at 2.5 µm. The peak detector with these settings was used to

measure the number concentration in the four size fractions defined by the thresholds. It was used together with four counters on a microprocessor adapted from an existing instrument from Casella CEL Ltd which was re-programmed for these tests.

4.2.4 Improvements

The calibration of the sizing capabilities of the OPC was performed with PSL spheres having a refractive index of 1.59. The OPC was, however, later to be used with ambient outdoor aerosol which typically has a lower average refractive index (Hering and McMurry, 1991). The OPC with its PSL based calibration will therefore overestimate the size of most ambient air particles (Liu and Daum, 2000). The calibration of the next prototypes, which were to be used in ambient field trials, had to be corrected to the average response to ambient aerosol. This could be achieved by calculating the response to both PSL and average properties of ambient aerosol and then accounting for the difference in the two (see section 5.1.2).

The laser beam and the sample-air column were focused more tightly than predicted when estimating the OPC response, as mentioned earlier. Although the laser was defocused prior to the OPC calibration, the pulse widths were still only around 8 µs (see figure 4.10), which was still too short for the amplifier with its gain fixed by the feedback resistor of 9.4 MΩ and the resulting rise time of ~ (4 to 5) µs. However, since calibration results showed that the signal magnitude was still linear with scattered power (as the calculated response could be scaled to fit the measured response), it was decided not to increase the bandwidth by reducing the amplifier gain. Nevertheless the conditions of pulse width, amplifier gain, and its bandwidth are not ideal and improvements should be addressed in the future. Electronic solutions to the problem, however, are not easy as the bandwidth and gain can be increased together only at the cost of higher electronic noise as, for example, by using a second amplifier stage (Graeme, 1995).

A disadvantage of the sheath air being recycled is that it might be heated up by the pump and consequently heat the sample slightly above ambient temperature (Biswas et al., 1987). This was not considered at the time of design. It should be further investigated in future work whether this affects the sizing capabilities of the designed OPC.

The laser alignment procedure proved to be difficult, especially because of the number of degrees of freedom. Consequently the OPC design was changed to fix the position of the photodiode. Also the allowed movement of the mirror adjustment flange was reduced to only one direction (parallel to laser beam) by slotting the holes for securing it with screws, rather than having them circular. This was subsequently implemented and tested in a second OPC prototype and should be used for the OPC implemented in the prototype instrument (see section 4.4). The remaining freedom of movement was sufficient and alignment easier when a certain order of alignment steps was followed, which is reported in section B.2 in the appendix.

Several design changes were already implemented before the calibration was carried out (see section 4.2.3) and can be seen in the mechanical section in figure 4.6. These early design changes include:

1. The polyamide screws initially used to fix the laser module in its holder and the holder in the OPC main body (see section 4.2.2) were replaced with metal grub screws having only a polyamide tip. While still protected from denting, the laser module and the laser module holder could be fixed more firmly than was possible with the screws entirely made from polyamide.

2. The position of the bleed-air nozzle in the scattering chamber was changed. This was because tests with smoke visualization of the bleed-air flow (adding smoke to the bleed air and viewing with a hand-guided laser) had shown that the bleed air, after leaving the nozzle, stayed in a jet across the chamber. Earlier, the nozzle axis was directed in the centre of the scattering chamber so that the bleed-air jet crossed the sample-air column deflecting it slightly.

3. The focusing nozzle was changed to the design described in section 4.2.1 (see page 40). Earlier, the nozzle had a contraction from 5.4 mm to 2.3 mm and needed to be used with a higher sheath-air flow rate and a thinner capillary tube (inner diameter of 0.43 mm), which might have been prone to blocking with droplets when the OPC would be used as detector for the CPC.

4. The bleed-air nozzle was widened (from an inner diameter of 0.8 mm

to 1.2 mm) to increase the amount of bleed air which for efficient operation needed a flow rate similar to the sheath-air flow rate.

5. The extractor nozzle diameter was increased. Earlier, the cross section was similar to that of the sheath-air column and the change accounts for the increased bleed-air flow. The smaller cross section would otherwise cause acceleration of air entering the extractor nozzle, which might form local eddies and cause sample recirculation.

4.3 Condensation Particle Counter

4.3.1 Implementation

Figure 4.13 shows the different components and flow arrangement of the prototype CPC to be used for ultrafine particle detection ($d_p < 250$ nm). The implementation of this design, which in respect of the arrangement of saturator and condenser and the introduction of sample air was based on an earlier design by Stolzenburg and McMurry (1991), is described in the following paragraphs. Theoretical modelling to predict the saturation ratio and the lower detection limit (d_{min}) was carried out for this CPC design and the results are presented in section 4.3.3.

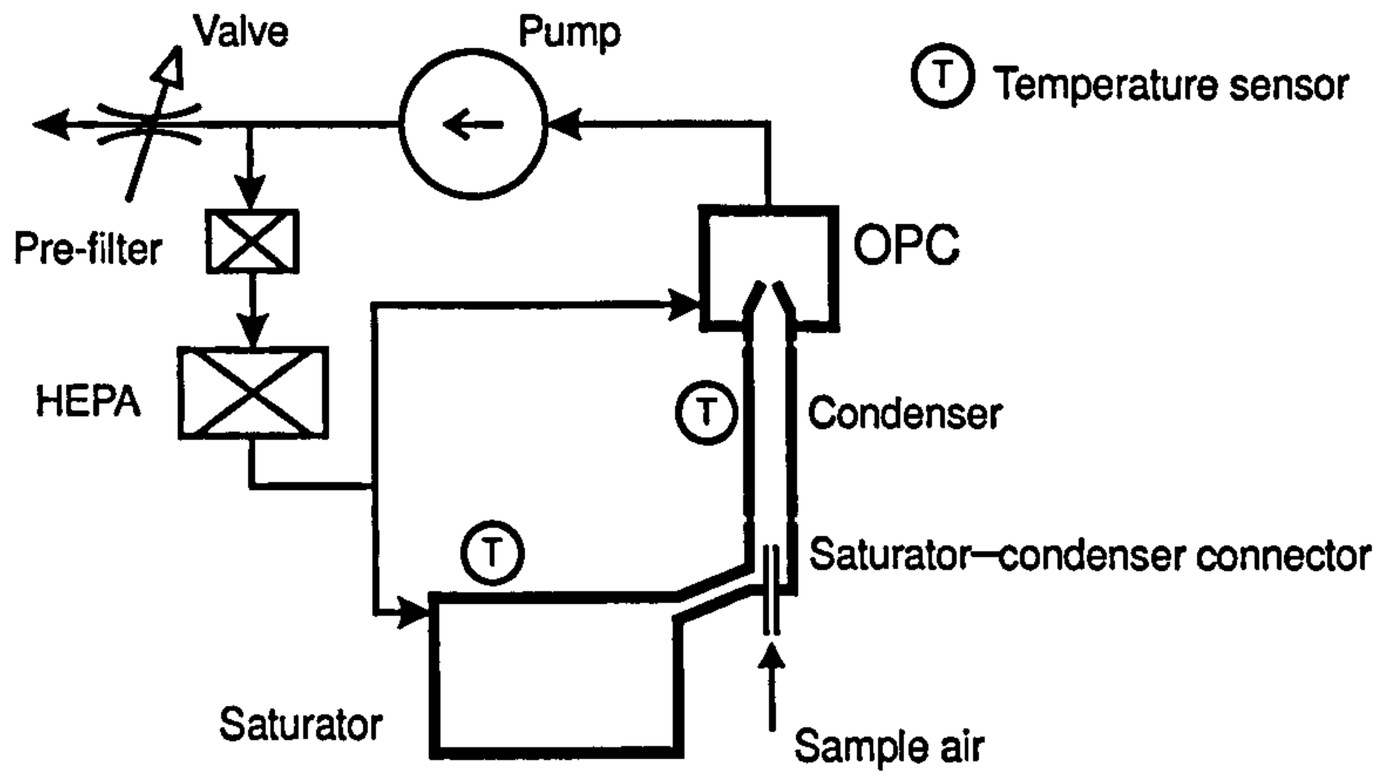

Figure 4.13: Flow arrangement of the CPC.

Saturator

Clean filtered air flows continuously through the saturator, which is heated. The inside wall of the saturator is covered with felt which is soaked with the

working fluid to increase the exposed surface and encourage evaporation. The working fluid is an alcohol, either iso-propanol or n-butanol.

Ideally the air leaving the saturator should be heated to the saturator temperature and its vapour pressure would be the saturation vapour pressure at this temperature. The volume of the saturator ($\sim$77 cm^3) was chosen sufficiently large and the air flow rate through it ($\sim$(300 to 400) ml$\cdot$min^{-1}) low enough to ensure a long residence time of the air in the saturator and, therefore a good approximation to this ideal situation. With these parameters the estimated residence time would be of approximately 12 s to 16 s.

The saturator volume is also required to be sufficiently large to take a quantity of alcohol which would permit operation of the CPC for at least a few days without refilling, necessary when used in field trials, and the above choice respects this consideration too.

Saturator–Condenser Connector

The alcohol-vapour laden air flows into the condenser via a connector piece. The sample air is introduced in the centre of the air from the saturator in this saturator–condenser connector. The connector was designed to join the two air flows without introducing turbulences so that the sample air remained in the centre of the flow throughout the cylindrical condenser. The cross section of the flow path through the connector was designed to remain constant and the dimensions of the saturator–condenser connector were chosen so that the mean flow velocities of the flow from saturator and the sample air flow were similar when joining. The maximum of saturation ratio S_R is reached on the centre line of the condenser (as will be shown later, see figure 4.16), so that the advantage of the sample air being in the centre is that all particles experience the same lower detection limit, resulting in a steep activation (and counting) efficiency curve (Stolzenburg and McMurry, 1991). Also diffusive losses of particles or particle containing droplets to the condenser wall are minimized by keeping the particles in the centre.

After the sample air is introduced in the air flow saturated with alcohol vapour from the saturator, the saturator–condenser connector extends for about 8 mm at saturator temperature, before it is joined to the condenser. This design was selected to allow vapour diffusion into the sample air flow before condensation starts in the condenser (Stolzenburg and Mc-

Murry, 1991). The saturator–condenser connector was thermally isolated from the cooled condenser ensuring the close to ideal situation of particles in saturated vapour at saturator temperature when encountering the cooler condenser temperature.

Condenser

The condenser is cooled to a temperature required to create the saturation ratio for the desired lower detection limit. For optimum operation the size of the condenser had to be chosen sufficiently long to include the maximum of S_R at a distance to the exit that permits the smallest particles—activating condensation only at maximum S_R—to grow to droplets which were sufficiently large for OPC detection. In a first instance, the length was chosen so that the transition time in the condenser was similar to that of the CPC described by Stolzenburg and McMurry (1991). At a later point, calculations were performed to verify the design. The results (see section 4.3.3) indicated potential improvements to guarantee sufficient droplet growth, which were addressed later (see section 4.3.4).

To permit the alcohol that condenses at the condenser wall to flow back to the saturator, the condenser axis is oriented vertically. Also the saturator–condenser connector design allows this liquid-flow without blocking the gas flow path.

Droplet Detection

Droplets produced by the condenser are detected by a second OPC. For clarity the original particle counting and size-classifying OPC will in the following be referred to as OPC1, whilst the droplet detector will be referred to as OPC2.

The OPC2 is essentially identical to the OPC1, with the exception that the former uses no sheath air to confine the sample flow, as the vapour-laden air coming from the saturator is surrounding the sample air in this design and hence the sheath air is not required. As no sheath air is used, the focusing nozzle of the OPC2 introduces the air flow from the condenser—including the sample air with the alcohol droplets in its centre—into the scattering chamber for detection of the droplets. It is expected that the sample in the

OPC2 would not be confined as well as in the OPC1 (sample introduced directly in the focusing nozzle, surrounded by sheath air), as the sample air is introduced upstream of the condenser, far from the focusing nozzle so that partial mixing with the surrounding air might occur. The sensing volume would in this case be larger. However, this would not increase the probability of coincidence as the mean number of particles in the sensing volume would remain the same. The sample would effectively be diluted (due to the mixing with part of the surrounding air) so that the number concentration n_p in equation (3.34) would decrease in the same ratio that the sensing volume ($V_s = q\tau$), or the flow rate q containing the sample, had increased. This would, therefore, result in the same under-reading as in case of the OPC1.

With high number concentrations, the concentration n_i indicated by the instrument could be corrected for coincidence errors by determining the exact under-reading using an acknowledged reference instrument. Comparing such results with equation 3.34 would give the effective sensing volume $V_s = q\tau$ responsible for the coincidence error, which could then be used to correct the indicated number concentration n_i using equation 3.36. Alternatively, one could directly determine the minimum time τ between two CPC droplets separately counted by the OPC2, for example, by observing many coincident and nearly-coincident signal pairs. While the latter approach has been done with the prototype instrument described in section 4.4, the former approach could be attempted in future work.

The laser on the OPC2 used for droplet detection is mounted with a 90° relative shift in axial orientation as compared to the laser on the OPC1 (see section 4.2), thus rotating the elliptical profile (laser diodes have typically an elliptical beam profile) of the collimated laser beam before focusing, yielding a wider beam profile. The laser here, is mounted so that the longer axis of the elliptical profile of the collimated laser beam is parallel to the mirror–detector axis. Thus, after focusing the beam with the cylindrical lens (which focuses only perpendicular to the mirror–detector axis) the sheet-like focused beam has still the width of the longer axis of the elliptical profile. This was done so that all air passing through the condenser will subsequently pass completely through the laser beam, as opposed to the OPC1 design which ensures only that the complete sample air will pass through the laser

and not the wider sheath air. The narrower beam used in the OPC1 results in a higher laser irradiance which was important for the sensitivity. This is different for the OPC2 where sensitivity is not the primary aim and the wider laser beam could be afforded without compromising the design.

The OPC2 uses bleed air, as does the OPC1, to avoid contamination of the scattering chamber with vapour and particle-containing droplets. This ensures that the optical components are maintained clean.

Flow Arrangement

As in the OPC1 design, the main part of the extracted air is recycled through a filter, here a HEPA filter (Whatman, HEPA-CAP 36) is used. The sample flow rate can be adjusted by the air released through a valve as shown in figure 4.13, in the same way as explained for the OPC1, as the flow arrangement is in most respects similar to that described in section 4.2.1. The resulting clean air is here used for the saturator and bleed-air flows respectively.

4.3.2 Construction and Set-Up

The dimensions and operating parameters of the first CPC prototype are presented in table A.5. Figure 4.14 shows a sectional view. The section through saturator, saturator–condenser connector, condenser, and OPC2 visualizes the air path through the instrument. The capillary tube that introduces the sample air into the centre of the flow from the saturator can be seen in the section. A box encloses the saturator and the HEPA filter (not shown in the section) for this first CPC prototype, thus providing thermal insulation of the heated saturator. In this way, also, the filter is heated, thus avoiding alcohol being collected in the filter as condensed liquid. The saturator is heated with a flat resistive wrap-around heater element.

The saturator–condenser connector is in thermal contact with the saturator, the two metal parts being glued together. It is thermally insulated from the condenser through a connector piece made of polyacetal, which has the same inner diameter as the condenser and the saturator–condenser connector.

The condenser is covered with an polyacetal enclosure to insulate it thermally. It is cooled with two Peltier elements which are placed between

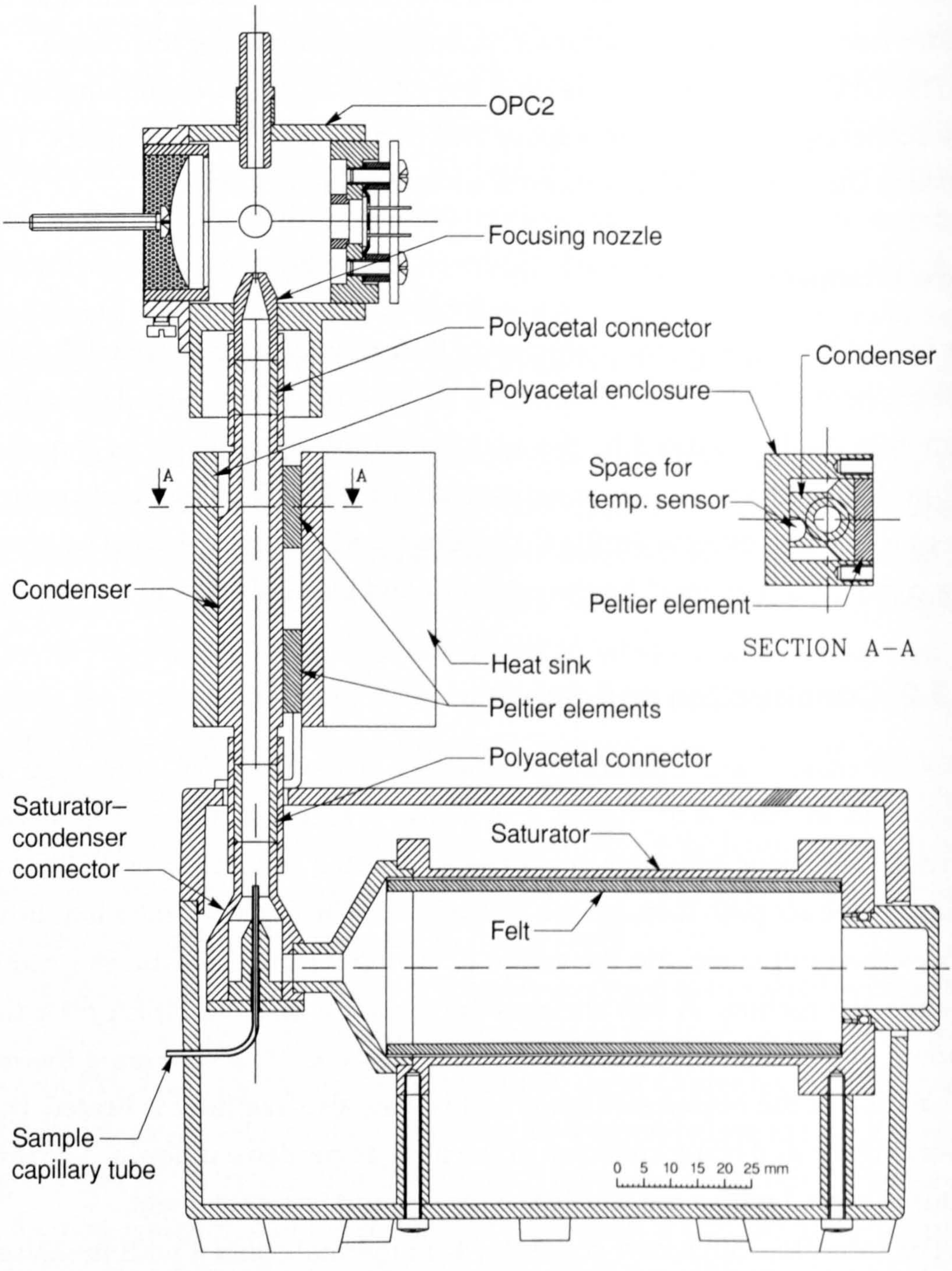

Figure 4.14: Section of the first CPC prototype. The section shows the saturator, saturator–condenser connector, condenser, and OPC2. The sample air is introduced through the capillary tube in the centre of the flow coming from the saturator.

the condenser and a heat sink. For effective cooling the heat sink needs to be large and ribbed with vertical fins to allow air circulation for enhanced heat dissipation by convection. With another polyacetal connector the condenser is connected to but thermally insulated from the focusing nozzle of the OPC2.

An integrated-circuit temperature sensor (LM335A, National Semiconductor) has been embedded in the metal of the condenser, while an external sensor of a digital thermometer has been fixed to the saturator (not shown in figure 4.14). The saturator can therefore be set manually to an arbitrary temperature above, and the condenser to an arbitrary temperature below ambient temperature by adjusting the heater and cooler currents until the desired temperatures are reached. While this was sufficient for testing this prototype, the temperatures would be controlled in the prototype instrument (see section 4.4.4) to maintain the stable conditions necessary for field tests.

4.3.3 Performance Evaluation

Calculations

Figures 4.15, 4.16, 4.17, and 4.18 show the results of modelling calculations performed for the CPC. The calculations, executed via a Perl program, compute the temperature profile, vapour pressure, saturation ratio, and resulting Kelvin diameter—indicating the minimum detectable particle diameter d_{min}—as well as the droplet growth after condensation has started. They were evaluated at a condenser temperature of 15°C, saturator temperature of 35°C, a flow rate through the condenser of 400 $\mathrm{ml \cdot min^{-1}}$, and assuming the air is saturated with alcohol vapour (iso-propanol for these calculations) at the saturator temperature. The program uses the analytical solution of the Graetz problem as described in section 3.3. The eigenvalues β_i were calculated with Mathematica as described by Mikhailov and Cotta (1997) and they agree with the values given by Brown (1960) (only first eigenvalue differs on the ninth digit after the decimal point). Here, for the calculations the first six eigenvalues were considered. The functions ψ_i were calculated using equation (3.18) for n up to 60 (from $n = 50$ no considerable difference in the calculation results was noticed). The coefficients a_i were calculated

using equation (3.20) by integrating over $\hat{r}$ from 0 to 1 in 50 equal steps, evaluating the function to integrate at the arithmetic mean of each interval. The solution was not computed at the boundary, but the values from boundary conditions (3.15) and (3.16) were taken instead. Table 4.4 shows all quantities with their respective values used by the Perl program.

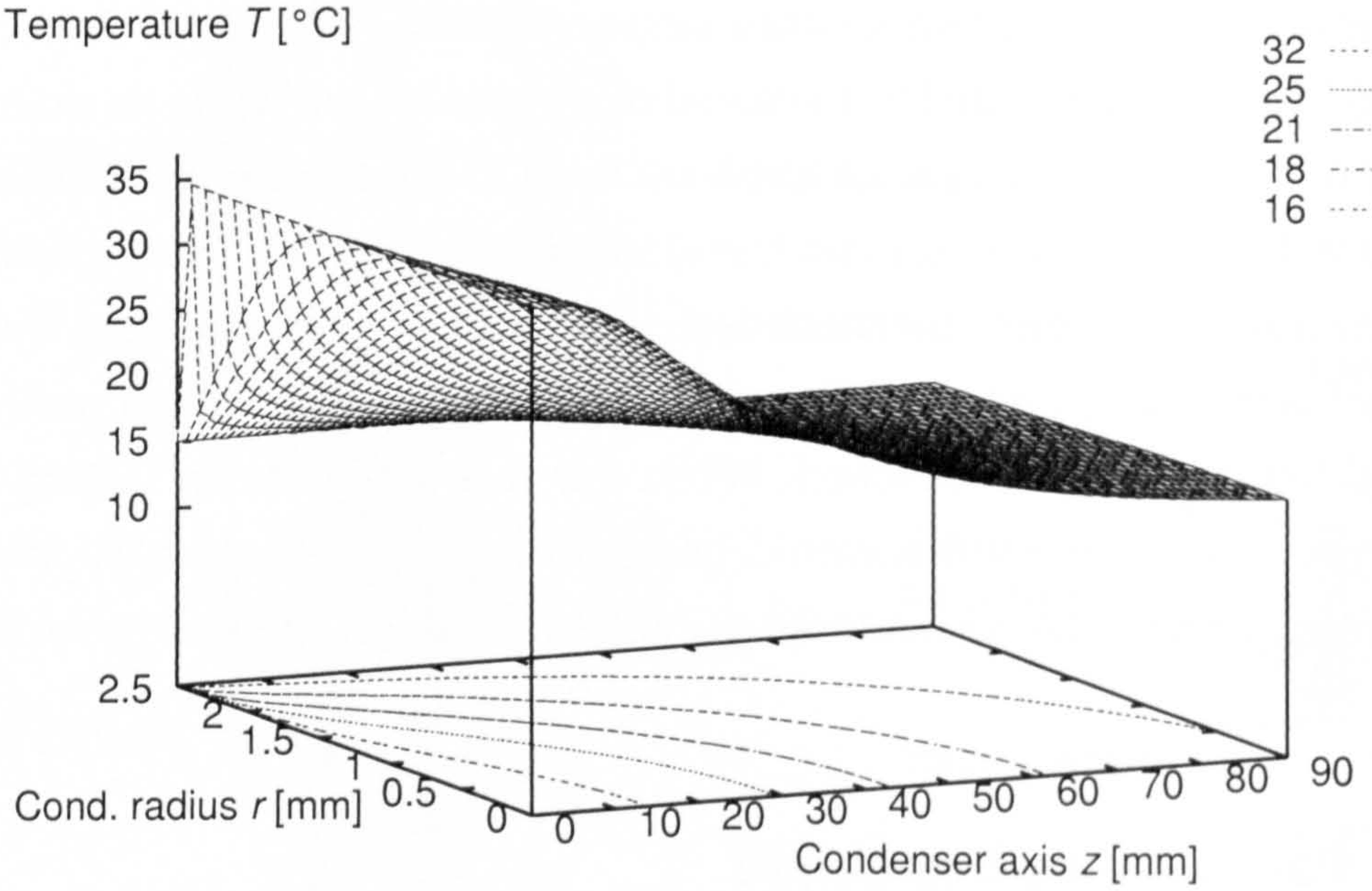

Figure 4.15: Calculated temperature profile inside the condenser at 15°C for air of a temperature of 35°C saturated with iso-propanol vapour flowing into the condenser at a flow rate of 400 $ml \cdot min^{-1}$. The air is cooled most efficiently near the wall. The vapour pressure has a similar profile (due to similarity of equations (3.8) and (3.9)), but is decreasing less rapidly. The air flow is from left to right and parallel to the condenser axis.

Figure 4.15 shows the temperature of the air flowing through the condenser. The temperature is plotted against the two coordinates of the condenser tube: the axial coordinate z and the radial coordinate r. The air temperature is decreasing from the temperature at the condenser entry to the temperature of the condenser wall. The thermal diffusion cools the air more rapidly near the wall, so that the saturation ratio rises shortly after the condenser entry (see figure 4.16). Vapour losses close to the condenser wall due to diffusion, however, let the saturation ratio drop again. The highest supersaturation is reached downstream on the condenser centre line, where temperature drops more rapidly than vapour pressure. Figure 4.17 shows a contour plot of the minimum detectable particle diameter inside the condenser calculated from the saturation ratio using equation (3.7).

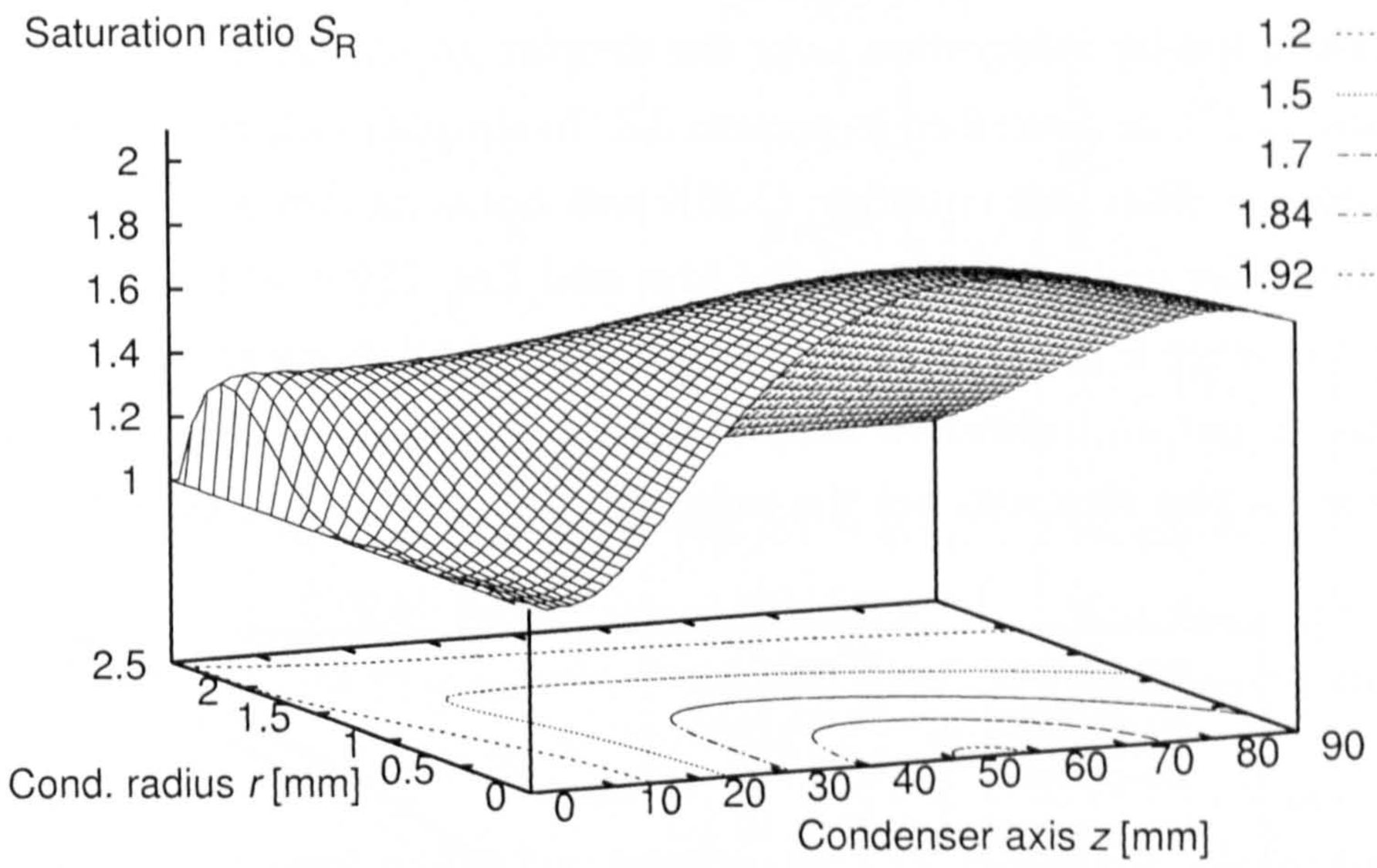

Figure 4.16: Calculated saturation ratio inside the condenser. Near the wall the saturation ratio is increasing immediately due to the reduced temperature. The maximum, however, is reached along the centre line farther inside the condenser tube. The vapour pressure here decreases slowly compared to temperature. The air flow is from left to right and parallel to the condenser axis.

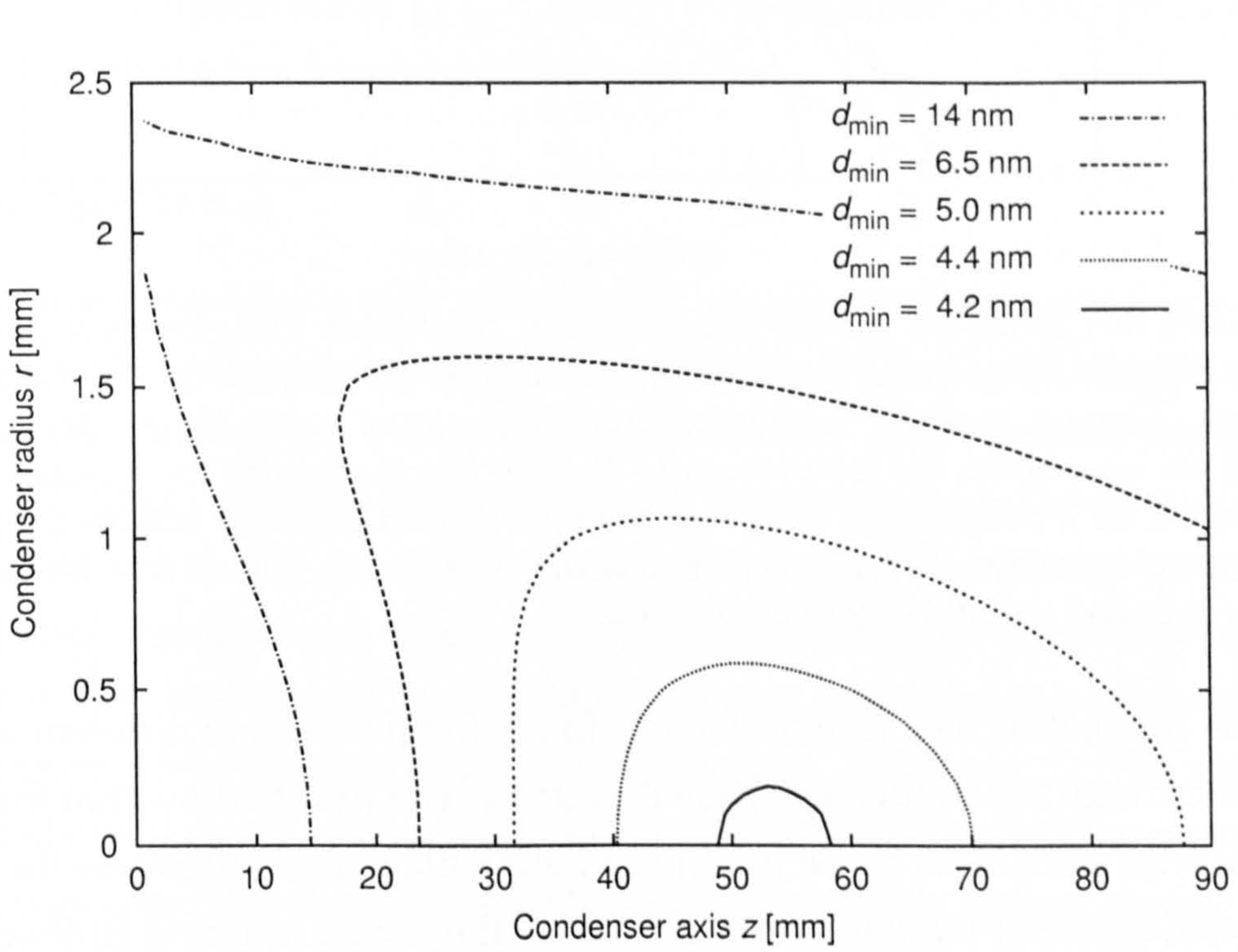

Figure 4.17: Minimum detectable particle diameter inside the condenser. Only if the particles are near the centre line do they all experience the same lower detection limit. The air flow is from left to right and parallel to the condenser axis.

The growth of the droplets (after condensation is initiated on a particle) was calculated by integration over the droplet growth given by its rate in equation (3.22), as described in section 3.3. To simplify calculations the temperature elevation (see equation (3.25)) was not considered. The elevation is in the order of only 2 K to 4 K (Ahn and Liu, 1990) so that its neglect will not change the results significantly. The calculations were performed in order to get an indicative droplet size to verify the design, so that an accurate droplet size was not the primary goal. Figure 4.18 depicts results

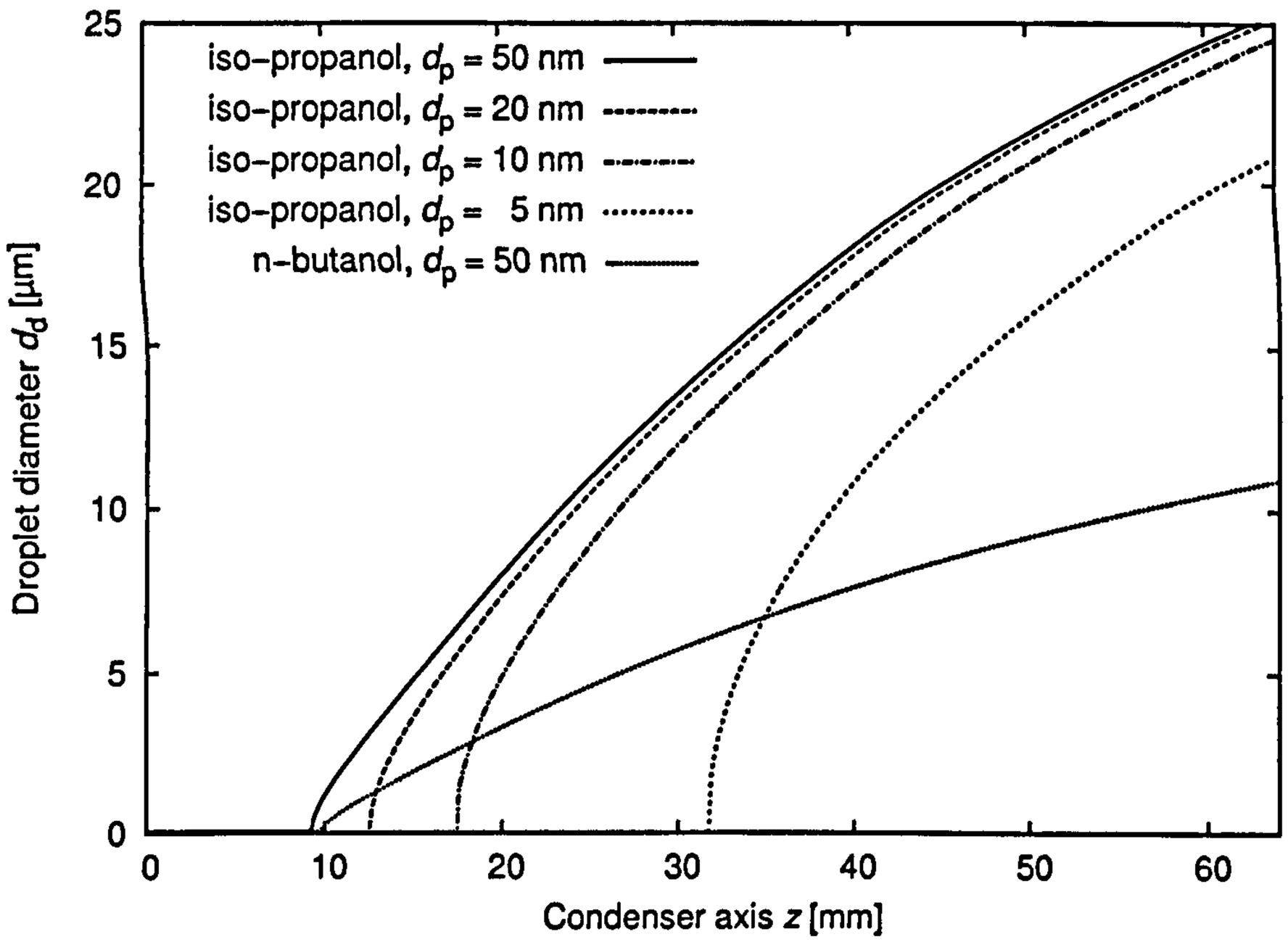

Figure 4.18: Calculated growth history in CPC condenser. The growth of particles to droplets is shown as droplet diameter against the position on the condenser axis. Growth histories for initial particle sizes d_p of 5 nm, 10 nm, 20 nm, and 50 nm are shown for iso-propanol. Results of calculations for n-butanol are shown for a particle size of 50 nm; the final droplet diameter achieved with n-butanol is smaller than that achieved with iso-propanol. The air flow is from left to right and parallel to the condenser axis.

of the calculation as a growth history following particles of different initial sizes through the condenser while they grow. The results show that for particles with sizes close to the minimum detectable particle diameter the final droplet diameter depends on their size as they need to travel further into the condenser to experience the necessary supersaturation, whilst for larger particles (>20 nm) the final droplet diameter depends little on the particle size. For the calculations the same parameters were used as in the above

	n-butanol	iso-propanol	
T_0	273.15 K	271.85 K	Lide (2002)
p_0	100 Pa	1 000 Pa	ibid.
T_1	337.15 K	306.75 K	ibid.
p_1	10 000 Pa	10 000 Pa	ibid.
L	55 095.5 J·mol^{-1}	45 743.5 J·mol^{-1}	Eq. (3.21) fitted to (T_0, p_0) and (T_1, p_1)
D_v (at 20°C)	$8.1 \cdot 10^{-6}$ m^2·s^{-1}	$9.4 \cdot 10^{-6}$ m^2·s^{-1}	Washburn (1929)
σ (at 20°C)	0.024 6 N·m^{-1}	0.021 7 N·m^{-1}	Washburn (1928)
M	74.12 g·mol^{-1}	60.10 g·mol^{-1}	Budavari (1996)
ρ_l	810 kg·m^{-3}	785 kg·m^{-3}	ibid.

Table 4.4: Values used by the Perl program for CPC modelling calculations. The saturation vapour pressure p_0 at the temperature T_0 is used in equation (3.21), p_1 at the temperature T_1 is a second literature value for the saturation vapour pressure. The molar latent vaporization heat L is calculated, so that equation (3.21) agrees with both literature values p_0 and p_1.

computations of the minimum detectable particle diameter, in particular a condenser temperature of 15°C, a saturator temperature of 35°C, and a flow rate through the condenser of 400 ml·min^{-1}.

Qualitative Tests

Preliminary qualitative tests with the CPC were performed sampling ambient aerosol from laboratory air and using both n-butanol and iso-propanol. With both alcohols the indicated particle number concentration increased notably with a measured temperature difference between saturator and condenser of ~ 5 K. The measured concentration changed at this temperature difference quickly from those typically measured with the OPC1 (about 100 cm^{-3}) to values well above 1 000 cm^{-3} and, increasing the temperature difference a few degrees more, to values above 10 000 cm^{-3}. The experiment showed clearly the capability of the CPC to detect ultrafine particles. This was observed at different ambient and condenser temperatures. Calculations did confirm that the temperature difference required for a certain lower detection limit varies very little with absolute condenser temperature and the type of alcohol used.

Blocking the sample inlet under normal operating conditions of the CPC

resulted in the count dropping to zero, thus confirming that only particles activate condensation of a droplet; there were no false counts. In particular, no homogeneous nucleation of the vapour took place. Indeed, homogeneous nucleation was observed only at a much increased temperature difference between saturator and condenser of around 30 K.

A difference in performance of the CPC with each of the two types of alcohol was noted only in respect of the final droplet size, which could be seen with the particle sizing ability of the OPC. Iso-propanol has a higher vapour pressure than n-butanol at the same temperature and, as expected, larger droplets were detected with iso-propanol. This finding was again confirmed by calculations which showed that the lower detection limit is nearly the same for both alcohols and that indeed only the final droplet size varied significantly due to the different vapour pressures (see figure 4.18).

Droplet detection coincidence could be observed at higher number concentrations, especially for high temperature differences between saturator and condenser (with the resulting lower minimum detectable particle diameter) and also for increased sample flow rates. Normally this should not increase the coincidence probability, as higher sample flow rate should result in faster flow in the sensing volume and hence shorter signals compensating for the increased flow rate. However, similar pulse widths (not much shorter) were observed at increasing flow rates due to bandwidth limitations of the OPC2. Figure 4.19 shows coincident signals in such a situation, at a sample flow rate of approximately 18 $ml \cdot min^{-1}$, a saturator temperature of 38°C and a condenser temperature of 16°C. The pulses had a width of 20 µs at 2 V. The relatively long signals caused a higher coincidence probability. On different occasions the under-reading due to coincidence was estimated from the oscilloscope traces. In one case, for example, the pulse width was around 14 µs at half the amplitude (with signals typically of 1 V). While one threshold at 0.7 V was triggered 44 times, another threshold of the OPC2 at 170 mV was triggered only 37 times due to coincidence (as observed on the oscilloscope). The ratio of 37 to 44 (0.84) was therefore an approximation of the under-reading factor, which with equation (3.34) corresponded to a mean number of droplets in the sensing volume $\nu \approx 0.17$ (at sample flow rate of 10 $ml \cdot min^{-1}$). Given the number concentration (as measured with signals counted by the higher threshold) of 60 000 cm^{-3}, a

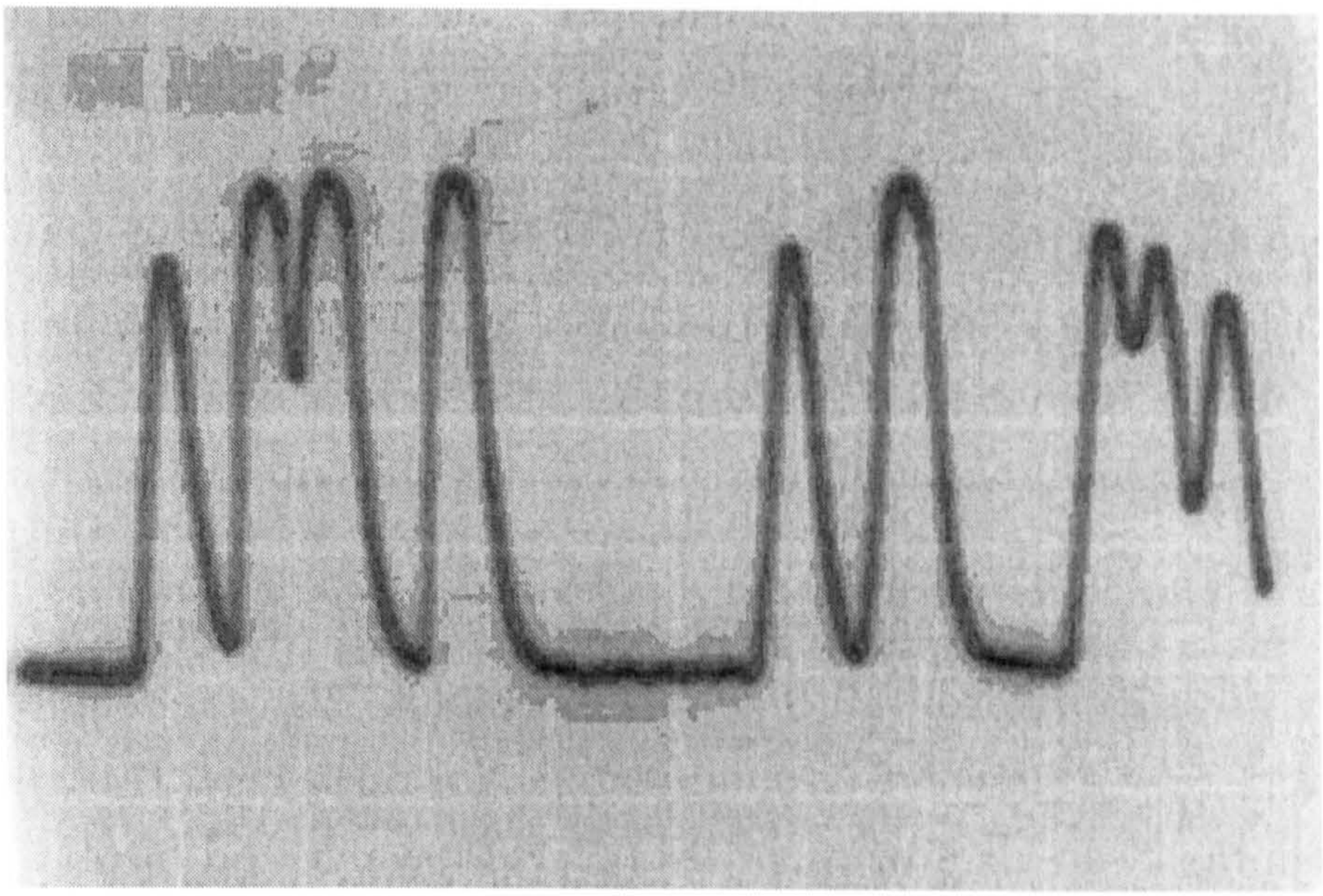

Figure 4.19: Coincident signals detected with the CPC. One horizontal division on the oscilloscope was 50 µs, one vertical 1 V. The pulse width at 2 V was about 20 µs. Particle concentration, as estimated from three oscilloscope pictures, was around 53 000 cm^{-3}.

minimum time τ of separately counted droplets by the lower threshold was approximately 17 µs. On another occasion with signals higher than 2 V, a threshold at 2 V would have been triggered 171 times from 175 droplets as could be observed on the oscilloscope while the number concentration was measured as $\sim$8 000 cm^{-3}. The resulting under-reading factor of 0.977 corresponded to $\tau \approx 9.6$ µs (at sample flow rate of 18 $ml \cdot min^{-1}$). Estimation of the under-reading at 100 000 cm^{-3} in both occasions is $\sim$ 25% (under-reading factor 0.75), which could still be corrected with equation (3.36). The gain of the amplifier of the OPC2 could be reduced (as signals are typically larger than 1 V), thus reducing signal width and τ and, therefore, reducing coincidence probabilities. The laser beam of the OPC2 should also be optimally focused to further reduce τ as much as possible. Consequently it should be possible to measure number concentrations of at least $\sim$200 000 cm^{-3} with under-reading below $\sim$20%.

4.3.4 Improvements

Besides the potential improvements regarding gain and coincidence level of the OPC2, other issues were identified, which are described in this section.

The calculations to predict the CPC performance indicated that the condenser length of 64 mm was relatively short. The position identified for maximum saturation ratio, and hence minimum detectable particle diameter, was close to the condenser exit as could be seen in figure 4.17. It is therefore desirable to extend the condenser to allow growth of the particles of the lowest size necessary for condensation to a detectable droplet size. This would be included in the next CPC design changes (see section 4.4.3).

In the flow design of both the OPC1 and the CPC, the pre-filter functioned not only as a filter, but also it determined the amount of clean-air flow by its pressure-drop–air-flow relationship. In fact, the required pressure drop, set by the valve (see figure 4.13), for releasing 10 $ml \cdot min^{-1}$ determined the clean-air flow rate. Therefore, the valve and filter needed to be selected accordingly and the two flows, sample and clean-air flow, could not be changed independently. While this arrangement was sufficient for testing OPC and CPC prototypes, this matter would need to be improved in subsequent design changes. The position of the pre-filter could be changed to directly downstream of the pump and before the point where pressure determines the 10 $ml \cdot min^{-1}$ sample flow rate (compare figure 4.13 and figure 4.20, which will be introduced in section 4.4). In this way, the flow control could be improved so that the clean-air flow did not depend on the pre-filter but instead on a newly introduced clean-air flow restriction and (to a much lesser extent) on the HEPA filter.

The heating up of the clean air (caused by the clean air being recycled, see section 4.2.4), which could be a disadvantage in the OPC1, might be of advantage for the CPC. If the OPC2 is heated by two or three degrees then this would reduce or avoid vapour condensation on the optics. Such vapour condensation, or a resulting decrease of the response to the droplets, was, in fact, never observed. This could be investigated by further tests with the OPC2 at different temperatures to find out under what conditions, if any, this could become a problem.

The necessity for airtight sealing created problems on occasions when air leaks changed the sample flow rate into the capillary tube. However, carefully sealing the assembly and selecting suitable tubing and joints always fixed the problem. As a consequence, to improve the accuracy of the number concentration measurements the sample flow rate of the CPC was reg-

ularly checked and the measured volumetric flow, if close to the nominal flow rate of 10 $ml \cdot min^{-1}$, was used to calculate the number concentration. The same was done for the OPC1 measurements where airtight sealing is also important.

4.4 Prototype Instrument

After the OPC1 and the CPC were designed, constructed, and tested, they were integrated in a complete prototype instrument. The following describes the implementation of the instrument design in this prototype. The flow arrangement is shown schematically in figure 4.20 and the mechanical sections in figures 4.21 and 4.22.

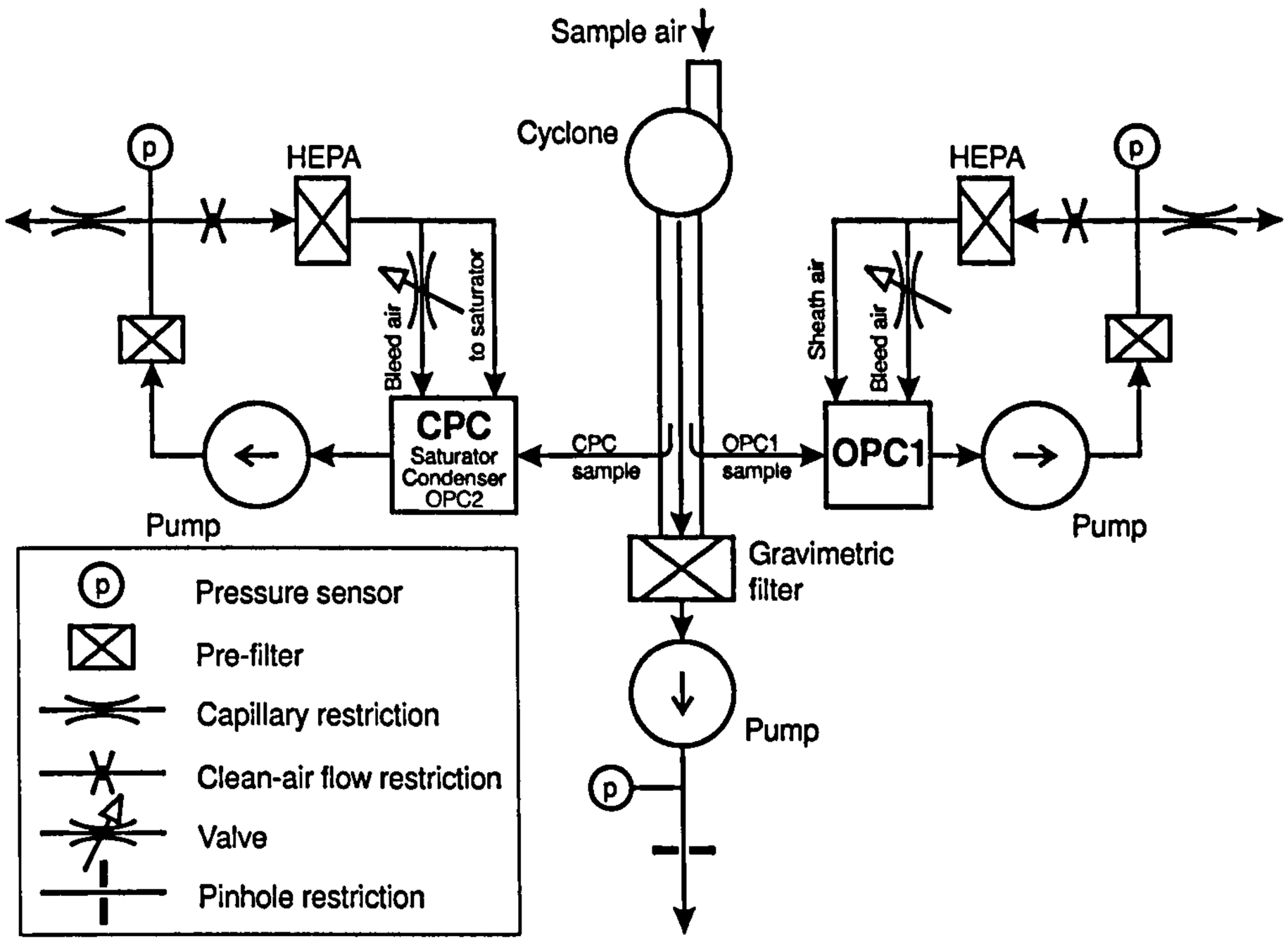

Figure 4.20: The flow systems for the main sample flow, the OPC1, and the CPC in the complete prototype instrument. The pressure sensors used for controlling the sub-sample flow rates of the OPC1 and the CPC are placed before capillary-tubes restrictions which release the same amount of air as is drawn in from the sampling duct.

4.4.1 Inlet

The upper limit of particle size for sampling is determined by a sharp-cut cyclone (Kenny and Gussman, 2000) having a steep transmission curve. The

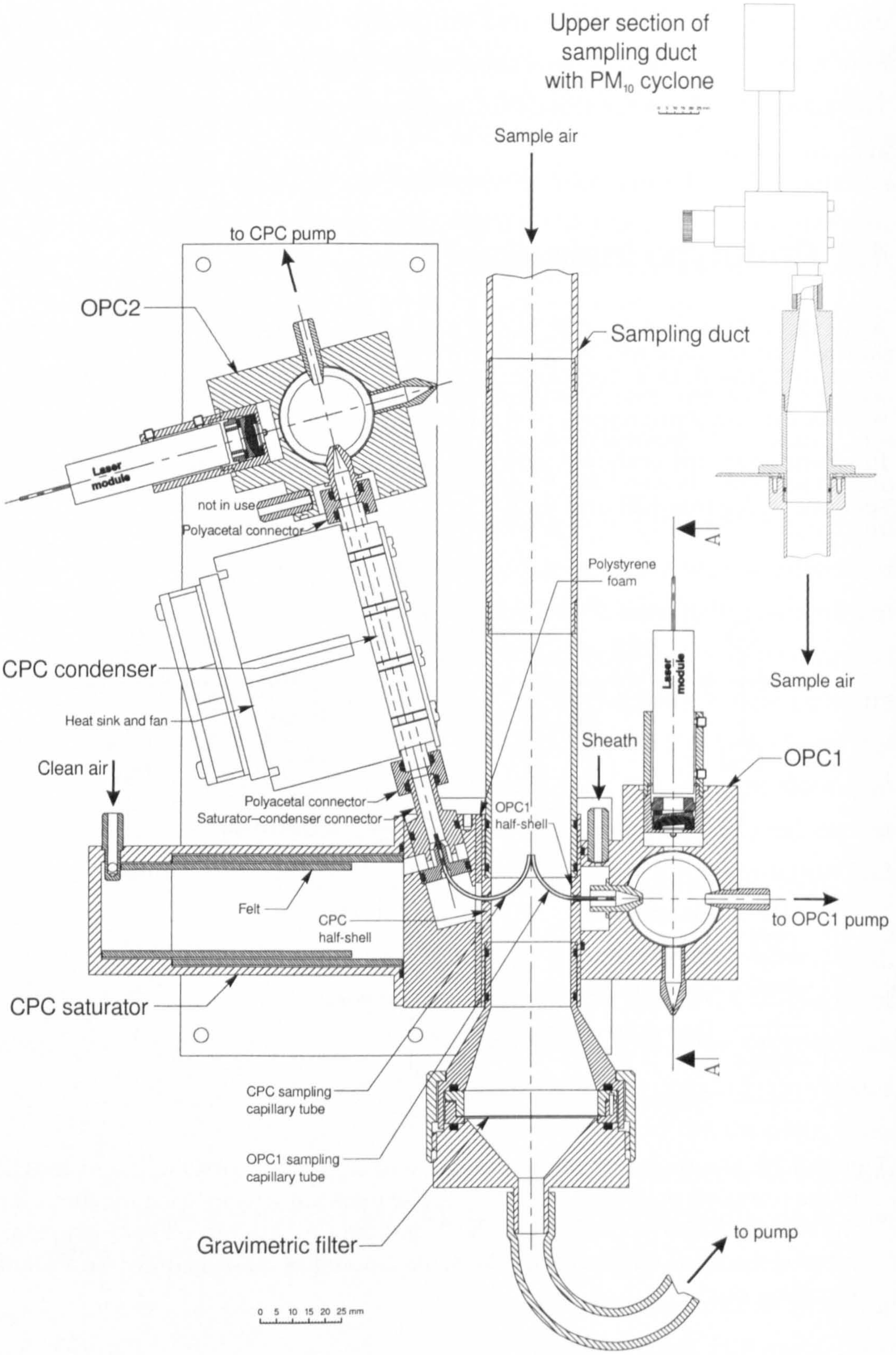

Figure 4.21: Section of the prototype instrument. The section shows the OPC1, the CPC (including OPC2), the sampling duct, and the gravimetric filter. The sample air is introduced through a cyclone on top of the duct. The indicated additional section (A–A) of the OPC1 is shown in figure 4.22.

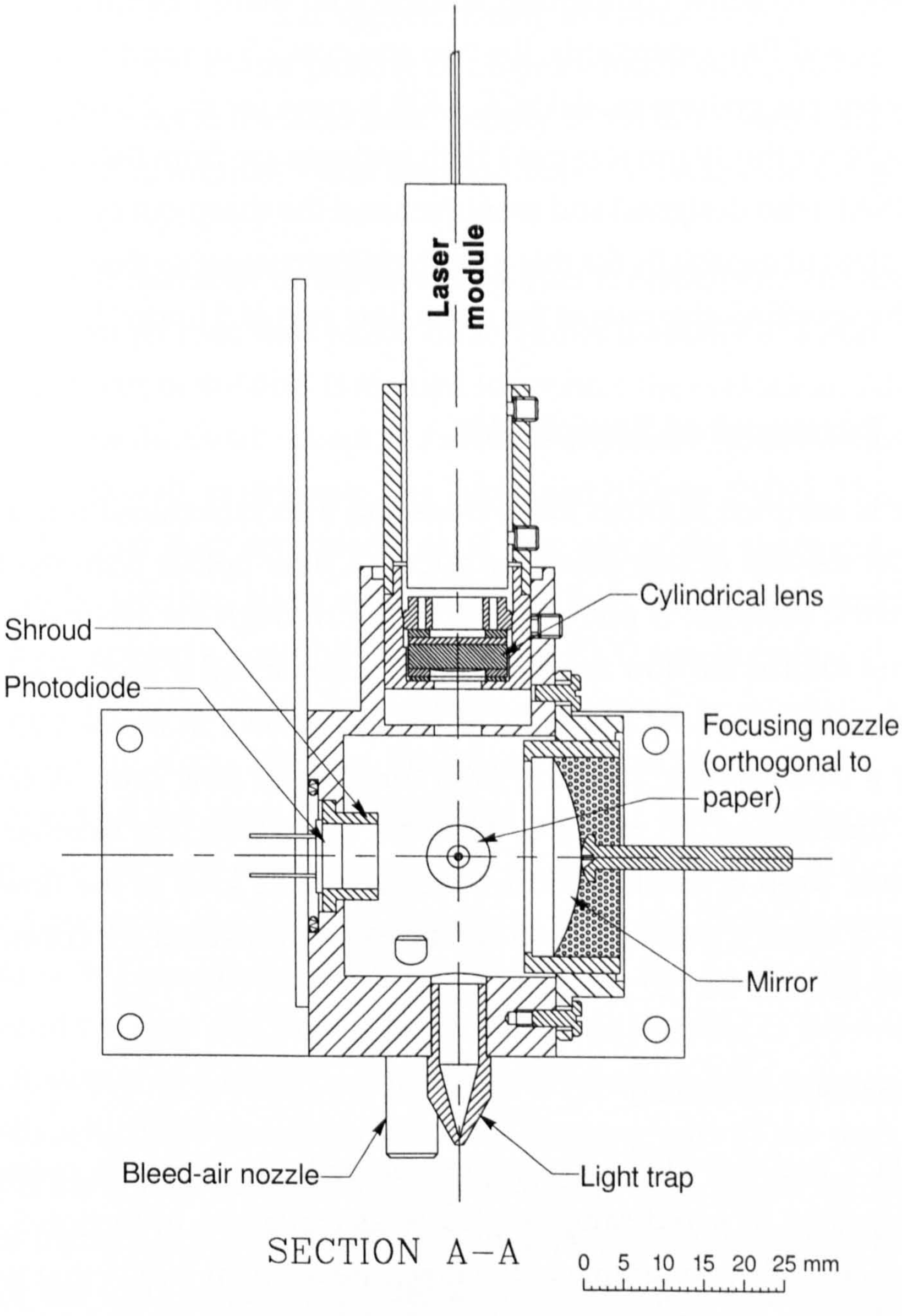

Figure 4.22: Mechanical section of the OPC with the new design of fixed photodiode position (OPC1 shown here). This section (A–A) is indicated in the section of the prototype instrument shown in figure 4.21.

use of a cyclone defines the upper size-limit as an aerodynamic size (a cyclone is an inertial classifier that uses a cyclonic spiral flow, in which the larger and heavier particles deposit to its wall and the smaller penetrate). The cyclone is interchangeable and therefore allows different upper limits to be used. To allow comparison studies with other instruments applying the $PM_{2.5}$ and PM_{10} standards, the two size cuts 2.5 µm and 10 µm are used. (The sharp-cut cyclone model SCC 1.828 is used for the 2.5 µm, and model SCC 3.474 for the 10 µm size cut.) Both cyclones are from BGI Inc (Waltham MA, USA), who designed and manufactured the sharp-cut cyclone with the 10 µm size cut especially for this prototype instrument so that both cyclones have the specified size cuts at the same flow rate of 5 $l \cdot min^{-1}$.

4.4.2 Transport of Sample Air

The air is sampled through the cyclone and then introduced into a vertical duct. At the end of this sampling duct is a filter holder with the filter for gravimetric analysis. A pump draws the air through the cyclone, sampling duct, and filter at the flow rate of 5 $l \cdot min^{-1}$ as specified in section 4.1.3. To be able to control the flow a pinhole restriction (shown in figure 4.20) is used having a characteristic pressure drop for a given flow rate. A restriction with a diameter of 1.6 mm and thickness of 1.0 mm was selected to give a pressure drop of around 1 kPa (calculated 1.12 kPa) at the flow rate of 5 $l \cdot min^{-1}$. Such a pressure drop can be easily measured for control of the flow (see section 4.4.4).

Isokinetic Sub-Sampling

The OPC1 and the CPC sub-sample isokinetically from the centre of the sampling duct to avoid sampling losses as explained in section 3.4. Both use capillary tubes to sample at the flow rate of 10 $ml \cdot min^{-1}$ that was used also in the first prototypes of OPC1 and CPC. The capillary inlets are both aligned along the centre line of the sampling duct and, therefore, along the streamlines of the 5 $l \cdot min^{-1}$ sample flow. The dimensions of the duct and the capillary tubes were selected to meet the condition for isokinetic sampling given in equation (3.26): the inner diameter of the cylindrical duct was chosen to be 25 mm; the inner diameter of the capillary tubes was chosen to

be 0.8 mm. The velocity of the sample air in the centre of the duct is then 0.340 $m \cdot s^{-1}$ at the flow rate of 5 $l \cdot min^{-1}$, which is twice the mean velocity in the duct (according to the Hagen–Poisseuille law of fully developed laminar flow). The mean velocity in the capillary tubes is 0.332 $m \cdot s^{-1}$ for the sample flow rate of 10 $ml \cdot min^{-1}$, i. e. approximately the same as the duct flow velocity. Consequently, the air passing through a surface area equal to the area of the capillary inlet at the local flow velocity in the duct centre, amounts to the flow rate of 10 $ml \cdot min^{-1}$ and the conditions for isokinetic sampling are met.

The required diameter of the sampling duct for isokinetic sub-sampling is, at 25 mm, larger than the cyclone outlet (inner diameter of 8 mm). Therefore, the first part of the duct is tapered to connect the cyclone and the duct. The taper of the duct wall is kept at a shallow angle of 7° to avoid flow separation from the wall, as suggested by Baron and Willeke (2001). This should maintain laminar flow conditions, or, if flow out of the sharp-cut cyclone should not be laminar, allow establishing of fully developed laminar flow further downstream where the OPC1 and the CPC sub-sample.

The capillary tubes used for sampling are placed at the same position in the sampling duct, 350 mm downstream from the sharp-cut cyclone in the centre of the duct. To guarantee laminar flow conditions at this position, the distance was chosen close to that required to fully develop laminar flow from the entry of a circular tube, which is approximately $0.056 d\mathrm{Re} \approx 390$ mm (Baehr and Stephan, 1998), with $d = 25$ mm being the diameter of the duct and $\mathrm{Re} = 280$, the Reynolds number in the duct at the sample flow rate of 5 $l \cdot min^{-1}$. The capillary tubes are held permanently in half-shells which are joined together thus forming part of the duct linking the upper section of the duct to the gravimetric filter holder on the lower side (see figure 4.21). Each half-shell is then permanently fixed to either the OPC1 or the CPC saturator–condenser connector block respectively. The OPC1 and the CPC can therefore be removed for testing and servicing as complete and still functioning units by disassembling the two half-shells.

The capillary tubes are bent with a radius of 13.6 mm, similar to the radius of the sampling duct, so that they leave the duct horizontally through the duct wall. The OPC1 capillary tube is bent 90° and continues outside the duct straight for a short distance and ends inside the OPC1 focusing

nozzle; its length is 33.7 mm. The CPC capillary tube is bent through 165°, its last part is straight too and ends 21.0 mm upstream of the condenser on the centre line of the saturator–condenser connector. The length of this tube is 49.7 mm. The condenser is nearly vertical, the inclination of 15° allows the condenser to be placed relatively close to the duct, so that the capillary tube could be kept as short as possible thus minimizing diffusion losses of particles (see section 3.4). The length of 49.7 mm (together with the sample flow rate of 10 ml·min^{-1}) results, according to equation (3.30), in 50% diffusion losses ($\eta_T = 0.5$) for particles with a diameter of 6 nm, at 10 nm the losses are only 28% ($\eta_T = 0.72$). In the OPC1 capillary tube diffusion losses are not relevant because of the lower detection limit of 250 nm ($\eta_T = 0.995$ for $d_p = 250$ nm at capillary length of 33.7 mm), whereas sampling losses due to inertial deposition in the bend of the capillary tube need to be considered. Losses due to this mechanism amount, according to equation (3.31), to 50% ($\eta_T = 0.5$) at a particle diameter of 12 µm, a particle density of 1 500 kg·m^{-3}, a sample flow rate of 10 ml·min^{-1}, and a capillary diameter of 0.8 mm. At a particle diameter of 10 µm the losses are 38% ($\eta_T = 0.62$), and at a diameter of 2.5 µm only 3% ($\eta_T = 0.97$). These losses were considered to be acceptable since the required lower detection limit is 10 nm (given by the limit of the CPC) and the required upper size limit is 10 µm or 2.5 µm (given by the limit of the OPC1 and the size cut of the PM_{10} or $PM_{2.5}$ cyclone respectively).

OPC1 and CPC Flow Systems

Sub-sampling for the OPC1 and CPC modules requires additional pumps. The method that is used to draw the small sample flow rate of 10 ml·min^{-1} through the capillary tubes is the same as that explained in sections 4.2.1 and 4.3.1. The flow arrangement of both the OPC1 and the CPC, however, has been changed to allow a better control of the sample air flow. The adjustable valve (see figures 4.5 and 4.13) has been replaced by a capillary restriction, as depicted in figure 4.20, which was selected to create a pressure drop of around 1 kPa, a value that can conveniently be controlled (see section 4.4.4). A capillary tube with inner diameter of 0.32 mm and length of 80 mm was chosen, giving this pressure drop at the sample flow rate of 10 ml·min^{-1}.

In the instrument prototype, similar flow rates were to be used for the

OPC1 (sheath and bleed air) and the CPC (saturator and bleed air) due to the similarity of the respective flow designs. In the previous design of the flow arrangement, these flow rates were determined and maintained constant using the pre-filter (see figures 4.5 and 4.13) and making use of its characteristic pressure drop. It is, however, not ideal for a monitoring instrument, or extended tests with a prototype instrument, to depend on filter characteristics, which may vary over time.

Therefore, in the new design of the OPC1 and CPC flow systems, the pre-filter has been placed directly at the pump outlet and is not involved in the flow control. Instead, a further restriction, shown as clean-air flow restriction in figure 4.20, is now used to fix the clean-air flow (sheath and bleed air together in the case of the OPC1; flow through saturator and bleed air in the case of the CPC). The pressure drop over the clean-air flow restriction is similar to that over the capillary restriction. Thus controlling the pressure drop over the capillary restriction would also maintain a constant clean-air flow rate. The pressure drop over the clean-air flow restriction, however, differs slightly from that over the capillary restriction. The side of the capillary restriction which is not connected to the clean-air flow restriction is at ambient pressure, whereas the other side of the clean-air restriction at a pressure close to ambient due to low pressure drops over the HEPA filter (measured as ~ 0.1 kPa) and the sampling capillary tube (calculated to be 15 Pa). As a consequence of this configuration, the clean-air flow rate may decrease slightly if the pressure drop over the HEPA increases due to the filter gradually blocking over time. This will, however, affect the flow rate only after a very long sampling time due to the low rate of contamination given by the low sample flow rate of 10 $ml \cdot min^{-1}$.

The clean-air flow restriction was chosen to be a short capillary with an inner diameter of 0.8 mm and a length of 15 mm. These dimensions would give a flow of around 0.8 $l \cdot min^{-1}$ at a pressure drop of 0.985 kPa (1 kPa reduced by typical pressure drops over the HEPA filter and the sampling capillary tube mentioned above). This would then allow a sheath-air flow rate or flow rate through the saturator of about (0.3 to 0.4) $l \cdot min^{-1}$ and a similar bleed-air flow rate, as required.

4.4.3 OPC1 and CPC

Besides the changes to the flow design outlined above, other design details were adapted while integrating the OPC1 and the CPC (including the OPC2) into the prototype instrument, as explained below.

Mechanical Design

The OPC1 and the OPC2 used a fixed photodiode position as mentioned in section 4.2.4, which reduced the number of degrees of freedom simplifying alignment (see section B.2). A mechanical section of the OPC1 shows this design in figure 4.22. The mechanical design of the scattering chamber was also changed slightly to allow better airtight sealing (adding grooves and chamfers for silicone-rubber sealing) and the possibility of mounting the OPC either directly on the sampling duct (as OPC1) or connecting it to the CPC condenser (as OPC2).

The cylindrical lens inside the laser module holder was tilted by 5° to avoid problems with laser light reflected at the flat surface of the lens being returned into the diode laser. This reflected light could disturb the laser power control if it falls on the laser power monitoring photodiode (called *monitordiode*) positioned behind the laser diode. This was observed when both OPC modules for the prototype instrument were mounted and first tested, and it resulted in decreased laser current (by ~10% to 20%) and output power (by up to 50% as measured with a laser power meter) when the OPC was properly aligned. While this problem exists with the first OPC design as well, it was not observed when testing the first OPC prototype, probably because of the higher number of degrees of freedom causing inadvertent misalignment of lens and laser (while still correctly imaging the sensing volume on the photodiode).

The CPC saturator volume was chosen to ensure complete saturation of the vapour at the temperature of the saturator; at 84 cm^3, it was slightly larger than that of the first CPC prototype (see page 56). The saturator is heated using heating resistors which are screwed to the metal block supporting the saturator and housing the saturator–condenser connector (see mechanical section in figure 4.21). In this way the heated block heats saturator and saturator–condenser connector, while the block is thermally in-

sulated from the half shell holding the CPC capillary tube (and hence from the sampling duct) using a thin sheet of polystyrene foam. The length of the condenser was extended to 84 mm (previously 64 mm) to improve the detection limit as explained in section 4.3.4. The condenser is again cooled using two Peltier elements between the condenser and a heat sink with vertical fins. A heat sink with cooling fan was selected to improve the heat dissipation further.

OPC Amplifier and Peak Detector

The gain of the OPC1 amplifier (given by the feedback resistor) was chosen similar to the gain used with the first OPC prototype as that gain was sufficiently high and the resulting magnitude of the amplifier output signal was linear with the light power of the particle scatter (see section 4.2.4). Due to the limited bandwidth of the amplifier with this gain, the laser was slightly defocused to make the signals longer, as with the first OPC prototype (see section 4.2.3).

The gain of the OPC2 amplifier, however, was not required to be as high due to the large signal amplitudes resulting from the alcohol droplets. It was, therefore, reduced to increase the bandwidth of the amplifier. As suggested in section 4.3.3, this reduced the pulse width of the signals, and reduced the coincidence error. The laser was then focused to achieve the shortest signals possible.

The peak detector used for the OPC1 and the OPC2 in the prototype instrument was the same as that used for the first OPC and CPC prototypes, and the circuit diagram is shown in figure A.3. The additional gain of the peak detector could be used after calibration of the sizing capabilities of the OPC to scale the output signals to match the operating range of the comparators on the circuit which implement the thresholds as was carried out in case of the first OPC1 (see section 4.2.3).

4.4.4 Microprocessor Control

A microprocessor is used to control the sample flows, control the CPC temperatures, record the measured data, and manage data storage. This is described in the following two sections. The data paths of the microprocessor

control are shown in figure 4.23.

Flow and Temperature Control

The flow system used to adjust sample-air and clean-air flows of the OPC1 and the CPC was explained in section 4.4.2. These flows are maintained stable by controlling the pressure drops over the capillary restrictions of the OPC1 and the CPC respectively (see figure 4.20). In each system (OPC1 and CPC) this pressure drop is measured with a pressure sensor (PCM0020, Sensortechnics) having an operational range of (0 to 20.7) mbar ((0 to 2.07) kPa) relative to ambient pressure (see figure 4.20). The output signal of the pressure sensor, an analogue voltage proportional to the pressure, is converted in an A/D-converter and then processed by the microprocessor (see figure 4.23). The microprocessor controls the pressure using the measured value in proportional and integral feedback to regulate the power supplied to the respective pump. The coefficients for the proportional and integral feedback are set separately for the OPC1 and the CPC. A third pressure sensor is used to maintain constant the sample flow rate of 5 $l \cdot min^{-1}$ through the duct via the pressure drop across the pinhole restriction (shown in figure 4.20). The signal from the pressure sensor is converted with the A/D-converter and then used to control the flow by regulating the power supplied to the pump, just as for the OPC1 and CPC sample flows.

The temperatures of the saturator and condenser of the CPC are measured by integrated-circuit temperature sensors (LM335A, National Semiconductor), with an analogue voltage output proportional to absolute temperature at 100 $K \cdot V^{-1}$. The output signal is again converted with the A/D-converter and the digital signal read by the microprocessor. The control of temperature uses proportional and integral feedback, as in the case of flow control. Here the driving currents for the heating resistors and the Peltier elements are pulse-width modulated to regulate heating and cooling power respectively; the heater current is modulated at a frequency of 1 kHz and the cooler current at 10 kHz.

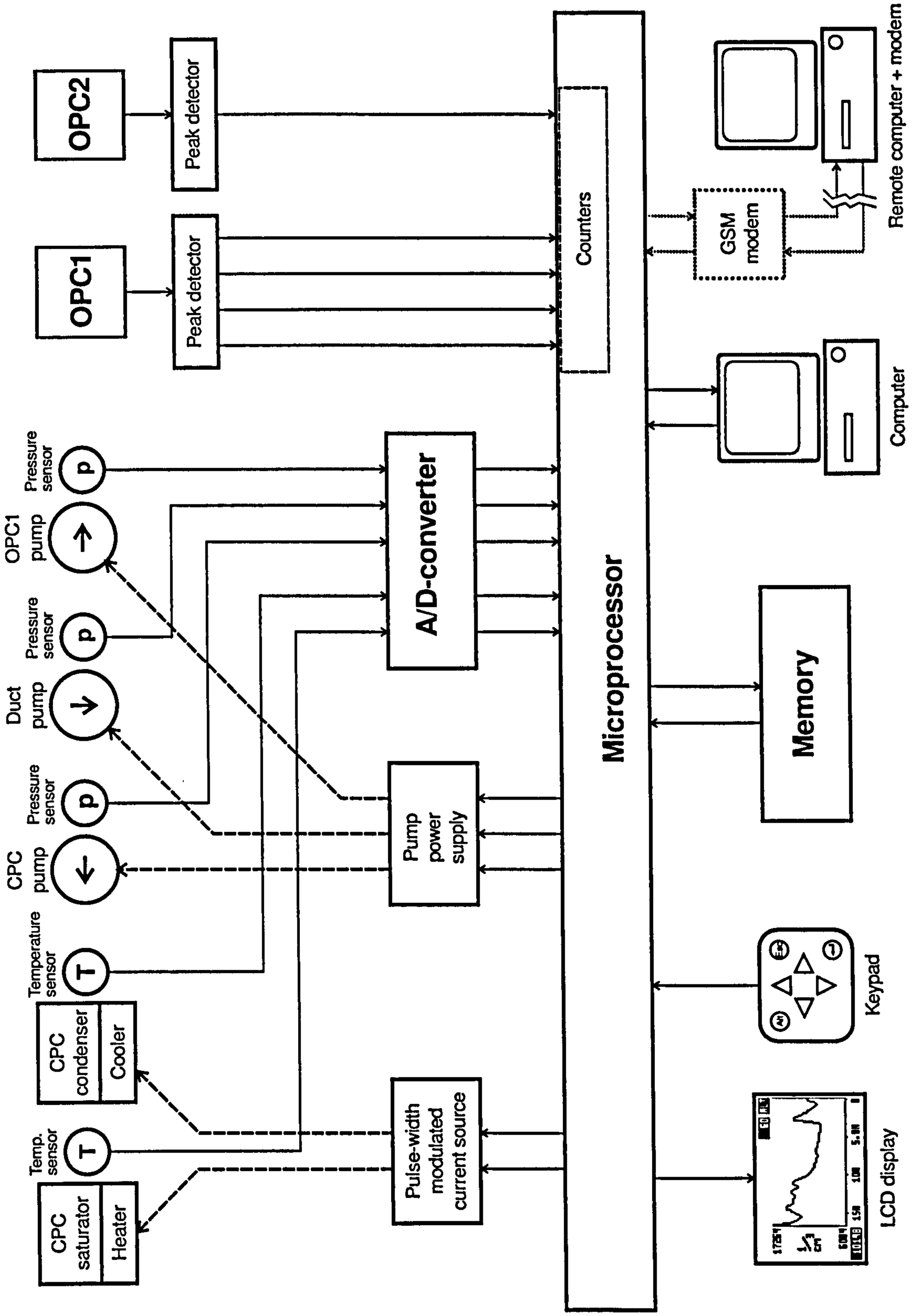

Figure 4.23: Data paths of microprocessor control used for the prototype instrument.

Data Handling

Data Acquisition The number concentrations in the four size fractions of the OPC1 and the number concentration of the CPC are delivered to the microprocessor as trigger signals from the respective peak detectors. The signals trigger internal counters of the microprocessor, the resulting raw data from the counter consist of numbers of particles divided by time. Four of these particle count rates correspond to the concentrations of particles larger than the respective threshold levels set on the peak detector of the OPC1, the fifth count rate corresponds to the total particle concentration of the CPC. The four count rates of the OPC1 are converted in the count rates corresponding to the number concentrations in the size fractions defined by the peak detector threshold. This is done by subtracting from the count rate corresponding to a given threshold (defining the lower limit of the size fraction in consideration) the count rate corresponding to the next higher threshold (defining the upper limit of the size fraction in consideration). The first three count rates are converted in this way, the fourth, corresponding to the concentration of particles larger than 2.5 µm does not need to be converted as it already has an upper size limit given by the PM_{10} sampling inlet. For data storage these count rates are not further converted to particle concentrations, such conversion would be performed on a computer using the measured volumetric sample flow rates of the OPC1 and the CPC respectively. Only for the purpose of data display on the instrument does the microprocessor convert the count rates (given in s^{-1}) to number concentrations (given in cm^{-3}) using the nominal sample flow rate of 10 $ml \cdot min^{-1}$.

User Interface A user interface for the microprocessor is provided using a keypad with seven buttons and an LCD display. The LCD display is used to show the measured data as graphs or numbers which are updated every second using rolling averages or displaying the data every second as measured. Also the saturator and condenser temperatures, the sample flow rate through the duct, and the OPC1 and CPC sample flow rates can be displayed as they are measured as feedback for the control. The microprocessor control is configured using also the LCD display and the keypad. The user can navigate through several user menus to calibrate temperature and pressure sensors, configure temperature and flow controls, set rolling aver-

age for display of data, set time scales for graph display, configure the data logger (see below), and set time and date for the data logger.

Data Logger An on-board data logger is realized using a memory chip with 500 kByte capacity. Data storage using this memory is managed by the microprocessor. The data logger can be configured to store the saturator and condenser temperatures, the sample flow rate through the duct, the OPC1 and CPC sample flow rates, the four OPC1 count rates (corresponding to the particle concentrations in the OPC1 size fractions), and the CPC count rate. Any of these can be separately enabled or disabled for data logging and logging intervals can be specified separately as 1 s or any multiple of 1 s such as for example 15 s, 1 min, and 1 h. Every quantity is stored using its own logging interval, the values stored are averages of the logging interval. The data logger is started and stopped using the user interface or with a computer via an RS232 interface (see below) which is also used to download stored data to a computer.

Interface to Computer The microprocessor can communicate with a computer using an RS232 interface. Besides the data download from the instrument to a computer for further analysis, the interface to a computer can also be used for operation of the instrument from the computer. It is also possible to use the interface in conjunction with a GSM modem connected to the instrument and a computer with modem for remote operation of the instrument (anywhere in a field study).

The data logger together with the low alcohol consumption of the CPC allows unattended operation for at least one week, but also several weeks is possible if appropriate logging intervals are chosen, as for example every 5 min for number concentrations of the OPC1 size fractions and every 1 min for the total number concentration of the CPC.

5 Instrument Performance

Two identical prototype instruments were produced according to the design described in section 4.4. This chapter describes tests performed with both instruments. Section 5.1 describes calibration and laboratory tests carried out to confirm the performance. A test with high ultrafine number concentrations is shown in section 5.2 to illustrate the effect of coincidence and the possibility of corrections. Side-by-side comparisons of the two prototype instruments are reported in section 5.5, while comparison with traditional instruments in a field trial is described in section 5.3. Results from this field trial were used to test number-to-mass conversion algorithms, which are discussed in section 5.4. Section 5.6 summarizes the results of all performance tests.

To avoid confusion later, the two prototype instruments are called *Ambi-*$Count_A$ and *AmbiCount*$_B$. The subscript 'A' or 'B' is now added to OPC1, OPC2, and CPC to specify which instrument they belong to. Hence:
$OPC1_A$, $OPC2_A$, and CPC_A belong to $AmbiCount_A$, while
$OPC1_B$, $OPC2_B$, and CPC_B belong to $AmbiCount_B$.

5.1 Calibration and Validation in the Laboratory

5.1.1 Flow Visualization and Laser Alignment

As during the verification of the laminar flow conditions in the first OPC prototype (see section 4.2.3), flow visualization was used again. With smoke introduced in the sheath air, it was found that contamination of the $OPC1_A$ and $OPC1_B$ scattering chambers with smoke can be mostly avoided if the bleed-air flow rate is high enough, and the optimum configuration seemed to be at a bleed-air flow rate similar to the sheath-air flow rate. The valve adjusting the ratio between these two flows was therefore adjusted accordingly to set both flow rates to approximately the same value. $OPC2_A$ and

$OPC2_B$ showed the same results—bleed-air flow comparable to the sheath-air flow (in this case the flow through the saturator) guaranteed largely contamination free operation.

The diameter of the sample-air column was determined by observing the sensing volume, visualized by smoke in the sample air, with a travelling microscope. The diameters in $OPC1_A$ and $OPC1_B$ were 0.19 mm ±0.01 mm and 0.17 mm ±0.01 mm respectively. Repeated measurements with the micrometer of the travelling microscope indicated a typical measurement error of 0.01 mm, which corresponds to one division of the micrometer, and therefore this value is stated here in case a smaller value resulted from the calculated standard deviation of the repeated measurements.

$OPC2_A$ and $OPC2_B$ had similar dimensions for the sample-air columns, which were 0.16 mm ±0.01 mm and 0.14 mm ±0.02 mm respectively. This indicates clearly that the sample introduced into the centre of the saturator–condenser connector does not mix with the surrounding air coming from the saturator which acts as sheath throughout the condenser and the OPC2. This has the advantage of producing a sharper lower size cut as all particles experience the same lowest detection limit corresponding to the maximum supersaturation encountered on the centre line of the condenser (see section 4.3.1 and figure 4.16).

Flow visualization was also used to optically align the lasers and mirrors of all four OPCs to ensure accurate passage of the sample-air flow through the laser beam (defining the sensing volume) and correct imaging of the sensing volume to the photodiode. The procedure described in section B.2 was followed. The lasers of $OPC2_A$ and $OPC2_B$ were focused tightly, minimizing the sensing volume to reduce the pulse width of the scattering signals and reducing the probability of coincidence (see section 4.4.3). These foci, measured using the vertical displacement of the travelling microscope (one vernier division corresponding to 0.01 mm), could be estimated to be 0.02 mm ±0.01 mm and 0.03 mm ±0.01 mm respectively. The resulting signals in $OPC2_A$ and $OPC2_B$ were found to have a typical pulse width (at half amplitude) of $\sim$2.5 µs which was well below pulse widths and shortest times τ between two separately detectable signals observed in case of the first CPC prototype (see section 4.3.3).

The laser foci of the OPCs ($OPC1_A$ and $OPC1_B$) were slightly defocused

to make the signal longer accounting for the limited bandwidth of the OPC amplifier (see section 4.4.3). The laser beam depths in the sensing volume were measured to be 0.09 mm ±0.01 mm and 0.08 mm ±0.01 mm respectively.

5.1.2 OPC Calibration

Before the calibration of the sizing capabilities of all four OPCs, it was necessary to adjust the gains of the transimpedance amplifiers (see figure A.2) to ensure the linearity of the amplifier outputs to light scattering. The gain of the two OPC1s was set using a feedback resistor of 6.6 MΩ (the value needed to be smaller than that used for the first OPC prototype). The gain of the two OPC2s was set using a feedback resistor of only 1 MΩ to guarantee short pulse widths and reduce the probability of coincidence error (see section 4.4.3). The choice of these feedback values was based on preliminary tests with the four OPCs using 1.053 µm PSL spheres and observing the scattering signals (height and pulse width) at different amplifier gains.

The two OPC1s were calibrated using PSL spheres with the following sizes: 0.356 µm, 0.548 µm, 1.053 µm, and 2.134 µm. Although the sizing capabilities of the two OPC2s, functioning only as detector for the alcohol droplets, were not to be used, they were calibrated as well. Due to their reduced sensitivity (as compared to the two OPC1s), not all sizes of PSL spheres could be used, so that $OPC2_A$ was calibrated with 0.548 µm, 1.053 µm, and 2.134 µm spheres. $OPC2_B$ was calibrated only with 1.053 µm spheres, sufficient to provide an indication of its sizing capabilities.

The PSL spheres for the calibration were generated from suspension in water with a nebulizer (TSI TRI-JET Aerosol Generator), which subsequently also dries the test particles in a diffusion dryer. For a low concentration of monodisperse PSL in the suspension this resulted in single monodisperse PSL spheres. The generated particles were collected in a ballast container (~20 l) from which the sample was drawn (see figure 4.9).

For every size of PSL spheres, 100 scattering signals from the spheres passing the sensing volume were recorded for the two particle counting OPCs and the two droplet counting OPCs (if the size was used for calibration). The average and standard deviation of the amplitudes were then determined. Subsequently, for each OPC the obtained set of responses to

the tested PSL spheres (average amplitudes corresponding to the sizes of the PSL spheres used) was compared to the calculated response, which was scaled to best fit the data.

This calibration of the two OPC1s for sizing PSL spheres needed to be corrected for average ambient air particles, which were found to scatter less light than PSL spheres of the same size due to their different optical properties (for example Hering and McMurry, 1991; Hand et al., 2002). Stolzenburg et al. (1998) sampled monodisperse ambient aerosol with a DMA, which was subsequently used to calibrate an OPC. This direct ambient calibration showed that the response of ambient aerosol and that of dioctyl sebacate (DOS) droplets were very similar. The refractive index of DOS ($m = 1.45$) was therefore used here to approximate average response to ambient aerosol. The calculated response for $m = 1.45$ was scaled with the best-fit scaling factor found for the PSL calibration yielding the response of the OPC to ambient aerosol. This ambient response curve was used to determine the signal thresholds to achieve the required size cuts. Figures 5.1 and 5.2 show results from calibration of $OPC1_A$ and $OPC1_B$ respectively.

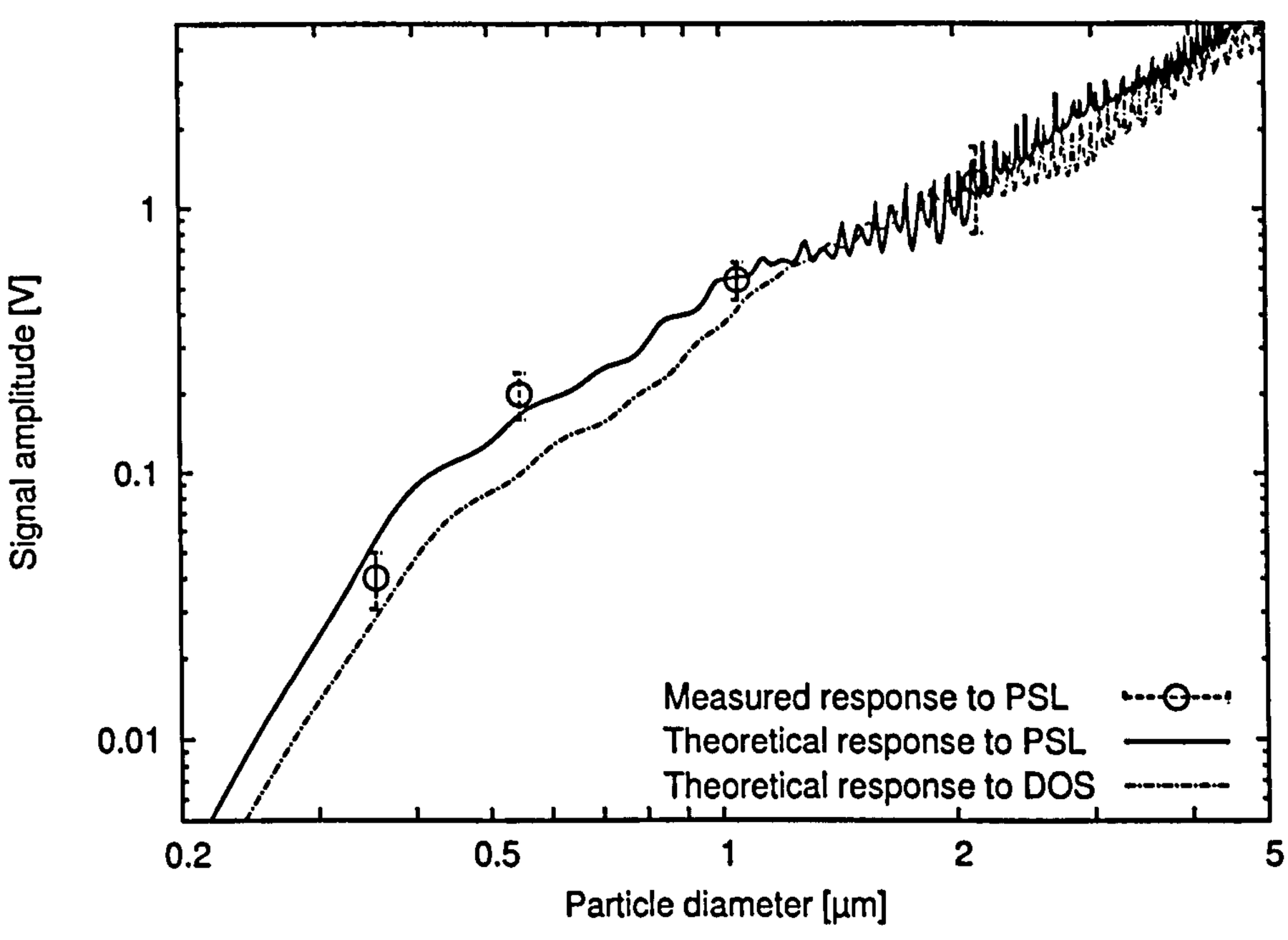

Figure 5.1: Measured response of $OPC1_A$ to PSL spheres (21 February 2002). The calculated theoretical response was scaled to best fit the measured data.

For the OPC2s the response to PSL is compared to the calculated response to iso-propanol droplets (refractive index $m = 1.38$, Budavari, 1996), so that

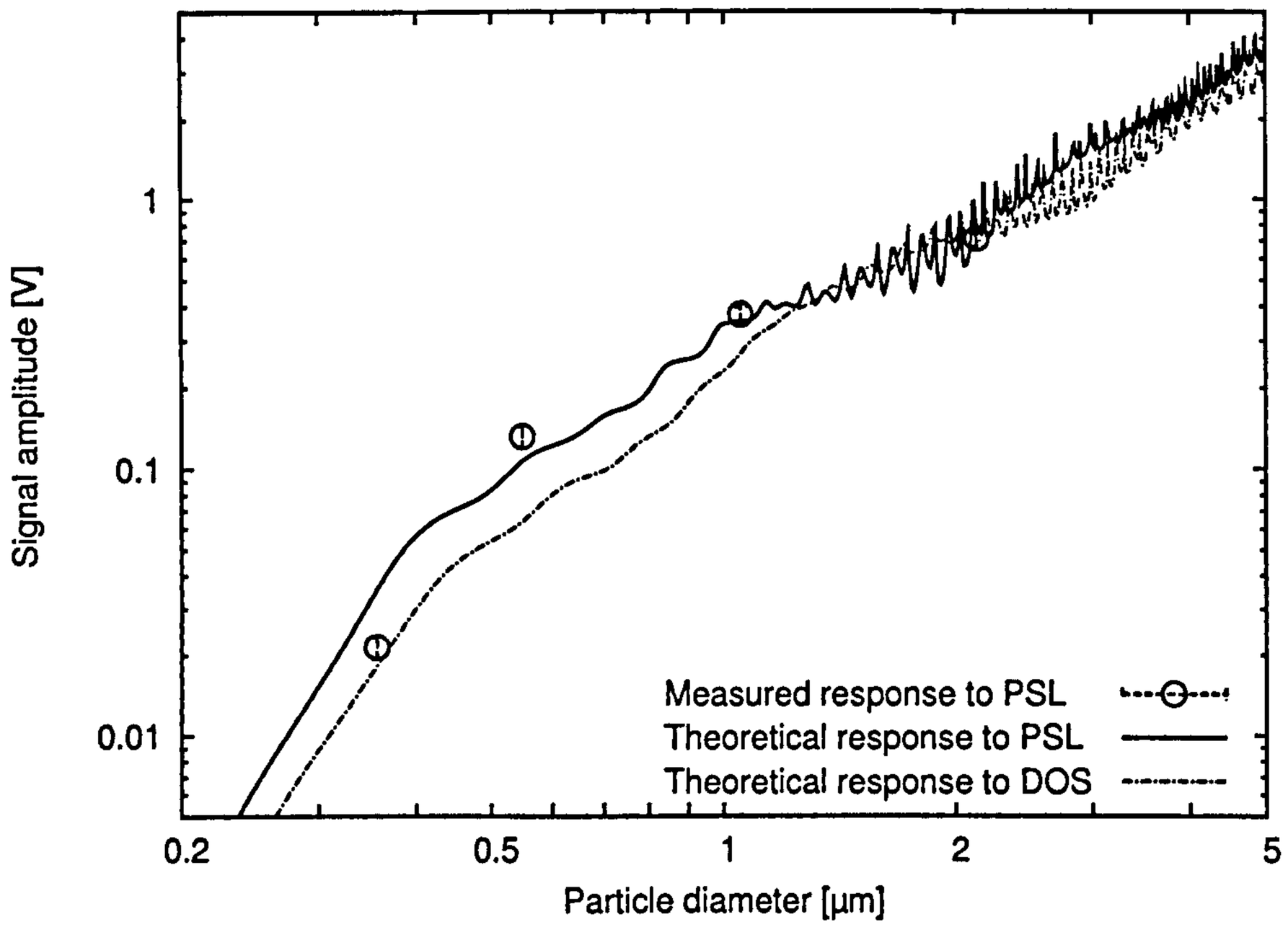

Figure 5.2: Measured response of $OPC1_B$ to PSL spheres (21 February 2002). The calculated theoretical response was scaled to best fit the measured data.

sizing of the droplets would be possible. Results of calibration of $OPC2_A$, depicted in figure 5.3 show that a 10 µm droplet would correspond to a response of ~ 1 V. Subsequently this CPC showed typical signal amplitudes of 2 V indicating that droplets are growing bigger than 10 µm. Figure 5.4 shows calibration results of $OPC2_B$. Because of the higher response as compared to $OPC2_A$, the gain of the peak detector electronics was reduced later.

5.1.3 Noise Reduction

The electronic noise present in the signals of the peak detectors (as used for threshold discrimination of signal amplitudes) was higher for the four OPCs of the two prototype instruments as compared to the first OPC prototype. It was found that the main part of the noise originated from the switching of heater and cooler currents for the control of saturator and condenser temperatures respectively. Noise spikes at the frequency of the switching currents were observed reaching amplitudes of around 50 mV. The operation of the three pumps (using mains supply) was identified as source of noise as well. This noise could be reduced by electrically isolating the four OPCs from other metal parts of the instrument prototype and directly earth-

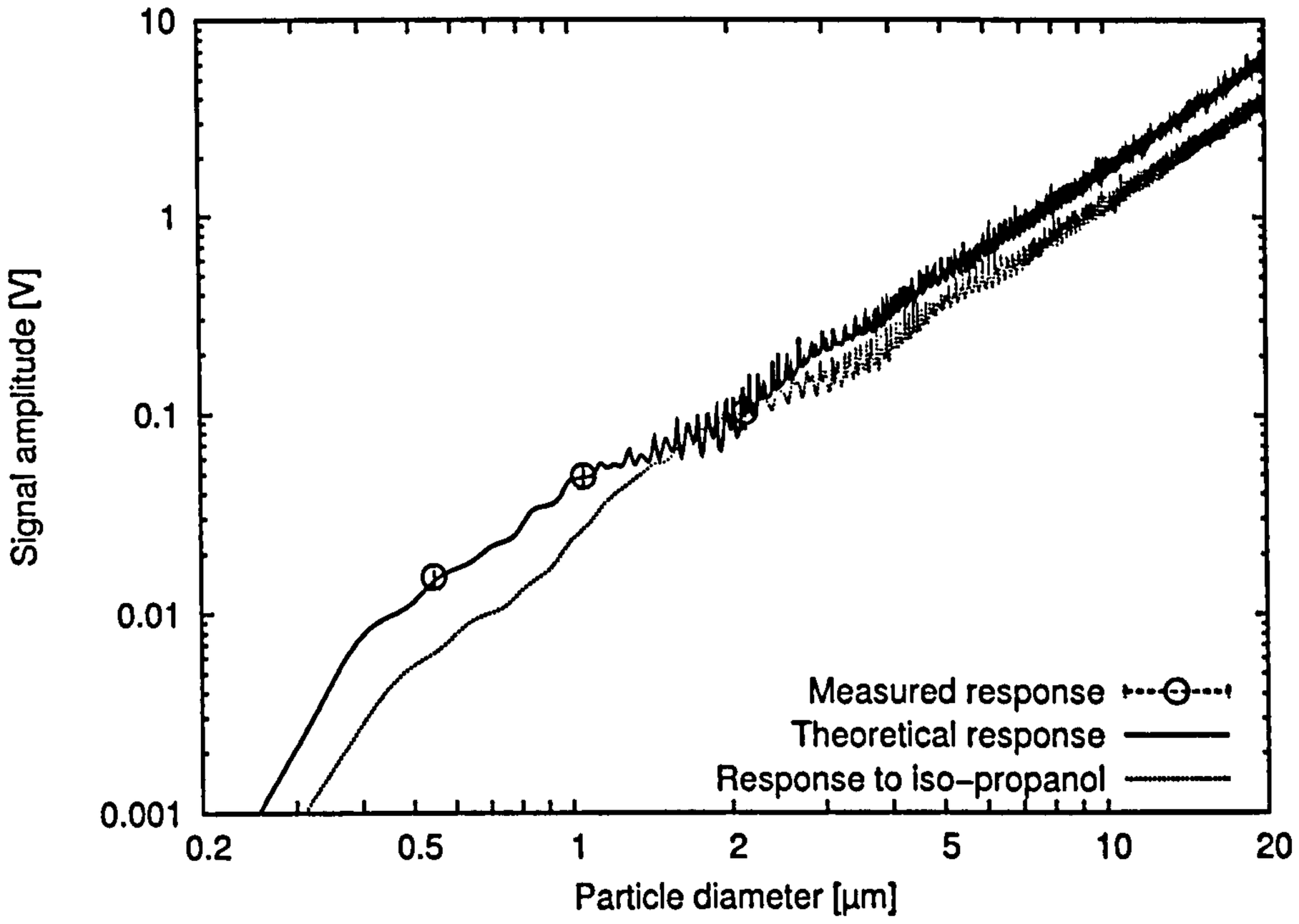

Figure 5.3: $OPC2_A$ calibration. Measured response to PSL spheres (21 February 2002). The calculated theoretical response was scaled to best fit the measured data.

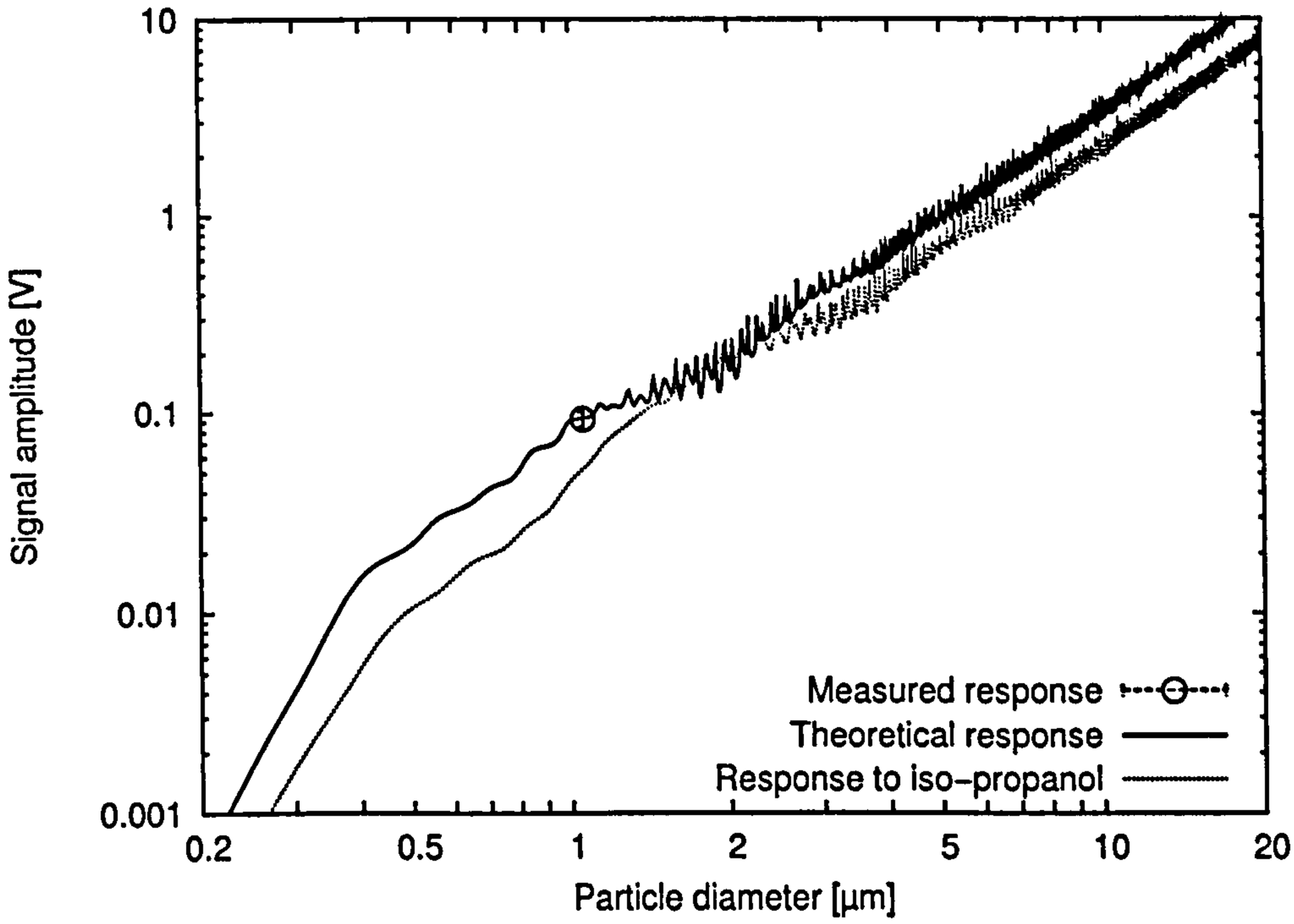

Figure 5.4: $OPC2_B$ calibration. Measured response to PSL spheres (21 February 2002). The calculated theoretical response was scaled to best fit the measured data.

ing them. The noise from the switching currents was not reduced with this measure, instead the time to switch the heater and cooler currents needed to be increased to reduce this part of the noise.

With the reduced noise the following threshold levels could be set for $OPC1_A$: 29.9 mV for size cut at 360 nm; 84.1 mV for size cut at 500 nm; 359 mV for size cut at 1.0 µm; 1.43 V for size cut at 2.5 µm. For $OPC1_B$ the set thresholds were: 19.2 mV for size cut at 360 nm; 53.9 mV for size cut at 500 nm; 230 mV for size cut at 1.0 µm; 884 mV for size cut at 2.5 µm. The achieved lowest detection limit of the OPC1s was, at 360 nm, considerably higher than the 250 nm achieved for the first OPC prototype. This was for three reasons: firstly, the size cuts are here defined using the refractive index $m = 1.45$ approximating average ambient aerosol properties which results in a lower response curve compared to the response curve for PSL spheres; secondly, the noise is still higher and a threshold level of about 14 mV, as was used for the first OPC prototype, was not achievable here; thirdly, the amplifier gain using a feedback resistor of 6.6 MΩ as compared to 9.4 MΩ, was lower than before. Also differences in the optical laser alignment and the laser output power might account for the higher response seen in case of the first OPC prototype (response higher even when considering different gain and different refractive index); this is suggested by differences between $OPC1_A$ and $OPC1_B$ response as well. While $OPC1_A$ could use a lower detection limit below 360 nm, this level was set so that both OPC1s would have the same characteristics making them comparable and interchangeable. The lower detection limit of 360 nm was accepted and it was not attempted to reduce it, as it was more important at this stage to calibrate the CPCs (see next section) and then to test the two prototype instruments.

5.1.4 CPC Calibration

The CPCs of the two prototype instruments were tested in the laboratory of netcen (operating division of AEA Technology, Abingdon, UK) by comparison with a TSI (St. Paul MN, USA) CPC model 3010, a well recognized condensation particle counter with a lower detection limit of 10 nm. The set-up of this calibration process is shown in figure 5.5. Both sodium chloride nanoparticles and background ambient aerosol sampled from inside the laboratory were used in the calibration process. The particles were

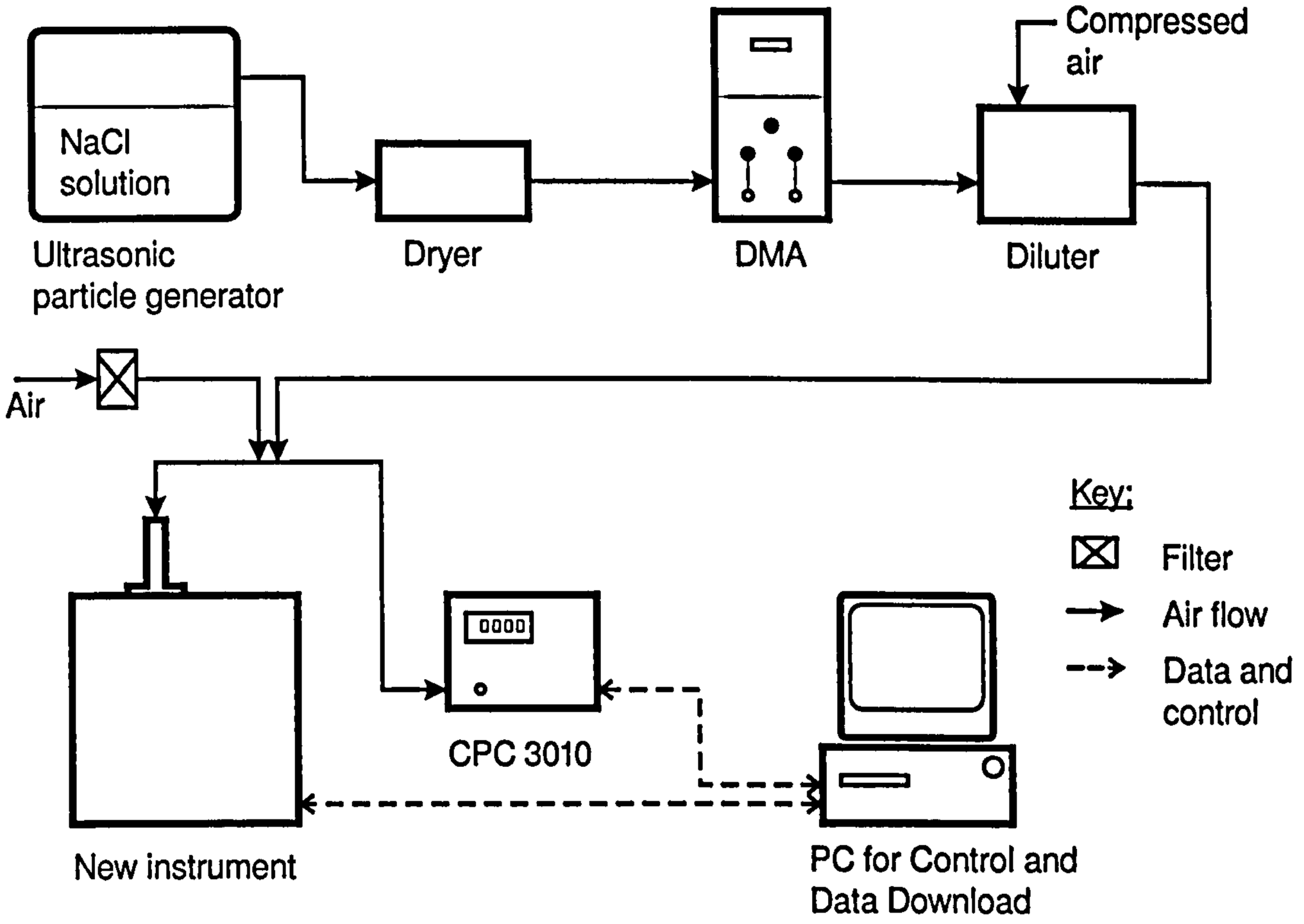

Figure 5.5: Schematic of set-up used for CPC calibration.

passed through a DMA (TSI model 3071) to select a particle size. The resulting monodisperse aerosol was then either passed directly to the sampling instruments or first passed through a diluting system in which the concentration of the test aerosol could be varied. To make up the necessary flow rate for the new instrument and the TSI CPC, further clean air was introduced through a HEPA filter and mixed with the test aerosol. Comparison was made by sampling for three minutes at fixed particle size and concentration. The experiment was repeated at different conditions: first with polydisperse aerosol at higher and lower particle concentrations by using the diluter; then, without dilution, at different particle sizes by using the DMA. Figures 5.6 and 5.7 show the results with polydisperse aerosol as a scatter plot comparing the readings of the two instruments for the various test concentrations. Results for monodisperse sodium chloride particles are depicted in figure 5.8; the particle size was varied between the measurements in the range 20 nm to 200 nm. Results for monodisperse and polydisperse sodium chloride particles as well as polydisperse background aerosol show good linearity. The two measurements at number concentrations above 10 000 cm^{-3} (included in figure 5.7) exceed the upper concen-

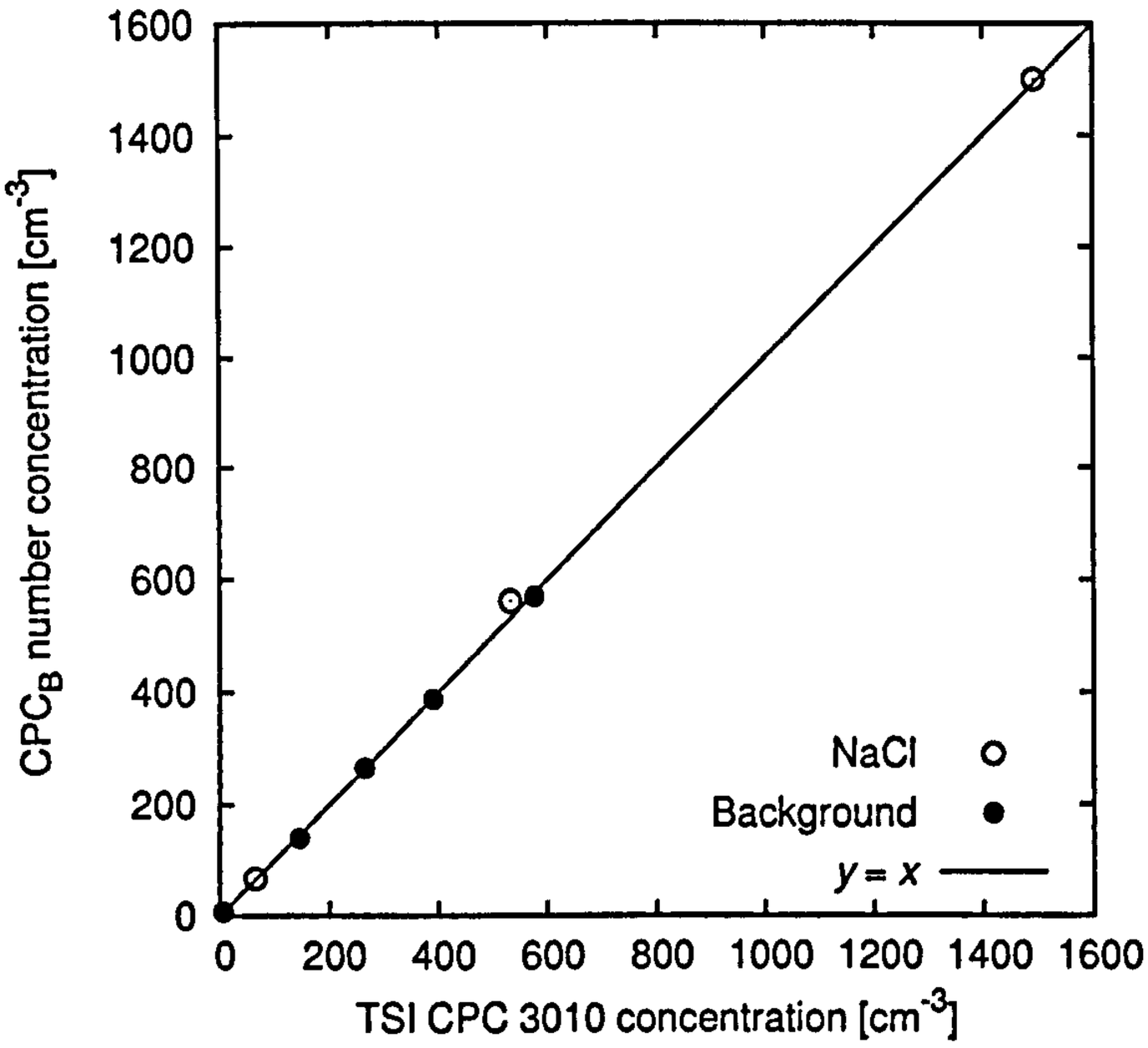

Figure 5.6: Comparison of number concentration measured by the new instrument CPC_B against number concentration measured by the TSI CPC, for polydisperse NaCl and background ambient particles. The correlation coefficient for the shown measurements is $r^2 = 0.992$ (slope = 1.00, intercept = -1.35 cm^{-3}).

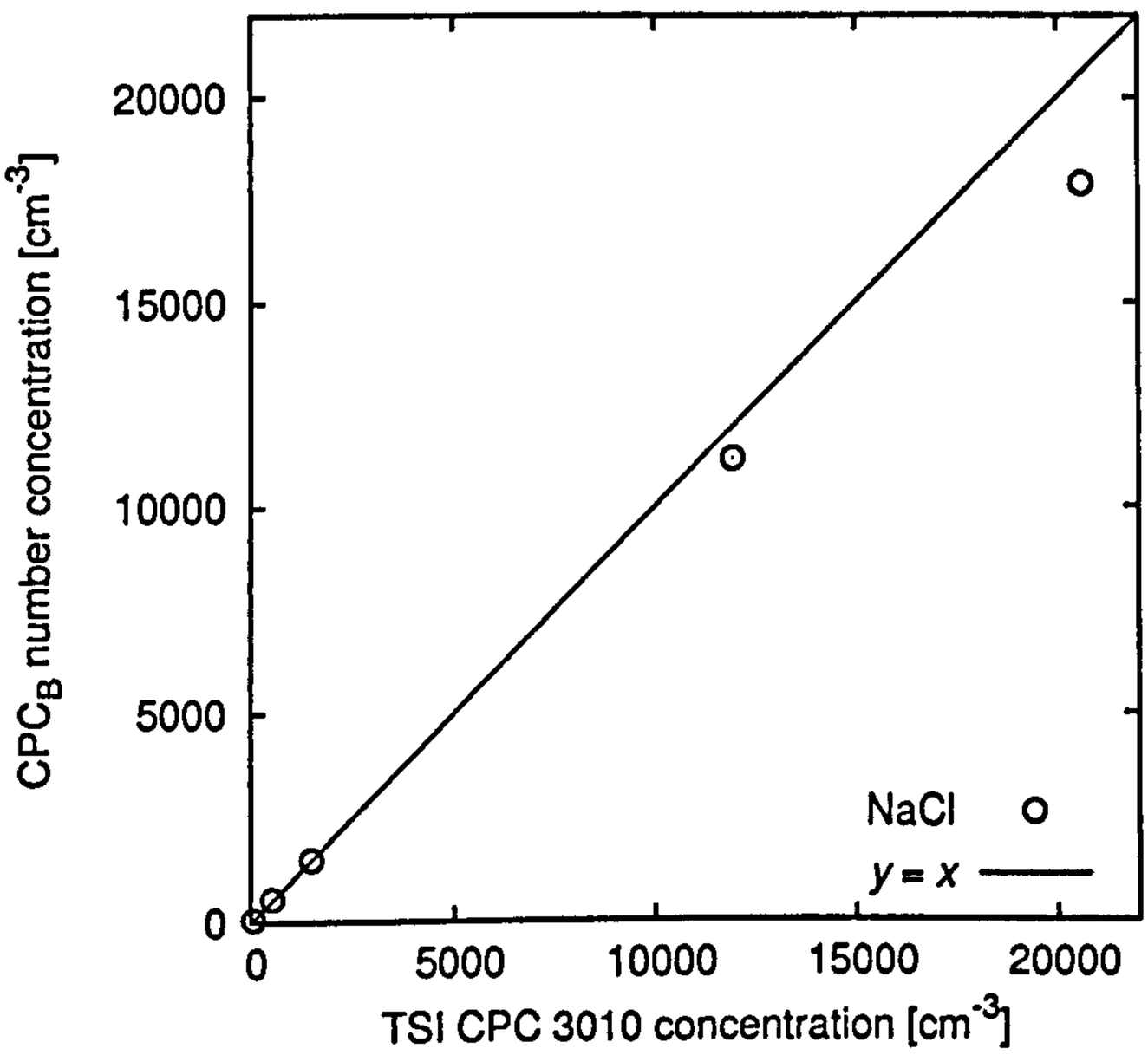

Figure 5.7: Comparison of number concentration measured by the new instrument CPC_B against number concentration measured by the TSI CPC, for polydisperse NaCl particles. The concentration range exceeds the upper limit of TSI CPC 3010 of 10 000 cm^{-3}.

tration limit of the TSI CPC of 10 000 cm^{-3}. The corresponding two values of the TSI CPC are therefore only indicative. The correlation coefficient r^2 for all data shown in the two figures 5.6 and 5.8 is $r^2 = 0.993$.

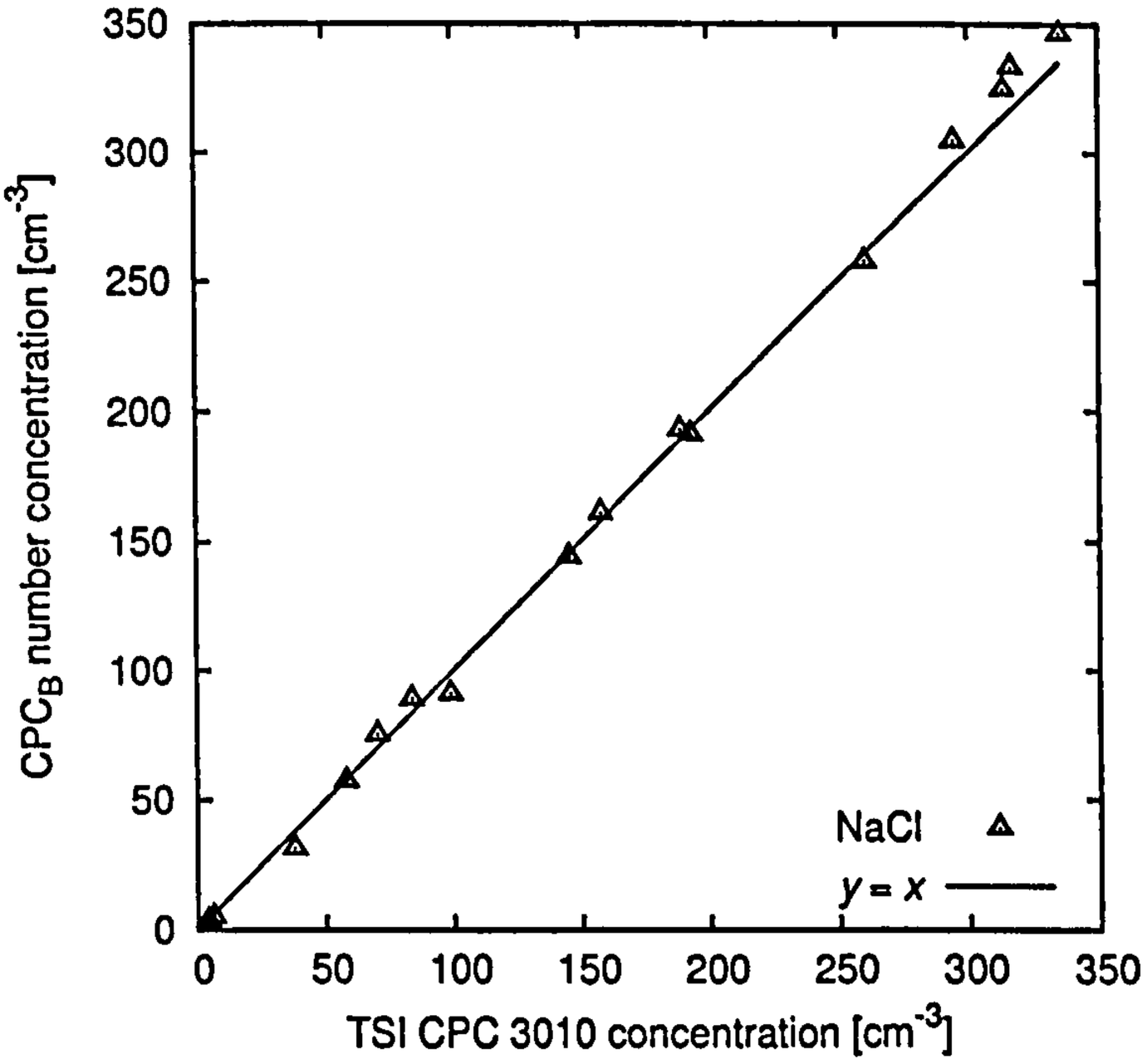

Figure 5.8: Comparison of number concentration measured by the new instrument CPC_B against number concentration measured by the TSI CPC, for monodisperse NaCl particles. The correlation coefficient for the shown measurements is $r^2 = 0.998$ (slope = 1.04, intercept = -0.56 cm^{-3}).

Figure 5.9 shows the counting efficiency of the instrument's CPC compared with the TSI CPC as a function of particle size for the same measurements with sodium chloride as shown in figure 5.8. The efficiency is close to 1 in the whole size range of the measurements, 20 nm to 200 nm, which shows that the linearity of the CPC does not change significantly with particle size in this range; this was expected as both CPCs have the same lower detection limit of 10 nm. The counting efficiency varies between 0.85 and 1.09 with efficiencies > 1 for particles of 40 nm size or larger.

Several tests were performed at decreased temperature difference between the CPC saturator and condenser, results of which are presented in figure 5.10. While for all other tests this difference was 20 K with the saturator temperature at 35°C, it was decreased in these tests to 4.5 K, very close to the point where the CPC starts functioning. At a difference of around 4 K or less the CPC operates simply like an OPC, measuring the low number

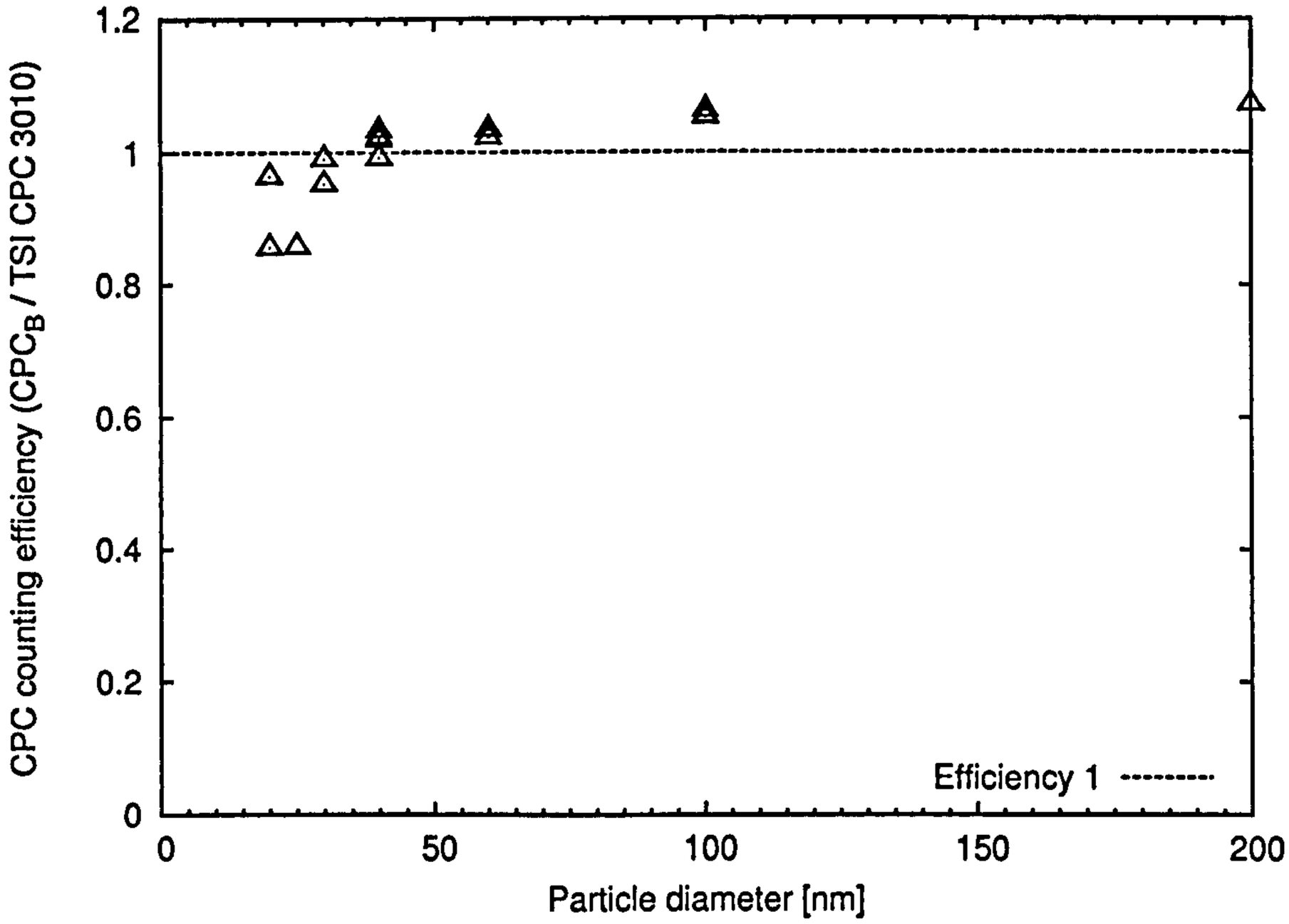

Figure 5.9: Counting efficiency of CPC_B for monodisperse NaCl particles. The efficiency is compared to TSI CPC model 3010.

concentrations typical for an OPC. At differences of 4.5 K, 5 K, and 10 K several measurements were performed at different sizes of monodisperse sodium chloride. Only at 4.5 K one can clearly see an increased lower detection limit due to the decreased temperature difference. This measurement was repeated on the next day, differences in the two measurements show how sensitive the CPC is to small changes in operating conditions, probably due to ambient temperature differences in the laboratory for the two measurements.

Although both prototype instruments were tested at netcen, the results presented here are from one only ($AmbiCount_B$), the other instrument suffered from continuously decreasing number concentration during the one week test period compared to the first and the TSI CPC. The failure was later found to be a leaking filter (the CPC pre-filter, see figure 4.20). The pre-filter was exchanged on the CPC in both instruments, as the material of the filter housing (polycarbonate) is not resistent to iso-propanol. Kynar-housing filters are now used instead, which have similar filtering specifications.

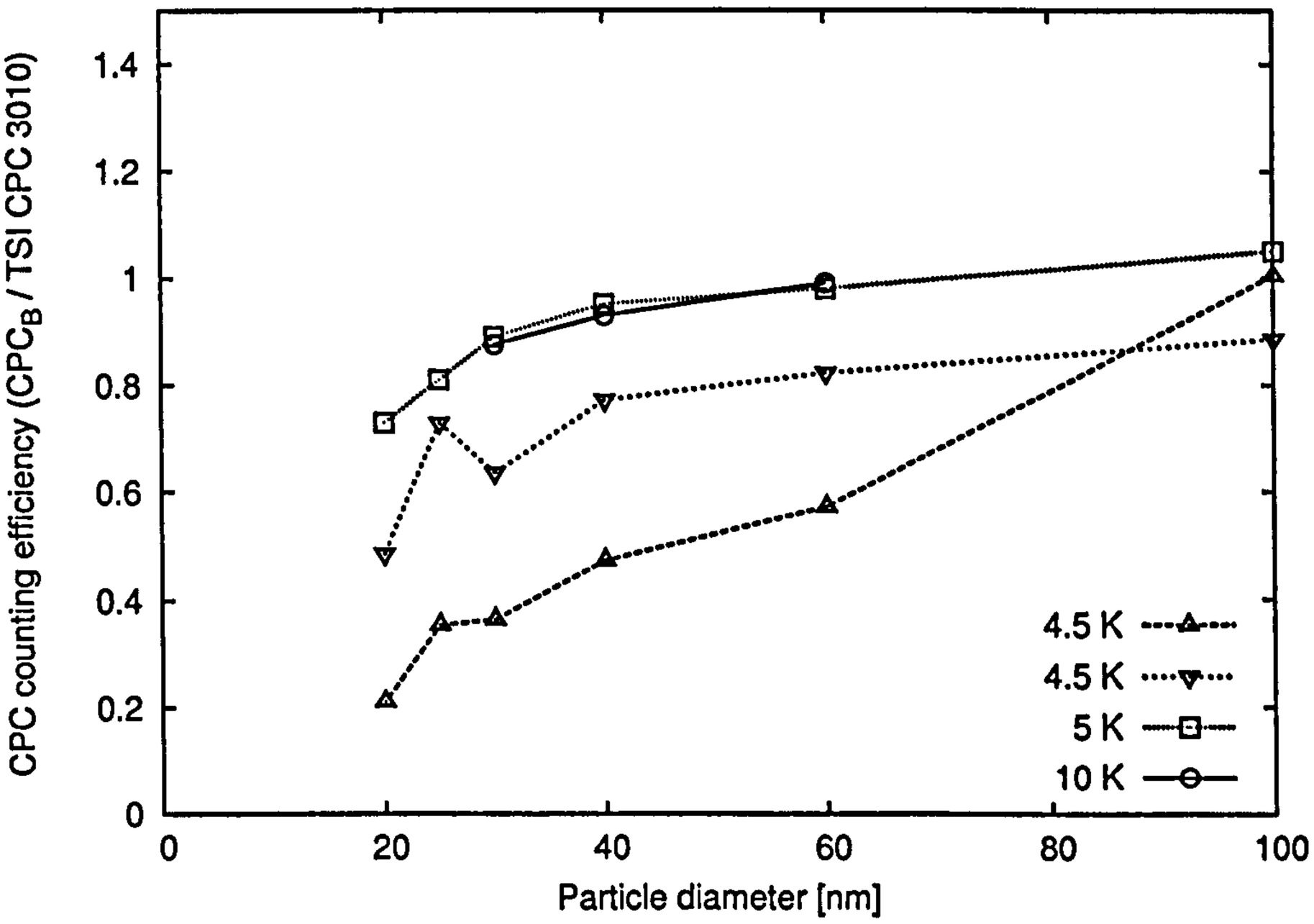

Figure 5.10: Counting efficiency of CPC_B for monodisperse NaCl particles at decreased temperature differences between saturator and condenser. The efficiency is compared to a TSI CPC model 3010 at different sizes of NaCl particles. The first series of measurements at a temperature difference of 4.5 K and the series at 10 K was performed a day before the other series of measurements at 4.5 K and the series at 5 K.

5.2 Coincidence Corrections

Immediately after the CPC calibration, the prototype instrument was tested with high ultrafine number concentrations to illustrate the effect of coincidence on the instrument performance and the possibility of coincidence corrections. Cooking on a gas cooker generates high number concentrations of ultrafine particles (Li et al., 1993; Dennekamp et al., 2001). The kitchen is therefore a well suited place for testing the instrument with high number concentrations prone to higher coincidence losses.

In this experiment, AmbiCount$_B$ was used to sample aerosol in a kitchen during cooking with a gas cooker (hobs and oven). Figure 5.11 shows the number concentrations measured during the experiment. The sample flow rate was measured before the experiment as $q = 9$ ml·min^{-1}, the CPC signal had on average an amplitude of 2.25 V and a width of 5.1 µs at the level of the threshold used in the CPC, which at 113 mV was relatively low (not ideal as it enhances coincidence, but suited to demonstrate high coincidence errors). The minimum time difference τ can therefore be estimated with 5.1 µs or a slightly higher value (width at threshold level). The corrected number concentration for the size fraction 10 nm to 360 nm was calculated with equation (3.36) using $\tau = 5.1$ µs.

The results of the experiment show that the measured ultrafine number concentration reaches a maximum at 436 900 cm^{-3}, which corresponds to the maximum count rate currently implemented on the microprocessor of 65.535 kHz. It seems that without this limit, the measured concentration would have been higher during certain periods, where now the maximum is reached. Without this technical limit, the indicated number concentration would eventually be limited by coincidence to the value $^{e^{-1}}/_{q\tau}$, the maximum of n_i at $\nu = 1$. From the fact that this limit was not reached within the technical limits ($^{e^{-1}}/_{q\tau} > 436\,900$ cm^{-3}), it follows that the effective sensing volume $q\tau$ is smaller than $e^{-1}(436\,900\ \text{cm}^{-3})^{-1} = 8.4 \cdot 10^{-13}$ m^3 and, therefore, $\tau < 5.6$ µs. This result agrees well with the estimated $\tau \approx 5.1$ µs, which corresponds to $\nu = 0.62$ at $n_p = 814\,980$ cm^{-3} resulting in under-reading by a factor of 0.54 which yields the measured maximum of $n_i = 436\,900$ cm^{-3}. The approximation of the true number concentration n_p by equation (3.36), however, gives a value of 772 240 cm^{-3} at $n_i = 436\,900$ cm^{-3} (see figure 5.11)

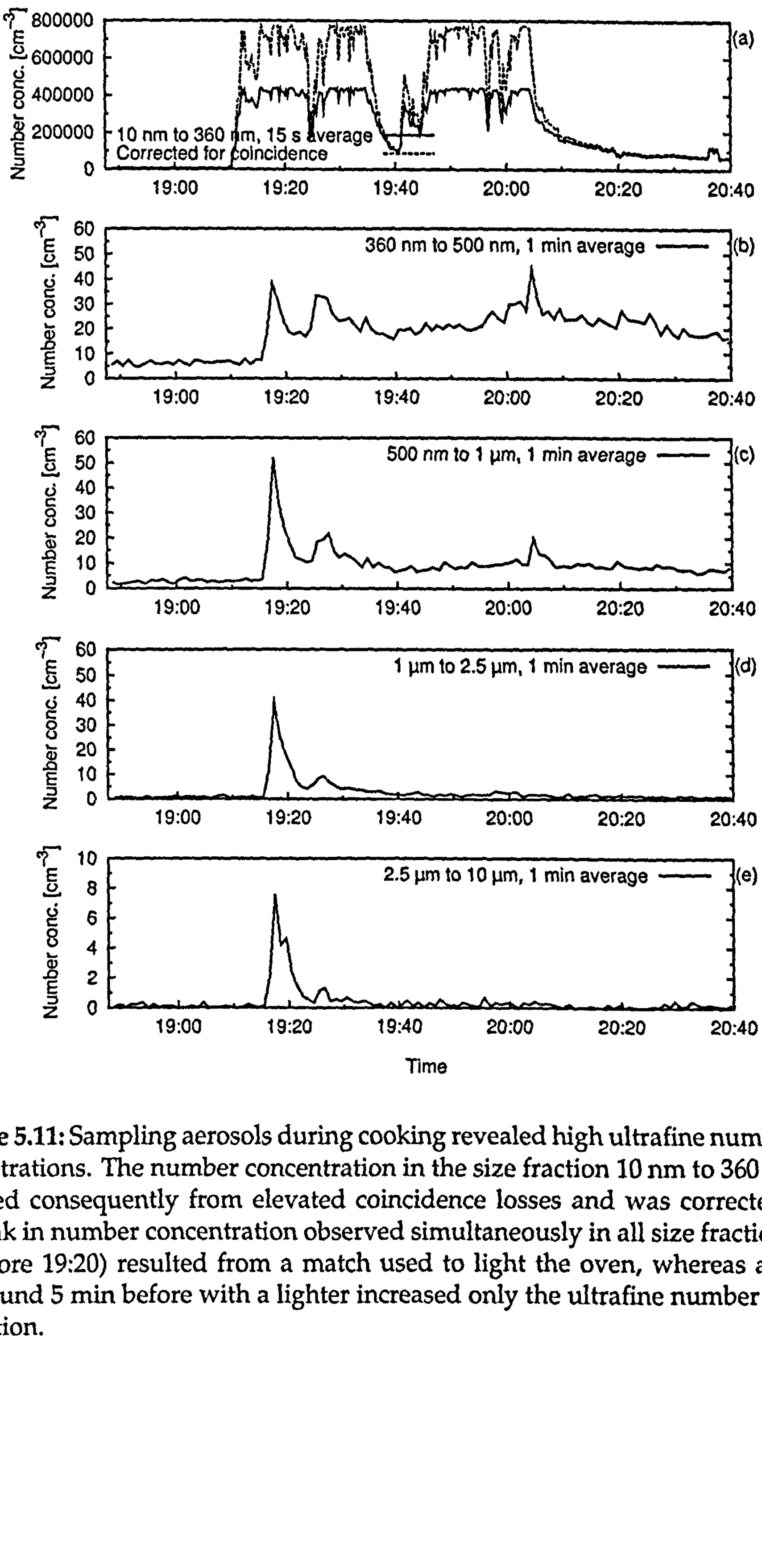

Figure 5.11: Sampling aerosols during cooking revealed high ultrafine number concentrations. The number concentration in the size fraction 10 nm to 360 nm suffered consequently from elevated coincidence losses and was corrected. The peak in number concentration observed simultaneously in all size fractions (just before 19:20) resulted from a match used to light the oven, whereas a hob lit around 5 min before with a lighter increased only the ultrafine number concentration.

showing the limitation of equation (3.36) when ν is too close to one.

If, however, equation (3.36) is used for $\nu \leq 0.5$ then n_p is underestimated by only 2% or less. This is, therefore, a method of correcting the ultrafine number concentration for coincidence losses, which would readily take the upper concentration limit of the instrument to over 500 000 cm^{-3}. In the following, however, the method was not used as number concentrations encountered were normally below 100 000 cm^{-3} so that coincidence correction was not necessary.

5.3 Comparison with Traditional Instruments

The new AmbiCount instruments were field tested under real ambient conditions and compared with instruments that are routinely used for ambient monitoring. The field tests were conducted at the monitoring station *Birmingham Centre* (part of the automatic network run by the UK Government's Department for Environment, Food & Rural Affairs, see figure 5.12). This site was selected because of its location in a busy city centre and the real-time instrumentation employed at the site. The instrument was collocated with a TSI CPC model 3022A and a TEOM measuring PM_{10}. The former was used for comparing of total number concentrations whereas the latter allowed comparison between the temporal trends of the total mass concentration and the five different number concentrations measured by the new instrument, as well as direct comparison of PM_{10} mass concentration calculated from the number concentrations with measured values. The sampling duct, which has an inner diameter of 25 mm, was extended with a straight metal tube of 1.35 m length, so that the sample could be taken outside the measurement cabin from a similar position as the inlets for TEOM and TSI CPC.

The duration of the complete trials was from 30 April to 10 September 2002. In order to demonstrate the performance of the instrument in the field, results are presented for one week, 27 June to 5 July. Starting with this week, one of the two prototype instrument ($AmbiCount_B$) was used continuously at the monitoring site and showed sustained performance and reliable operation. The instrument was never stopped during this period and data logging was interrupted only for around 30 min once every week for down-

loading data to a computer and refilling the CPC with alcohol. The performance characteristics of the instrument during the week presented here were typical of the other periods of the trial as well. In the period before 27 June, problems with the printed circuit board containing the microprocessor led to a malfunctioning and loss of data during parts of that period, affecting subsequently both AmbiCount_B and AmbiCount_A. The failure was caused by loosened contact pins resulting from board flexure under the weight of a transformer mounted on the board. The problem was fixed by changes to the printed circuit board (transformer taken off the board and supported independently) in both prototype instruments.

The linearity between the responses of the new instrument CPC and the TSI CPC at normal ambient concentrations is demonstrated in figure 5.13. The total number concentration measured by the CPC of AmbiCount_B is plotted in this figure against the values obtained with the TSI CPC. The instrument's results correlated well (correlation coefficient $r^2 = 0.96$) for all concentrations encountered at this site. However, CPC_B consistently read approximately 40% higher than the TSI CPC. A possible cause is believed to be the different lower detection limits of the TSI CPC 3022A with 50% detection efficiency at 7 nm (Sem, 2002) and CPC_B. The lower detection limit of the latter was not yet defined through calibration, as necessary test equipment was not available. The calculated lower limit for the operating conditions is $\sim$4.2 nm whereas diffusion losses indicate 50% penetration at 6 nm. The lower detection limit of the AmbiCount CPCs is, therefore, believed to be around 6 nm. Differences in the true lower detection limits will result in different number concentrations. Harrison et al. (1999a), for example, compared measurements with the TSI CPCs model 3022A and model 3025 with respective lower limits of 7 nm and 3 nm; they found that the model 3022A reported on average a number concentration of about 10% lower than that of the model 3025. They also observed that this difference increased markedly during sunny periods and suggested that particle formation by photochemistry would lead to a substantial increase of number concentration in the size range between the lower limits of the two CPCs. While for the comparison of the new instrument with the TSI CPC model 3022A there were no sunshine data available at the monitoring site, the average diurnal variations of the ratio between the total number concentration of these two instru-

Figure 5.12: The photograph in the left shows the measurement cabin at the monitoring site Birmingham Centre. On the right the sampling inlets are shown in an enlargement, the PM_{10} cyclone of AmbiCount and the inlets of TEOM and TSI CPC 3022A are indicated.

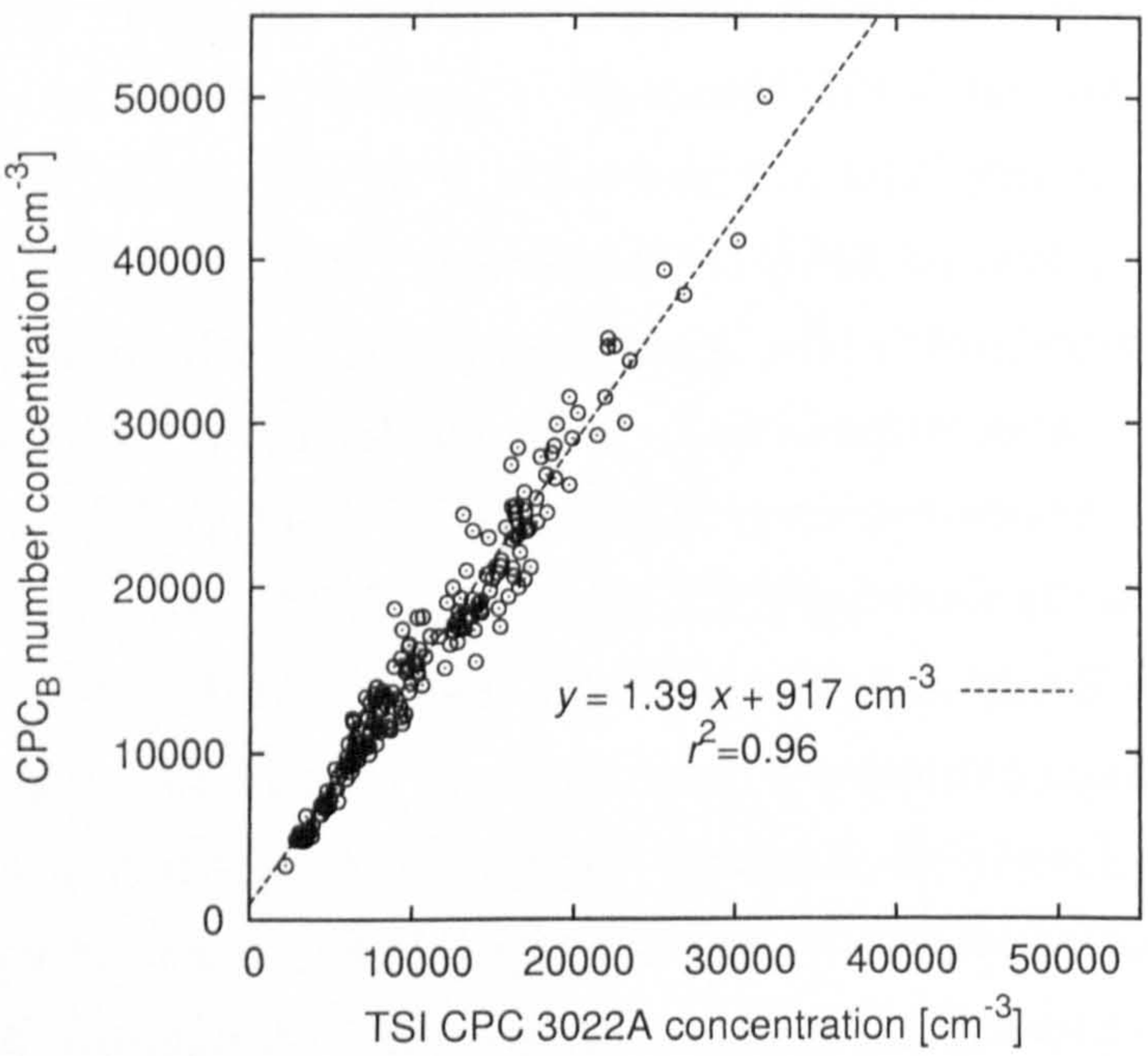

Figure 5.13: Comparison of number concentration measured by CPC_B against number concentration measured by TSI CPC model 3022A at the monitoring site Birmingham Centre (UK), showing the linearity of its response. Hourly averages are shown for the week 27 June to 5 July 2002.

ments was studied here instead, as shown in figure 5.14. Despite the large

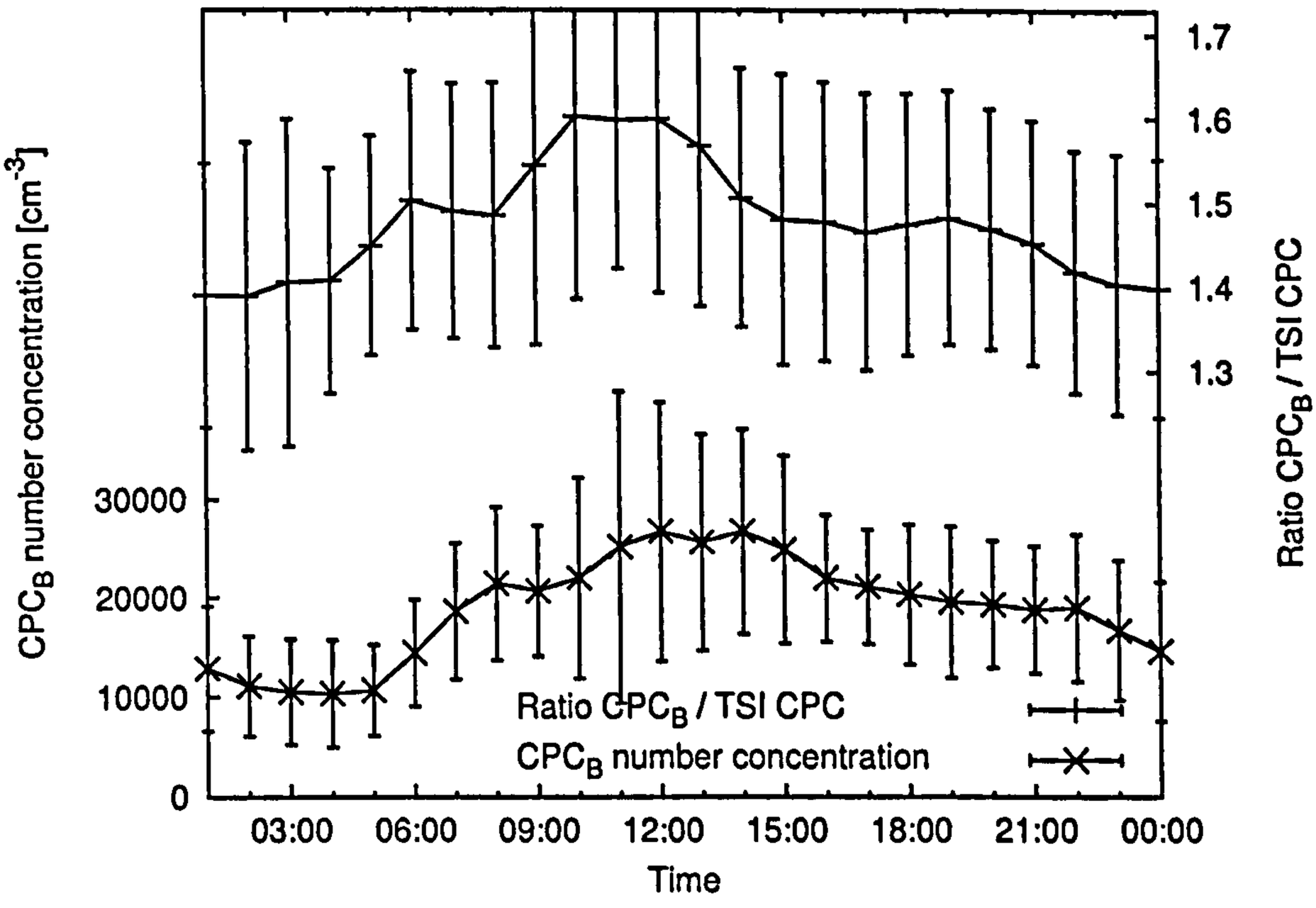

Figure 5.14: Diurnal variation of the ratio of the total number concentrations measured by AmbiCount$_B$ and the TSI CPC. Hourly data between 27 June and 26 July 2002 were used to calculate the average diurnal data.

variations—the error bars show the standard deviation—there is clearly a dependence with the highest ratios between 10:00 and 12:00 (times in GMT), suggesting that the different instruments measure different size ranges. It is interesting to note that the averaged total number concentration is correlated to the ratio, as one would expect if particle formation is the cause for changes in the ratio of values from the two instruments. The significant difference observed in number concentration, however, is not easily explained with the expected lower limits of the two instruments.

The steepness of the cut-off curves (detection efficiency against particle diameter) of each CPC may also be different, with the newly built CPC having the steeper curve due to the sample being introduced in the centre of the condenser (Stolzenburg and McMurry, 1991), resulting again in a higher reading than that in the TSI instrument. The TSI CPC might also suffer from higher sampling losses due to its lower sample flow rate (1.5 $l\,min^{-1}$ versus 5 $l\,min^{-1}$ in the new instrument) through the inlet tubes employed at the Birmingham site. This should, however, not significantly affect particles above 5 nm, as for a flow rate of 1.5 $l \cdot min^{-1}$ and a tube length of 2 m the

transmission efficiency is 0.7 for 5 nm particles. Apart from being longer and narrower, the inlet tube to the TSI instrument included several bends; this might have a further influence on the sampling losses (Wang et al., 2002). Whilst more investigations would be required to clarify this issue, it should also be noted that the TSI CPC uses the photometric mode above 10 000 cm^{-3} (which occurred for more than 60% of the 1 h average data during the field trial), whereas the new instrument counted single particles in the whole range of concentrations encountered.

The linearity of the total number concentration was also tested using a much higher time resolution of 15 s in order to evaluate the instrument's capability to capture short incidents of very high ultrafine particle concentrations. Figure 5.15 shows a period of 40 min on the morning of 28 June 2002 with two such ultrafine peaks. The trend of the aerosol concentration as indicated by the TSI CPC is followed closely by the concentration measured by the CPC of the new instrument. However, the 40% difference in concentration measurements, mentioned above for the hourly averages, can be clearly observed at this resolution too.

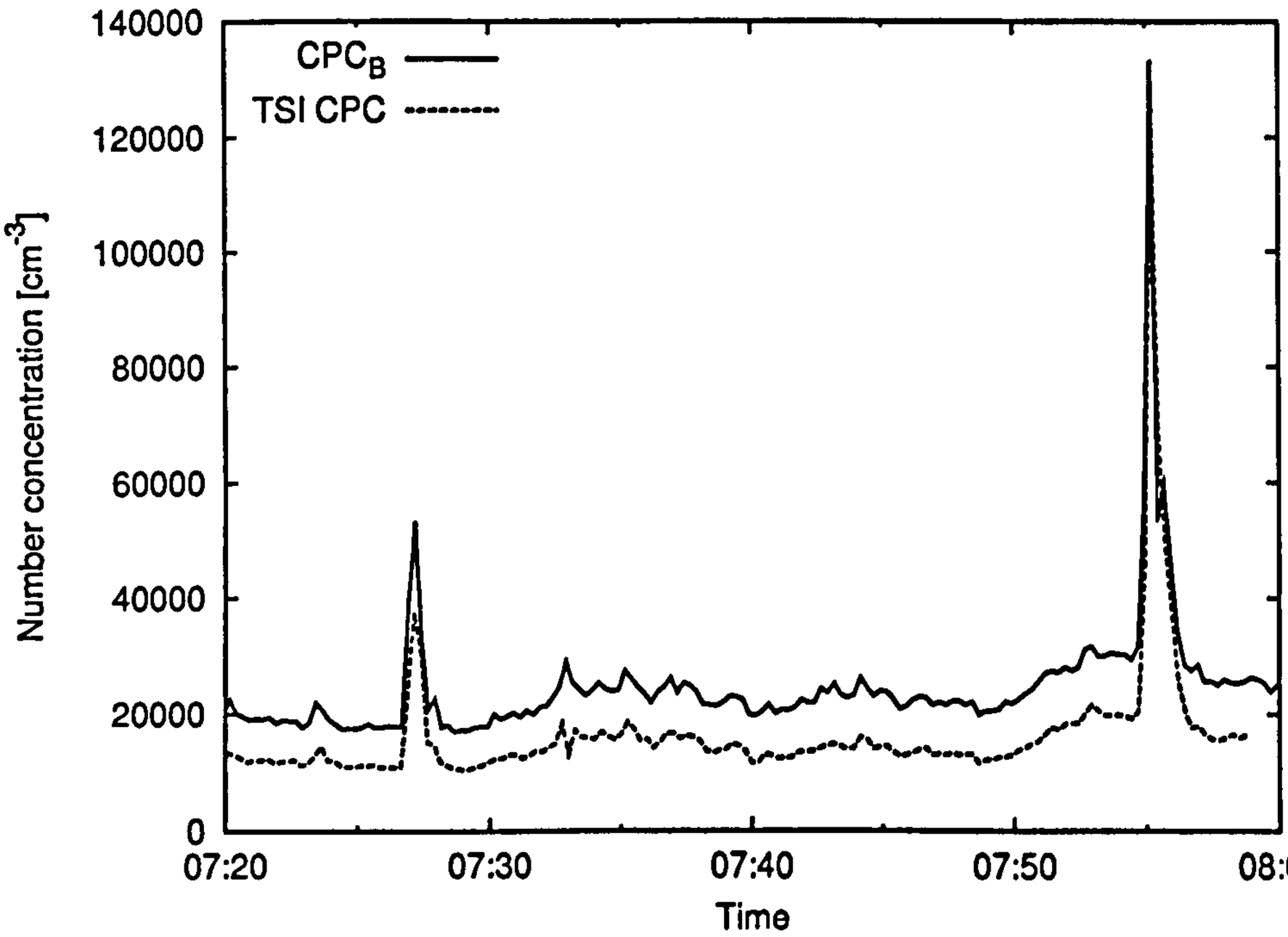

Figure 5.15: Total number concentration measured by the instrument compared to the TSI CPC number concentration at a time resolution of 15 s. The two peaks that occurred in the shown period are followed nearly identically by both instruments.

The instrument is unique in giving real-time size-resolved information in the form of the number concentrations in five size fractions. Figure 5.16 shows, as an example, the results for one week of measurements at the Birmingham site as hourly averages. For comparison, TSI CPC and TEOM data are also reported. The number concentrations in the five size fractions are shown in figures 5.16a–5.16e. One can clearly observe the large differences in the number concentrations encountered in the different size fractions with a maximum of 50 000 cm^{-3} for the ultrafine fraction (see figure 5.16a) and a maximum of 0.35 cm^{-3} in the coarse fraction (see figure 5.16e). The fractions from 0.5 µm to 1.0 µm and 1.0 µm to 2.5 µm are relatively similar (see figures 5.16c and 5.16d), possibly indicating similar sources.

The other size fractions, however, differ from these significantly and show different trends. This was also observed for the other weeks of the field trial. This means that the different modes of the ambient aerosol size distribution are not well correlated for most of the fractions sampled, which may be caused by different sources contributing to the different size fractions, or by the particles being affected differently according to their size by various meteorological processes. Further investigation, beyond the scope of this thesis, would be needed to fully interpret these data. It can be noted in figure 5.16 that the trend of the ultrafine number concentration, representing the nucleation mode, is very different from all other size fractions and hence the larger size fractions cannot be used to predict the ultrafine number concentration.

The PM_{10} mass concentration from the TEOM (see figure 5.16f) is best correlated to the coarse size fraction 2.5 µm to 10 µm, with a correlation coefficient of $r^2 = 0.77$ for the data shown in figure 5.16e, and shows weak correlation with the size fraction 1 µm to 2.5 µm ($r^2 = 0.41$). The number concentrations in the other size fractions show very weak or no correlation with TEOM data ($r^2 = 0.26$ for fraction 500 nm to 1 µm shown in figure 5.16c, $r^2 = 0.004$ for fraction 360 nm to 500 nm shown in figure 5.16b, and $r^2 = 0.24$ for fraction 10 nm to 360 nm shown in figure 5.16a). The mass concentration can also be calculated from the number concentrations measured by the instrument. Results from calculations using the geometric mean diameter of each size fraction and a particle density of 1 600 $kg \cdot m^{-3}$ as explained in section 5.4 are shown in figure 5.16f. Because of the size information provided

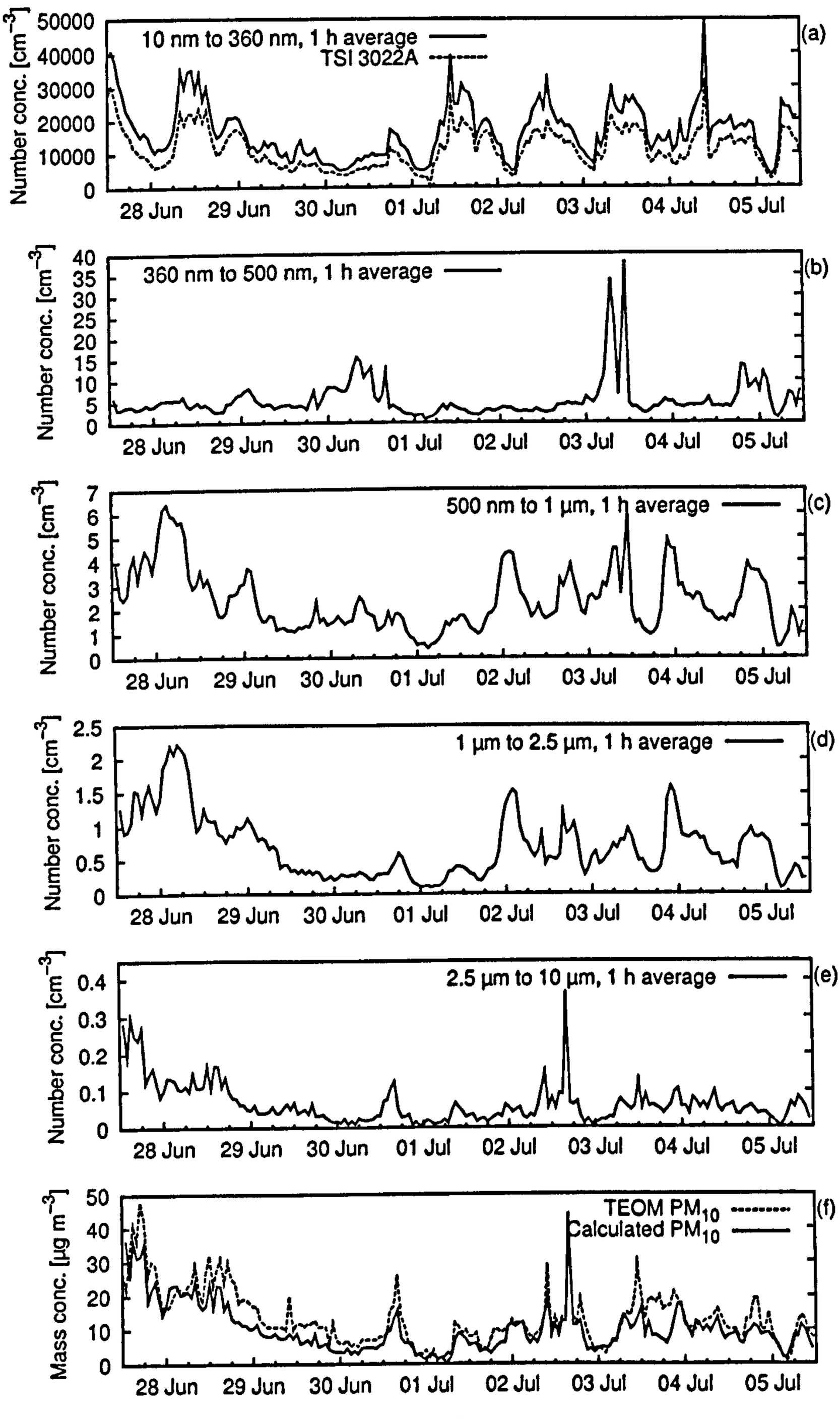

Figure 5.16: Number concentrations of the five size fractions measured by the new instrument (AmbiCount$_B$). The ultrafine concentration (10 nm to 360 nm) is compared to the TSI CPC number concentration. The TEOM PM_{10} mass concentration is shown for comparison.

by the instrument, not only PM_{10} but also $PM_{2.5}$ and PM_1 can be given, and if required, also $PM_{0.5}$ or $PM_{0.36}$. Contribution to PM_{10} mass concentration from the different size fractions can therefore be estimated and variation, with time and parameters such as meteorological conditions, can be studied. Figure 5.17 shows the contribution to calculated PM_{10} mass concentration from the different size fractions for the week presented in figure 5.16. The next section reports on studies that were carried out to find a suitable

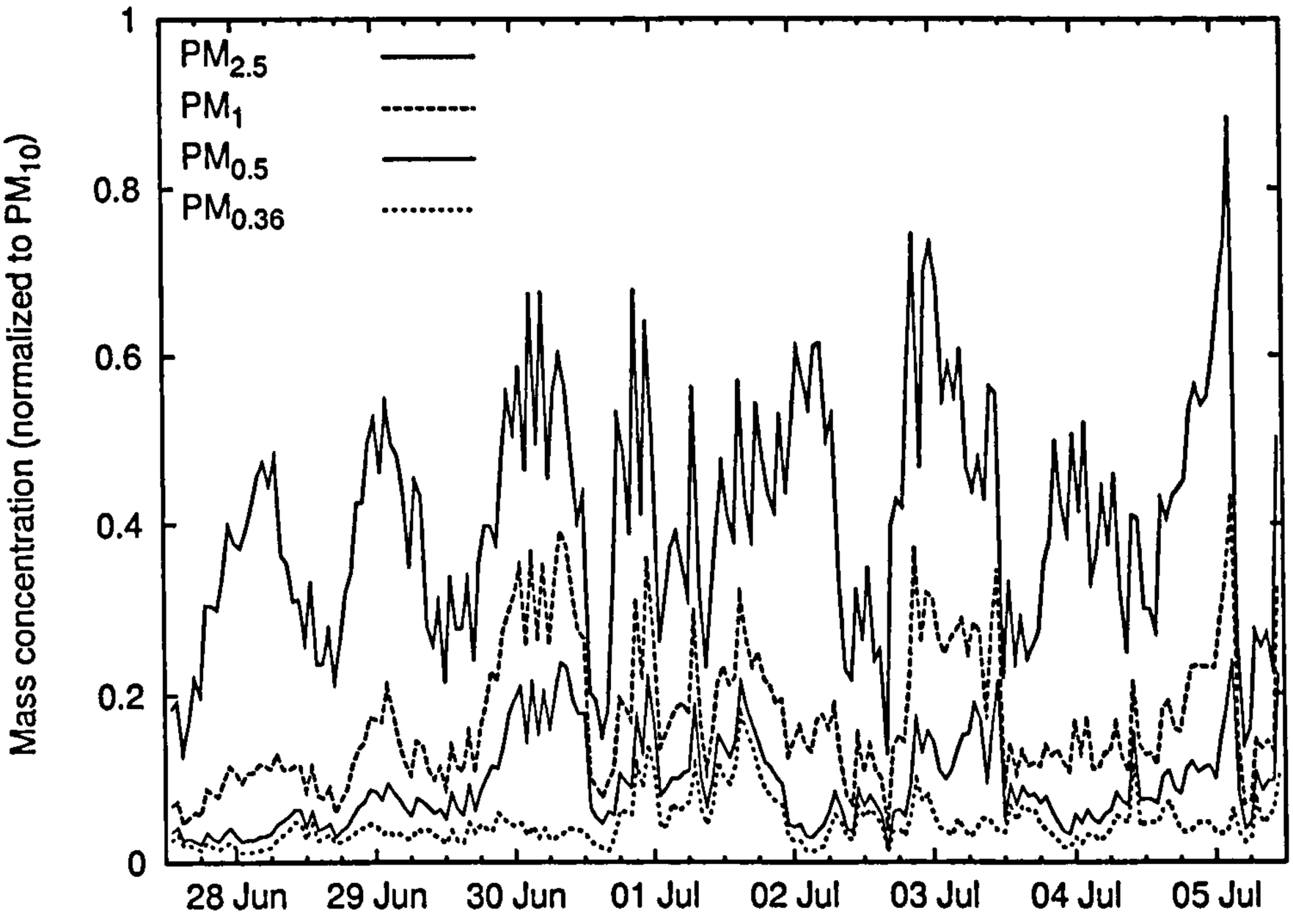

Figure 5.17: Relative contribution to calculated PM_{10} mass concentration from the different size fractions. The mass concentration is normalized to PM_{10} mass concentration.

number-to-mass conversion algorithm.

5.4 Number-to-Mass Conversion

The calculation of the mass concentration from number concentration in the size fractions is complicated by uncertainties such as particle density, shape, and exact number size distribution. Certain assumptions are necessary and need to be carefully chosen. While there is a linear relationship between mass and particle densities, mass is related to the third power of particle size. As a consequence, inaccuracies in the knowledge of the size distribution of the particles can lead to large errors in computed mass concentra-

tion and it is very important to achieve realistic assessment about the size distribution. Three algorithms for such a number-to-mass conversion were studied and results were compared to the measured values of PM_{10} mass concentrations from the monitoring campaign in Birmingham (measured by the TEOM).

5.4.1 Smoothing Method

To get a continuous number size distribution from measurements in a limited number of size fractions, a high-resolution reconstruction method was proposed by Lawless (2001). The size distribution measured by the instrument, given as number concentrations in relatively broad size fractions, is normalized to the logarithmic width of the fractions (dividing the number concentration of every size fraction by the difference between the logarithms of the upper and lower limits of the fraction). The size distribution is then subdivided in many sub-channels of similar logarithmic widths. The normalized concentration of a size fraction is taken as initial value of the concentrations in the sub-channels of that fraction. The concentrations of the sub-channels are then varied in order to achieve a smooth size distribution. Different criteria for smoothness can be applied, as for example minimizing a quantity such as the sum of squares of the differences between the concentrations of adjacent sub-channels. For OPCs, the author suggested using relative differences in the form of logarithmic differences as concentrations usually vary over many orders of magnitude. In fact, using the sum of logarithmic differences as a criterion of smoothness on data from the instrument showed the best results.

While modifying the concentrations in the sub-channels, the concentration in the size fractions of the instrument is maintained. In this way the method does not alter the original data and no assumptions are made other than that a smooth distribution is more likely to be closer to the actual distribution than a step-like distribution. The resulting smoothed distribution is therefore only an alternative presentation of the same data, and in particular the resolution remains the same—no finer structure of the distribution is revealed. Some structure, however, might now be seen, which before was difficult to recognize.

Figure 5.18 shows an example of a smoothed size distribution; the data

shown are for demonstration purpose. The size fractions selected are as used in Birmingham, whereas the number concentrations are selected so that presentation on a non-logarithmic scale is possible. The figure does therefore not represent a typical set of data, for which the number concentration in the ultrafine size fraction (10 nm to 360 nm) would differ from the concentration in the other size fractions by many orders of magnitude. The

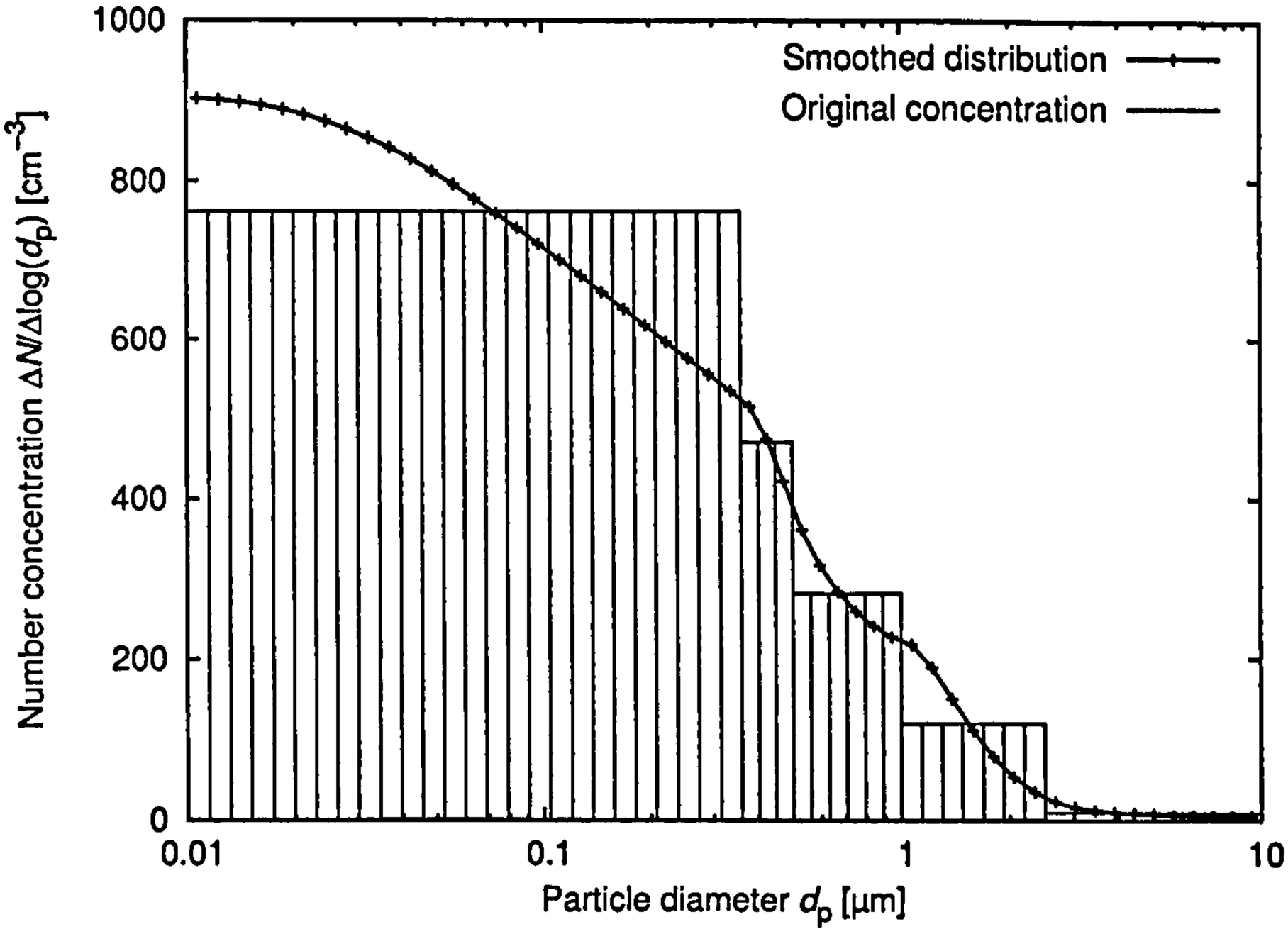

Figure 5.18: The original data given by number concentrations in the size fractions are normalized by dividing every number concentration by the difference $\Delta \log(d_p)$ between the logarithms of the upper and lower limits of the corresponding size fraction. The normalized concentrations are shown as "Original concentration". Every size fraction is subdivided in many sub-channels of equal logarithmic width. The number of sub-channels in every size fraction is selected so that the sub-channels of the different size fractions have similar logarithmic widths. The normalized concentration of a size fraction is taken as initial value of the concentrations in the sub-channels of that fraction. The concentrations of the sub-channels are then smoothed to the shown size distribution. In every size fraction, the areas under the distributions of original data and smoothed data are the same, indicating the same number concentration. (In this example, the number concentrations in the different size fractions are: 1 185 cm^{-3} in size fraction 10 nm to 360 nm; 67.12 cm^{-3} in size fraction 360 nm to 500 nm; 84.95 cm^{-3} in size fraction 500 nm to 1.0 µm; 47.53 cm^{-3} in size fraction 1.0 µm to 2.5 µm; and 5.956 cm^{-3} in size fraction 2.5 µm to 10 µm.)

non-logarithmic scale of the normalized number concentration as presented in figure 5.18 has the advantage that the area under the size distribution curve is proportional to the number concentration, hence it can be seen that

the number concentration in the size fractions is the same in original data and smoothed data.

The mass size distribution can be calculated from the smoothed number size distribution, assuming spherical particles and a certain particle density (which may be size dependent). Figure 5.19 shows this for the example data, the volume size distribution is shown, before applying the density. The mass concentration is calculated by summing the contribution from the

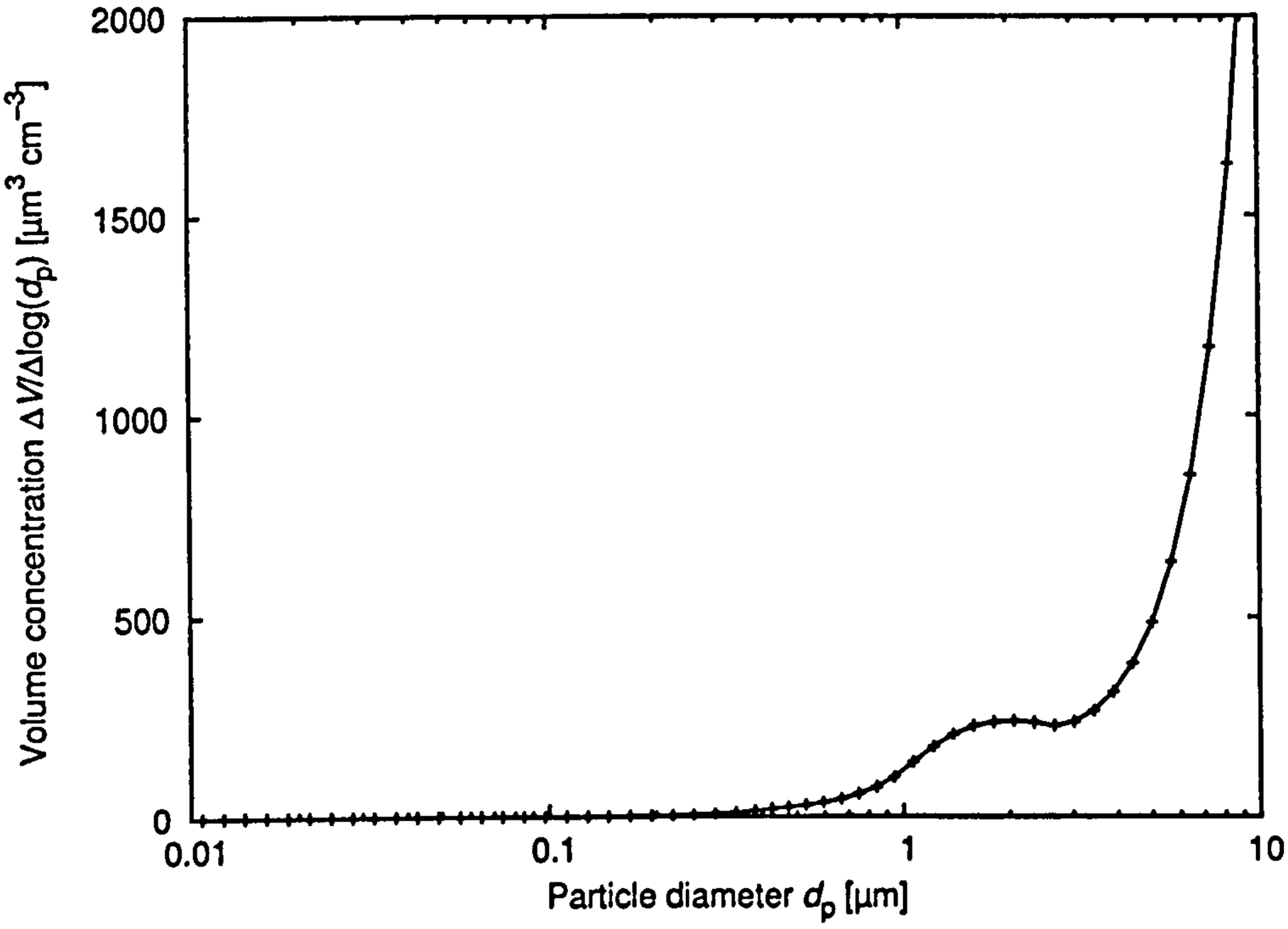

Figure 5.19: Volume concentration resulting from the smoothed number size distribution assuming spherical particles.

single sub-channels. As the smoothed number size distribution is probably closer to the underlying true size distribution, the resulting mass concentration will be a better estimate than a mass concentration calculated by simply integrating the step-like number size distributions while applying the same assumptions.

To calculate the contribution to the mass concentration of a single sub-channel, the normalized number concentration of the sub-channel is first converted in volume concentration assuming spherical particles with a diameter equal to a mean diameter of the sub-channel. The geometric mean is used here. However, different means will give very similar results if the sub-channels are small enough. For the automated conversion of many data sets, an algorithm has been programmed in Perl to subdivide original data

in sub-channels and then minimize the sum of logarithmic differences. As output of the program, for every data set the smoothed size number and volume distributions as well as PM_{10} mass concentration and the mass concentrations of the different size fractions are given.

5.4.2 Geometric Mean Diameter

Without knowledge of the size distribution, the mass concentration could be calculated for every size fraction directly from the respective number concentrations, if the average mass of particles in the size fraction were known or could be estimated. The average mass corresponds, assuming a spherical particle, to the *diameter of average mass* (Hinds, 1999). The problem of number-to-mass conversion reduces to assuming good diameters of average mass for all size fractions, besides the assumptions of spherical particles and certain particle densities. As a first choice, the geometric mean diameter was tested here, together with assuming the same density for all size fractions. For every size fraction a mass concentration can then be directly calculated and PM_{10} mass concentration is simply the sum of those. This method gives a linear relationship between the count in the size fractions and the mass contributed from them. First tests showed that the mass concentration for ultrafine particles in the size fraction from 10 nm to 360 nm calculated with this method was unexpectedly high, sometimes up to 50% of calculated PM_{10} mass concentration. The choice of the geometric mean diameter (using 60 nm for the (10 to 360) nm size fraction) as diameter of average mass was, therefore, for this size fraction changed to 30 nm. This choice agrees with typically found mean diameters of the nucleation mode in ambient air (for example Morawska et al., 1999b; Harrison et al., 2000; Longley et al., 2003) and it is believed to be a better choice than the geometric mean diameter of the size fraction. Halving the choice for the mass mean diameter results in reducing the contribution to the mass concentration by a factor of eight according to the volume, and hence mass, going at the third power of the diameter. For the automated calculations of the mass concentration with this method, the same Perl program which was used for the smoothing method also includes the mass concentrations calculated by this method in its output.

5.4.3 Fit to Trimodal Log-Normal Distribution

The log-normal distribution (for example Heintzenberg, 1994; Hinds, 1999) is often used to fit atmospheric particle concentrations. The log-normal distribution has the form

$$\frac{\mathrm{d}N(d_\mathrm{p})}{\mathrm{d}\ln d_\mathrm{p}} = \frac{N_0}{\sqrt{2\pi}\ln\sigma}\exp\left(-\frac{\left(\ln\frac{d_\mathrm{p}}{\mu}\right)^2}{2(\ln\sigma)^2}\right) \tag{5.1}$$

where N_0 is the total number concentration, σ and μ are the geometric standard deviation and the geometric mean respectively. Whitby (1978) used three log-normal distributions to fit the three modes (the nuclei, the accumulation, and the coarse mode) he identified in measured size distributions. Birmili et al. (2001) used three modes for particles with a diameter below 1 µm. Horvath et al. (1990) fitted one log-normal mode to OPC data of particles having a diameter above 1 µm.

In order to fit the sum of several log-normal distributions to the number concentration values in a few size fractions, the number concentration data are first converted to a cumulative distribution (Hinds, 1999), with values at the size cuts between the size fractions. The cumulative log-normal distribution function, $N(d_\mathrm{p})$ obtained by integrating equation (5.1) in the form

$$N(d_\mathrm{p}) = \frac{N_0}{2}\left(\mathrm{erf}\left(\frac{\ln\frac{d_\mathrm{p}}{\mu}}{\sqrt{2}\ln\sigma}\right) - \mathrm{erf}\left(\frac{\ln\frac{d_\mathrm{p}}{d_\mathrm{L}}}{\sqrt{2}\ln\sigma}\right)\right) \tag{5.2}$$

is then fitted to these points of the cumulative number distribution. The lower limit of the lowest size fraction is d_L and the cumulative number distribution is fixed to zero at d_L. The error function is defined as $\mathrm{erf}(x) = \frac{2}{\sqrt{\pi}}\int_0^x \mathrm{e}^{-t^2}\mathrm{d}t$.

To describe the size distribution between $d_\mathrm{L} = 10$ nm and 10 µm at least three log-normal modes are necessary. As every log-normal mode has three parameters, the total number concentration in the mode N_0, the geometric standard deviation σ, and the geometric mean μ, a size distribution with three log-normal modes is described by nine parameters. With five data points, assumptions are required to avoid multiple solutions and to make the fitting process feasible. To fit the data to more than three modes, more points would be necessary, so that it would not improve the quality of the

fit. Figure 5.20 shows a fit for the example data which was used in the smoothing method (see figure 5.18). Figure 5.21 shows the corresponding log-normal distribution function.

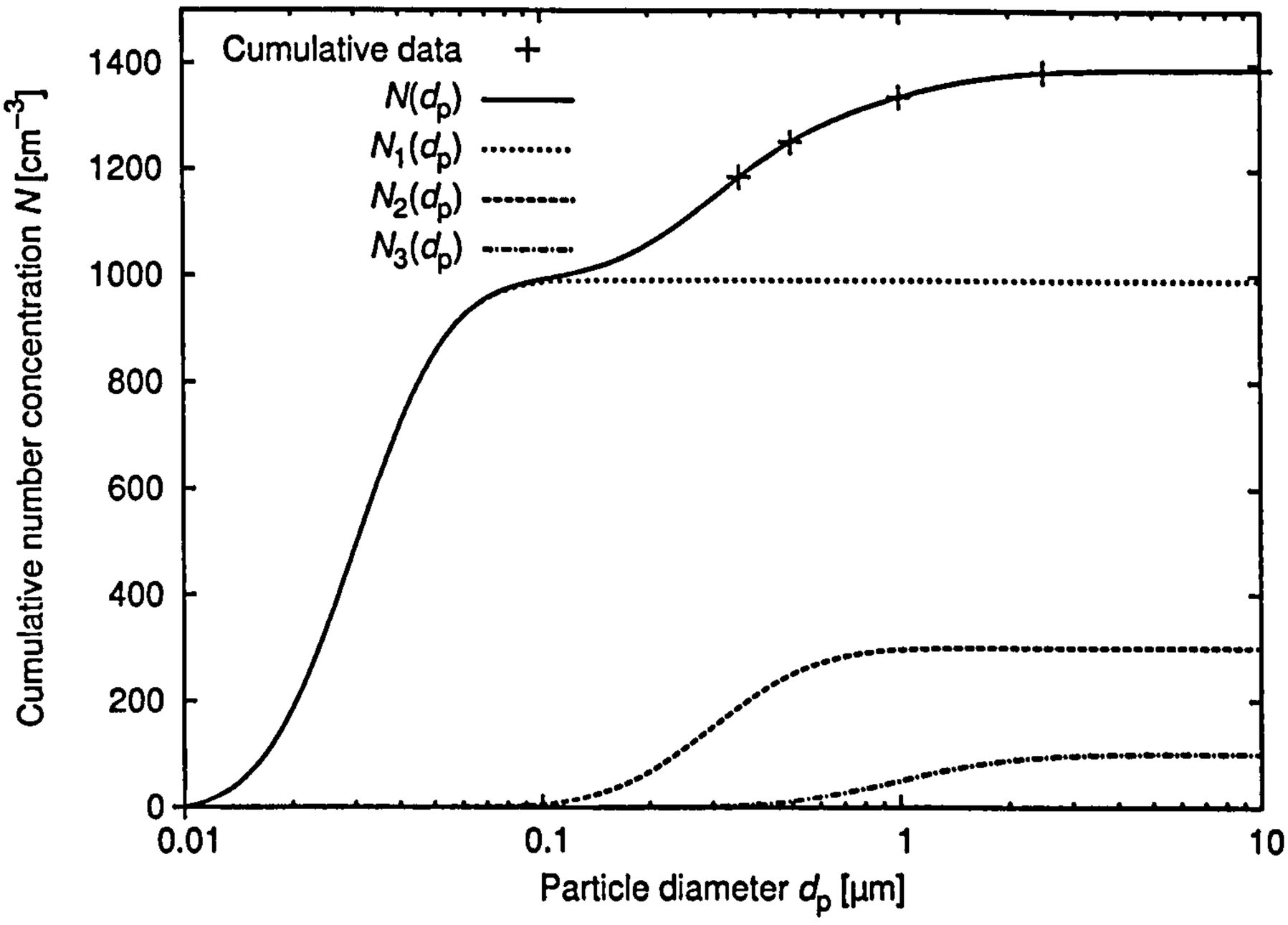

Figure 5.20: Data presented as cumulative number concentration and fitted cumulative number size distribution N, which is the sum of three log-normal modes. (The fitted values of N_0, σ, and μ for the three modes are: 1 000 cm^{-3}, 1.6 (was fixed), and 30 nm (was fixed) respectively for nuclei mode; 300 cm^{-3}, 1.7, 300 nm respectively for accumulation mode; and 100 cm^{-3}, 1.8 (was fixed), and 1.0 µm (was fixed) for the coarse mode.)

The assumptions chosen here to test number-to-mass conversion with log-normal fit are the geometric means and standard deviations of the first (ultrafine) and the third (coarse) mode. Assumptions are based on literature values (Whitby, 1978; Whitby and Sverdrup, 1980) and evaluation of quality of fit achievable with chosen values. The selected values are 1.6 and 30 nm, and 1.8 and 1.0 µm for geometric standard deviations and means of the two modes respectively. The value of the geometric mean of the coarse mode was selected lower than values found in the literature in order to obtain a better fit with the data. Assuming spherical particles and a certain particle density, the volume size distribution (depicted in figure 5.22) and mass concentration are calculated from the log-normal distribution function (see figure 5.21) which results from the fitted cumulative log-normal distribution.

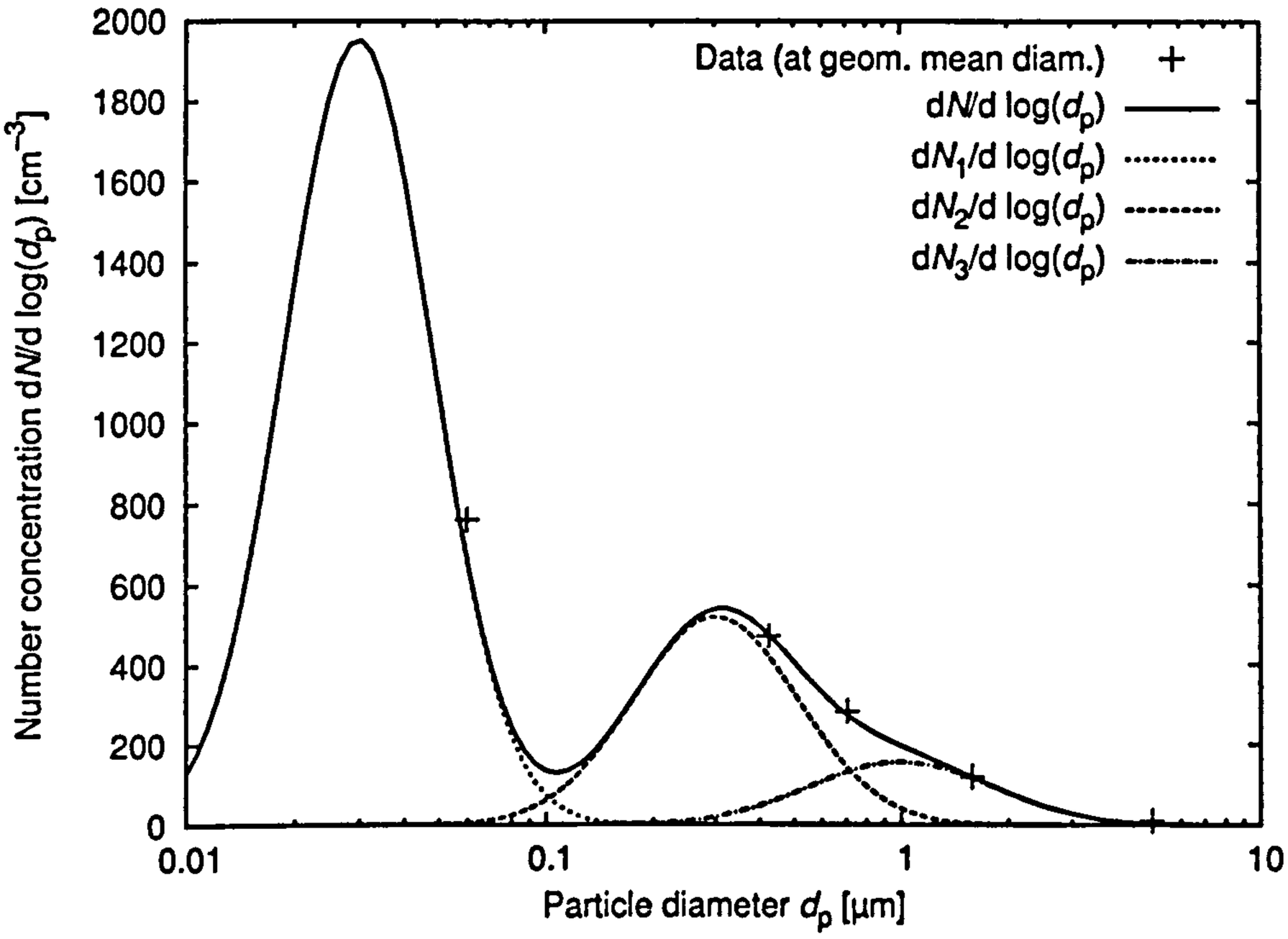

Figure 5.21: Size distribution resulting from the fitted cumulative number concentration. The three log-normal modes are also shown.

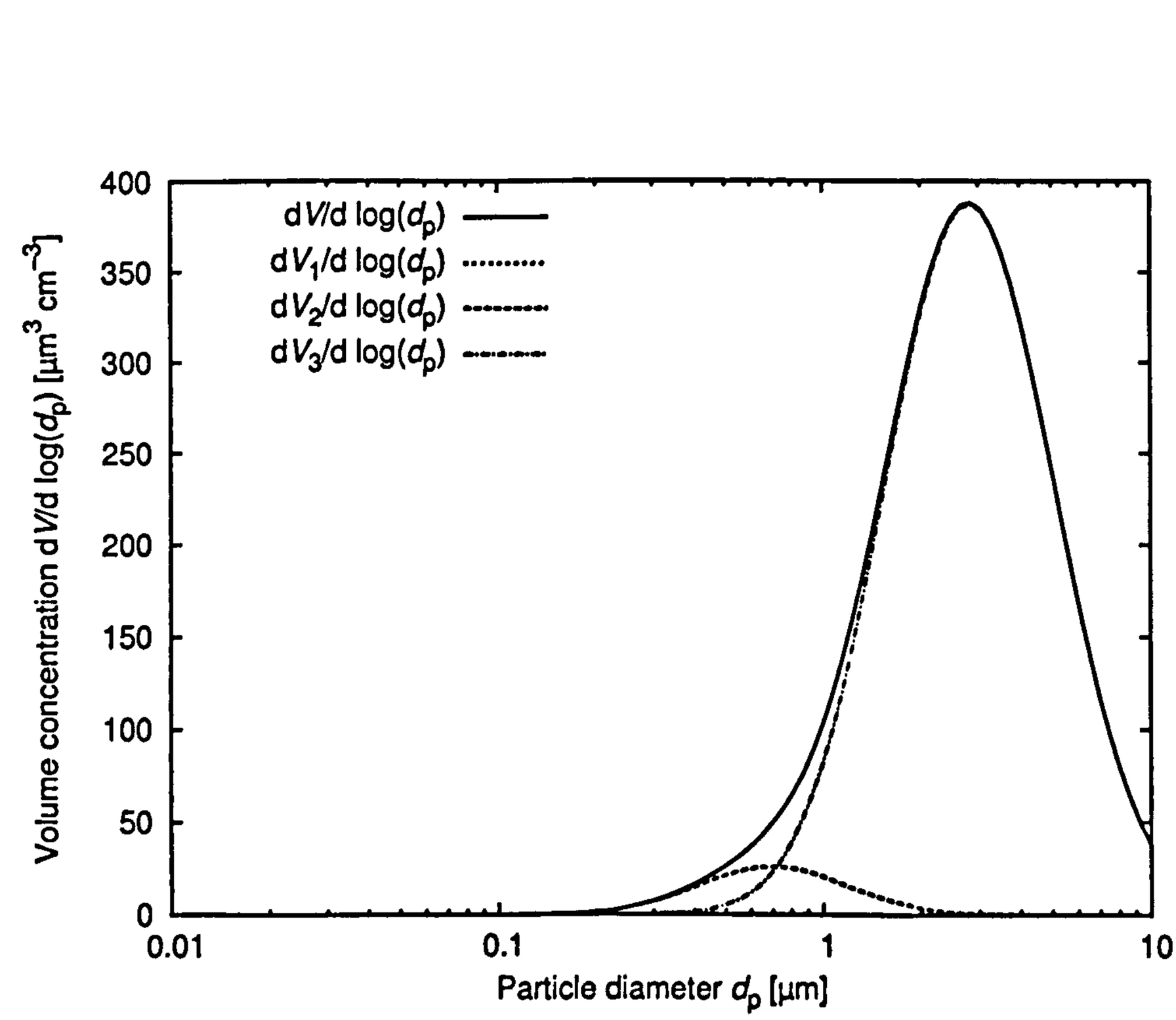

Figure 5.22: Log-normal volume size distribution resulting from the fitted cumulative number concentration. The three log-normal modes are also shown.

An algorithm to perform the fit was programmed in Perl. It varies the geometric standard deviation and mean of the second mode (accumulation) independently. For every pair of values for the geometric standard deviation and mean the total number concentrations of the three modes are calculated exactly from the first three data points of the measured cumulative number concentration. This results in a complete set of the nine parameters describing the three modes. The difference between the corresponding distribution and the remaining two points of the measured cumulative number concentration represents a measure of how good this log-normal distribution fits the measured data. The best fit is given by the geometric standard deviation and mean of the second mode with the least difference. The output of the program is, for every measurement data set, the best fit as given by the parameters describing the three modes as well as the PM_{10} mass concentration and the mass concentrations of the single size fractions computed from this best fit.

5.4.4 Results of Number-to-Mass Conversion

Comparison of Computed with TEOM Measured Mass

The PM_{10} data measured with the TEOM alongside the new instrument in Birmingham were compared to the results from the number-to-mass conversion of the number concentration data and used as an indicator of the quality of the conversion. However, it must be noted that TEOM PM_{10} data might not at all times accurately represent the actual PM_{10} mass concentration (TEOM is suspected to suffer from losses of semi-volatile particles, see, for example Green et al., 2001). Computed PM_{10} mass concentration data of each of the three conversion algorithms for hourly average measured data from the new prototype instrument were separately compared against hourly average measurements of the TEOM PM_{10} data. By linear regression, using least square fit, the quality of the conversion can be evaluated using the three parameters slope, intercept, and correlation coefficient r^2. In the three algorithms tested, the slope depends to a large degree on the assumptions of the particle density, whereas the intercept and in particular the correlation coefficient are more characteristic of the algorithm used. The data used for the following comparisons are from the four weeks between

27 June 2002 and 26 July 2002. Results of the linear regression are shown in table 5.1. All different algorithms assume the same particle density of 1 600 kg·m^{-3} for all size fractions which is based on particle densities found in the literature (Morawska et al., 1999a; Hand and Kreidenweis, 2002; McMurry et al., 2002).

Week	Smoothing Method			Geom. Mean Diam.			Log-Normal Fit		
starting	slope	inter.	r^2	slope	inter.	r^2	slope	inter.	r^2
27 June	0.96	-0.68	0.78	0.76	0.01	0.81	0.34	3.40	0.48
5 July	1.04	-0.27	0.60	0.77	0.52	0.59	0.95	-1.56	0.59
12 July	1.09	-0.33	0.67	0.82	0.44	0.65	0.52	3.71	0.35
19 July	1.24	-0.70	0.52	1.02	-0.86	0.54	0.77	-0.12	0.47

Table 5.1: Linear regression of number-to-mass conversion results with TEOM data. The intercepts are given in µg·m^{-3}.

The results from both the smoothing-method and the geometric-mean-diameter conversions correlate reasonably well with the TEOM PM10 data. The correlation coefficients r^2 for the studied weeks vary between 0.52 and 0.78 for the smoothing method and between 0.54 and 0.81 for the geometric mean diameter. The slopes of the best fitting straight lines are generally smaller for the geometric mean diameter. The intercepts are relatively low and range between -1.56 µg·m^{-3} and 3.71 µg·m^{-3}. The results of the log-normal fit conversion algorithm most often do not correlate well with the TEOM PM_{10} data with correlation coefficients r^2 of about 0.5 or below.

Intercomparisons between Conversion Algorithms

The following comments on comparisons between mass and number concentrations in the different size fractions and intercomparisons between the different algorithms are based on observations of results from conversion of $AmbiCount_A$ data from the week 29 May to 7 June 2002 and PM_{10} data of the same week from the collocated TEOM. Qualitatively the same observations could be made for data from other periods of the Birmingham campaign.

Smoothing Method The number concentrations in the week 29 May to 7 June 2002 are shown in figure 5.23 together with TEOM PM_{10} measured

mass concentrations in comparison with the mass concentration calculated by the smoothing method. The calculated mass concentrations in the different size fractions are shown in figures 5.24, 5.25, and 5.26. They are shown in comparison with results from the geometric-mean-diameter algorithm.

Although the number concentrations of the size fractions 10 nm to 360 nm and 360 nm to 500 nm are not correlated (see figures 5.23a and 5.23b), the mass contributions of the smoothing method from these size fractions are similar in their trends, the mass from the size fraction 10 nm to 360 nm being slightly higher (see figure 5.24, upper and lower part). All size fractions apart from the 10 nm to 360 nm fraction exhibit a correlation between mass calculated from the smoothing method and number concentration (see figures 5.24, 5.25, 5.26, and 5.23a-5.23e). This missing relationship for the ultrafine size fraction 10 nm to 360 nm is the result of the typically missing ultrafine mode in the volume distribution from the smoothing method. As a consequence the volume distribution, and hence the mass concentration, increases from nearly zero to the value at 360 nm while the volume distribution then often decreases significantly until about 500 nm so that the mass from the ultrafine size fraction is correlated with mass from the 360 nm to 500 nm size fraction. This can be seen, for example, in figure 5.27, which shows the volume size distribution resulting from the smoothing method in comparison with the fitted log-normal distribution for data from 1 June 2002, at 11:00 (GMT).

Geometric Mean Diameter versus Smoothing Method The algorithm of the geometric mean diameter yields automatically a linear relationship between the number concentration in the size fractions and the mass contributed from them (due to multiplication of number concentration data with the volume of the sphere having a diameter equal to the geometric mean diameter in the respective size fraction, see figures 5.24, 5.25, 5.26, and 5.23a-5.23e). The calculated PM_{10} mass concentration from this algorithm correlates well with the PM_{10} mass concentration from the smoothing method (with $r^2 = 0.65$, intercept = 1.93 $\mu g \cdot m^{-3}$, slope = 0.78, see figure 5.26, lower part). The resulting mass concentrations are nearly identical in the 360 nm to 500 nm size fraction (see figure 5.24, lower part) and very similar in the 500 nm to 1 µm (see figure 5.25, upper part) and 2.5 µm to

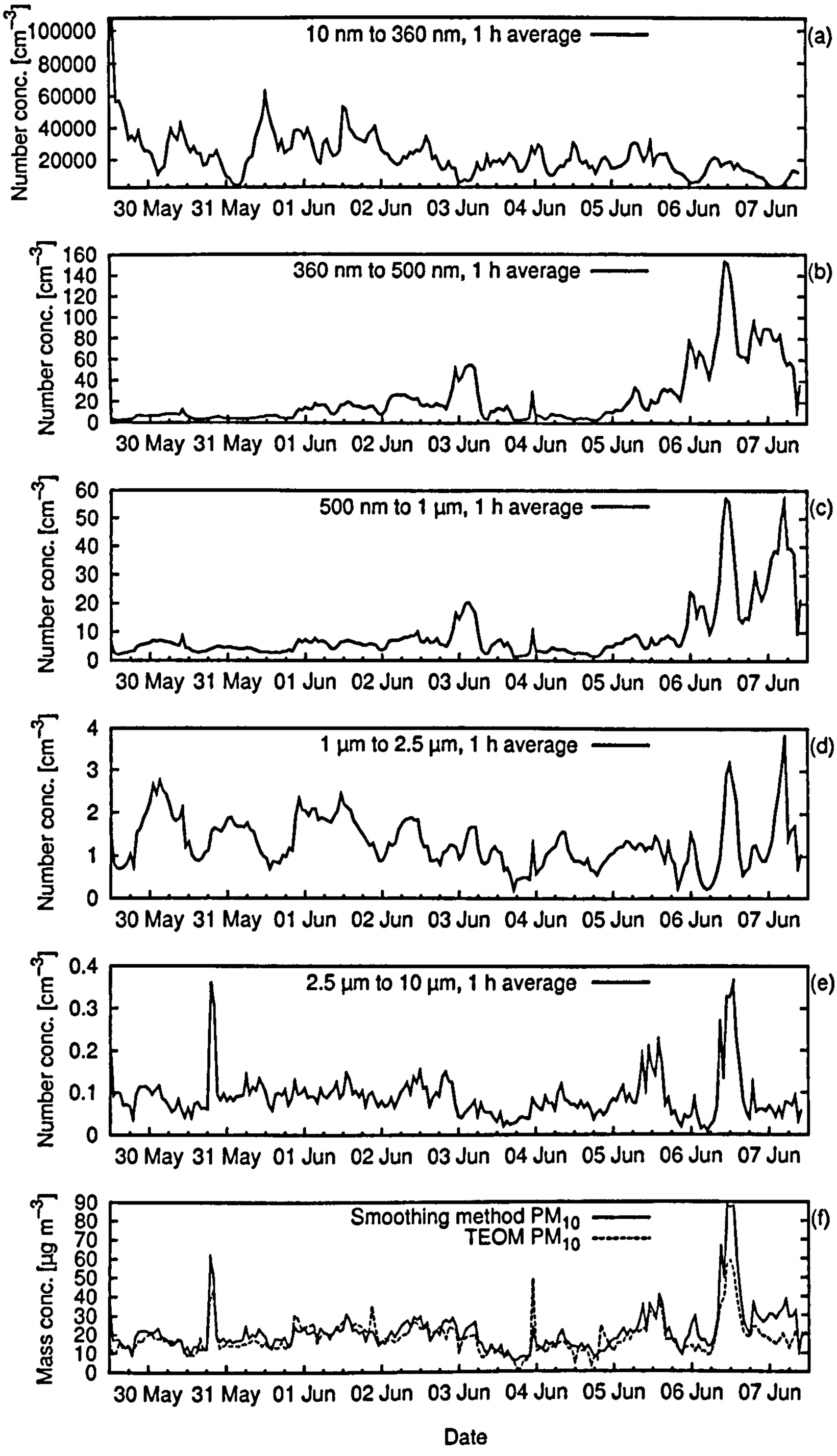

Figure 5.23: Number concentrations of the five size fractions and TEOM PM_{10} measured mass concentrations in comparison with calculated mass concentration (smoothing method) for the week from 29 May to 7 June 2002. The data shown are 1 h averages.

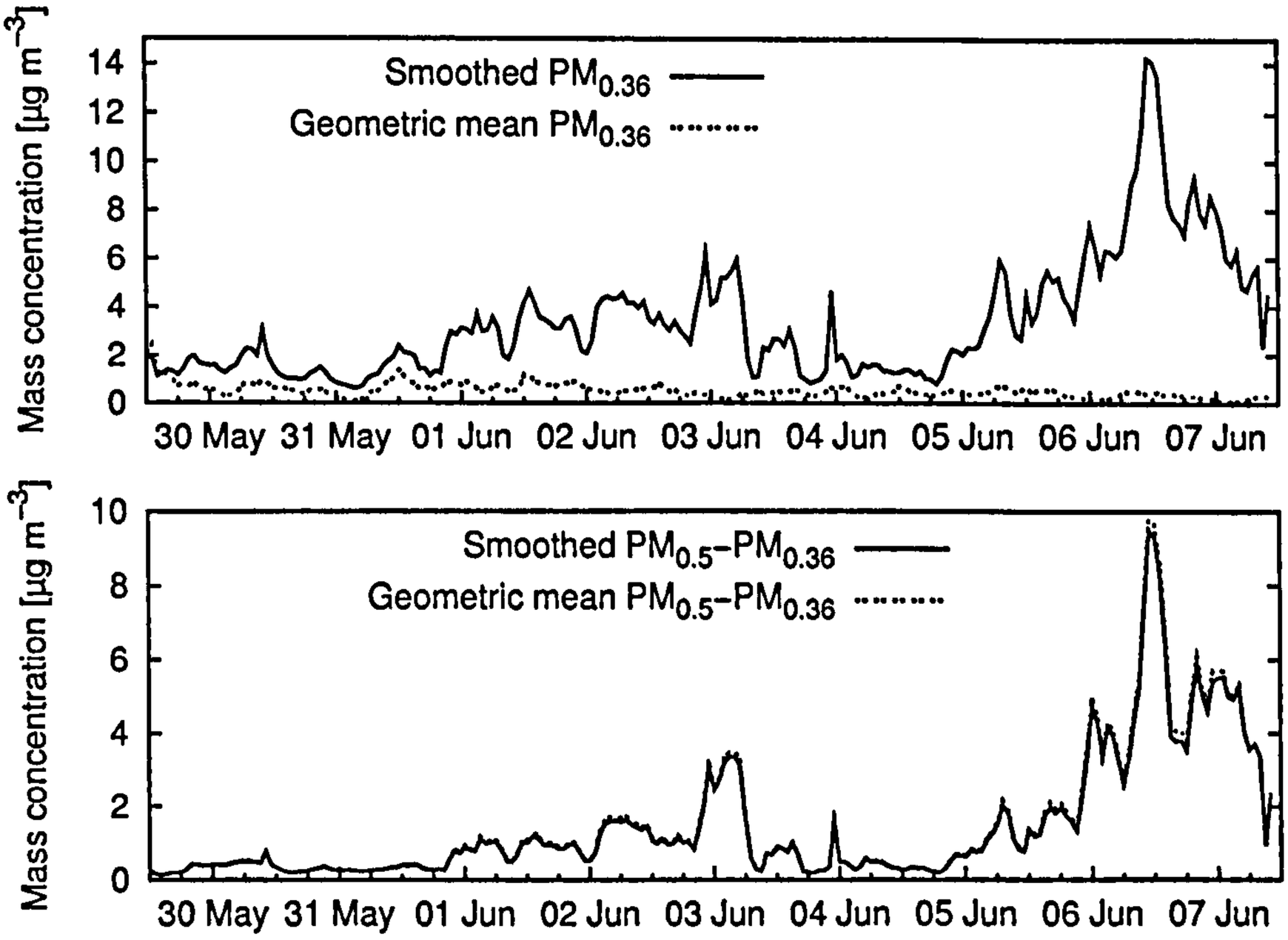

Figure 5.24: Comparison of calculated mass concentration of smoothing method and geometric mean diameter for the size fractions from 10 nm to 360 nm ($PM_{0.36}$) and 360 nm to 500 nm ($PM_{0.5}-PM_{0.36}$).

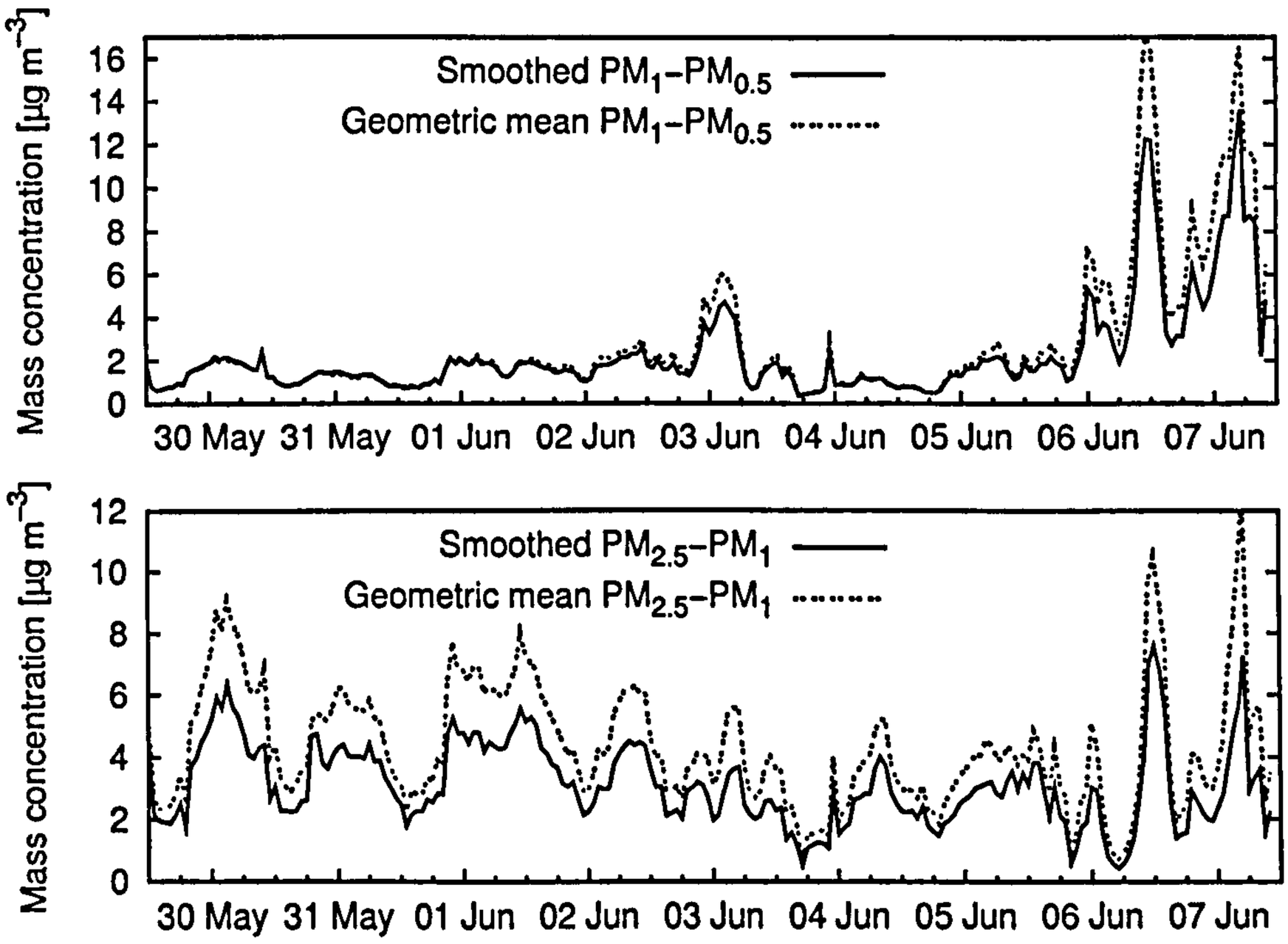

Figure 5.25: Comparison of calculated mass concentration of smoothing method and geometric mean diameter for the size fractions from 500 nm to 1.0 µm ($PM_1-PM_{0.5}$) and 1.0 µm to 2.5 µm ($PM_{2.5}-PM_1$).

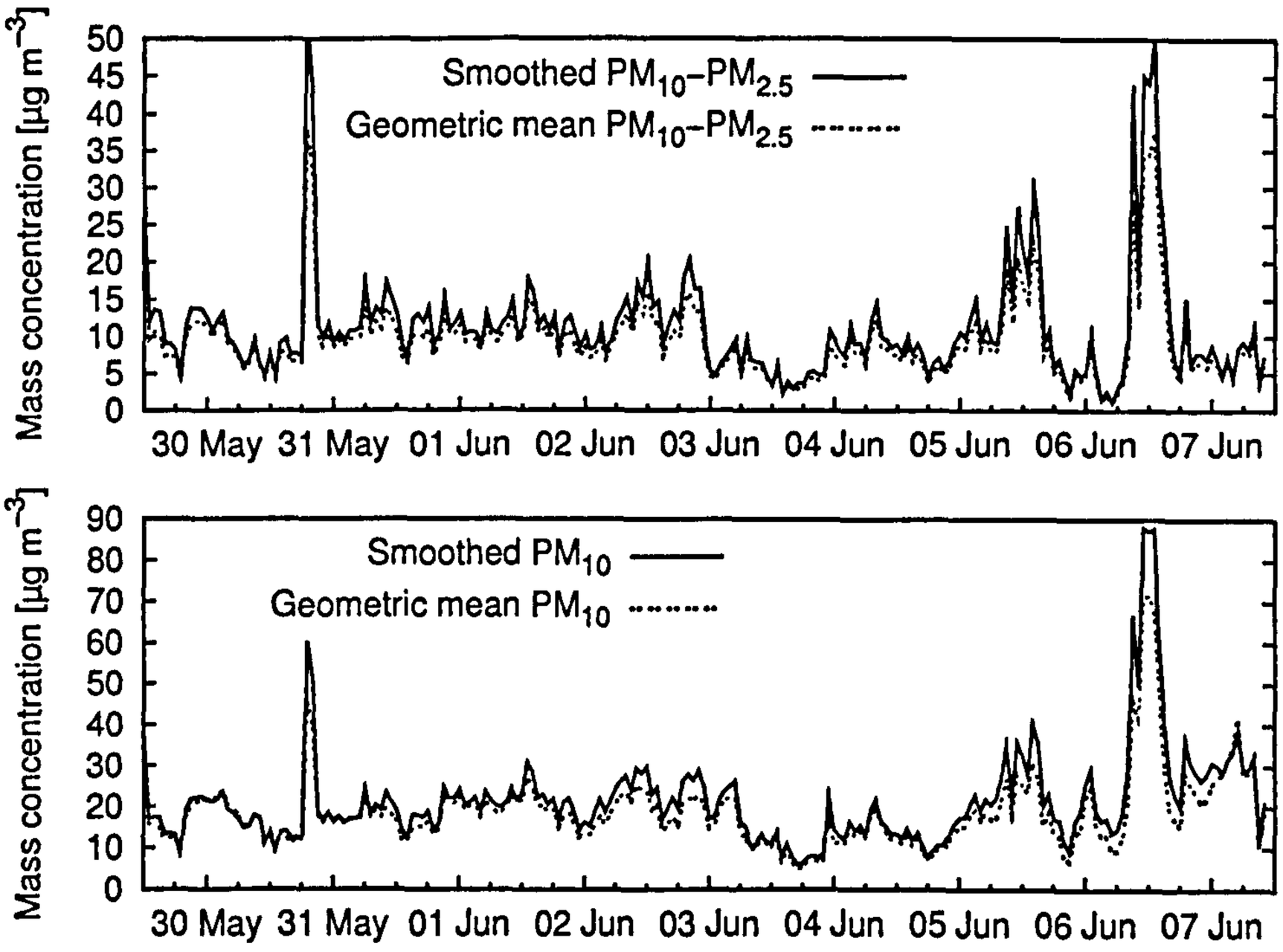

Figure 5.26: Comparison of calculated mass concentration of smoothing method and geometric mean diameter for the size fraction from 2.5 µm to 10 µm (PM_{10}–$PM_{2.5}$) and for total PM_{10} mass concentration.

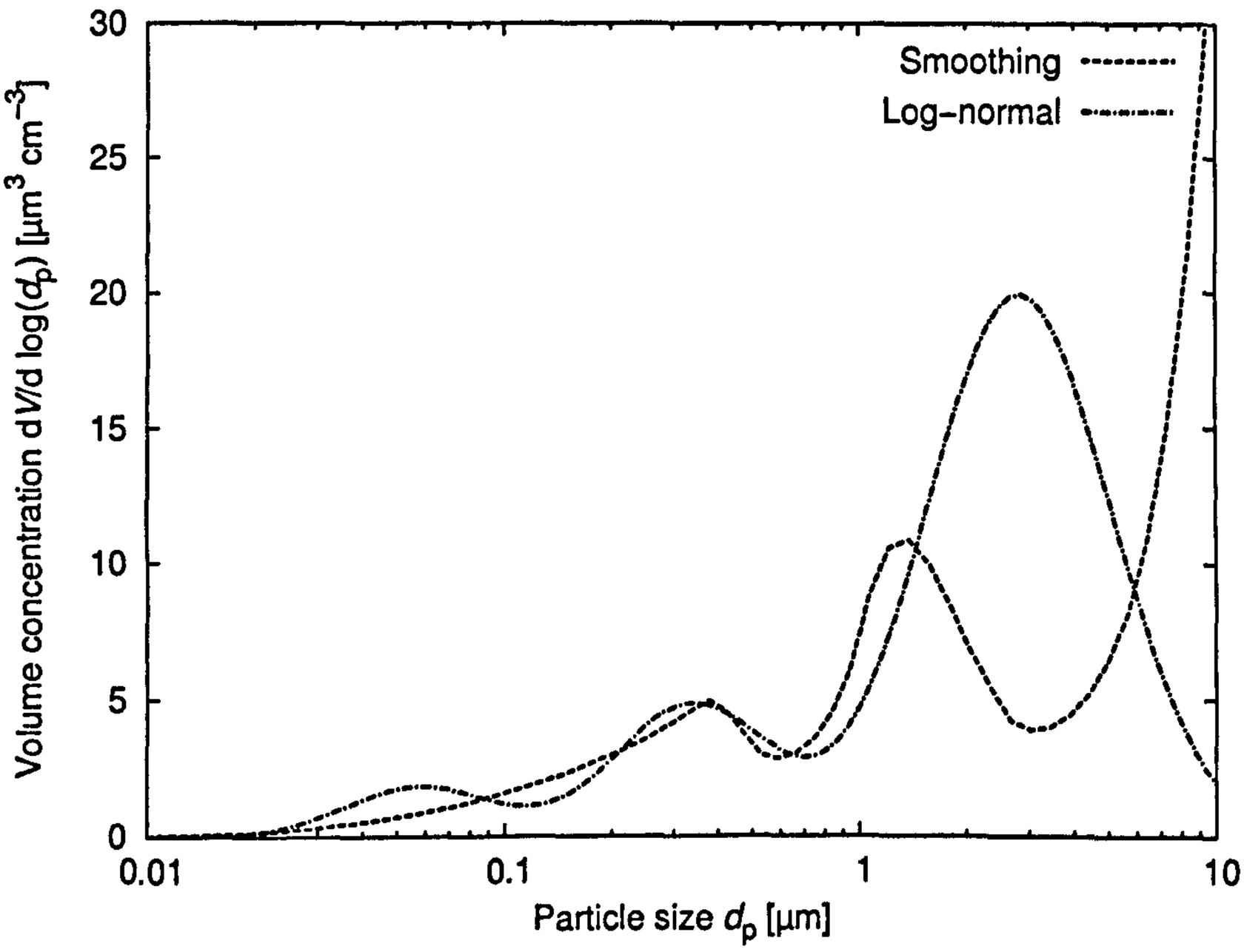

Figure 5.27: Comparison of volume size distribution resulting from smoothing method and log-normal fit to data from 1 June 2002, at 11:00 (GMT).

10 µm fractions (see figure 5.26, upper part). For these size fractions the geometric mean diameter is therefore a good approximation of the diameter of average mass of the size distribution given by the smoothing method. The mass concentration from the size fraction 1 µm to 2.5 µm is on average 1.4 times higher than that from the smoothing method (see figure 5.25, lower part), however, the two mass concentrations are again well correlated ($r^2 = 0.96$, intercept $= -0.12$ µg·m^{-3}, slope $= 1.45$) The mass concentration in the ultrafine size fraction 10 nm to 360 nm does not show any correlation between geometric mean and smoothing method, as mass concentration from the geometric-mean-diameter algorithm is correlated with the number concentration in that size fraction but the mass from the smoothing method is correlated with mass concentration in the adjacent size fraction 360 nm to 500 nm, as mentioned above.

Log-normal Fit versus Smoothing Method The calculated mass concentrations for the log-normal fit in the different size fractions are shown in figures 5.28, 5.29, and 5.30 in comparison with results from the smoothing method. The PM_{10} mass concentration computed from the algorithm using

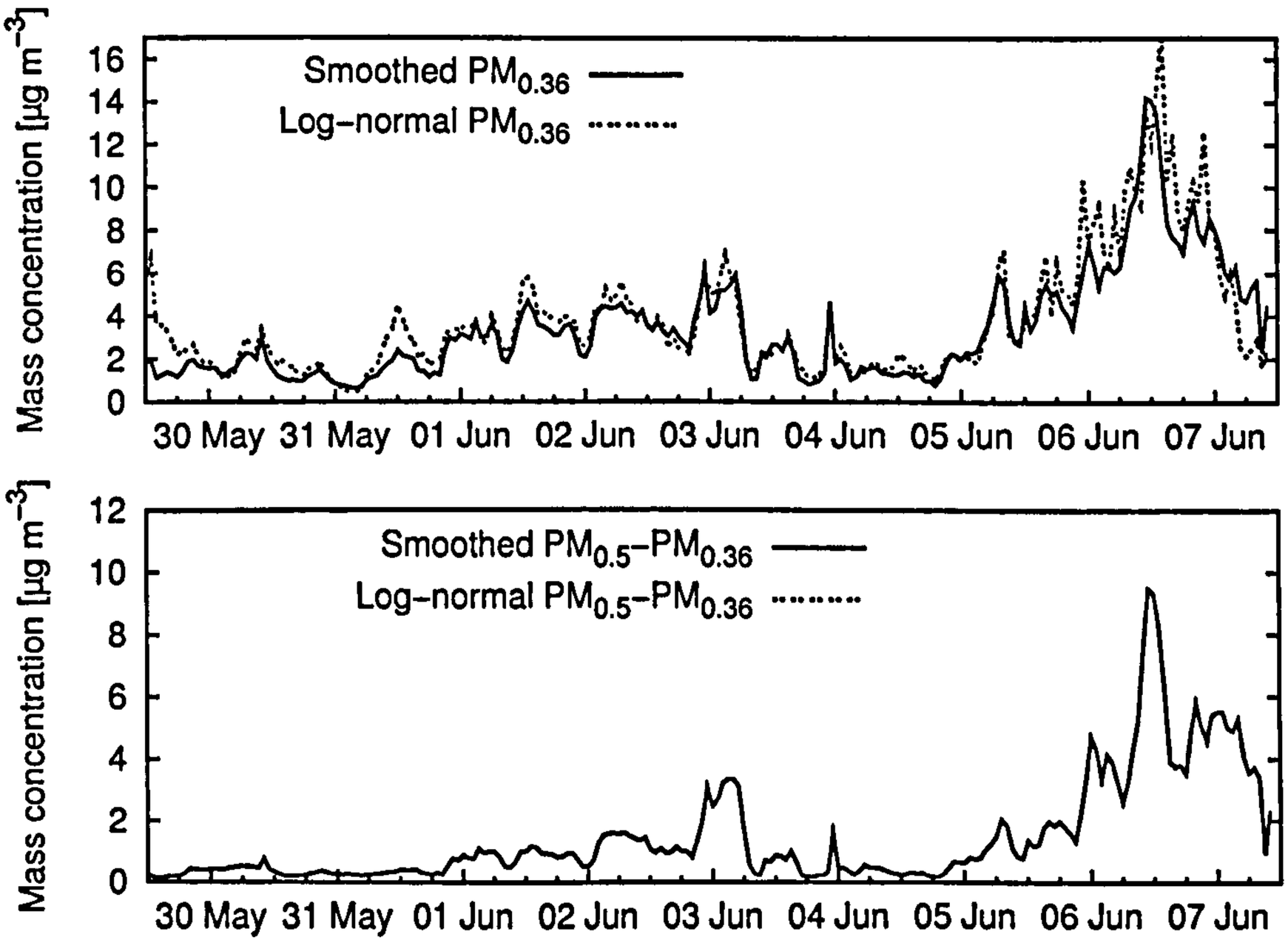

Figure 5.28: Comparison of calculated mass concentration of smoothing method and log-normal fit for the size fractions from 10 nm to 360 nm ($PM_{0.36}$) and 360 nm to 500 nm ($PM_{0.5}-PM_{0.36}$).

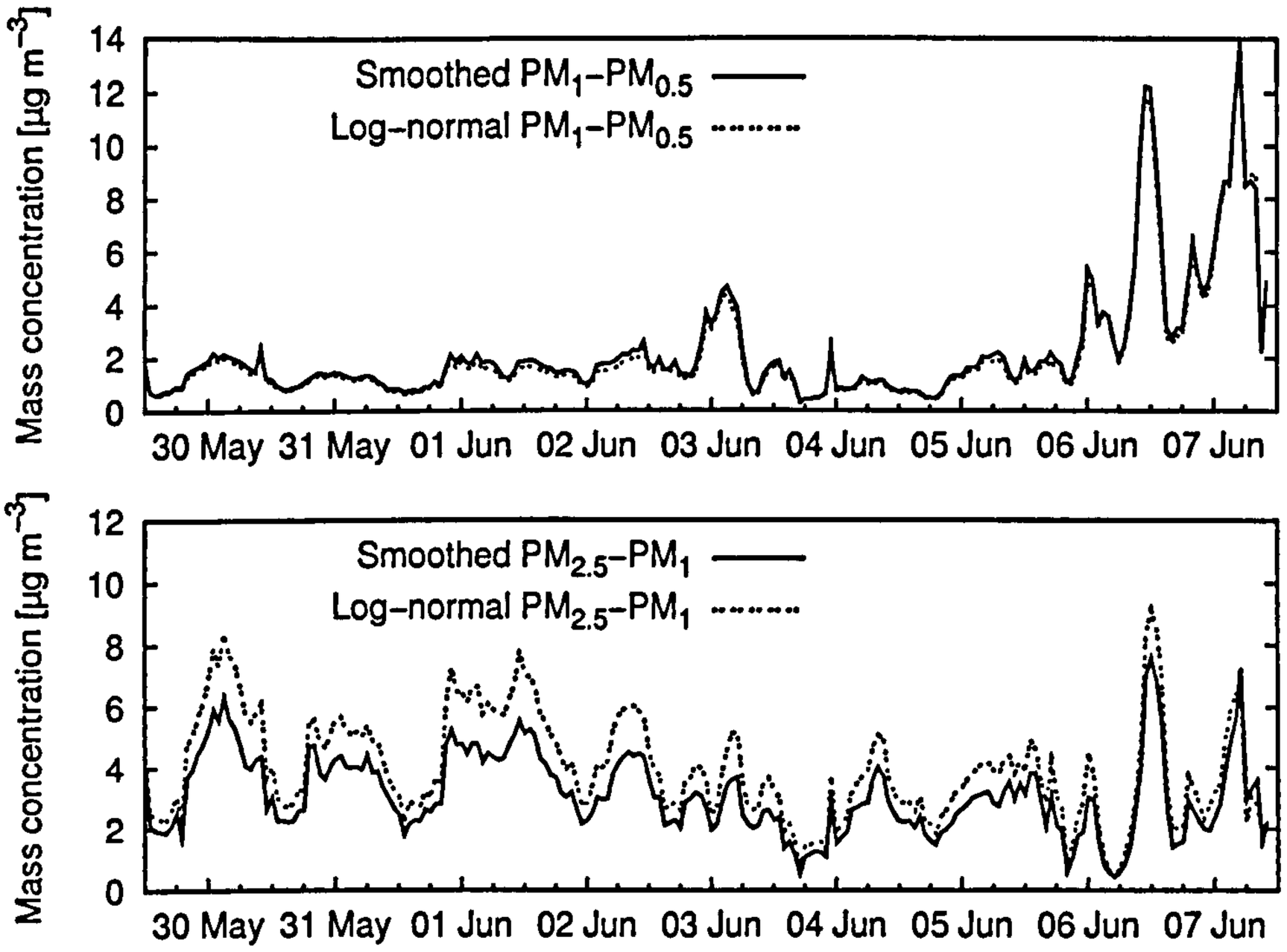

Figure 5.29: Comparison of calculated mass concentration of smoothing method and log-normal fit for the size fractions from 500 nm to 1.0 µm (PM_1–$PM_{0.5}$) and 1.0 µm to 2.5 µm ($PM_{2.5}$–PM_1).

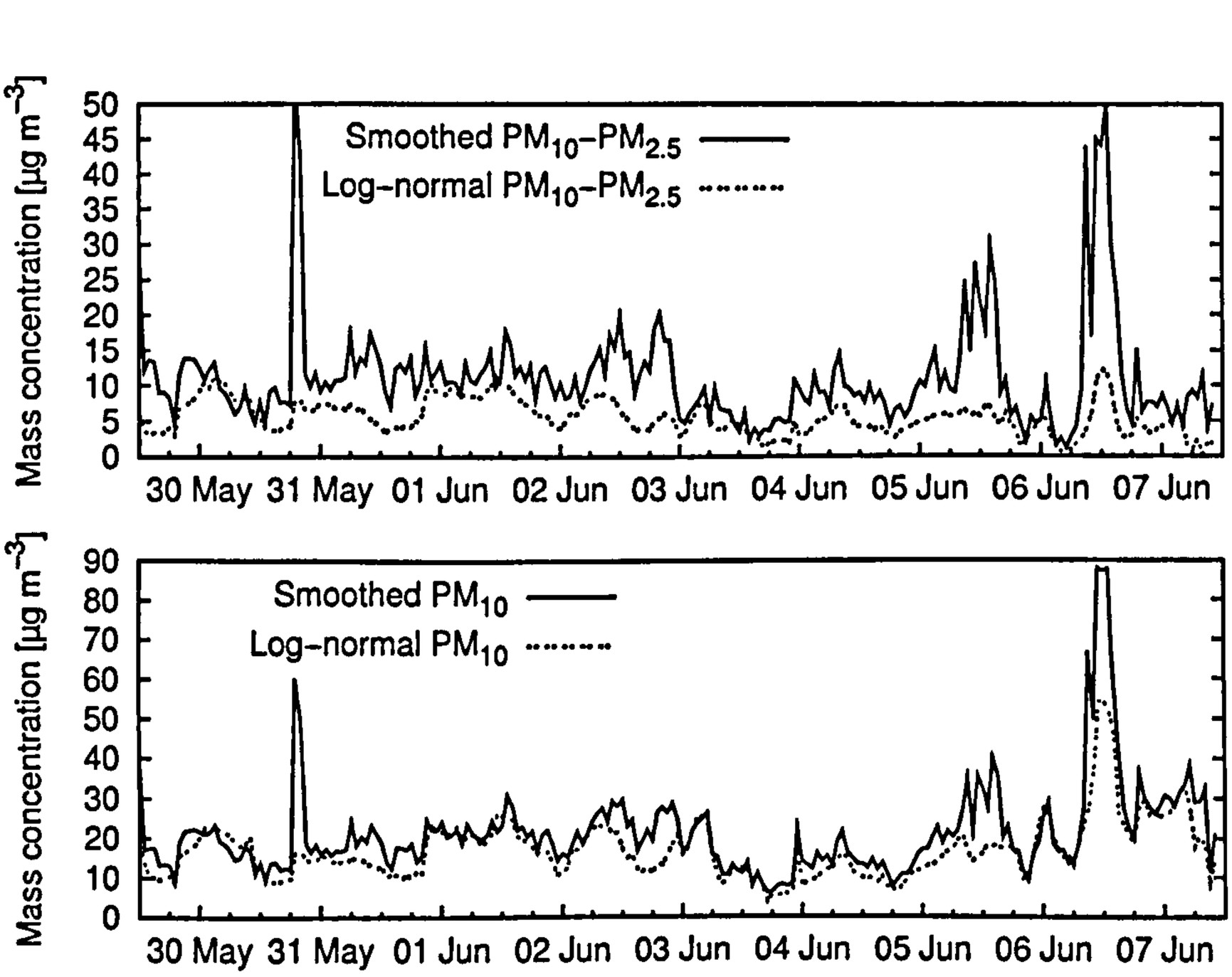

Figure 5.30: Comparison of calculated mass concentration of smoothing method and log-normal fit for the size fraction from 2.5 µm to 10 µm (PM_{10}–$PM_{2.5}$) and for total PM_{10} mass concentration.

the log-normal fit shows weaker correlation with TEOM PM_{10} measured data than the PM_{10} mass concentration computed from the other two algorithms (see figure 5.30, lower part). Comparing the log-normal fit with the smoothing method shows a very good agreement of the respective mass contributions from the 360 nm to 500 nm and the 500 nm to 1 µm size fractions (see figures 5.28, lower part, and 5.29, upper part). The two size fractions 10 nm to 360 nm and 1 µm to 2.5 µm still show quite a good agreement, while the contribution of the log-normal fit in both size fractions is slightly higher (see figures 5.28, upper part, and 5.29, lower part). In the size fraction 2.5 µm to 10 µm, however, the agreement is very poor, the mass contribution from the log-normal fit is not following the peaks shown by the smoothing method (see figure 5.30, upper part). Figure 5.31 and figure 5.32 show the results for data falling in such a peak (Birmingham, 30 May 2002, 19:00 GMT). A large difference in volume concentration (and hence mass) results from the different number size distribution in the coarse size fraction above 2.5 µm particle diameter. The reason for this is believed to be

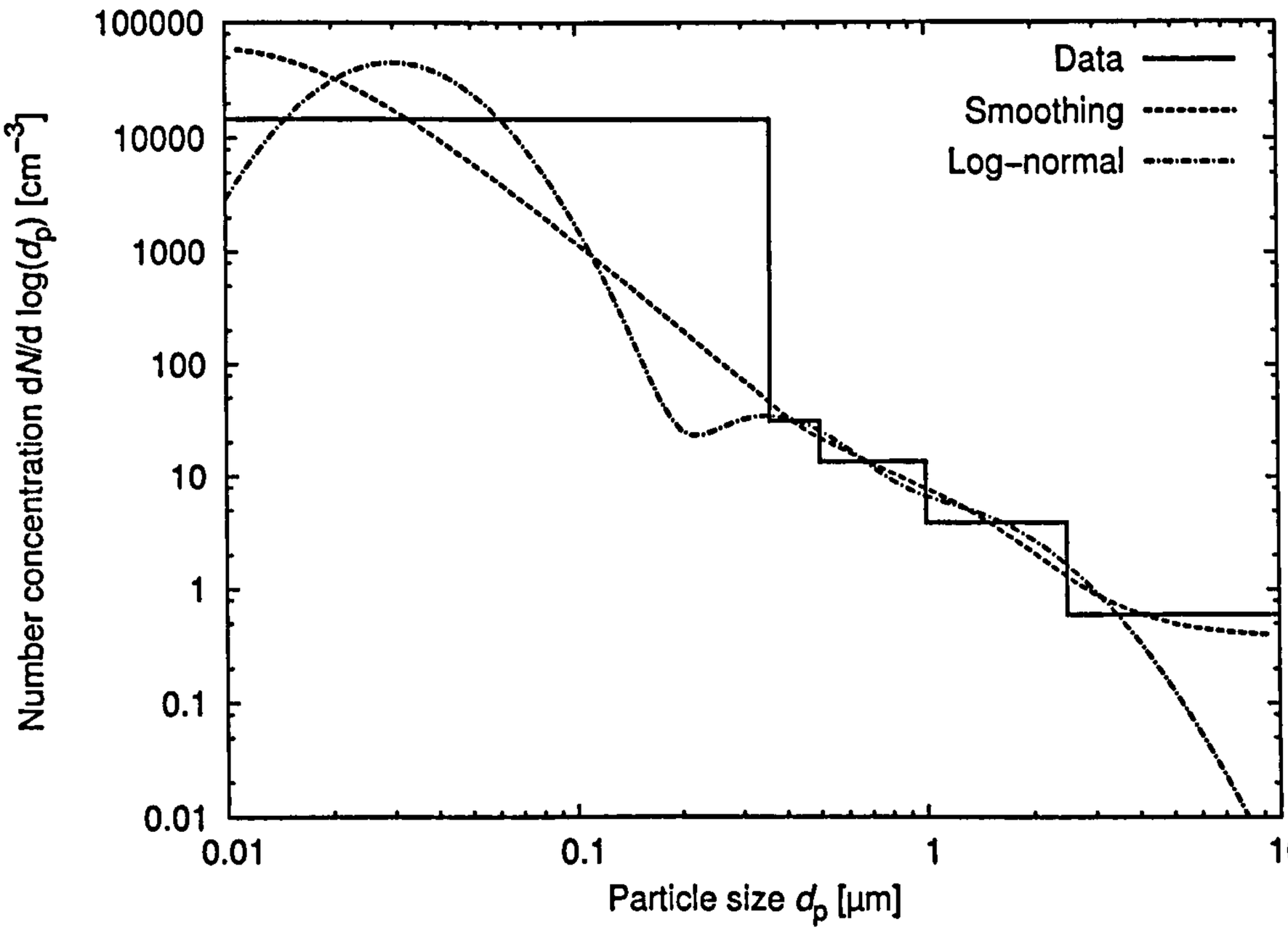

Figure 5.31: Comparison of number size distribution resulting from smoothing method and log-normal fit to data from 30 May 2002, 19:00 (GMT). Number size distribution is shown on a logarithmic scale. A large difference can be noticed in the size fraction 2.5 µm to 10 µm.

a bad representation by the log-normal fit of the size distribution above ap-

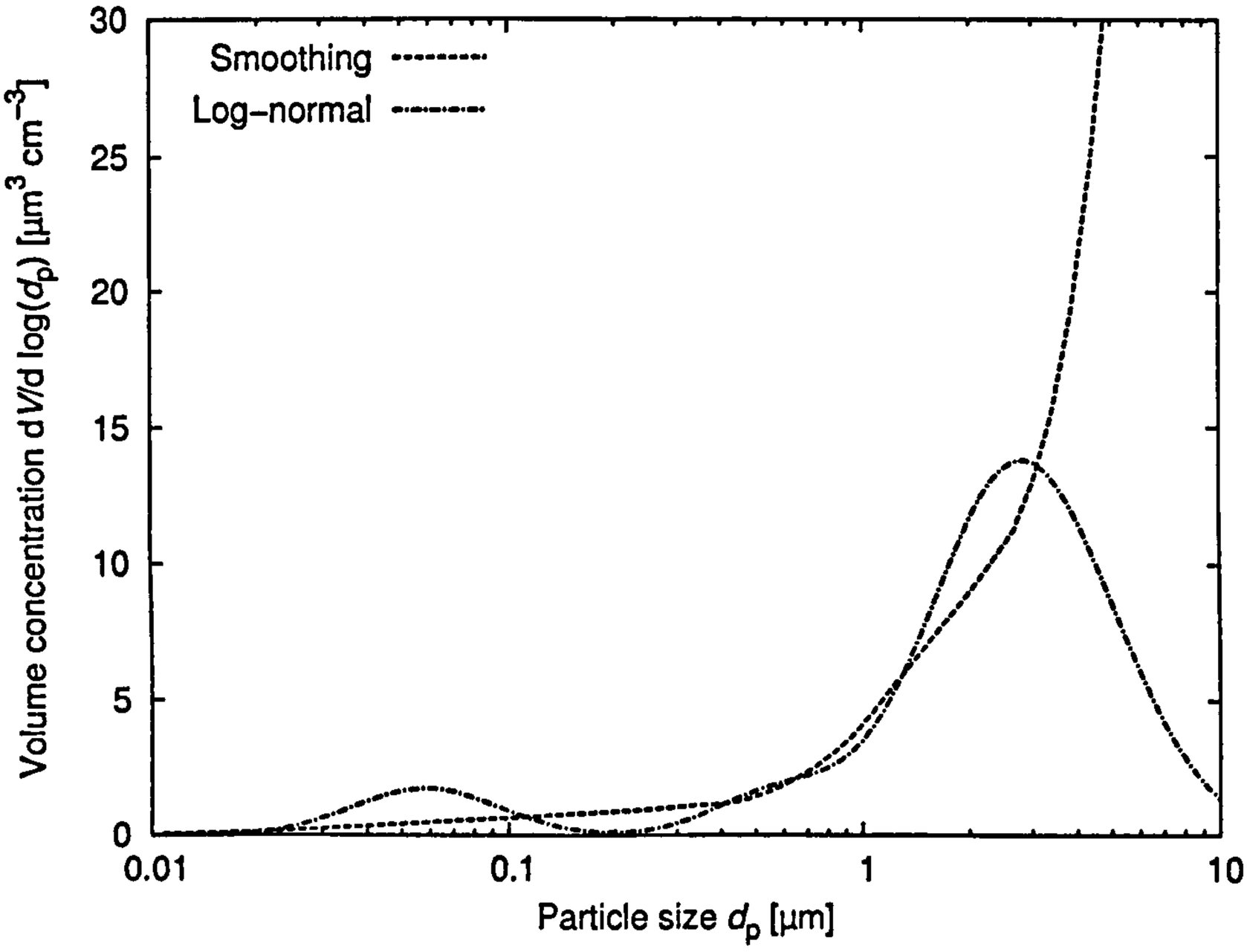

Figure 5.32: Comparison of volume size distribution resulting from smoothing method and log-normal fit to data from 30 May 2002, 19:00 (GMT). The large difference in number concentration in the size fraction 2.5 µm to 10 µm translates in a large difference in the volume concentration too.

proximately 2.5 µm. The third log-normal mode is apparently at a too low mean diameter and falling off too rapidly towards higher particle sizes (see figures 5.31 and 5.33). As mentioned earlier, this mode was fixed at 1 µm. Increasing this geometric mean will increase the mass significantly without improving the correlation to the TEOM PM_{10} data. Furthermore, it will result in a reduced quality of the fit. It suggests that a log-normal distribution is not suitable to fit the available data in the coarse size range.

Summary of Number-to-Mass Conversion Algorithm

In conclusion from these tests of number-to-mass conversion algorithms, it can be said that the fit to three log-normal modes does not give satisfactory results, while the conversion algorithms using the smoothing method and the geometric mean diameter give very similar results and are relatively well correlated to TEOM PM_{10} data (with $r^2 = 0.68$ and $r^2 = 0.65$ respectively). The algorithm using the geometric mean diameter is simpler compared to the smoothing method and requires only very little computation. This method can be "calibrated" by comparing the results against a

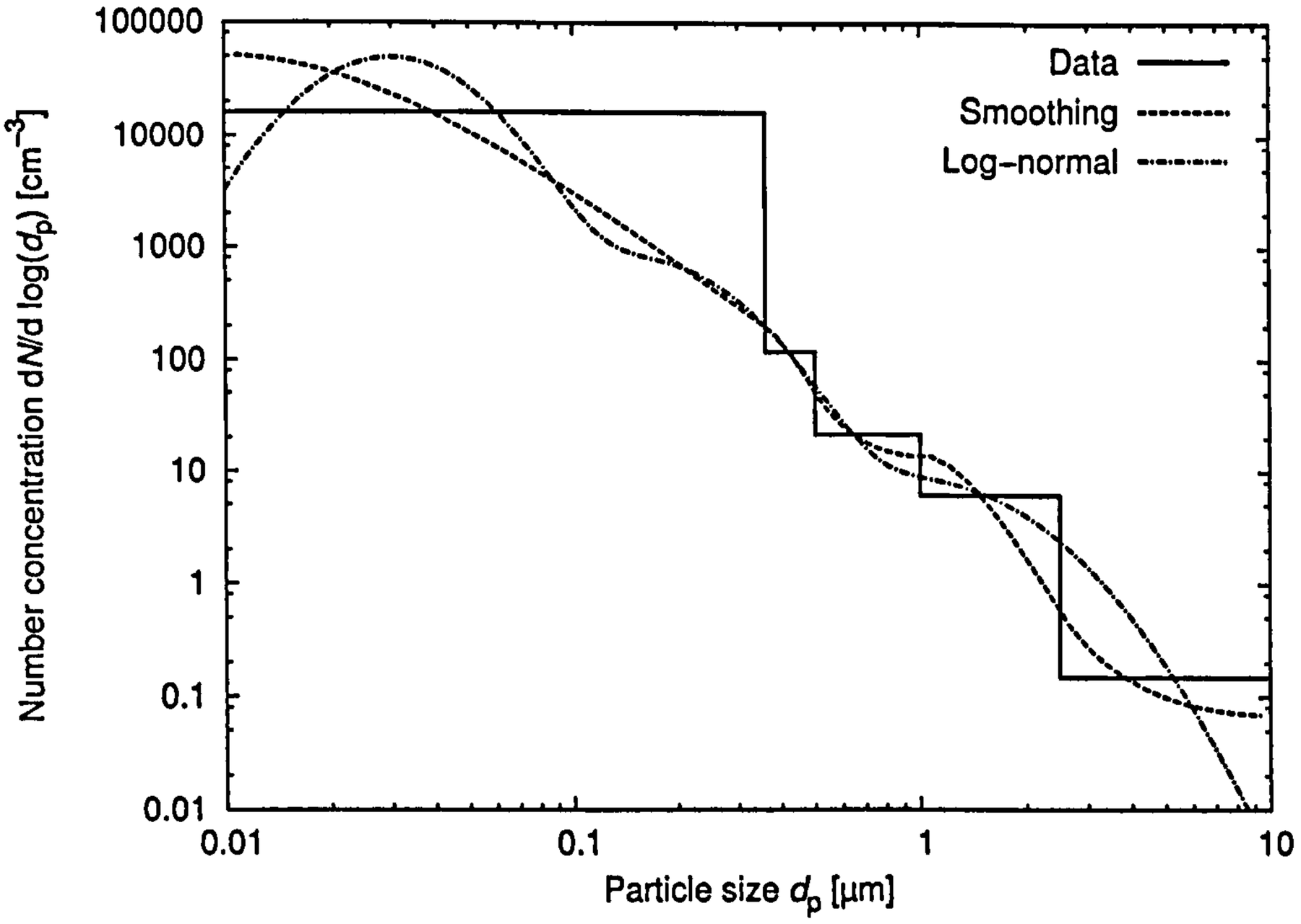

Figure 5.33: Comparison of number size distribution resulting from smoothing method and log-normal fit to data from 1 June 2002, 11:00 (GMT). Number size distribution is shown on a logarithmic scale.

mass concentration measurement, as for example with a TEOM. This will result in an apparent particle density which accounts for the specific conditions at the site where the comparison was done. The assumed density of 1 600 kg·m^{-3} can be changed so that the slope of the linear correlation fit between the computed and the measured mass concentration will become unity. Alternatively the average computed mass can be compared to the average measured mass concentration and then the assumed density can be corrected so that the two averages are the same. Applying this mass calibration to the algorithm using the geometric mean method, the apparent density, based on the data from 27 June to 10 September 2002, is 1 590 kg·m^{-3} in the former (slope = 1) and 1 640 kg·m^{-3} in the latter case (comparison of average mass). For the smoothing method the apparent density would be lower at 1 310 kg·m^{-3} and 1 330 kg·m^{-3} respectively.

5.5 Intercomparisons of the two Prototype Instruments

The advantage of producing two prototypes was that it was easier to track problems if one instrument could be directly compared to another identical instrument. If both instruments were functioning well, then a side-by-side comparison should yield identical results within measurement errors. Such side-by-side comparisons were performed on several occasions. The first comparisons after the calibration of the sizing capabilities of the OPC1s and the OPC2s, were the CPC calibration tests at netcen (see section 5.1.4), which showed good performance of one CPC ($\text{AmbiCount}_\text{B}$), but revealed malfunctioning of the CPC of the other instrument ($\text{AmbiCount}_\text{A}$). In another comparison, the two instruments were operated on the roof of Casella CEL Ltd at a height of $\sim$ 15 m. Both CPCs were measuring the same number concentration but the OPCs showed a difference with OPC1_A sometimes even reading less than 50% compared to OPC1_B. Tests a few days later using PSL spheres with the diameters 0.548 µm and 1.053 µm showed that the response to PSL spheres of OPC1_A had significantly decreased since its calibration (two months earlier, see figure 5.1), while OPC1_B gave very similar results. The problem was solved by improving the laser scattering signal of OPC1_A through changes to the laser focus so that the amplitude was increased and the signal width decreased, followed by an adjustment of the thresholds in order to match the response of OPC1_A to that of OPC1_B, which was unchanged. A short side-by-side comparison showed the positive result of these adjustments.

After the laser diode of OPC1_B failed and its laser module was replaced, it was necessary to calibrate this OPC again. Calibration was performed for both OPC1s following the same procedure as described in section 5.1.2. This was used as an opportunity to repeat the OPC response calculations taking into account the polarization of the incident laser light this time to evaluate the effect of polarization. The incident laser light in the OPC1s is polarized parallel to the mirror–detector axis. Scattered power must be integrated over the solid angle of the mirror as seen from the sensing volume. For all scattering and azimuthal angles θ and ϕ within this solid angle the scattered intensity is calculated using equations (3.3) and (3.4) after splitting

the incident intensity I_i in the components parallel and perpendicular to the scattering plane ($I_i = I_{\parallel i} + I_{\perp i}$). These intensity components are proportional to the squares of the magnitudes of the corresponding electric field vector components (see figure 3.1), so that $I_{\parallel i} = I_i \sin^2\phi$ and $I_{\perp i} = I_i \cos^2\phi$, where $\phi = 90°$ corresponds to the case of the scattering plane oriented so that mirror–detector axis (y-axis in figure 3.1) is falling on the plane. The scattered intensity I_s is the sum of the scattered intensities resulting from the two incident components:

$$I_s = \left((S_{11} + S_{12})\sin^2\phi + (S_{11} - S_{12})\cos^2\phi\right) I_i \qquad (5.3)$$

This integration was added to the Fortran program from Bohren and Huffman (1983), which was then used to calculate the response curve to be used for this calibration of the sizing capabilities of $OPC1_A$ and $OPC1_B$. Figures 5.34 and 5.35 show the results of the calibration (performed on 11 February 2003) with theoretical (calculated) responses for the two cases of unpolarized and polarized incident light fitted to the measured response. The theoretical response to DOS particles, which is used as average response to ambient particles (see section 5.1.2), is shown for both cases as well. By comparing these two response curves for DOS, the effect of polarization can be evaluated. The PSL response curve for polarized light fits the measured data better than the response curve for unpolarized light. If the response curve for unpolarized light is used to determine thresholds for size cuts at 360 nm and 500 nm respectively, the thresholds correspond to slightly higher size cuts for polarized incident laser light (~380 nm and ~520 nm respectively). For the higher size cuts these differences become insignificant. This confirms that the effect of beam polarization is only secondary (as claimed in section 4.2.3). However, to enhance the OPC performance in the following the polarization was taken into account to determine the thresholds for the size cuts.

Subsequent side-by-side comparisons showed differences in the number concentrations measured with the OPCs. $OPC1_B$ indicated lower number concentrations in all four size fractions, so its response was tested again with PSL spheres (on 28 April 2003). The signal was found to be lower than during the previous calibration, so that the signal needed to be improved by re-alignment of the laser and then recalibrated. This incident, which repeated the experience with the calibrations carried out a year before (see

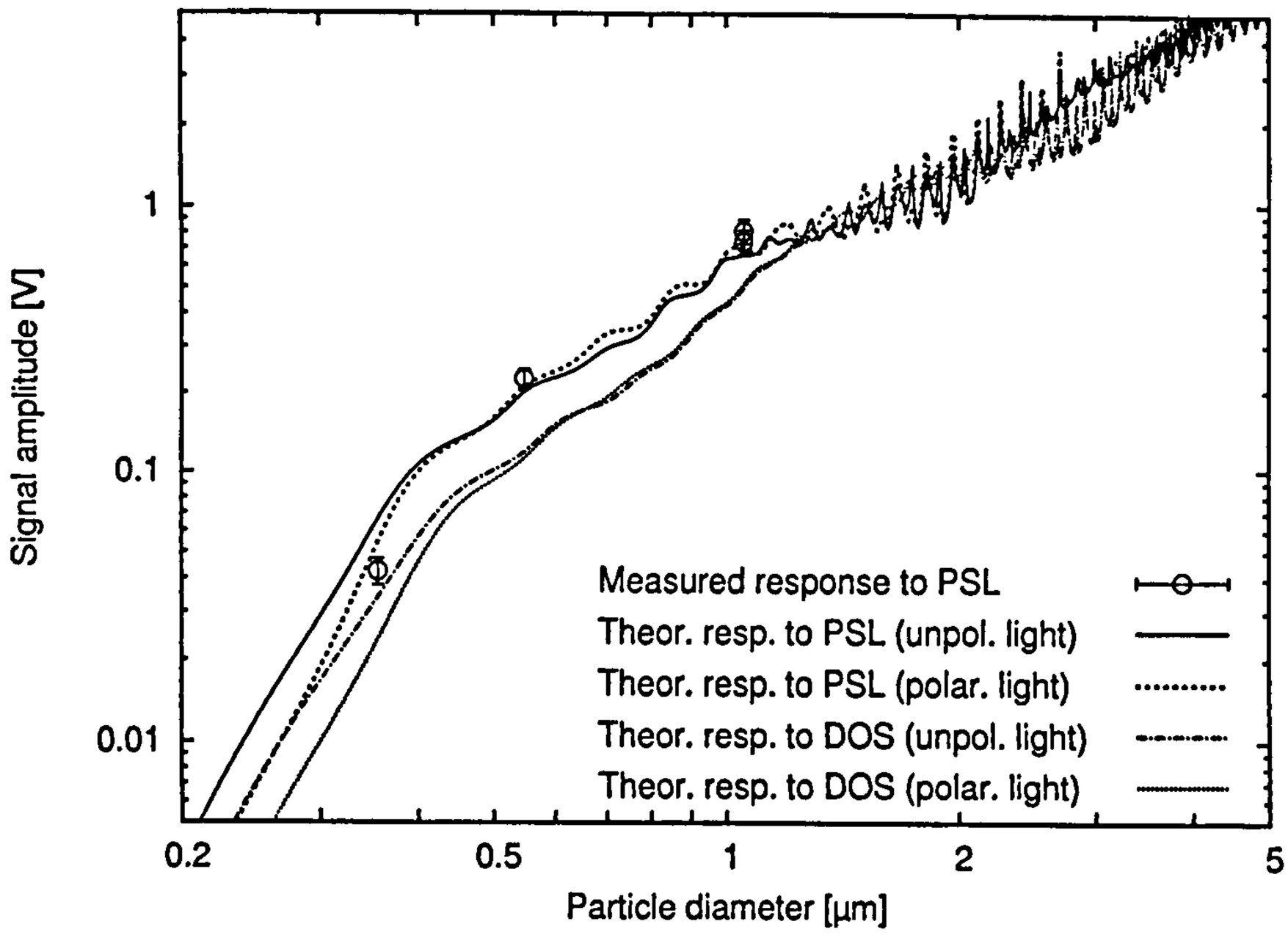

Figure 5.34: Measured response of $OPC1_A$ to PSL spheres (11 February 2003). Theoretical response was calculated for the two cases of unpolarized light and linearly polarized light with polarization parallel to mirror–detector axis. Both response curves are scaled individually to best fit the measured data. The two measurements at 1.053 µm were performed immediately one after the other.

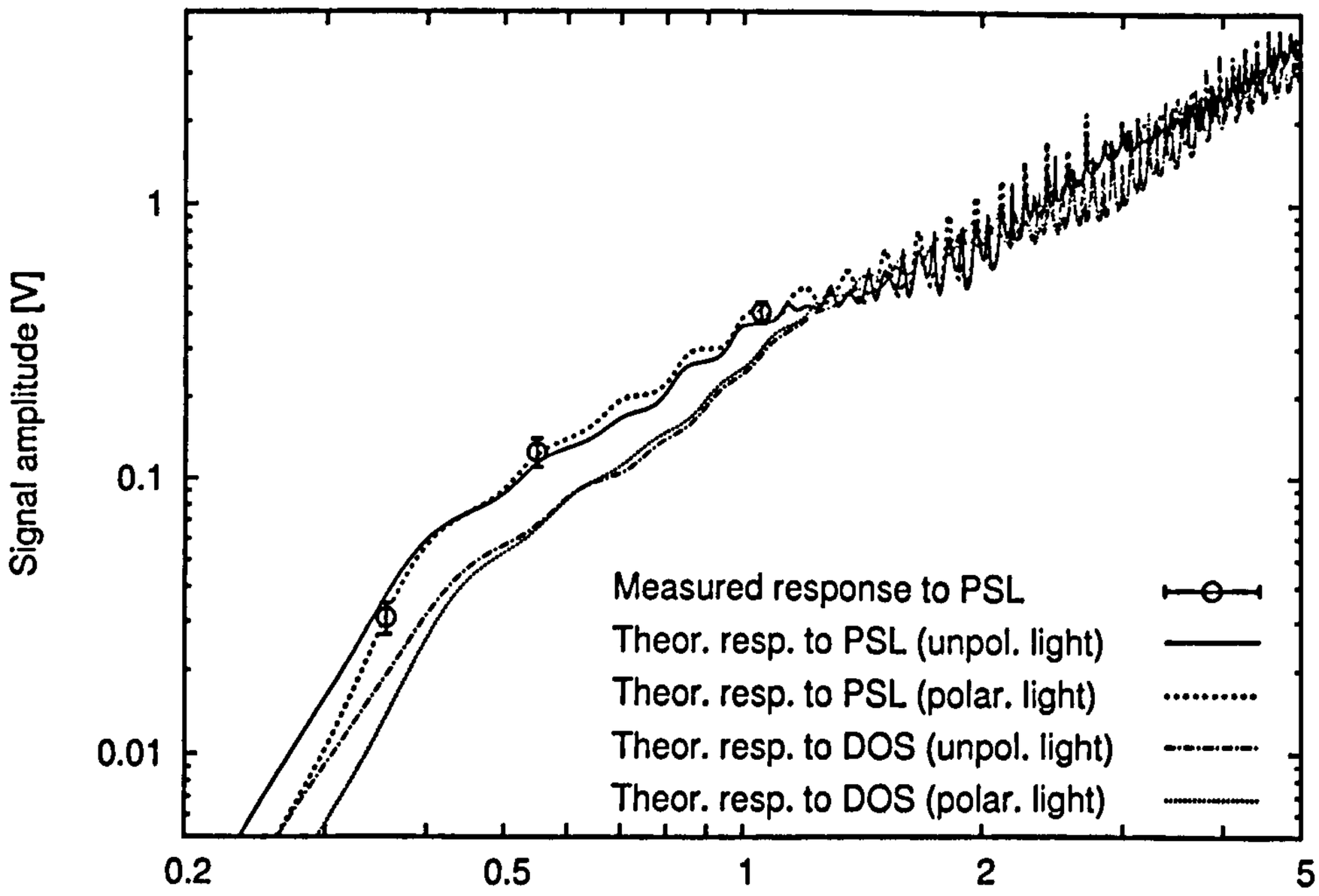

Figure 5.35: Measured response of $OPC1_B$ to PSL spheres (11 February 2003). Theoretical response was calculated for the two cases of unpolarized light and linearly polarized light with polarization parallel to mirror–detector axis. Both response curves are scaled individually to best fit the measured data.

above), suggests that the alignment of the laser is very sensitive and that the laser may, over time, fall out of alignment. This last calibration was therefore concluded with sampling the same particle diameter (0.548 µm) that was sampled first, to confirm its average response had not changed. In figure 5.36, depicting the results of recalibration, these two measurements can be seen as the two points at 0.548 µm, where the second measurement, though reading slightly less, agreed within measurement error of the first measurement.

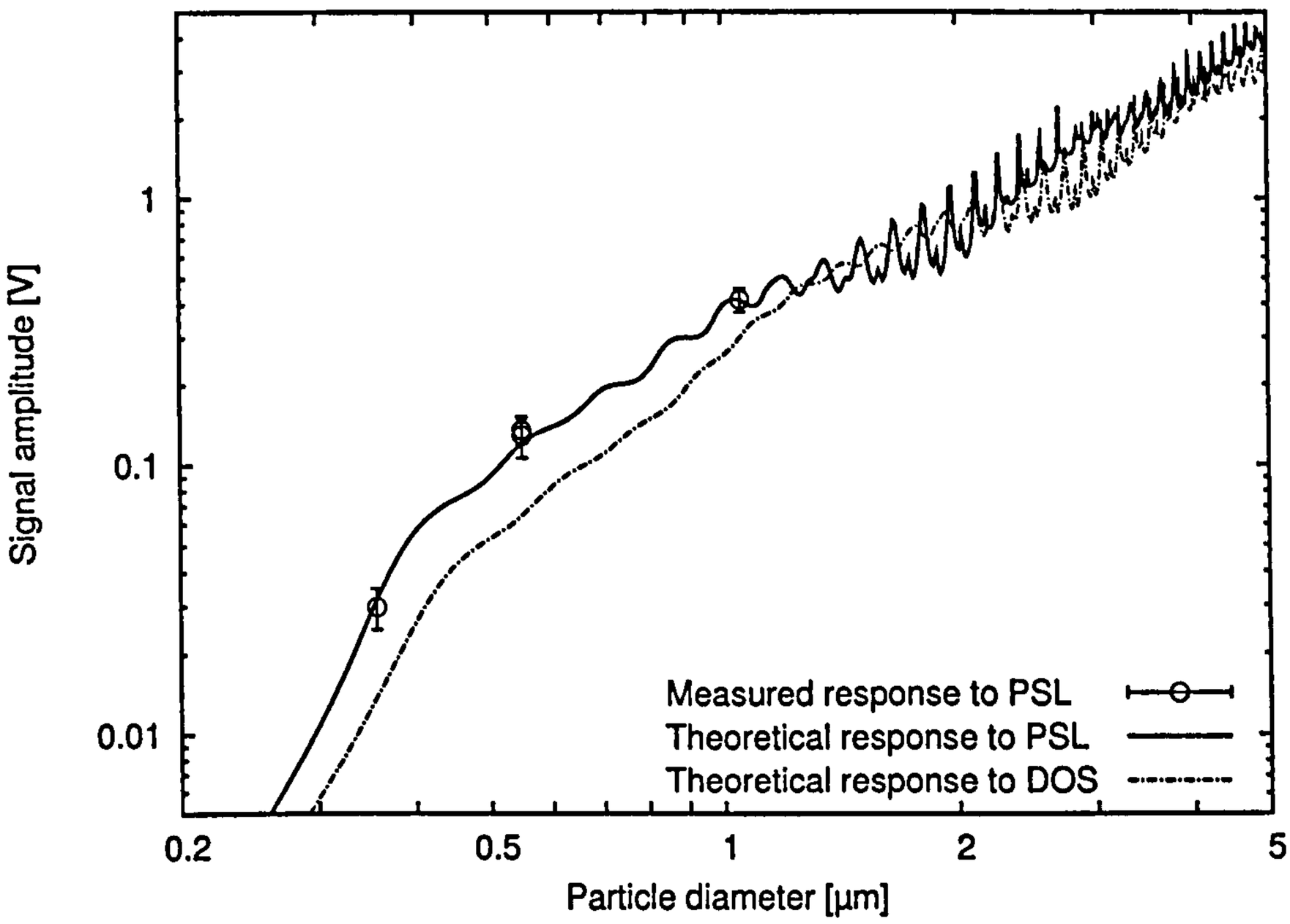

Figure 5.36: $OPC1_B$ recalibration. Measured response to PSL spheres (28 April 2003). The calculated theoretical response was scaled to best fit the measured data. The two measurements at 0.548 µm were performed at the beginning and end of the measurements.

A week after the recalibration another side-by-side comparison was performed, results can be seen for the five different size fractions in figures 5.37, 5.38, 5.39, 5.40, and 5.41. They show that the number concentrations in the size fractions of the OPCs agreed reasonably well. Table 5.2 lists the results of linear regression to show correlation of $AmbiCount_B$ measurements with $AmbiCount_A$ measurements. The observed differences are believed to have resulted from the thresholds and size-cut characteristics of the two OPC1s being slightly different.

	Slope	Intercept	r^2
CPC (total number conc.)	1.03	26.397	0.997
OPC, 360 to 500 nm	1.23	-0.132	0.998
OPC, 500 nm to 1.0 µm	1.32	-0.751	0.978
OPC, 1.0 to 2.5 µm	0.89	0.095	0.869
OPC, 2.5 to 10 µm	0.76	0.010	0.924

Table 5.2: Results of linear regression of side-by-side comparison of the two prototype instruments between 6 May, 17:00 and 8 May 2003, 9:00 (GMT). Measurements of AmbiCount_B are compared against measurements of AmbiCount_A. The intercepts are given in cm^{-3}.

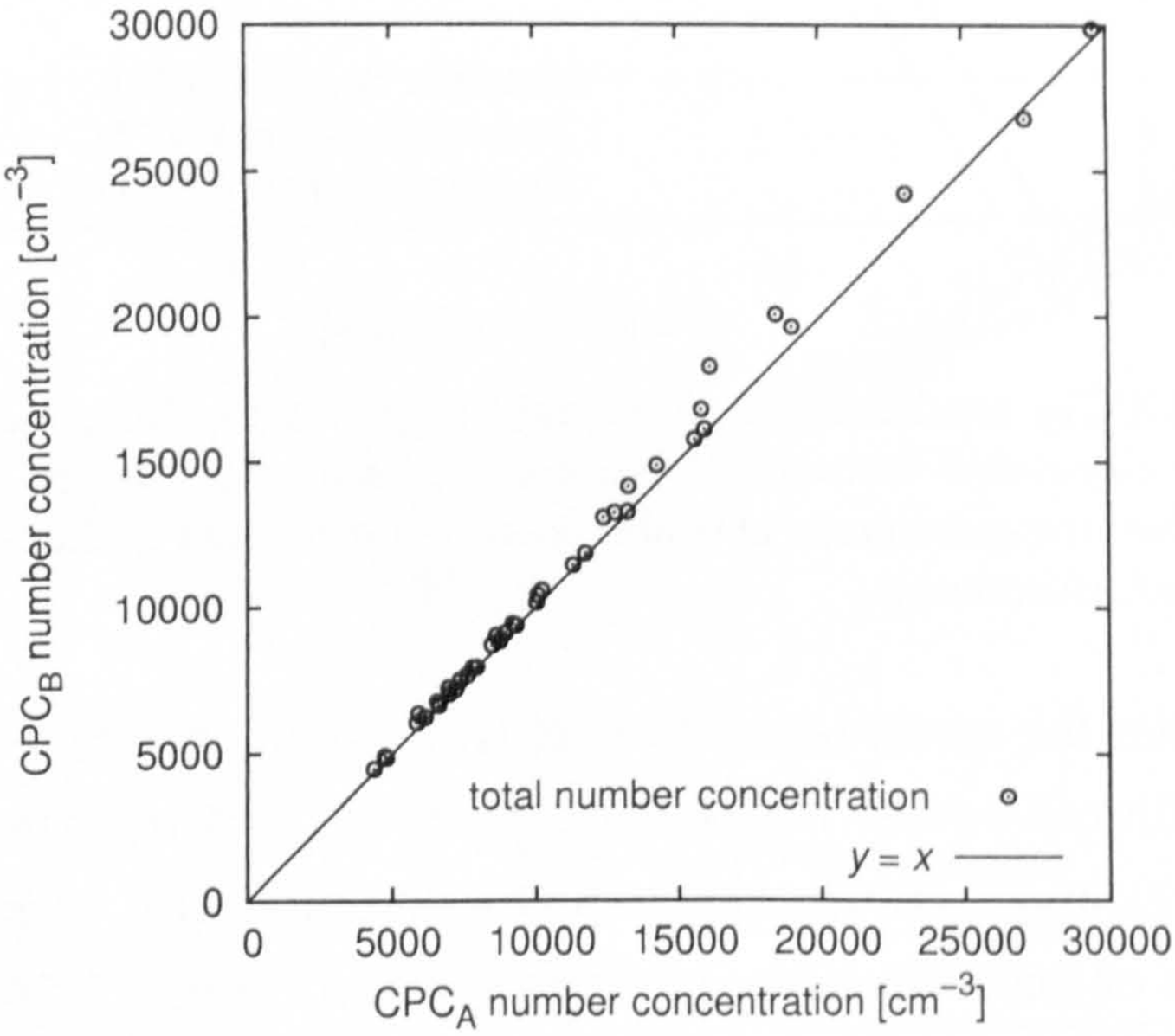

Figure 5.37: CPC scatter plot of side-by-side comparison of the two prototype instruments. Data between 6 May, 17:00 and 8 May 2003, 9:00 (GMT) are shown. Points correspond to 1 h averages.

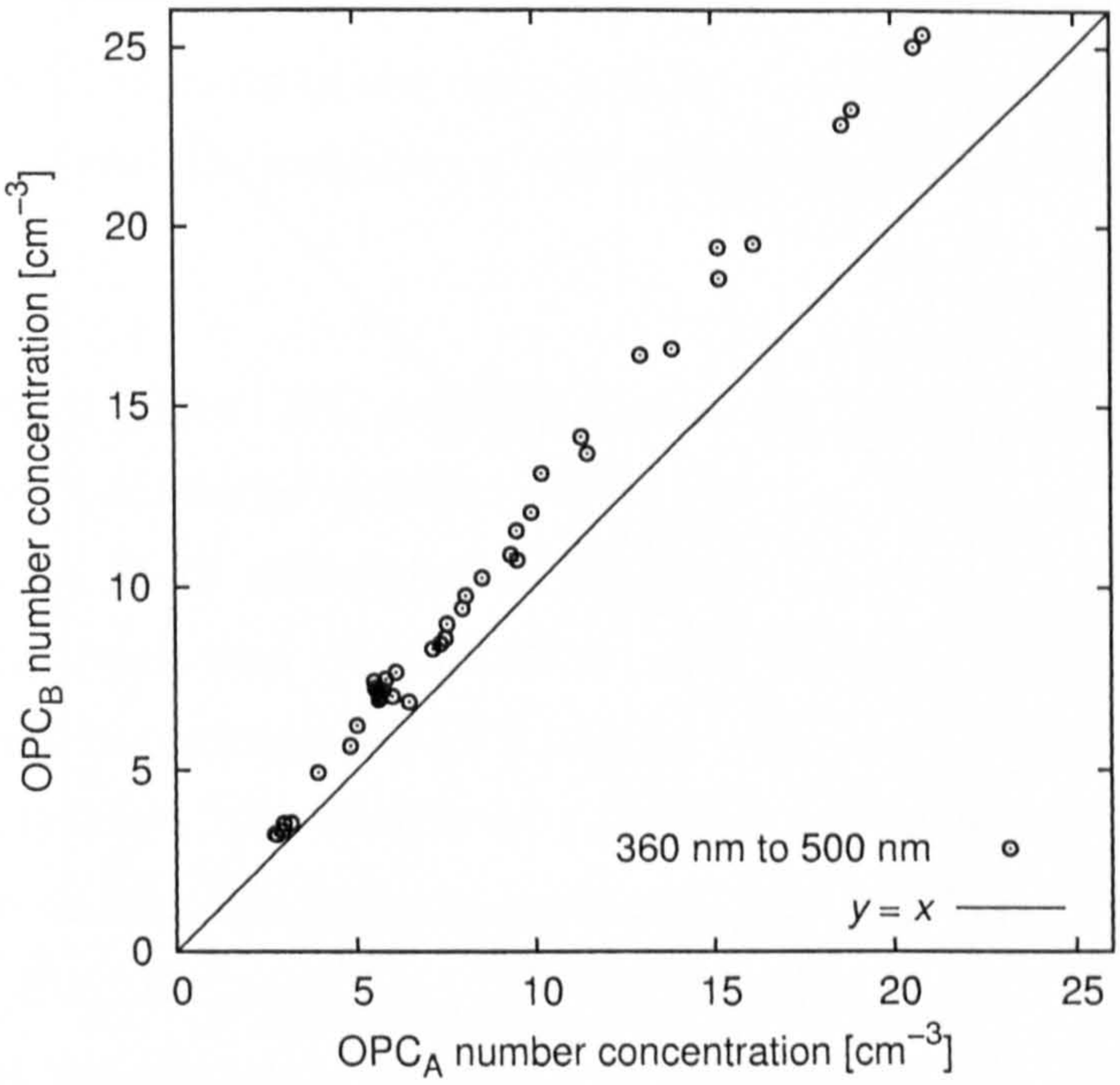

Figure 5.38: OPC scatter plot of side-by-side comparison of the two prototype instruments. Data between 6 May, 17:00 and 8 May 2003, 9:00 (GMT) are shown for the size fraction 360 nm to 500 nm. Points correspond to 1 h averages.

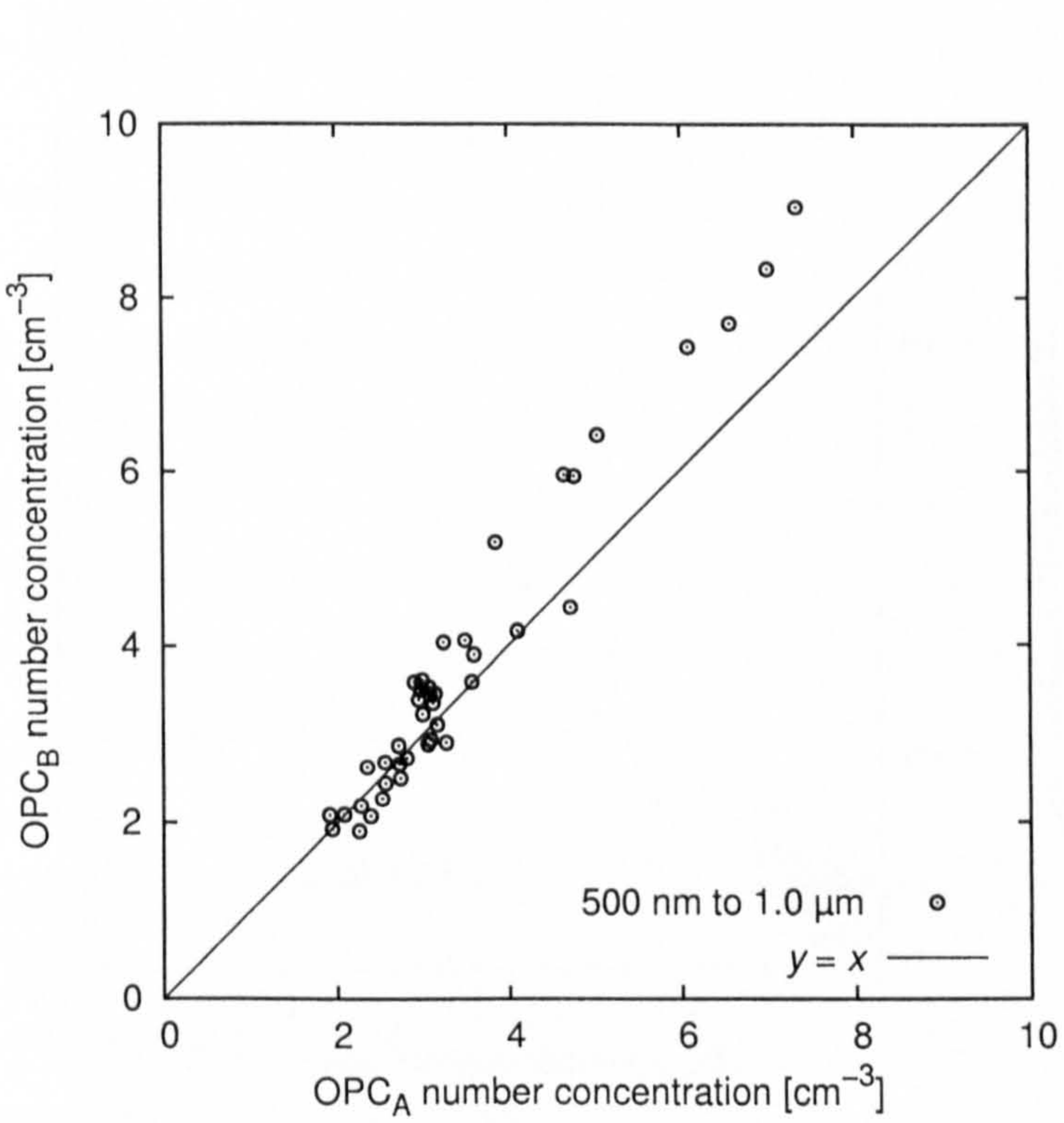

Figure 5.39: OPC scatter plot of side-by-side comparison of the two prototype instruments. Data between 6 May, 17:00 and 8 May 2003, 9:00 (GMT) are shown for the size fraction 500 nm to 1 µm. Points correspond to 1 h averages.

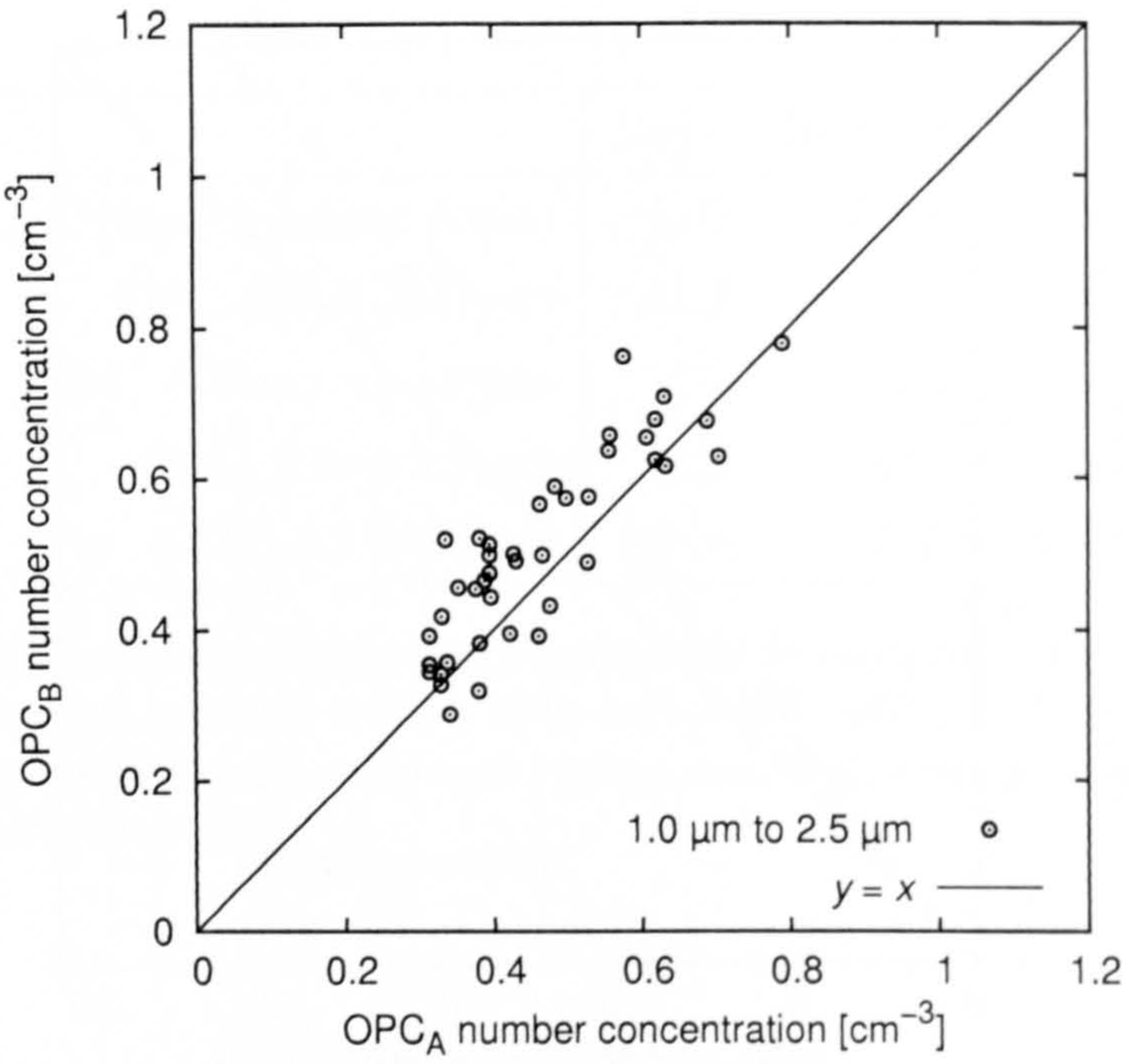

Figure 5.40: OPC scatter plot of side-by-side comparison of the two prototype instruments. Data between 6 May, 17:00 and 8 May 2003, 9:00 (GMT) are shown for the size fraction 1 µm to 2.5 µm. Points correspond to 1 h averages.

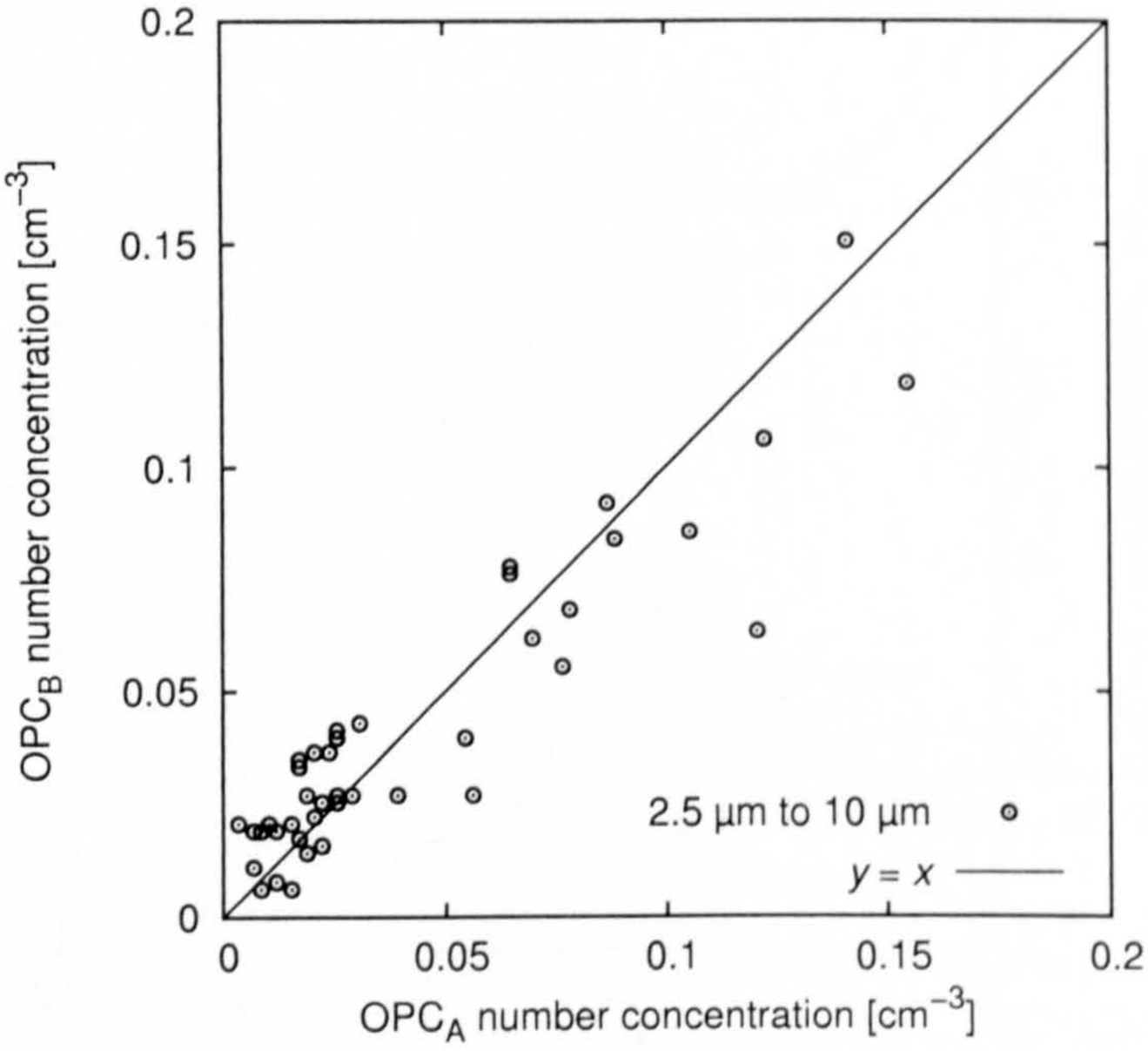

Figure 5.41: OPC scatter plot of side-by-side comparison of the two prototype instruments. Data between 6 May, 17:00 and 8 May 2003, 9:00 (GMT) are shown for the size fraction 2.5 µm to 10 µm. Points correspond to 1 h averages.

5.6 Summary of Instrument Performance

The OPC and CPC parts of the new AmbiCount instrument were successfully calibrated and the instrument performed well in the field trial at Birmingham.

OPC Calibration The OPC calibration showed that the detector response was linear with scattered power of particles, as scaling was sufficient to achieve a good fit of calculated response to measured response to PSL spheres. This check was important because the amplifier bandwidth was close to its limit to measure the OPC signals with their relatively short pulse widths (see section 4.2.4). The OPC calibration was corrected to reflect optical properties of average ambient particles. The resulting ambient response was smaller than the response to PSL, which together with an increased noise level of the electronic signal, was responsible for the slightly higher value of the lower detection limit of the OPC1s of 360 nm, as compared to that achieved with the first OPC prototype (see section 4.2.3). The noise increased because of the operation of the three mains pumps, and especially because of switching noise from the control of heater and cooler currents.

CPC Performance While the CPC calibration showed excellent agreement with TSI CPC 3010, comparison of the CPC data with TSI CPC model 3022A during the Birmingham field trial revealed large differences. Despite these differences, the correlation was very good and the instrument proved to be capable of resolving short incidents of very high ultrafine number concentrations. The differences to the TSI CPC 3022A could not be explained satisfactorily. To further investigate this, the lower detection limit of the CPC should be defined by calibration and by further verification tests at Birmingham.

The effect of coincidence errors on the measurement with the CPC of AmbiCount was demonstrated. The test showed that it is possible to measure number concentrations with the CPC of $\sim 500\,000\ \mathrm{cm}^{-3}$ if the correction proposed in equation (3.36) is applied.

Comparison of Number Concentration and TEOM PM_{10} Two important results from comparing the number concentrations with TEOM PM_{10} mass

concentration at Birmingham were: Firstly, TEOM PM_{10} is correlated with the size fraction 2.5 µm to 10 µm ($r^2 = 0.77$) and to a lesser extent with 1 µm to 2.5 µm ($r^2 = 0.41$). Correlation with the other size fractions is much lower. This indicates that main part of the PM_{10} mass concentration is contributed by particles residing in the coarse fraction 2.5 µm to 10 µm and, to a certain extent, by particles in the fraction 1 µm to 2.5 µm. Mass residing in the sub-micrometer size fractions, can therefore not be predicted by PM_{10} measurements alone. Secondly, the ultrafine number concentration is not correlated with either the number concentration of the other size fractions nor with PM_{10} mass concentration. This repeats observations made in other studies (for example Harrison et al., 1999b; Greig, 2000) and illustrates that ultrafine number concentration cannot be predicted, but must be measured directly.

Number-to-Mass Conversion Number-to-mass conversion was successful for two of the three proposed and tested algorithms—the smoothing method and the algorithm using the geometric mean diameter. The comparison between the different conversion algorithms has shown, however, that more size resolution in the coarse size range above 2.5 µm and in the ultrafine size range below 360 nm is necessary to improve the quality of the conversion algorithms further. Additional fractionation in the ultrafine size range would help to avoid overestimating the mass concentration in that range. An additional size fraction in the coarse size range would help to calculate the mass more accurately, since most of the mass resides in this size range.

Number-to-mass conversion also provided a method for estimating the aerosol density, which by comparing the average TEOM to the average calculated (with geometric mean method) PM_{10} mass concentration resulted in 1641 $kg \cdot m^{-3}$, a value close to values found in literature (for example Morawska et al., 1999a; Hand and Kreidenweis, 2002; McMurry et al., 2002).

Statistical Counting Error The accuracy of the number concentration measurement in the coarse size fraction suffered from a relatively large statistical counting error. From equation (3.33) the relative statistical counting error can be calculated and is, for a number concentration of typically 0.1 cm^{-3},

13% for sampling a one-hour average. The other size fractions, having typically higher concentrations, have lower relative counting errors. Because of the importance of this size fraction, this limits the possible time resolution for the number-to-mass conversion process to currently around one hour. In certain cases, as for example sampling close to roads with at times high and fast fluctuations, a higher time resolution would be beneficial. The accuracy in the coarse size fractions could be improved using a higher sample flow rate for the OPC, which exhibits low coincidence up to 100 000 cm^{-3}. The statistical counting error would be reduced in this way and necessary averaging times could be reduced. However, this would require some redesigning of the OPC, for example regarding isokinetic sampling.

OPC Laser Particle sizing accuracy is also vital for number-to-mass conversion. Experience has shown that this is difficult to guarantee with the current design of laser mounting and alignment. In two cases, a laser module needed replacing after failure of the laser diode (CPC_B laser at Birmingham in week following 15 May 2002, $OPC1_A$ laser before calibration on 11 February 2003), contradicting the typical lifetimes of 10 000 h (more than a year of continuous operation). Laser diodes are very sensitive devices. The driver electronics of the laser modules used here include protection against over-voltages from the supply. After the second laser was replaced, the protection was further improved with fast switching transient voltage suppressors, added in parallel at the supply voltage for the laser module, to avoid any short voltage peaks on the supply to reach the laser diodes putting them at risk of degradation and permanent damage. The laser diodes are operated close to their rated maximum, which may reduce their lifetime. To maintain the necessary laser intensity, while reducing the risk of damage, laser diodes with higher nominal power could be used working at the same power as the currently employed lasers. Laser diodes might also suffer damage if exposed to strong electrical fields such as those generated by mobile phones. Both failed lasers were, in fact, used for some time close to a GSM modem with antenna, which was used to access the instrument remotely. Occasionally, mobile phones were also used while operating the instrument. Such use of mobile phones and GSM modem antenna close to the laser diodes should be reduced and necessary precautions taken. Even-

tually, a better shielding of the two lasers in the instrument should avoid exposure to harmful radiation even if a mobile phone would be used in the vicinity and a GSM antenna placed close to the lasers.

Operating Temperatures On some occasions, the instrument tended to heat up if the enclosure was closed. This was observed, for example, in relatively warm internal environments and during outside use during sunny days. When the instrument was originally operated with a saturator temperature controlled to 35°C, the saturator temperature was found to increase together with the instrument's temperature, while the condenser temperature was still controlled to 15°C. The temperature difference between saturator and condenser, therefore, increased, which can affect the lower detection limit of the CPC. The problem was solved by changing the control algorithm for condenser and saturator temperatures so that the difference was maintained constant in case one of the set temperatures could not be controlled. If the instrument heats up inside now, the condenser temperature will be increased together with the saturator temperature, maintaining the constant difference defined by the set points of the two temperatures. The instrument operated in this mode, for example, during the field trial in the Birmingham monitoring station, where the temperature inside the instrument rose to about 38°C. For outside use, however, the instrument should be ventilated better so that the temperature could be maintained ambient temperature and excessive heating would be avoided. Currently, the instrument is effectively ventilated only at the sample flow rate of 5 $l \cdot min^{-1}$, which is released inside after sampling from ambient air. While the CPC condenser is thermally insulated in foam, the saturator was not insulated so that part of the heater energy is dissipated. Insulation of CPC saturator would reduce this, though the control would need to be slower as the passive cooling would be much slower. The quality of insulation needs, therefore, to be a compromise of reduction of heat dissipation, response time of control, and also stability of temperature.

6 Ultrafine Fractionation

The final objective of the project was to develop a method by which the ultrafine size fraction (~10 nm to 360 nm) could be further subdivided into size fractions as anticipated in section 4.1.2. This would be advantageous because of the importance of this size range for health effects. Further fractionation in the ultrafine size range would enable the new instrument to monitor processes which involve different sizes in this range and to identify and distinguish between sources of ultrafine particles by their contribution to the ultrafine number concentration predominantly in certain size fractions. It would also improve the ability of the new instrument to provide mass concentration from number-to-mass conversion algorithms, as further fractionation would reduce the uncertainties of the algorithms in the ultrafine size range (see section 5.4).

The single ultrafine size fraction at this stage is confined between the lower detection limits of CPC and OPC (see section 4.1.3). The following section describes briefly existing techniques capable of size fractionation in the ultrafine size range. Section 6.2 explains the selection of techniques which could be implemented in the new instrument. The selected techniques were tested as described in section 6.3. Finally, section 6.4 discusses the results of these tests.

6.1 Methods of Ultrafine Fractionation

Electrostatic Classification

Charged particles in an electric field E experience a force, and as a result they drift with a velocity v given by the balance of drag force and electric force. For particles an electric mobility Z is defined such that $v = ZE$. The electrical mobility is proportional to the charge of the particles and d_p^{-1}:

$$Z = \frac{neC_C}{3\pi\eta d_p} \tag{6.1}$$

The charge carried by the particle is expressed as the number n of elementary charges e, C_C is the slip correction factor. The size dependence of Z is used for the so called *electrostatic classification* of particle size. Electrostatic classification was one of the earliest methods used for size classifying particles (Whitby, 1966; Flagan, 1998). Today it is used in DMAs, where particles are charged and then passed through an electric field where, due to the resulting drift of particles, only particles having an electrical mobility Z within a narrow region will exit through an outlet slit.

To use this technique, an electrostatic classifier (consisting of a particle charger and electrodes to create the electric field) would need to be added to the new instrument. The electrostatic classifier would sub-sample from the duct carrying the main sample flow a larger sample than the CPC sample flow rate of 10 $ml \cdot min^{-1}$. This would be necessary since only part of the sub-sampled flow (the part containing the particles of the selected electrical mobility) would be passed on to the CPC after exiting the classifier.

Diffusion Techniques

Diffusion describes random Brownian motion of airborne particles using the diffusion coefficient D (diffusivity), which depends on the size of the particle (see equation (3.27) in section 3.4). The smaller the particles the higher are their diffusion coefficients, and the more they move randomly. As a consequence smaller particles are more likely to move out of the flow path and to be lost (see section 3.4). The size dependence of these sampling losses can be used for ultrafine fractionation. Using a sampling device with high losses and a transmission efficiency of 50% at a certain particle diameter, provides a lower size cut at that diameter below which particles are not sampled efficiently (transmission efficiency decreasing to zero). A review of diffusion size separation techniques can be found in Cheng (2001).

Equations (3.29) and (3.30) for diffusion parameter and transmission efficiency of a circular tube show that sampling losses can be enhanced by an increased length of the device or by a decreased flow. Two possible devices are therefore a long tube or many tubes used in parallel (low flow in each tube).

Using a similar space as a circular tube, size cuts at higher particle sizes can be achieved with thin rectangular channels. The diffusion parameter ξ

in this case is defined as

$$\xi = \frac{8DLW}{3qH} \tag{6.2}$$

where H is the height (or separation), W the width of the channel, with $H << W$. The length of the channel is L, the flow rate through it is q. The transmission efficiency η_T through a rectangular channel is

$$\begin{aligned} \eta_T &= 0.9104e^{-2.8278\xi} + 0.0531e^{-32.147\xi} \\ &\quad +0.01528e^{-93.475\xi} + 0.00681e^{-186.805\xi} \quad \text{for} \quad \xi > 0.05 \qquad (6.3) \\ \eta_T &= 1 - 1.526\xi^{2/3} + 0.15\xi + 0.00342\xi^{4/3} \quad \text{for} \quad \xi \leq 0.05 \qquad (6.4) \end{aligned}$$

The formula for $\xi > 0.05$ is given by Tan and Thomas (1972), the formula for $\xi \leq 0.05$ by Ingham (1976). Other devices were studied, as for example screens of fine wire meshes (Cheng and Yeh, 1980; Cheng et al., 1985), annular tubes, and circular disks (Cheng, 2001). A *diffusion battery* uses several stages of such devices to provide several size cuts in the ultrafine size range (Cheng et al., 1980; Brown et al., 1984).

Ultrafine fractionation could be added to the new instrument using such devices to sub-sample from the main sample flow of 5 l·min^{-1} the required sample for the CPC. A single tube could simply extend the CPC capillary tube as proposed above. Alternatively, many tubes in parallel could be connected to the CPC capillary tube using a funnel-like connector. In a similar approach, a rectangular channel could be connected to the CPC capillary tube by funnelling the channel. More than one channel in parallel could be used to enhance the diffusive losses. This implementation would require the diffusive devices to be small enough not to obstruct the main sample flow.

The diffusivity of particles also depends on temperature, however, using the dependency for size separation by varying the temperature of a diffusive device is impractical as size cut changes due to varying diffusivity are small for moderate temperature changes. If, for example the temperature was changed from 20°C to 100°C—a temperature already too high for ambient sampling—the diffusivity of a 30 nm particle would increase by 42%. Although diffusivity changes considerably, a size cut of 28.8 nm for diffusion tubes would, as a consequence, shift to 34.5 nm. This illustrates, on the other hand, that for typical ambient temperature changes, size cut changes can be neglected. Changing the sample flow rate instead of temperature,

may be a possibility to adjust the size cut of diffusive sampling devices. Diffusion tubes with a size cut of 28.8 nm would, if doubling the flow, have a size cut at 24.3 nm; or, if halving the flow, have a size cut at 49.2 nm.

Inertial Techniques

Inertial techniques are commonly used for separation of particles typically larger than 1 µm, as for example in cyclones, impactor inlets, or virtual impactors. Because of decreasing mass, it becomes more difficult to use inertial techniques for smaller particles. Impactors must be used with either low pressure or small dimensions of the impactor nozzle to be able to size-segregate ultrafine particles, which is realized, for example, in the ELPI and micro-orifice impactor respectively (see chapter 2). At very low pressures of less than 500 Pa, cut-off sizes of lower than 10 nm can be achieved with an impactor (Gomez-Moreno and Fernández de la Mora, 1996); sizing can be improved by aerodynamically focusing particles before the impactor, and hence produce a sharper cut-off curve as all particles are initially on the same streamline (Liu et al., 1995; Fernández de la Mora, 1996). This is achieved by drawing the sample air flow through a series of aerodynamic lenses (orifice plates), thus bringing particles in a wide size range close to the centre of the flow and creating a particle jet which is then impacted through a small nozzle onto an impactor plate. Particles below a critical inertia will not impact and can subsequently be analyzed by, for example, a CPC, giving the number concentration below the size cut.

After sub-sampling from the main sample flow, the sub-sample could be drawn through such an impactor with either fixed size cut or variable size cut using variable pressure (Fernández de la Mora, 1996) or variable distance of the impactor plate from the nozzle (Fernández de la Mora et al., 1990). The CPC could then detect particles which escape from impaction.

Thermophoresis

In presence of a temperature gradient, particles move towards the region of lower temperature (Waldmann and Schmitt, 1966). This is caused by a net difference of kinetic energy transferred from collisions with molecules on the "hot side" and molecules on the "cold side" (Zheng, 2002). The ef-

fect depends, apart from the temperature gradient, also on particle thermal conductivity and size. Thermophoresis is used for example to collect small particles for further analysis (thermophoretic precipitation) on a cold microscope slide, or to protect surfaces from particle deposition by heating them above ambient temperature (Zheng, 2002). For particle sizes much smaller than the mean free path l of air molecules ($\mathrm{Kn} >> 1$, where $\mathrm{Kn} = {}^{2l}/_{d_\mathrm{p}}$ is the Knudsen number), the thermophoretic force approaches the free molecular limit where the force is proportional to d_p^2 and to the temperature gradient, but independent of particle thermal conductivity. The *thermophoretic velocity*—a constant velocity reached when thermophoretic force and drag force are in balance for a given temperature gradient—assumes the form (Waldmann and Schmitt, 1966)

$$v_\mathrm{th} = -\frac{\eta d_\mathrm{p} C_\mathrm{C}}{6\rho_\mathrm{g} l}\frac{\nabla T}{T} \tag{6.5}$$

where η, ρ_g, and l are the gas viscosity, density, and molecular mean free path respectively. The thermophoretic velocity is independent of particle size since the slip correction factor C_C is proportional to d_p^{-1} for $\mathrm{Kn} >> 1$, which can be seen from equation (3.28).

It is not yet possible to give a theoretical formula for the thermophoretic force or velocity in the complete range of particle sizes. Talbot et al. (1980) proposed a fitting formula for the thermophoretic force which approximates experimental results for all Knudsen numbers (Zheng, 2002). In the proposed formula (which approaches the free molecular limit for Knudsen numbers $\mathrm{Kn} \to \infty$), the resulting velocity is

$$v_\mathrm{th} = -\frac{2C_\mathrm{s}\frac{\eta}{\rho_\mathrm{g}}C_\mathrm{C}\left(\frac{k_\mathrm{g}}{k_\mathrm{p}} + C_\mathrm{t}\mathrm{Kn}\right)}{\left(1+3C_\mathrm{m}\mathrm{Kn}\right)\left(1+2\frac{k_\mathrm{g}}{k_\mathrm{p}}+2C_\mathrm{t}\mathrm{Kn}\right)}\frac{\nabla T}{T} \tag{6.6}$$

where k_g and k_p are the thermal conductivities of the gas and particle respectively. Kinetic theory values for the momentum exchange coefficient C_m, the temperature jump coefficient C_t, and the thermal slip coefficient C_s, are $C_\mathrm{m} = 1.14$, $C_\mathrm{t} = 2.18$, and $C_\mathrm{s} = 1.17$ (Talbot et al., 1980). The Knudsen number is defined as mentioned above ($\mathrm{Kn} = {}^{2l}/_{d_\mathrm{p}}$), where for this formula the gas mean free path l is defined as $l = \frac{2\eta}{\rho_\mathrm{g}\bar{c}}$, where $\bar{c}$ is the mean molecular speed with $\bar{c} = \sqrt{\frac{8kT}{\pi m}}$, m is the molecular mass (mass of one molecule), and ρ_g is the density of the air.

Creating a temperature gradient perpendicular to the streamlines in the sample flow, upstream of the CPC sampling capillary tube, would change the distribution of particles across the duct due to the thermophoretic velocity. This could be used for size fractionation in the ultrafine size range, as the smallest particles (Kn $\rightarrow \infty$) would move with the velocity given by equation (6.5) and larger particles at the different and size dependent velocity given by equation (6.6).

CPC Possibilities

The ultrafine particles act as condensation nuclei and grow in the alcohol to droplets, whose size is independent of particle size for particles down to a certain limit, below which the final droplet size decreases with further decreasing particle size (see section 3.3 and figure 4.18). If flow and vapour saturation are stable then this dependence of the droplet diameter on the particle size allows retrieval of information on the size distribution of particles in this lower part of the ultrafine size fraction (typically below $\sim$20 nm) by analysing the pulse heights of the signals from the droplet detecting OPC (Saros et al., 1996; Weber et al., 1998).

The size distribution in the lower part of the ultrafine size fraction can also be obtained by changing the lower detection limit of the CPC. This may be changed by varying the temperature difference between the saturator and the condenser, which varies the vapour pressure and hence the saturation ratio and the lower detection limit (see equation (3.7)). One can then use two or more CPCs in parallel (Brock et al., 2000; Stein et al., 2001), or alternatively scan continuously the lower detection limit of only one CPC. In this case, instead of changing the temperatures in the CPC, which might be quite slow, the saturation ratio may also be varied by changing the vapour pressure in the condenser directly through dilution with dry air, for example by bypassing the saturator. Implementation of the technique using variable temperature in the CPC would only require changes to the temperature control as the CPC of the new instrument could be used as it is.

6.2 Selection of Size Fractionation Technique

Electrostatic Classification In electrostatic classification a certain particle size range, for example 5 nm to 400 nm or 10 nm to 1 µm, is scanned with high size resolution. Usually, this scan takes several minutes, which can be a disadvantage if dynamic processes cannot be followed simultaneously in the different size channels. The scan time could be reduced by reducing the size resolution, but the principal problem remains. Inversion of particle concentrations measured for different electrical mobilities to the underlying particle size distribution is not an easy task, as particles may carry one or more elementary charges, so that particles having different sizes may have the same electrical mobility. It is important that the particles after charging have a known and stable charge distribution. If the size resolution of an instrument using electrostatic classification were reduced, then the inversion would be more difficult and assumption of the size distribution would be necessary since charging efficiency varies significantly with particle size. Ultrafine particles are charged with a very low efficiency, further complicating the use of electrostatic classification. This option for ultrafine fractionation of the ultrafine size range was therefore rejected.

Diffusion Techniques Diffusion techniques present no major problems for size separation in the particle size range up to 100 nm. While the presented tubes and thin rectangular channels could be easily added to the existing instrument, screens of fine wire meshes, circular disks, and also annular tubes might present some technical problems. Screens of fine wire meshes and annular tubes would also have size cuts not as sharp as could be realized with tubes and thin rectangular channels (Cheng, 2001).

Inertial Techniques Inertial techniques need to use low pressure which is a disadvantage when sampling ambient aerosol. Temperature and pressure should not be changed significantly from ambient conditions to avoid changes in particle size distribution by condensation or evaporation. For this reason, inertial techniques were not considered further for the ultrafine fractionation requirement.

Thermophoresis Thermophoresis might be used for size separation of particles. However, the size dependence of thermophoretic force or velocity is only weak. The size cut of a thermophoretic device would therefore be relatively broad, not sharp as would be desired. A difficulty would be the necessity for a high temperature gradient, which, if achieved with high temperatures, could disturb flow conditions and change or destroy particles through, for example, evaporation. Close to a heated wire aligned parallel to the streamlines in an air flow, the temperature gradient would be relatively high even for only moderate wire temperatures, especially at the start of the heated wire, before the air stream is heated significantly. Such a wire could be placed in the centre of the duct before the CPC sampling capillary tube. Particles sampled by the CPC would then, prior to entering the capillary tube, flow alongside the wire. Heating the wire would repel particles, which will be lost for sampling if they drift a sufficient distance away from the wire. This phenomenon is particle size dependent due to the size dependence of the thermophoretic velocity. The use of this technique for size fractionation in the ultrafine range, was investigated as will be shown in section 6.3.2.

CPC Possibilities The use of the CPC to further size fractionate the ultrafine particles is limited to the sizes below ~20 nm. Even if size cuts at higher sizes were theoretically possible, practically they would be difficult to maintain, as lower detection limits above 20 nm would be very sensitive to operating conditions. Theoretically, a size limit of 50 nm would change to 100 nm if the temperature difference between saturator and condenser decreased by only 1 K. The test of the temperature dependence of the lower detection limit of the CPC did confirm this difficulty (see figure 5.10). For this reason, the option of using the CPC to achieve size fractionation was rejected.

6.3 Evaluation Tests

Investigations were undertaken to assess the practicality of using diffusion techniques or thermophoresis for ultrafine size fractionation.

6.3.1 Diffusion

The use of a low sample flow rate of only $10\,\mathrm{ml{\cdot}min^{-1}}$ is an advantage for diffusion techniques, as a low flow rate results in high diffusion losses. While the CPC sampling capillary is kept short enough to not compromise the lower detection limit (length of the capillary tube of $L = 50$ mm and sample flow rate of $q = 10\,\mathrm{ml{\cdot}min^{-1}}$ yield $\eta_T = 0.5$ for a spherical particle with a diameter of 6.0 nm), it is sufficient to simply extend the sampling inlet of the CPC to achieve a higher size cut; an extension, for example, by further 222 mm would yield $\eta_T = 0.5$ for a particle diameter of 14.1 nm. Such a modified CPC will measure a reduced number concentration. The difference in number concentration measured by this CPC and an unmodified CPC will give an indication of the number concentration below the new size cut of 14 nm. This difference and the ratio of the two number concentrations will depend on the number size distribution, and hence change with changes in the distribution. A test was performed with such a 222 mm extension on one CPC sampling alongside the other, unmodified CPC. Figure 6.1 depicts the results, comparing the number concentrations on a logarithmic scale. Both CPCs sampled indoor air close to an opened window. The capillary tube extension was removed from CPC_B at 16:16, and the number concentrations of CPC_B increased immediately to values very close to those of CPC_A. The ratio of the number concentration of CPC_B with the enhanced sampling losses to the concentration of the unmodified CPC_A, which is depicted in figure 6.2, showed the expected variations over time, especially during some of the peaks in the total number concentration. This indicated changes of the sampled particle size distribution, in particular changes in the ratio of the number concentration of particles with a diameter >14 nm to the concentration of particles greater than the lower detection limit (either 6 nm if limited by diffusion or slightly higher if limited by level of supersaturation).

While ultrafine fractionation at this size cut of 14 nm would provide valuable additional information, other size cuts, for example at 30 nm, 50 nm, or even 100 nm would be of interest too. These higher size cuts, however, cannot easily be achieved by simply extending the inlet tube length further because it would increase the pressure drop in the extension and make the dimensions of the sampling inlet very impractical. A potential solution is to

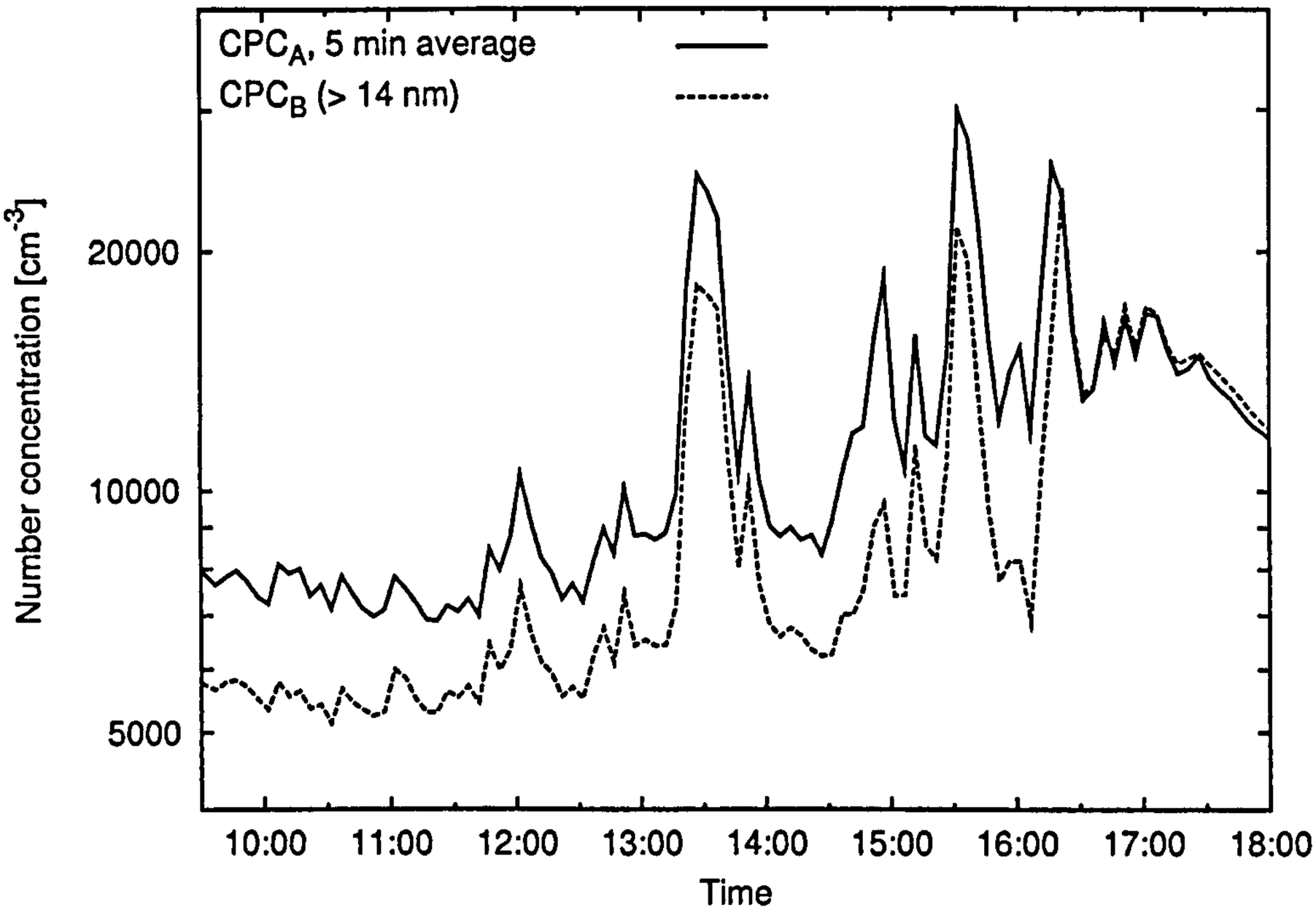

Figure 6.1: Test of an extension to the capillary inlet of CPC$_B$ to enhance sampling losses. The capillary tube of 222 mm length changes the lower detection limit from ~7 nm to ~15 nm. The measurement with this CPC is compared with the other, unmodified CPC.

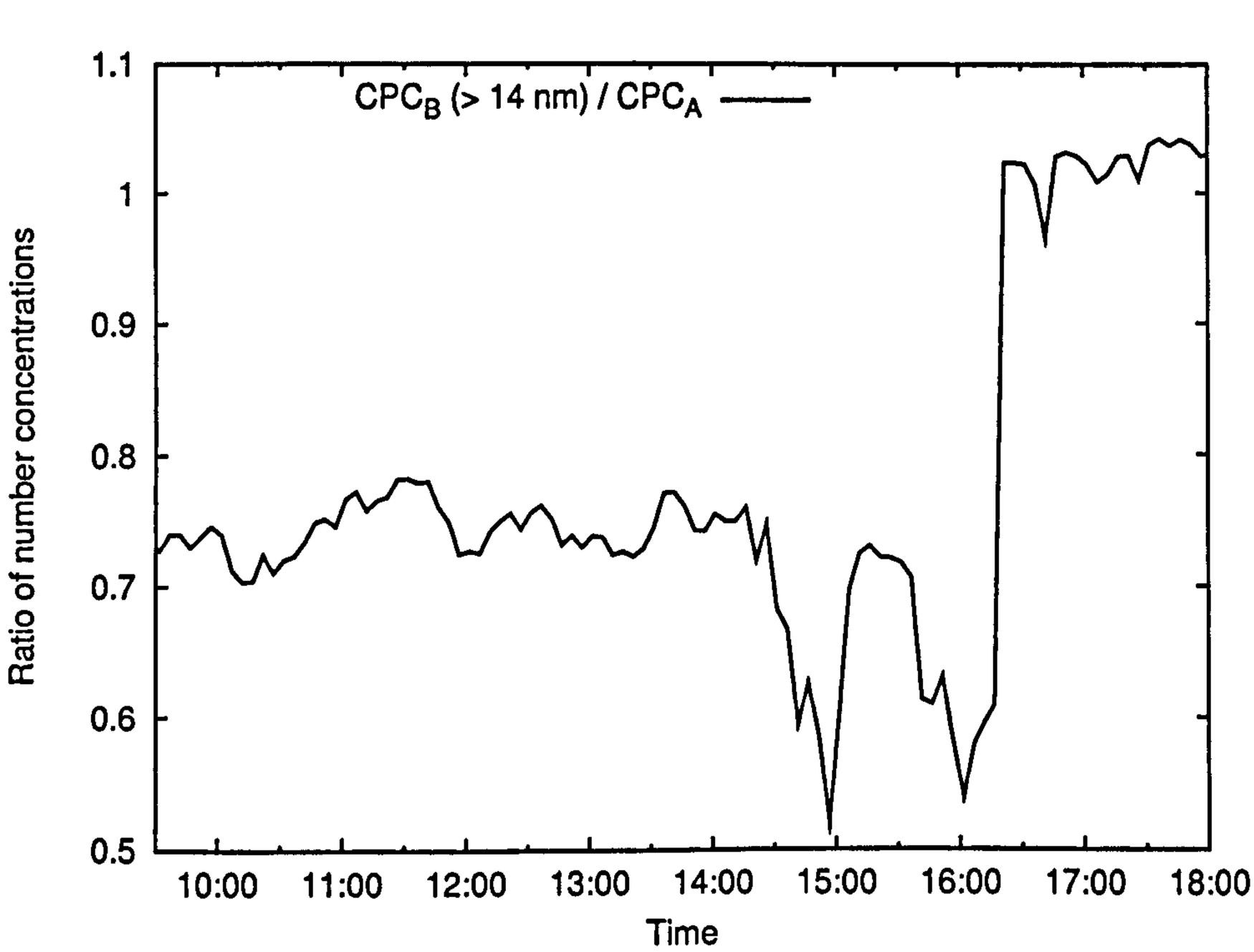

Figure 6.2: Ratio of the number concentration of the CPC with the capillary tube of 222 mm length extending the sampling inlet to the concentration of the unmodified CPC. It does not remain constant indicating changes in the number size distribution during the test.

split the flow between many capillary tubes in parallel. The flow through a single tube is reduced, and from equation (3.29) it follows that the length of the tubes can be reduced by the same ratio while maintaining the same diffusion losses. The relatively small diameter of the capillary tubes would allow the use of a sufficient number of capillary tubes to significantly increase the size cut. An alternative would be to use thin rectangular channels; a few of these may be easily stacked to increase the size cut too. These two possibilities have been evaluated theoretically and experimentally, and results are presented below.

Seven capillary tubes may be conveniently placed together in one larger tube, and this number has therefore been considered. Such a configuration would reduce the flow by a factor of seven, so that with a practical length of less than 200 mm a size cut at ~30 nm can be achieved. The transmission efficiency is 0.5 for $\xi = 0.137$, which, for a particle diameter of ~30 nm is, for example given by $L = 160$ mm and $q = {}^1/_7 \cdot 10$ ml·min^{-1}. The diameter of the tubes does not matter, though they should not be chosen too small so as to avoid clogging and higher pressure drops. Capillaries with an internal diameter of 0.8 mm were used for the tests.

The use of thin rectangular channels can easily take the size cut from 30 nm to 100 nm. The transmission efficiency is 0.5 for $\xi = 0.212$, which, for a particle diameter of ~100 nm is, for example, given by $H = 0.25$ mm, $W = 13$ mm, $L = 125$ mm, and $q = {}^1/_3 \cdot 10$ ml·min^{-1}. Three of these rectangular channels would therefore give a size cut at 100 nm. When equation (6.3) is compared to equation (3.30) it may be noted that the size cut of rectangular channels is sharper than that of tubes.

Figure 6.3 depicts the theoretical transmission efficiencies of the seven capillary tubes and the three rectangular channels presented in the above examples as function of particle size. The seven capillary tubes—called diffusion tubes in the following—and the three rectangular channels, were built and tested. They are shown in figures 6.4 and 6.5. Three rectangular channels were built from a PVC sheet of 0.25 mm thickness which was cut into strips to form the channel walls and spacers creating the separation between the channels as shown in figure 6.6. At the end the three rectangular channels were funnelled so that these channels could be fitted on the sampling inlet capillary of the CPC. The actual size of the rectangular channels

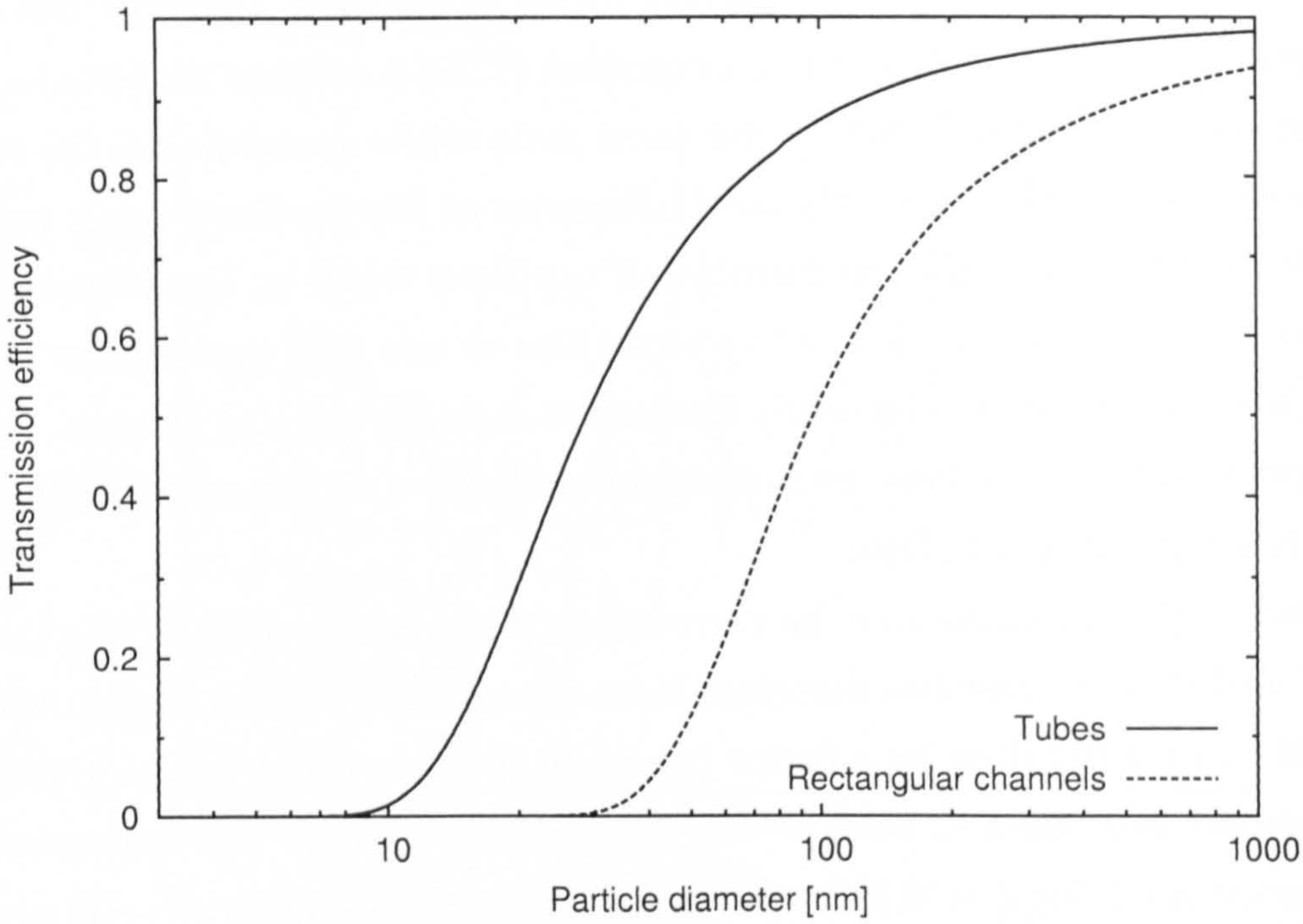

Figure 6.3: Theoretical transmission efficiencies of circular tubes and rectangular channels as function of particle diameter. Seven tubes are used in parallel to achieve a size cut (transmission efficiency of 0.5) at 30 nm and three rectangular channels in parallel to achieve a size cut at 100 nm (sample flow rate of 10 ml·min^{-1}; for dimensions see in text).

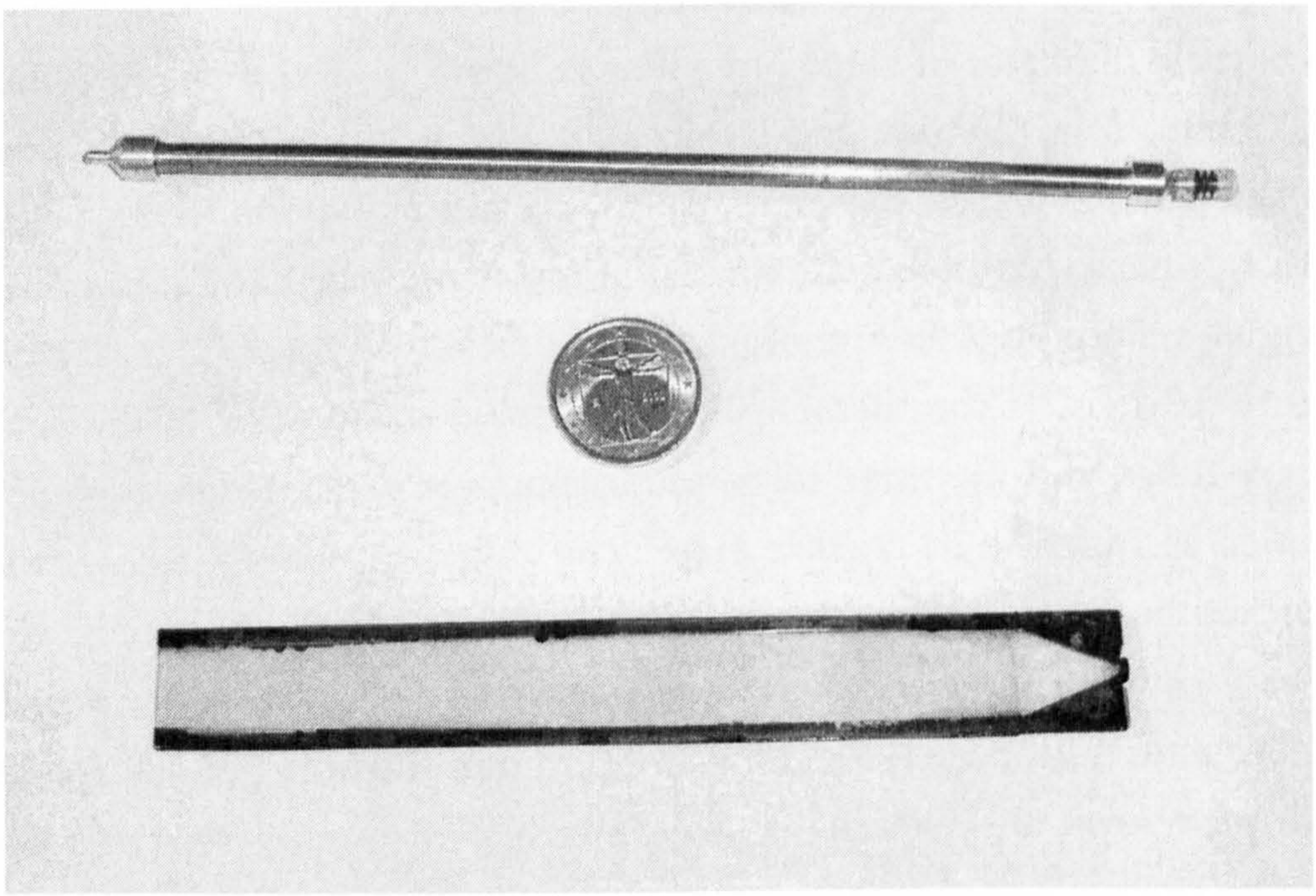

Figure 6.4: Diffusion tubes and rectangular channels. These were connected with the CPC sampling capillary tube for the tests.

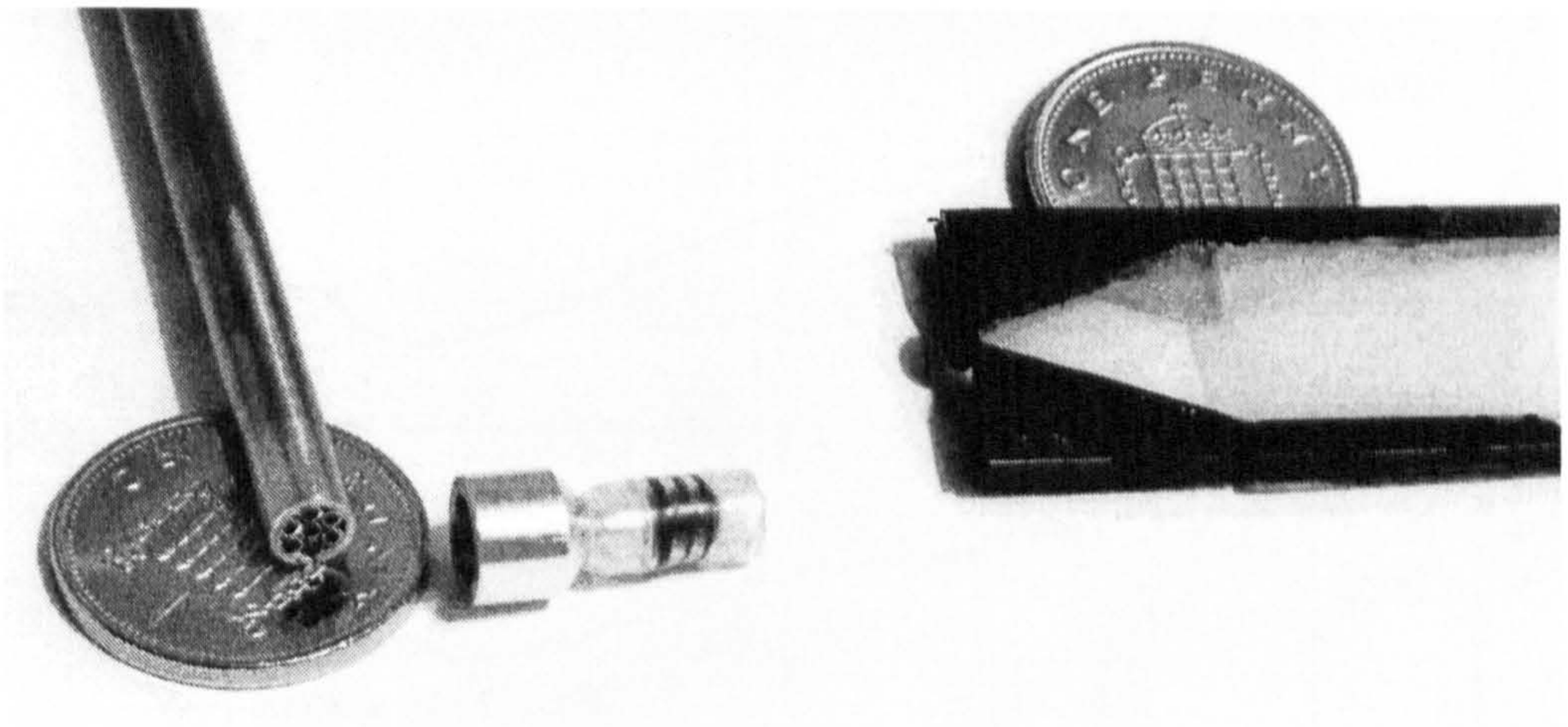

Figure 6.5: Entrance of diffusion tubes and rectangular channels. These were connected with the CPC sampling inlet capillary and sealed with O-rings.

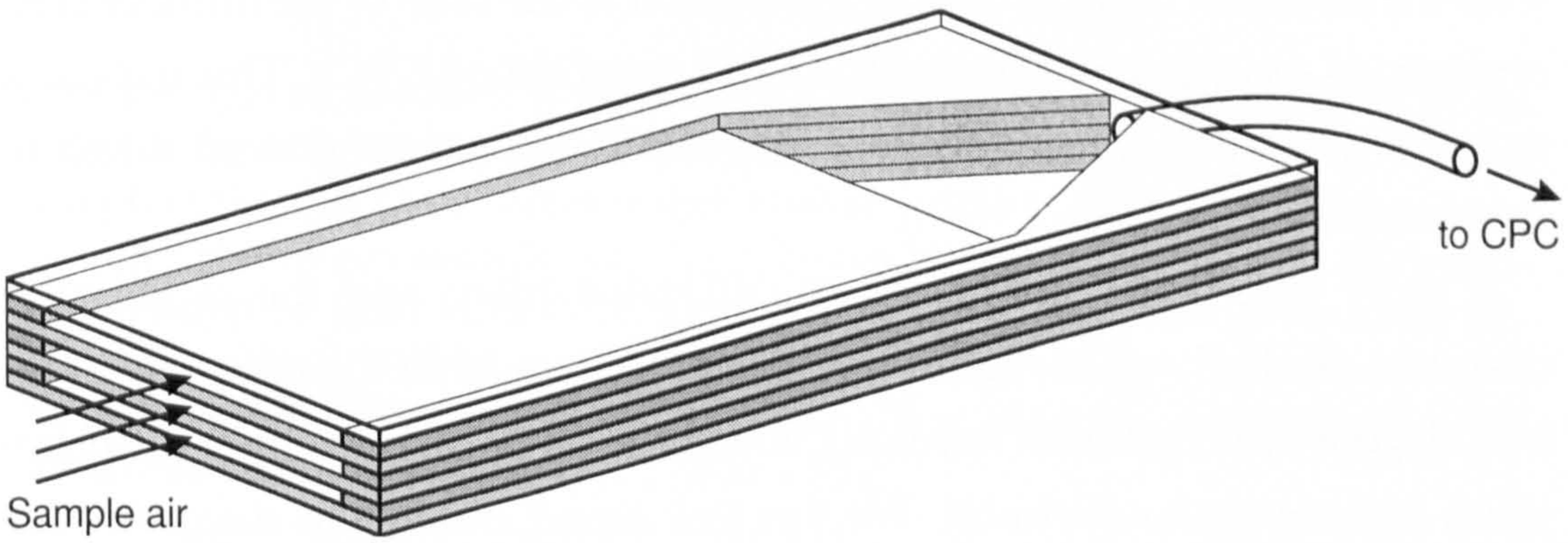

Figure 6.6: Diagram showing the construction of the diffusion device with three rectangular channels. The sample air enters in the three channels. After exiting the rectangular channels, the sample air is funnelled to the exit of the device, which is connected airtightly to the CPC sampling capillary tube. The uppermost layer of the device is shown transparent.

and the diffusion tubes can be seen in figures 6.4 and 6.5.

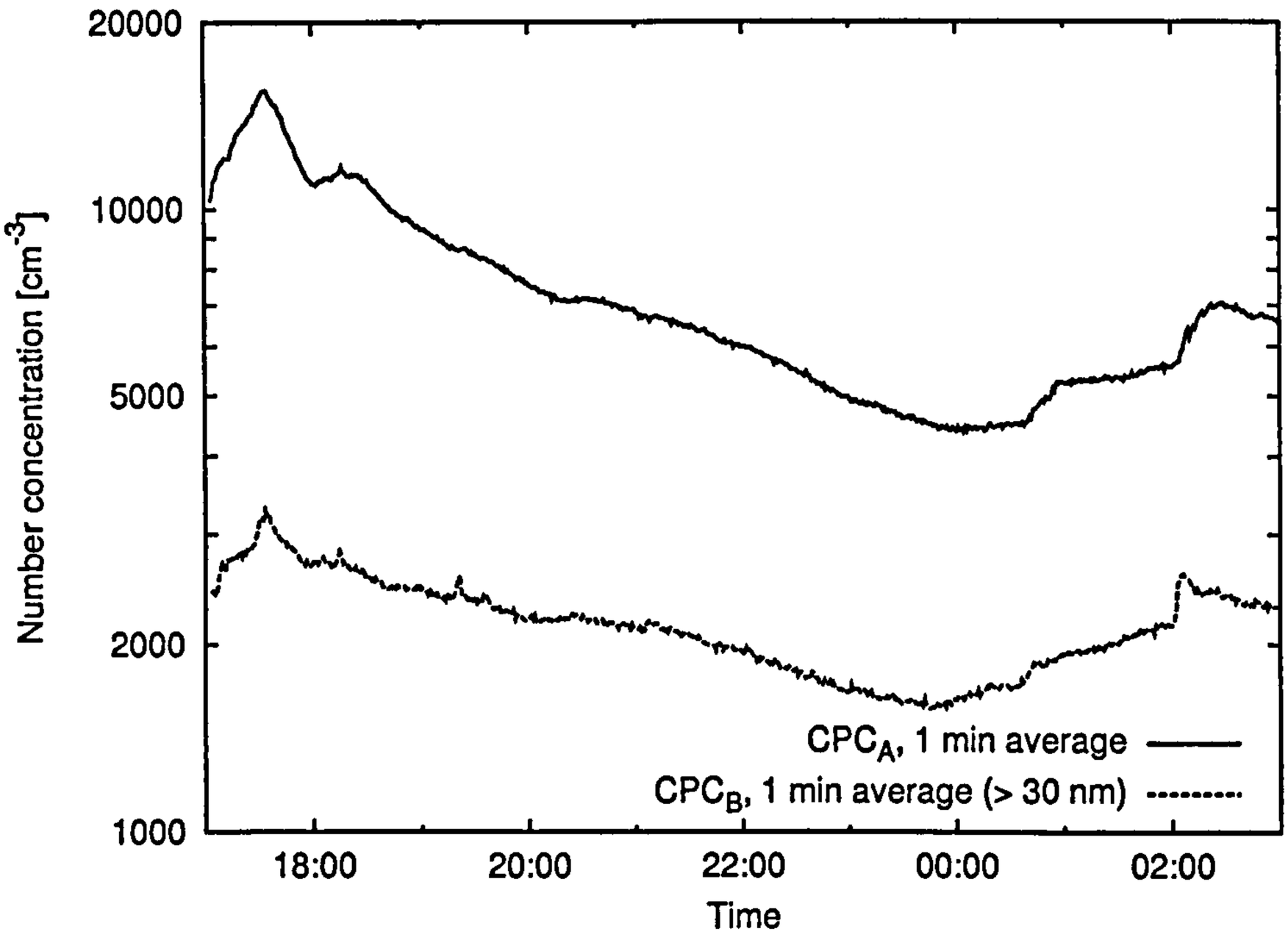

Figure 6.7: Test of diffusion tubes on CPC_B. Total number concentration of the CPCs of the two instruments are compared on a logarithmical scale. CPC_B was sampling through the diffusion tubes, so that its lower detection limit should be changed to ~30 nm according to the diffusion losses. During the test the instruments sampled from indoor air.

As seen previously in figure 6.2, the tests depicted in figures 6.7 and 6.8 with the diffusion tubes fitted show variation in the ratio of the number concentrations recorded by the modified and unmodified CPCs. This indicates that the two CPCs effectively measure number concentration in different size ranges.

A short test, which compared the diffusion tubes and the rectangular channels, is depicted in figure 6.9. Here, with two CPCs sampling side-by-side, one was operated normally whilst the other carried either diffusion tubes or rectangular channels. For this test $AmbiCount_B$ was disassembled and CPC_B removed from the main sampling duct to be able to access the sampling capillary tube for fitting the diffusion devices. CPC_A operated within $AmbiCount_A$ which was not disassembled. The diffusion tubes reduced the total number concentration to ~ 40%, whereas the rectangular channels reduced it to only ~ 10% of the values without diffusion losses measured by the normally operating CPC. A similar test was performed with the diffusion devices fitted on $OPC1_B$ to ensure diffusion losses of

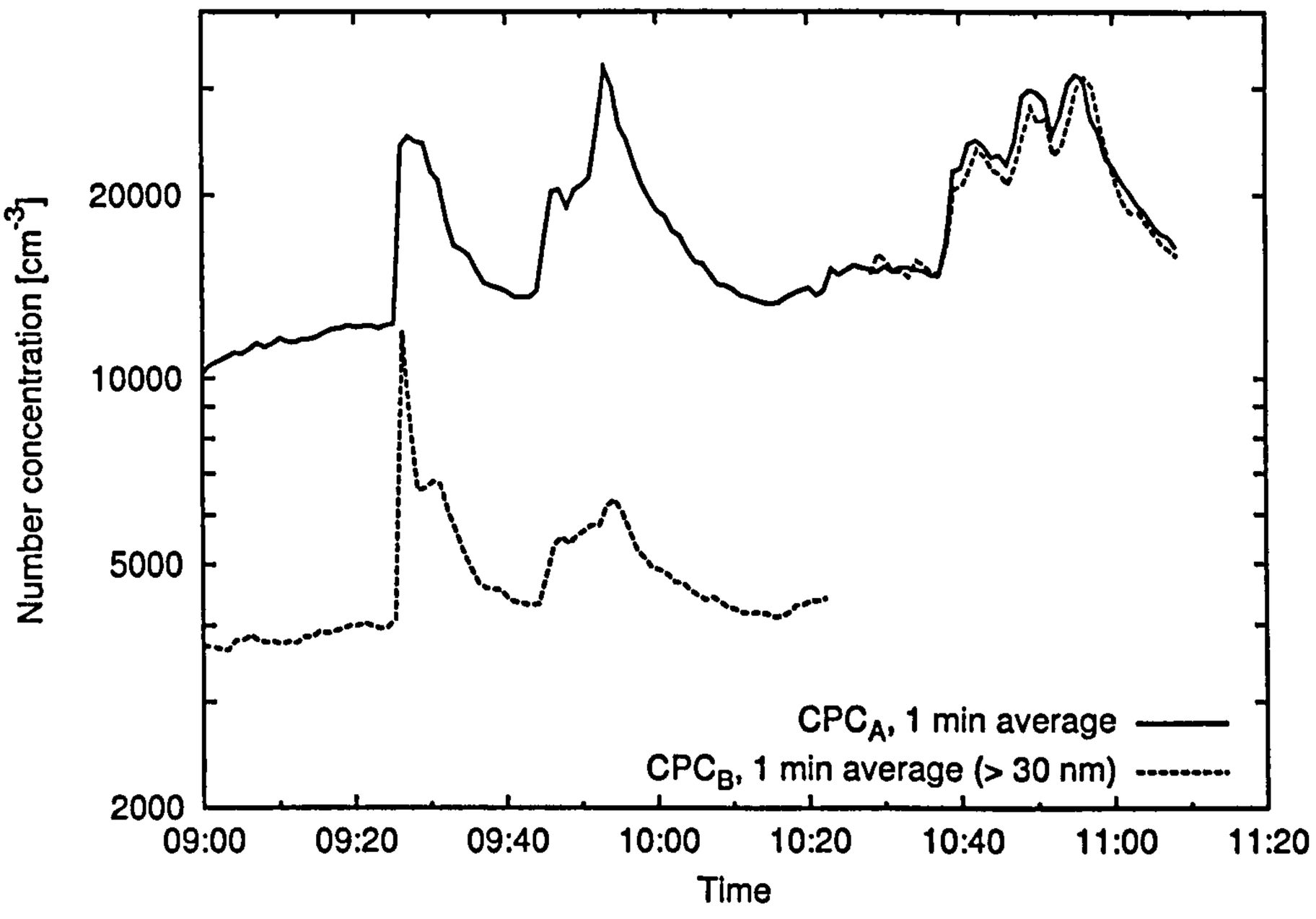

Figure 6.8: Test of diffusion tubes on CPC_B. Total number concentrations of the CPCs of the two instruments are compared on a logarithmical scale. CPC_B was sampling through the diffusion tubes, so that its lower detection limit should be changed to ~30 nm according to the diffusion losses. During the test the instruments sampled from indoor air. At 09:25 an incense stick was lit for a few seconds. From 09:44 to 09:53, and 10:37 to 10:56 a window close to the instruments—facing on a non-busy car park and a road at ~50 m distance—was open. At 10:25 the diffusion tubes were removed from CPC_B.

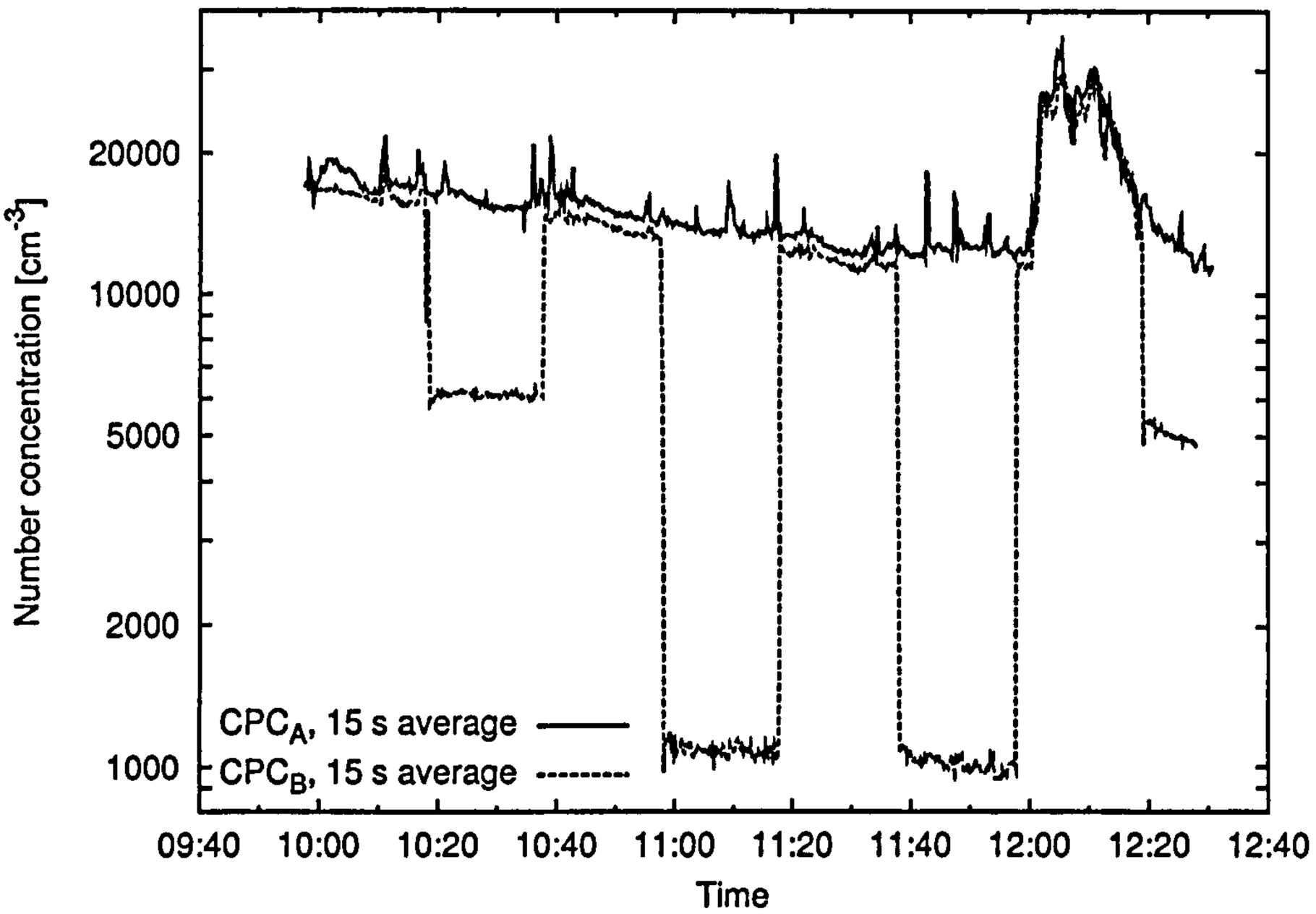

Figure 6.9: Reduction of total number concentration by diffusion tubes and rectangular channels. Side-by-side comparison of CPC_A and CPC_B, CPC_A was operated normally whilst CPC_B carried either diffusion tubes or rectangular channels. The diffusion tubes were fitted on CPC_B at 10:20 and 12:20 for a duration of 20 min, the rectangular channels were used for sampling at 11:00 and 11:40 for 20 min periods, again on CPC_B. Number concentrations are compared on a logarithmic scale.

particles in the OPC size fractions were low as compared to CPC losses—mainly representing losses in the ultrafine size fraction—as would be expected from the size dependence of the losses (see figure 6.3). The number concentrations in the size fractions 360 nm to 500 nm, 500 nm to 1 µm, 1 µm to 2.5 µm, and 2.5 µm to 10 µm were, in case of the diffusion tubes, reduced to ~ 80%, ~ 80%, ~ 65%, and ~ 15% respectively of the levels measured without the diffusion devices. In case of the rectangular channels the number concentrations were reduced to only ~ 20%, ~ 20%, ~ 20%, and ~ 10% respectively. While it was expected to see larger losses in the rectangular channels having the higher size cut, the losses here were substantial. For the diffusion tubes the losses were a little higher than expected too, however much lower as compared to CPC losses with the diffusion tubes. Both devices showed increased losses for coarse particles as opposed to what theory would predict. This might involve some inertial losses at entrance and exit of the devices and, in case of the rectangular channels also losses of charged particles since the device, made of plastic, was non-conducting. While these results are indicative only, such enhanced losses for the OPC would not matter, as the diffusion devices would be used on the CPCs only, where they showed to work well.

6.3.2 Thermophoresis

Tests were performed with a heated copper wire aligned along the axis of the CPC capillary inlet in the duct of the prototype instrument. The wire, with a diameter of 0.32 mm, was heated by wrapping around it an insulated nichrome heating wire with a diameter of 0.10 mm. The copper wire was supported by a holder fixed to the wall of the duct. This test configuration is shown in figure 6.10. The wire was aligned with the CPC capillary inlet by rotating the duct (the capillary inlet is not exactly in centre, as the centre is located between OPC and CPC capillaries). A tiny thermocouple made from 2 solid strands of 0.076 mm diameter (Chromel-Alumel, type K) was attached to the copper wire close to the windings of the nichrome wire. A photograph of this test device is shown in figure 6.11. The wires connected to the thermocouple and to the nichrome wire windings were taken out through the top of the duct (through duct–cyclone connector, cyclone was not fitted). During tests the temperature of the copper wire was varied

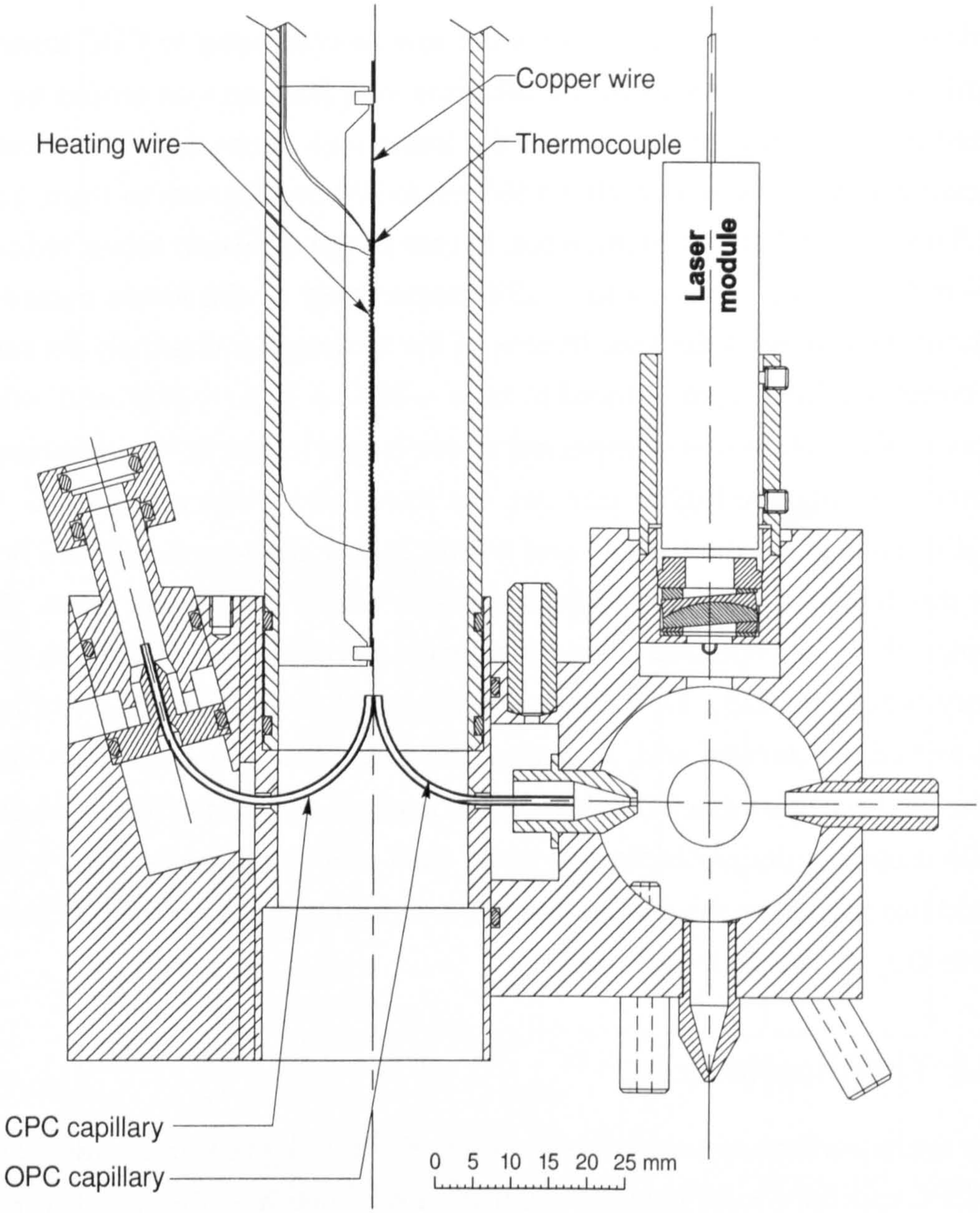

Figure 6.10: Thermophoresis test configuration with copper wire.

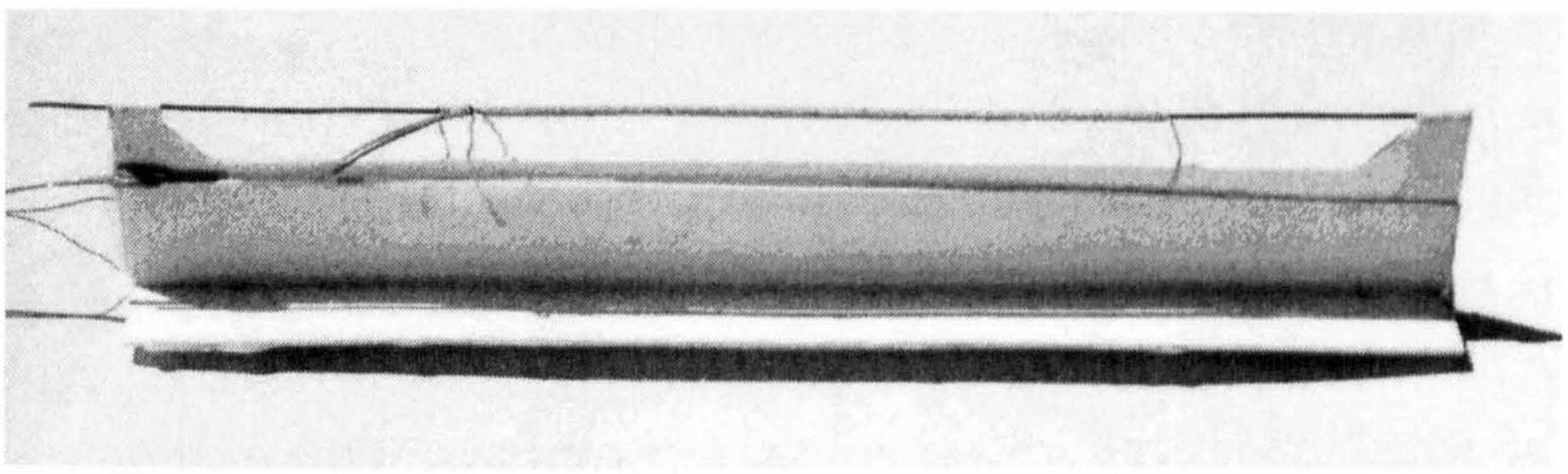

Figure 6.11: Heatable copper wire for thermophoresis tests. The copper wire has a diameter of 0.315 mm and is heated over 38 mm of its total length of 78 mm. During tests it was placed at a distance of 3.9 mm from the sampling capillary tube. A tiny thermocouple attached to the wire measured the temperature.

between 40°C and about 80°C (at air temperatures in the duct of ~25°C).

When aligned with the CPC inlet, the ultrafine number concentration (CPC total number concentration) decreased with increasing temperature of the copper wire up to a point, where further increase in temperature let the number concentration rise again. The concentration typically decreased by 20% to 50% at a wire temperature of 41°C to 64°C and then increased again if the wire was heated further to 79°C. An example of a measurement with the heated wire aligned with CPC_B is shown in figure 6.12. Heating

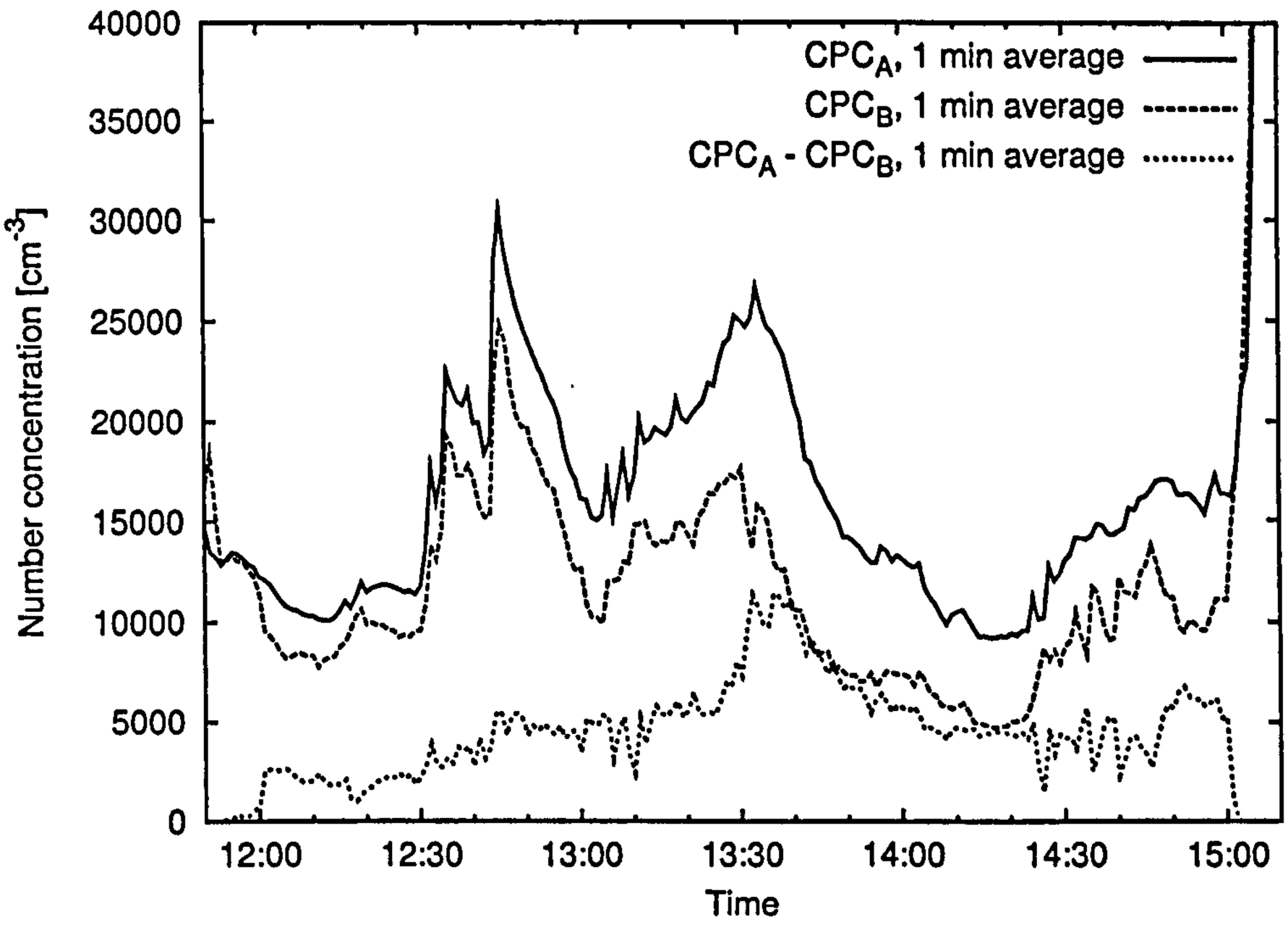

Figure 6.12: Thermophoresis tests with heated wire aligned with CPC_B sample inlet. Heating was switched on at 12:00 at a heating current of 75 mA and reached within about a minute 40.6°C. At 13:00 heating current was increased to 100 mA and the temperature reached 50.7°C, and at 13:30 further to 125 mA and the temperature reached 63.7°C. At 14:30, the heating current was set to 150 mA and the temperature increased to 78.8°C. At 15:00 the heating was switched off.

was switched on at 12:00 at a heating current of 75 mA and reached within about a minute 40.6°C. At 13:00 heating current was increased to 100 mA and the temperature reached 50.7°C, and at 13:30 further to 125 mA and the temperature reached 63.7°C. Eventually, at 14:30, the heating current was set to 150 mA and the temperature increased to 78.8°C. At 15:00 the heating was switched off.

The effect of the heating can clearly be seen when heating is turned on or off. When heating is off then the two CPCs read the same, with heating

the number concentration of CPC_B decreases immediately as compared to the concentration of the reference instrument, CPC_A. Similar measurements were performed with the copper wire aligned with the OPC capillary inlet to see whether the particles in the different size fractions behave differently. In a test on the same day as the measurement shown in figure 6.12, the number concentration in the size fraction 360 nm to 500 nm decreased by ~40% for a wire temperature of up to 63°C, while number concentrations in the other OPC size fractions were reduced by ~20% or less.

The temperature in the duct with the heated wire was calculated numerically using a Fortran program from Schiesser and Silebi (1997) for computation of solutions to the Graetz problem. The problem is very similar to the Graetz problem, the only difference being the boundary conditions which here fix the temperature not only at the wall of the duct but also in the centre at the position of the heated wire. For these differences, the analytical solution used for calculations of temperature in the CPC condenser could not be utilized and therefore the numerical solution was used instead. The Fortran program was modified to account for the changed boundary conditions. Results from calculation of the temperature for the conditions in the duct at a temperature of 25°C, a wire temperature of 65°C, and assuming a uniformly heated wire of 60 mm length, are shown in figure 6.13. From the temperature the temperature gradient was calculated, which close to the wire was around 40 000 $K \cdot m^{-1}$. If one wants to calculate the pathlines of particles which experience the thermophoretic force flowing close to the heated wire, then the path would need to be integrated over local velocities. The velocity of a particle would need to be calculated integrating over the local acceleration due to thermophoretic and drag forces, depending on the local temperature gradient and on the local velocity respectively. The procedure can be simplified assuming that the thermophoretic velocity is reached immediately so that no acceleration needs to be considered. To get an indication on how fast the thermophoretic velocity is reached, the velocity can be divided by the acceleration resulting from the thermophoretic force. The resulting time is independent of the temperature gradient, as both velocity and force are linear with the temperature gradient. At a temperature of 25°C and particle density of 1 800 $kg \cdot m^{-3}$, the time is $1.3 \cdot 10^{-8}$ s for a 10 nm particle and $6.3 \cdot 10^{-6}$ s for an 1 µm particle. Comparing these times with

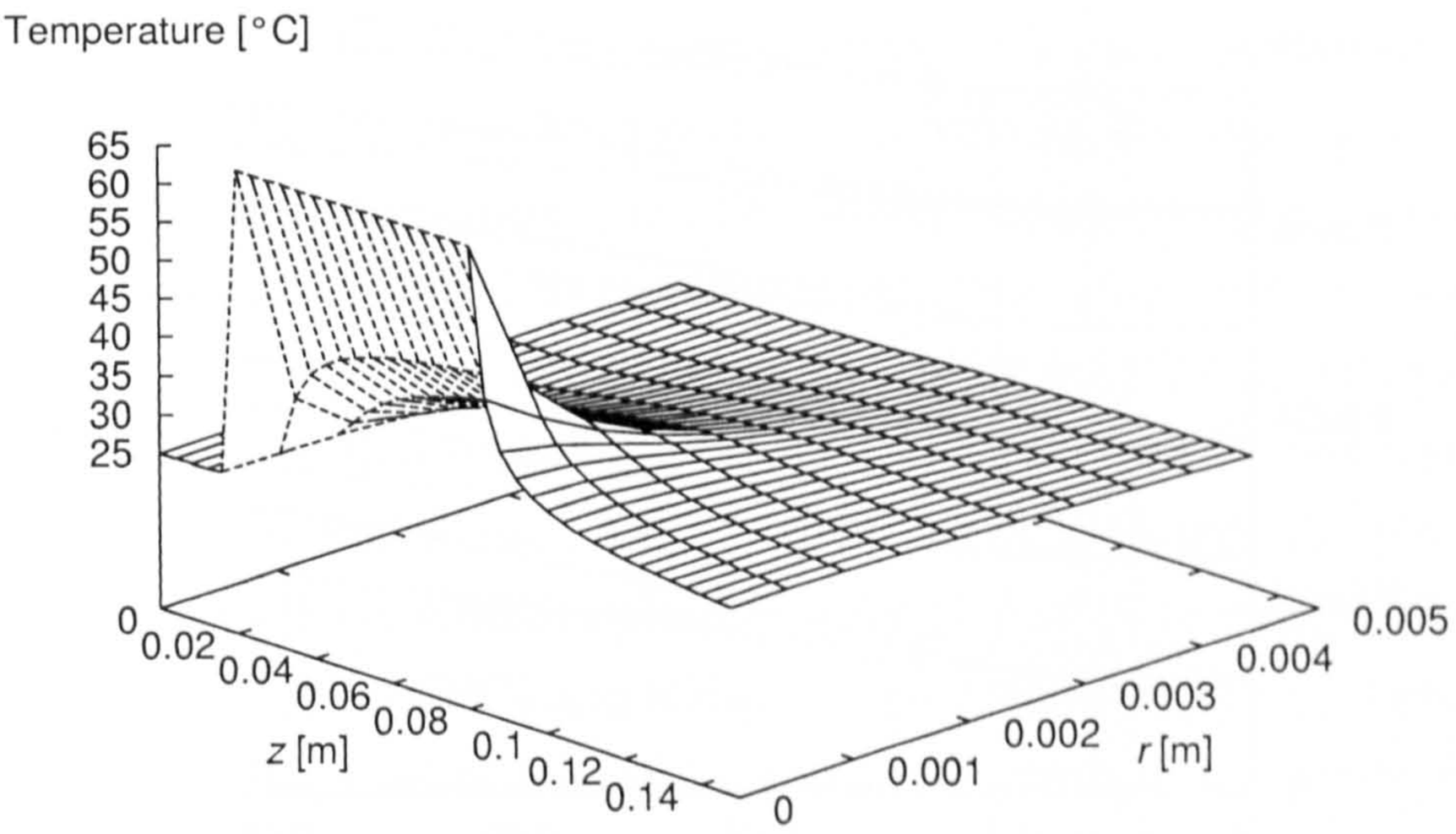

Figure 6.13: Calculated temperature profile in air flow over heated wire. Flow is along the z-axis in the centre of the duct; the wire is on the axis between $z = 20$ mm and $z = 80$ mm. The radial position from the z-axis is indicated by r.

the 0.18 s a particle in the centre of the duct needs to travel 60 mm, shows that the assumption is well justified. Therefore, the paths of particles can be calculated integrating directly the thermophoretic velocities. Figure 6.14 depicts the calculated pathlines for test particles with diameters of 10 nm and 1 µm respectively introduced at different radial distances from the centre line. The heated wire on the centre line of the duct and the wall of the capillary tube are indicated as thick lines in the graph.

The results of the calculations indicate that size dependence is not strong enough to separate particles of different sizes efficiently. The differences in particle concentration reduction observed for the different size fractions seem to be larger than what would be predicted from these calculations. There might, therefore, be a different effect causing the observed changes which has not yet been considered. Thermal expansion of the air passing by the heated wire can cause dilution of particle concentration. Maximum dilution is given in the case that all particles follow the expanding streamlines. The particle concentration is then diluted by the ratio of expansion, which follows from ideal gas law as ratio of temperatures at the capillary entry for the two cases of heated and unheated wire. The calculations for the heated

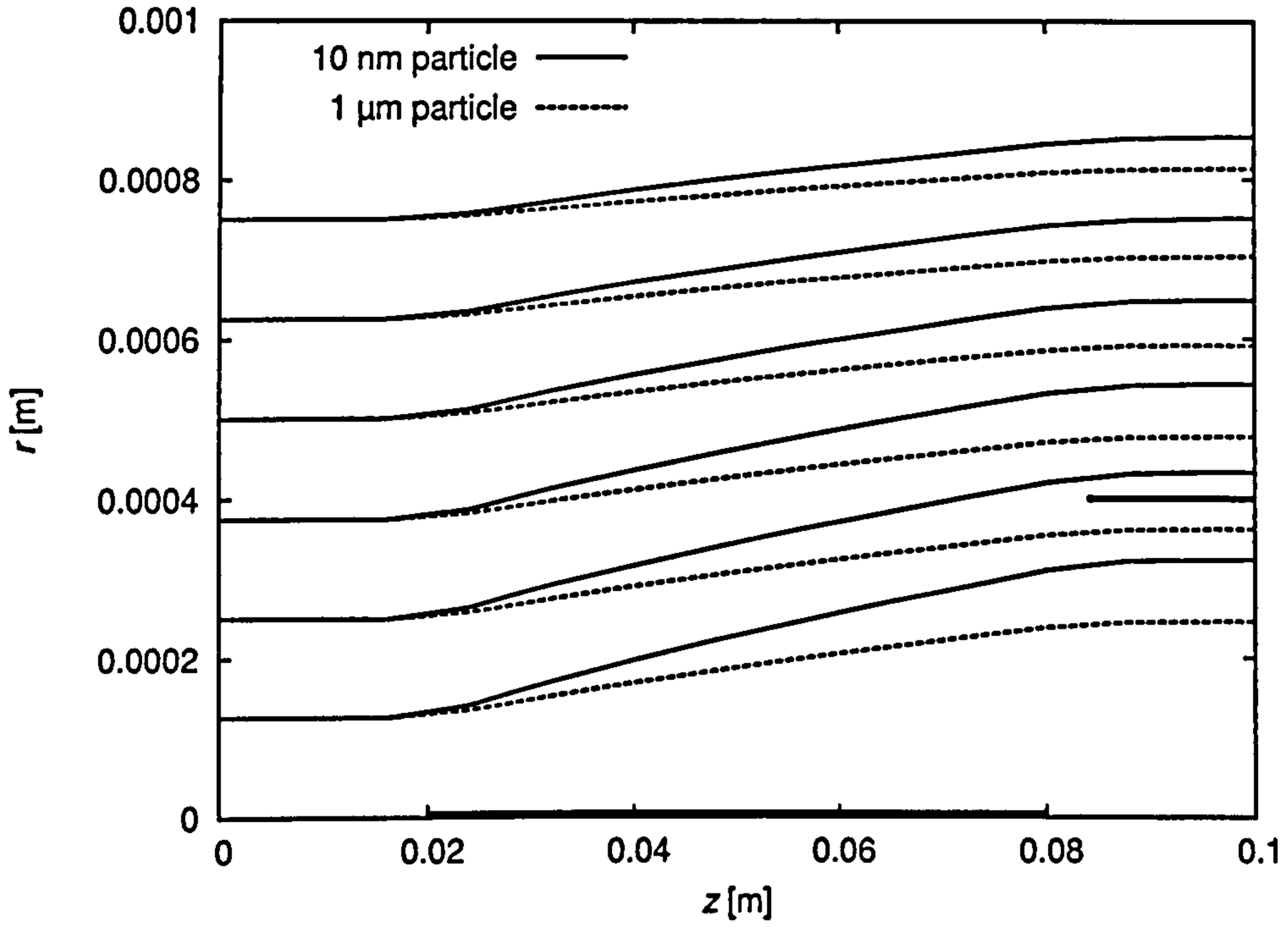

Figure 6.14: Calculated pathlines of particles drifting away from a heated wire due to thermophoresis. The heated wire on the centre line of the duct and the wall of the capillary tube are indicated as thick lines.

wire at 65°C in air at 25°C (298 K) predict a temperature at the capillary entry of 45°C (318 K, 4 mm after the heated wire). The ratio is, therefore, $^{298}/_{318} \approx 0.94$. Thus, thermal expansion plays a certain role, which, however, yields particle concentration reduction of less than 10% and cannot be responsible for the observations in the experiments, and hence is not the effect necessary to predict experimental results.

6.4 Discussion

Diffusion techniques tested showed good results, in accordance with theoretical predictions. These devices could readily be used with the instrument prototypes. Modifications could be implemented to sample alternately either directly or through a diffusion device, which would yield an additional size fraction in near real-time. As only two size fractions are "scanned", concentrations in the two fractions could be measured frequently at short time intervals; for example, sampling 10 s with the diffusion device, allowing 5 s for switching and flow stabilization, sampling 10 s without diffusion device, and again 5 s for switching, and then repeating this 30 s cycle. If the

additional size information is required in real time, then two CPCs would need to sample in parallel one with and one without the diffusion device.

The rectangular channels are better suited for size cuts higher than 30 nm. With micromachining or techniques such as etching, the channels could be produced in good reproducible quality. Alternatively two sets of rectangular channels could be built in one device, thereby obtaining two size cuts in one unit. The two sets could have a different number of channels or a different width, so that without the need for more space, or the risk of obstructing the flow in the duct, further size cuts could be introduced. Again, one would have the option of either switching between the size fractions or employing additional CPCs and sample in parallel. Figure 6.15 shows such a device including a set of four 100 mm long channels of 10 mm by 0.2 mm for a size cut at ~100 nm, a set of four 100 mm long channels of 2 mm by 0.2 mm for a size cut at ~40 nm, and a wider channel to carry sample air without significant diffusion losses for the lowest size cut at ~7 nm. The device could have one common inlet to three compartments housing the two sets of thin channels and the wider channel. The sample air to be delivered to the CPC would be taken from one of these three compartments by the use of microvalves placed just before the sample air is funnelled in the CPC capillary tube. The OPC capillary tube could be extended to sample from a similar position as the presented device for ultrafine fractionation.

Thermophoresis, although providing encouraging test results, could not be explained (yet) theoretically. Either thermophoresis is stronger than theoretically predicted, or there is another effect that was not considered. Further analysis and more experiments would be necessary to be able to explain the situation. However, even if the theory could explain better the test results, quantitative tests with monodisperse aerosol would be necessary to determine the size cut characteristics, which are believed to be relatively broad, as compared to the diffusion devices.

While it was shown that size fractionation would be possible with a diffusion device, time limitations prevented the further implementation and development of the diffusion-based size fractionation. Following the above idea of having two size cuts in one unit consisting of two sets of rectangular channels, such implementation could be realized as presented in figure 6.15.

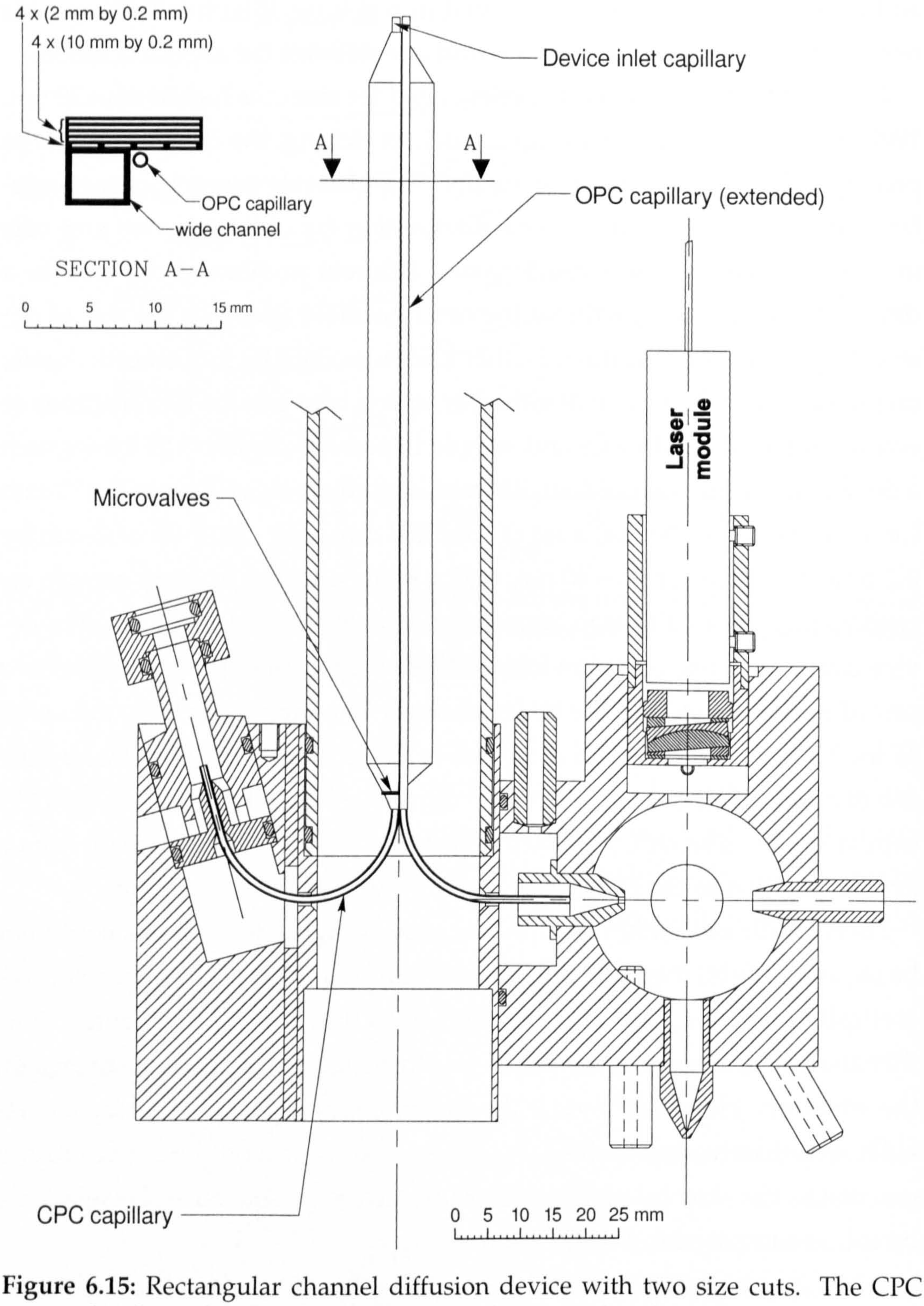

Figure 6.15: Rectangular channel diffusion device with two size cuts. The CPC samples through either of the two sets of rectangular channels for a size cut at ~100 nm (10 mm by 0.2 mm channels) or ~40 nm (2 mm by 0.2 mm channels) respectively or through a wider channel sampling without significant losses. The arrangement of the channels in three compartments is shown in a section view. Which compartment is sampling, and hence which size cut is in use, is controlled by using microvalves to close or open the compartments.

7 Conclusions and Future Possibilities

7.1 Conclusions

The aim of this project was to :
Develop an instrument for simultaneously measuring particle number concentration, size distribution, and mass concentration in ambient air.
This aim was achieved through the following objectives:

1. Identify technologies to be used and design a new instrument integrating these technologies.

2. Build prototype modules for testing single stages of the new instrument and compare their performance with results from theoretical modelling.

3. Build a complete prototype instrument.

4. Test the performance of the new instrument in the laboratory.

5. Compare the new instrument in field trials with current instrument standards.

To achieve the first objective, technologies of optical particle counting, condensation particle counting, and gravimetric mass measurement have been selected and were integrated in the design of the new instrument. The diffusion technique was identified for adding further ultrafine fractionation to the instrument and a possible implementation was outlined.

Early tests of the design were possible with prototypes built for the OPC and CPC parts of the instrument. The second objective was achieved through tests and theoretical modelling of these prototype modules which confirmed the design and performance characteristics and represented important steps towards a complete prototype instrument.

In fulfilling the third objective, two complete prototype instruments were then built. The identical prototype instruments were designed with all aspects of ambient monitoring in mind. Potential causes of sampling losses were carefully considered in order to avoid, or at least minimize such losses over the complete particle size range measured.

The prototype instruments were first tested in the laboratory to achieve the fourth objective. In particular, the OPC part was calibrated with monodisperse PSL spheres and the CPC part by comparison with a reference CPC instrument (TSI CPC model 3010) at the laboratories of netcen. The calibration tests confirmed the performance characteristics as in case of the tests performed earlier with the prototype modules of OPC and CPC. The extended tests carried out with the CPC part of the prototype instrument showed its proper operation confirming results from qualitative tests and theoretical modelling.

In accordance with the fifth objective, the instruments were then used in a four-months field study, collocated at the monitoring site Birmingham centre with a PM_{10} TEOM and a TSI CPC model 3022A. This provided an extended set of data to examine performance and capabilities of the instrument. Data analysis from this monitoring campaign showed the usefulness of the detailed and additional information provided by the instrument as compared to information from a TEOM only, often used for monitoring particulate matter. This data set was also used to test three number-to-mass conversion algorithms identifying two of the algorithms (using smoothing method and the geometric mean diameter) as suitable near real-time methods to provide mass concentration.

In conclusion, the aim of providing an instrument for simultaneously measuring particle number concentration, size distribution, and mass concentration in ambient air has been achieved. A valuable new instrument has been provided. Overall, the reliable performance was shown. The main performance specifications are:

Sample flow rates	$5\ l \cdot min^{-1}$ main sample (and for gravimetric) $10\ ml \cdot min^{-1}$ OPC sample $10\ ml \cdot min^{-1}$ CPC sample
Size range	Lower limit: ≤ 10 nm ($\eta_T = 0.5$) Upper limit: PM_{10} or $PM_{2.5}$ size cut

Size fractions	10 nm to 360 nm 360 nm to 500 nm 500 nm to 1.0 µm 1.0 µm to 2.5 µm 2.5 µm to 10 µm
Number concentration	100 000 cm^{-3} coinc. error < 10% (under-read. f. > 0.9) 500 000 cm^{-3} using coinc. corr. 0.1 cm^{-3} stat. count. error 13%
CPC parameters	Working fluid: iso-propanol Saturator temp.: 35°C Condenser temp.: 15°C

Possible improvements have been identified and, in many cases, already implemented. The next section will outline future possibilities for this instrument.

7.2 Future Possibilities

Ultrafine Fractionation A future version of the instrument may include a further ultrafine size fractionation technique using the diffusion technique discussed in chapter 6. The number-to-mass conversion algorithm using the geometric mean diameter (see section 5.4.2) can be implemented in the firmware of the instrument to give mass concentration in near real time. The algorithm would benefit from the further ultrafine size fraction, as well as it would from a further coarse size fraction of the OPC. In this case, the two successful algorithms, the geometric mean and the smoothing methods, can be compared again to identify the most suitable algorithm and studying the dependency of the quality of the conversion from other factors such as site specific aerosol properties.

Coincidence Correction The correction of coincidence errors could be implemented in the instrument since tests (see section 5.2) have shown that it would extend the upper concentration limit to 500 000 cm^{-3}. As proposed, the correction method could also be tested by comparing with a reference instrument to determine the under-reading factor at several number concentrations.

OPC Improvements In side-by-side comparisons of the two prototype instruments the CPC parts proved to be very reliably matched and to be stable over time, while the OPCs were sensitive to small differences in thresholds. The OPCs needed re-alignment and recalibration due to involuntary misalignment on several occasions. Changes should, therefore, be made to the mechanical design of the OPC and to the laser alignment procedure to improve the reliability of OPC calibration and its sizing capabilities. Ideally an easy way of detecting a possible problem and fixing it by recalibration that can be performed also in the field would enhance the instrument.

To enhance the accuracy of number concentration measurements in the coarse size range, the flow rate of the sample delivered to the OPC could be increased, and hence the statistical counting error reduced. Since the OPC number concentrations are typically less than 1 000 cm^{-3}, this would not cause considerable losses due to coincidence errors. Design changes, such as the choice of the sampling capillary tube, would need to be considered to ensure isokinetic sub-sampling.

Future Field Trials Further extended field studies with the instrument would demonstrate its performance under different conditions. Experiences gained during such trials will be very useful and help with the suggested improvements. More side-by-side comparisons with instrument standards will provide valuable data sets for further evaluation of the instrument. The instrument's results in such monitoring campaigns would also enrich possibilities of the campaign to study detailed aspects of air pollution, in accordance with its original aim. The instrument could, for example, be used in epidemiological studies where the simultaneous monitoring of number and mass of ambient particles would aid the understanding of the relations between particle exposure and effects on human health.

Another important possibility would be to demonstrate the equivalence of the gravimetric mass measurement of the new instrument with the gravimetric reference method as defined by EN12341 (1998). It would be valuable to study the number concentration, size distribution, and number-to-mass conversion in a field test together with a well defined comparison of gravimetric mass measurements. Such a comparison would be a further demonstration of the instrument's performance.

References

K.-H. Ahn and B. Y. H. Liu [1990]. Particle activation and droplet growth processes in condensation nucleus counter—I. Theoretical background. *Journal of Aerosol Science*, **21**(2), pp. 249–261.

APEG [1999]. *Source Apportionment of Airborne Particulate Matter in the United Kingdom*. Report of the Airborne Particles Expert Group, London: Department of the Environment, Transport and the Regions.

H. D. Baehr and K. Stephan [1998]. *Heat and mass transfer*. Springer, Berlin; New York.

P. A. Baron [1994]. Direct-reading instruments for aerosols, a review. *Analyst*, **119**, pp. 35–40.

P. A. Baron, M. K. Mazumder, and Y.-S. Cheng [2001]. Direct-reading techniques using particle motion and optical detection. In: K. Willeke and P. A. Baron, editors, *Aerosol Measurement: Principles, Techniques, and Applications*, pp. 495–535. John Wiley and Sons, New York, 2nd edition.

P. A. Baron and K. Willeke [2001]. Gas and particle motion. In: K. Willeke and P. A. Baron, editors, *Aerosol Measurement: Principles, Techniques, and Applications*, pp. 61–82. John Wiley and Sons, New York, 2nd edition.

W. Birmili, A. Wiedensohler, J. Heintzenberg, and K. Lehmann [2001]. Atmospheric particle number size distribution in central Europe: Statistical relations to air masses and meteorology. *Journal of Geophysical Research-Atmospheres*, **106**(D23), pp. 32 005–32 018.

P. Biswas, C. L. Jones, and R. C. Flagan [1987]. Distortion of size distributions by condensation and evaporation in aerosol instruments. *Aerosol Science and Technology*, **7**(2), pp. 231–246.

C. F. Bohren and D. R. Huffman [1983]. *Absorption and Scattering of Light by Small Particles*. Wiley-Interscience, New York.

D. R. Booker, W. D. Griffiths, C. P. Lyons, D. Mark, S. L. Upton, and A. L. N. C. ordinating editor) [1998]. *Aerosol Sampling Guidelines*. The Royal Society of Chemistry (for AEA Technology), London.

C. A. Brock, F. Schröder, B. Karcher, A. Petzold, R. Busen, and M. Fiebig [2000]. Ultrafine particle size distributions measured in aircraft exhaust plumes. *Journal of Geophysical Research-Atmospheres*, **105**(D21), pp. 26 555–26 567.

J. E. Brockmann [2001]. Sampling and Transport of Aerosols. In: K. Willeke and P. A. Baron, editors, *Aerosol Measurement: Principles, Techniques, and Applications*, pp. 143–195. John Wiley and Sons, New York, 2nd edition.

G. M. Brown [1960]. Heat or mass transfer in a fluid in laminar flow in a circular duct or flat conduit. *Amer. Inst. Chem. Eng. J.*, 6(2), pp. 179–183.

K. E. Brown, J. Beyer, and J. W. Gentry [1984]. Calibration and design of diffusion batteries for ultrafine aerosols. *Journal of Aerosol Science*, **15**(2), pp. 133–145.

S. Budavari, editor [1996]. *Merck Index*. Merck & Co, Whitehouse Station, 12th edition.

Y.-S. Cheng [2001]. Condensation detection and diffusion size separation techniques. In: K. Willeke and P. A. Baron, editors, *Aerosol Measurement: Principles, Techniques, and Applications*, pp. 569–601. John Wiley and Sons, New York, 2nd edition.

Y. S. Cheng, J. A. Keating, and G. M. Kanapilly [1980]. Theory and calibration of a screen-type diffusion battery. *Journal of Aerosol Science*, **11**(5–6), pp. 549–556.

Y. S. Cheng and H. C. Yeh [1980]. Theory of screen-type diffusion battery. *Journal of Aerosol Science*, **11**(3), pp. 313–320.

Y. S. Cheng, H. C. Yeh, and K. J. Brinsko [1985]. Use of wire screens as a fan model filter. *Aerosol Science and Technology*, 4(2), pp. 165–174.

M. Dennekamp, S. Howarth, C. A. J. Dick, J. W. Cherrie, K. Donaldson, and A. Seaton [2001]. Ultrafine particles and nitrogen oxides generated by gas and electric cooking. *Occupational and Environmental Medicine*, **58**(8), pp. 511–516.

D. W. Dockery, C. A. Pope III, X. Xu, J. D. Spengler, J. H. Ware, M. E. Fay, B. G. Ferris, and F. E. Speizer [1993]. An association between air pollution and mortality in six U.S. cities. *New England Journal of Medicine*, **329**(24), pp. 1753–1759.

K. Donaldson, X. Y. Li, and W. MacNee [1998]. Ultrafine (nanometre) particle mediated lung injury. *Journal of Aerosol Science*, **29**(5/6), pp. 553–560.

EN12341 [1998]. *Air quality—Determination of the PM10 fraction of suspended particular matter—Reference method and field test procedure to demonstrate reference equivalence of measurement methods*. European Standard, European Committee for Standardization (CEN).

EPAQS [2001]. *Airborne Particles: What is the appropriate measurement on which to base a standard?* Expert Panel on Air Quality Standards, London: Department for Environment, Food & Rural Affairs.

J. Fernández de la Mora [1996]. Drastic improvement of the resolution of aerosol size spectrometers via aerodynamic focusing: The case of variable-pressure impactors. *Chemical Engineering Communications*, **151**, pp. 101–124.

J. Fernández de la Mora, S. V. Hering, N. Rao, and P. H. McMurry [1990]. Hypersonic impaction of ultrafine particles. *Journal of Aerosol Science*, **21**(2), pp. 169–187.

B. Figler, W. Sahle, S. Krantz, and U. Ulfvarson [1996]. Diesel exhaust quantification by scanning electron microscope with special emphasis on particulate size distribution. *The Science of the Total Environment*, **193**(23), pp. 77–83.

R. C. Flagan [1998]. History of electrical aerosol measurements. *Aerosol Science and Technology*, **28**(4), pp. 301–380.

J. Gebhart [2001]. Optical Direct-Reading Techniques: Light Intensity Systems. In: K. Willeke and P. A. Baron, editors, *Aerosol Measurement: Principles, Techniques, and Applications*, pp. 419–454. John Wiley and Sons, New York, 2nd edition.

J. Gebhart, P. Blankenberg, and C. Roth [1984]. Counting efficiency and sizing characteristics of optical-particle counters. *Journal of Aerosol Science*, **15**(3), pp. 279–281.

F. J. Gomez-Moreno and J. Fernández de la Mora [1996]. Continuous aerosol size spectrometry with a variable-orifice impactor. *Journal of Aerosol Science*, **27**(8), pp. 1243–1256.

P. G. Gormley and M. Kennedy [1949]. Diffusion from a stream flowing through a cylindrical tube. *Proceedings of the Royal Irish Academy*, **A52**, pp. 163–169.

J. G. Graeme [1995]. *Photodiode amplifiers: op amp solutions*. McGraw-Hill, New York.

L. Graetz [1883]. Über die Wärmeleitungsfähigkeit von Flüssigkeiten. *Annalen der Physik (3. Folge)*, **18**, pp. 79–94.

D. Green, G. Fuller, and B. Barratt [2001]. Evaluation of TEOM^{TM} "correction factors" for assessing the EU Stage 1 limit values for PM10. *Atmospheric Environment*, **35**(14), pp. 2589–2593.

A. J. Greig [2000]. Monitoring airborne particles as mass and number concentrations: Implications for air quality management and health. *International Journal of Environmental Studies*, **57**(6), pp. 641–662.

J. L. Hand and S. M. Kreidenweis [2002]. A new method for retrieving particle refractive index and effective density from aerosol size distribution data. *Aerosol Science and Technology*, **36**(10), pp. 1012–1026.

J. L. Hand, S. M. Kreidenweis, N. Kreisberg, S. Hering, M. Stolzenburg, W. Dick, and P. H. McMurry [2002]. Comparisons of aerosol properties measured by impactors and light scattering from individual particles: refractive index, number and volume concentrations, and size distributions. *Atmospheric Environment*, **36**(11), pp. 1853–1861.

R. M. Harrison, M. Jones, and G. Collins [1999a]. Measurements of the physical properties of particles in the urban atmosphere. *Atmospheric Environment*, **33**, pp. 309–321.

R. M. Harrison, J. P. Shi, and M. R. Jones [1999b]. Continuous measurements of aerosol physical properties in the urban atmosphere. *Atmospheric Environment*, **33**, pp. 1037–1047.

R. M. Harrison, J. P. Shi, S. H. Xi, A. Khan, D. Mark, R. Kinnersley, and J. X. Yin [2000]. Measurement of number, mass and size distribution of particles in the atmosphere. *Philosophical Transactions of the Royal Society of London Series a-Mathematical Physical and Engineering Sciences*, **358**(1775), pp. 2567–2579.

R. M. Harrison and J. Yin [2000]. Particulate matter in the atmosphere: which particle properties are important for its effects on health? *The Science of the Total Environment*, **249**(1–3), pp. 85–101.

J. Heintzenberg [1994]. Properties of the log-normal particle-size distribution. *Aerosol Science and Technology*, **21**(1), pp. 46–48.

S. V. Hering and P. H. McMurry [1991]. Optical counter response to monodisperse atmospheric aerosols. *Atmospheric Environment*, **25**(2), pp. 463–468.

W. C. Hinds [1999]. *Aerosol Technology: Properties, behavior, and measurement of airborne particles*. John Wiley & Sons, New York, second edition.

S. Hochrainer [2000]. Further developments of the particle counter sizer PCS-2000. *Journal of Aerosol Science*, **31**(Suppl. 1), pp. S771–S772.

H. Horvath, R. L. Gunter, and S. W. Wilkison [1990]. Determination of the coarse mode of the atmospheric aerosol using data from a forward-scattering spectrometer probe. *Aerosol Science and Technology*, **12**(4), pp. 964–980.

L. S. Hughes [1999]. Size and composition distribution of atmospheric particles in southern California. *Environmental Science and Technology*, **33**(20), pp. 3506–3515.

A. Ibald-Mulli, H. E. Wichmann, W. Kreyling, and A. Peters [2002]. Epidemiological evidence on health effects of ultrafine particles. *Journal of Aerosol Medicine-Deposition Clearance and Effects in the Lung*, **15**(2), pp. 189–201.

D. B. Ingham [1976]. Simultaneous diffusion and sedimentaion of aerosol particles in rectangular tubes. *Journal of Aerosol Science*, **7**, pp. 373–380.

L. C. Kenny and R. A. Gussman [2000]. A direct approach to the design of cyclones. *Journal of Aerosol Science*, **31**(12), pp. 1407–1420.

R. G. Knollenberg [1985]. The measurement of particle sizes below 0.1 micrometers. *Journal of Environmental Sciences*, **28**(1), pp. 32–47.

P. A. Lawless [2001]. High-resolution reconstruction method for presenting and manipulating particle histogram data. *Aerosol Science and Technology*, **34**(6), pp. 528–534.

M. Lehtimäki and K. Willeke [1993]. Measurement methods. In: K. Willeke and P. A. Baron, editors, *Aerosol Measurement: Principles, Techniques, and Applications*, pp. 112–129. Van Norstrand Reinhold, New York.

C. S. Li, W. H. Lin, and F. T. Jenq [1993]. Size distributions of submicrometer aerosols from cooking. *Environment International*, **19**(2), pp. 147–154.

D. R. Lide, editor [2002]. *Handbook of Chemistry and Physics*. CRC Press, Boca Raton, 83rd edition.

P. Liu, P. J. Ziemann, D. B. Kittelson, and P. H. McMurry [1995]. Generating particle beams of controlled dimensions and divergence. 1. Theory of particle motion in aerodynamic lenses and nozzle expansions. *Aerosol Science and Technology*, **22**(3), pp. 293–313.

Y. Liu and P. H. Daum [2000]. The effect of refractive index on size distributions and light scattering coefficients derived from optical particle counters. *Journal of Aerosol Science*, **31**(8), pp. 945–957.

I. D. Longley, M. W. Gallagher, J. R. Dorsey, M. Flynn, J. D. Allan, M. R. Alfarra, and D. Inglis [2003]. A case study of aerosol (4.6 nm $< D_p <$ 10 µm) number and mass size distribution measurements in a busy street

canyon in Manchester, UK. *Atmospheric Environment*, **37**(12), pp. 1563–1571.

M. Marjamäki, J. Keskinen, D.-R. Chen, and D. Y. H. Pui [2000]. Performance evaluation of the electrical low-pressure impactor (ELPI). *Journal of Aerosol Science*, **31**(2), pp. 249–261.

V. A. Marple, B. A. Olson, and K. L. Rubow [2001]. Inertial, Gravitational, Centrifugal, and Thermal Collection Techniques. In: K. Willeke and P. A. Baron, editors, *Aerosol Measurement: Principles, Techniques, and Applications*, pp. 229–260. John Wiley and Sons, New York, 2nd edition.

P. H. McMurry [2000]. A review of atmospheric aerosol measurements. *Atmospheric Environment*, **34**(12–14), pp. 1959–1999.

P. H. McMurry, X. Wang, K. Park, and K. Ehara [2002]. The relationship between mass and mobility for atmospheric particles: A new technique for measuring particle density. *Aerosol Science and Technology*, **36**(2), pp. 227–238.

G. Mie [1908]. Beiträge zur Optik trüber Medien, speziell kolloidaler Metallösungen. *Annalen der Physik (4. Folge)*, **25**(3), pp. 377–445.

M. D. Mikhailov and R. M. Cotta [1997]. Eigenvalues for the graetz problem in slip-flow. *International Communications in Heat and Mass Transfer*, **24**(3), pp. 449–451.

L. Morawska, G. Johnson, Z. D. Ristovski, and V. Agranovski [1999a]. Relation between particle mass and number for submicrometer airborne particles. *Atmospheric Environment*, **33**(13), pp. 1983–1990.

L. Morawska, S. Thomas, M. Jamriska, and G. Johnson [1999b]. The modality of particle size distributions of environmental aerosols. *Atmospheric Environment*, **33**(27), pp. 4401–4411.

G. Oberdörster, J. Ferin, and B. E. Lehnert [1994]. Correlation between particle-size, in-vivo particle persistence, and lung injury. *Environmental Health Perspectives*, **102**(Suppl. 5), pp. 173–179.

G. Oberdörster, R. M. Gelein, J. Ferin, and B. Weiss [1995]. Association of particulate air pollution and acute mortality: Involvement of ultrafine particles? *Inhalation Toxicology*, 7(1), pp. 111–124.

T. Osunsanya, G. Prescott, and A. Seaton [1999]. Acute health effects of ultrafine particles. *Thorax*, 54(Suppl. 3), p. P33.

T. Osunsanya, G. Prescott, and A. Seaton [2001]. Acute respiratory effects of particles: Mass or number? *Occupational and Environmental Medicine*, 58(3), pp. 154–159.

J. Pekkanen, K. L. Timonen, J. Ruuskanen, A. Reponen, and A. Mirme [1997]. Effects of ultrafine and fine particles in urban air on peak expiratory flow among children with asthmatic symptoms. *Environmental Research*, 74(1), pp. 24–33.

P. Penttinen, K. L. Timonen, P. Tiittanen, A. Mirme, J. Ruuskanen, and J. Pekkanen [2001]. Ultrafine particles in urban air and respiratory health among adult asthmatics. *The European Respiratory Journal*, 17(3), pp. 428–435.

A. Peters, H. E. Wichmann, T. Tuch, J. Heinrich, and J. Heyder [1997]. Respiratory effects are associated with the number of ultrafine particles. *American Journal of Respiratory and Critical Care Medicine*, 155(4), pp. 1376–1383.

T. M. Peters, M. Chein, H, D. A. Lundgren, and P. B. Keady [1993]. Comparison and combination of aerosol-size distributions measured with a low-pressure impactor, differential mobility particle sizer, electrical aerosol analyzer, and aerodynamic particle sizer. *Aerosol Science and Technology*, 19(3), pp. 396–405.

J. F. Pisani and G. H. Thomson [1971]. Coincidence errors in automatic particle counters. *Journal of physics E: scientific instruments*, 4(5), pp. 359–361.

C. A. Pope III, M. J. Thun, M. M. Namboodiri, D. W. Dockery, J. S. Evans, F. E. Speizer, and C. W. Heath [1995]. Particulate air-pollution as a predictor of mortality in a prospective-study of US adults. *American Journal of Respiratory and Critical Care Medicine*, 151(3), pp. 669–674.

D. J. Rader and T. J. O'Hern [2001]. Optical direct-reading techniques: In situ sensing. In: K. Willeke and P. A. Baron, editors, *Aerosol Measurement: Principles, Techniques, and Applications*, pp. 455–494. John Wiley and Sons, New York, 2nd edition.

M. T. Saros, R. J. Weber, J. J. Marti, and P. H. McMurry [1996]. Ultrafine aerosol measurement using a condensation nucleus counter with pulse height analysis. *Aerosol Science and Technology*, **25**(2), pp. 200–213.

W. E. Schiesser and W. A. Silebi [1997]. *Computational transport phenomena: numerical methods for the solution of transport problems*. Cambridge University Press, Cambridge.

J. Schwartz and A. Marcus [1990]. Mortality and air pollution in London: a time series analysis. *American Journal of Epidemiology*, **131**(1), pp. 185–194.

A. Seaton, W. MacNee, K. Donaldson, and D. Godden [1995]. Particulate air pollution and acute health effects. *Lancet*, **345**(8943), pp. 176–178.

A. Seaton, A. Soutar, V. Crawford, R. Elton, S. McNerlan, J. Cherrie, M. Watt, R. Agius, and R. Stout [1999]. Particulate air pollution and the blood. *Thorax*, **54**(11), pp. 1027–1032.

G. J. Sem [2002]. Design and performance characteristics of three continuous-flow condensation particle counters: a summary. *Atmospheric Research*, **62**(3–4), pp. 267–294.

J. P. Shi, A. A. Khan, and R. M. Harrison [1999]. Measurements of ultrafine particle concentration and size distribution in the urban atmosphere. *The Science of the Total Environment*, **235**, pp. 51–64.

C. Stein, F. Schröder, and A. Petzold [2001]. The condensation particle size analyzer: a new instrument for the measurement of ultrafine aerosol size distributions. *Journal of Aerosol Science*, **32**(Suppl. 1), pp. S381–S382.

M. Stolzenburg, N. Kreisberg, and S. Hering [1998]. Atmospheric size distributions measured by differential mobility optical particle size spectrometry. *Aerosol Science and Technology*, **29**(5), pp. 402–418.

M. R. Stolzenburg and P. H. McMurry [1991]. An ultrafine aerosol condensation nucleus counter. *Aerosol Science and Technology*, **14**(1), pp. 48–65.

L. Talbot, R. K. Cheng, R. W. Schefer, and D. R. Willis [1980]. Thermophoresis of particles in a heated boundary-layer. *Journal of Fluid Mechanics*, **101**(4), pp. 737–758.

H. Tammet, A. Mirme, and E. Tamm [2002]. Electrical aerosol spectrometer of Tartu University. *Atmospheric Research*, **62**(3–4), pp. 315–324.

C. W. Tan and J. W. Thomas [1972]. Aerosol penetration through a parallel-plate diffusion-battery. *Journal of Aerosol Science*, **3**, pp. 39–43.

T. Tuch, P. Brand, H. E. Wichmann, and J. Heyder [1997]. Variation of particle number and mass concentration in various size ranges of ambient aerosols in Eastern Germany. *Atmospheric Environment*, **31**(24), pp. 4193–4197.

T. Tuch, A. Mirme, E. Tamm, J. Heinrich, J. Heyder, P. Brand, C. Roth, H. E. Wichmann, J. Pekkanen, and W. G. Kreyling [2000]. Comparison of two particle-size spectrometers for ambient aerosol measurements. *Atmospheric Environment*, **34**, pp. 139–149.

H. Umhauer [1983]. Particle size distribution analysis by scattered light measurements using an optically defined measuring volume. *Journal of Aerosol Science*, **14**(6), pp. 765–770.

L. Waldmann and K. H. Schmitt [1966]. Thermophoresis and diffusiophoresis of aerosols. In: C. N. Davies, editor, *Aerosol Science*, pp. 137–162. Academic Press, London.

J. Wang, R. C. Flagan, and J. H. Seinfeld [2002]. Diffusional losses in particle sampling systems containing bends and elbows. *Journal of Aerosol Science*, **33**(6), pp. 843–857.

E. W. Washburn, editor [1928]. *International critical tables of numerical data, physics, chemistry and technology. Vol. 4.* McGraw-Hill, New York, London.

E. W. Washburn, editor [1929]. *International critical tables of numerical data, physics, chemistry and technology. Vol. 5.* McGraw-Hill, New York, London.

R. J. Weber, M. R. Stolzenburg, S. N. Pandis, and P. H. McMurry [1998]. Inversion of ultrafine condensation nucleus counter pulse height distri-

butions to obtain nanoparticle (3 to 10 nm) size distributions. *Journal of Aerosol Science*, **29**(5/6), pp. 601–615.

K. T. Whitby [1966]. Electric aerosol particle counting and size distribution measuring system for the 0.015 to 1 µm size range. *Tellus*, **13**, pp. 573–586.

K. T. Whitby [1972]. The aerosol size distribution of Los Angeles smog. *Journal of Colloid and Interface Science*, **39**(1), pp. 177–204.

K. T. Whitby [1978]. The physical characteristics of sulphur aerosols. *Atmospheric Environment*, **12**, pp. 135–159.

K. T. Whitby and G. M. Sverdrup [1980]. California aerosols: Their physical and chemical characteristics. In: G. Hidy, P. Mueller, D. Grosjean, B. Appel, and J. Wesolowski, editors, *The Character and Origins of Smog Aerosols: A Digest of Results from the California Aerosol Characterization Experiment (ACHEX)*. John Wiley & Sons, New York.

G. W. K. Wong, F. W. S. Ko, T. S. Lau, S. T. Li, D. Hui, S. W. Pang, R. Leung, T. F. Fok, and C. K. W. Lai [2001]. Temporal relationship between air pollution and hospital admissions for asthmatic children in Hong Kong. *Clinical and Experimental Allergy*, **31**(4), pp. 565–569.

F. Zheng [2002]. Thermophoresis of spherical and non-spherical particles: a review of theories and experiments. *Advances in Colloid and Interface Science*, **97**(1–3), pp. 255–278.

Bibliography

APEG [1999]. *Source Apportionment of Airborne Particulate Matter in the United Kingdom*. Report of the Airborne Particles Expert Group, London: Department of the Environment, Transport and the Regions.

H. D. Baehr and K. Stephan [1998]. *Heat and mass transfer*. Springer, Berlin; New York.

C. F. Bohren and D. R. Huffman [1983]. *Absorption and Scattering of Light by Small Particles*. Wiley-Interscience, New York.

D. R. Booker, W. D. Griffiths, C. P. Lyons, D. Mark, et al. [1998]. *Aerosol Sampling Guidelines*. The Royal Society of Chemistry (for AEA Technology), London.

J. E. Brockmann [1993]. Sampling and Transport of Aerosols. In: K. Willeke and P. A. Baron, editors, *Aerosol Measurement: Principles, Techniques, and Applications*, pp. 77–111. Van Norstrand Reinhold, New York.

EPAQS [2001]. *Airborne Particles: What is the appropriate measurement on which to base a standard?* Expert Panel on Air Quality Standards, London: Department for Environment, Food & Rural Affairs.

J. Gebhart [1993]. Optical Direct-Reading Techniques: Light Intensity Systems. In: K. Willeke and P. A. Baron, editors, *Aerosol Measurement: Principles, Techniques, and Applications*, pp. 313–344. Van Norstrand Reinhold, New York.

W. C. Hinds [1999]. *Aerosol Technology: Properties, behavior, and measurement of airborne particles*. John Wiley & Sons, New York, second edition.

M. Lehtimäki and K. Willeke [1993]. Measurement methods. In: K. Willeke and P. A. Baron, editors, *Aerosol Measurement: Principles, Techniques, and Applications*, pp. 112–129. Van Norstrand Reinhold, New York.

R. Xu [2000]. *Particle Characterization: Light Scattering Methods*. Kluwer Academic Publishers, Dordrecht.

Index

Appendix

A Design Details

A.1 Dimensions and Parameters

OPC flow system:	
Inlet nozzle diameter	1.0 mm
Inlet nozzle (before restriction)	5.0 mm
Capillary tube ID	0.76 mm
Capillary tube OD	1.59 mm
Sample flow rate	10 $ml \cdot min^{-1}$
Sheath-air flow rate	320 $ml \cdot min^{-1}$
Bleed-air flow rate	480 $ml \cdot min^{-1}$
Pump flow rate	0.8 $l \cdot min^{-1}$
Bleed air nozzle diameter	1.2 mm
Extractor tube diameter	3.0 mm
Clean-air filter	Whatman®: Polycap™ TF(75) PTFE membrane Pore size: 0.2 µm

Table A.1: Dimensions and operating parameters of OPC flow system (as used during calibration). The capillary tube is tapered (on the outside) to avoid locally turbulent flow when sample and sheath air come together. ID denotes the inner diameter and OD the outer diameter of the capillary tube.

OPC optical system:	
Focal length of cylindrical lens	25.00 mm
Back focal length	23.09 mm
Radius of spherical mirror surface	20.0 mm
Diameter of mirror	25.0 mm
Half angle of mirror	52.4°
Distance mirror–sensing volume	9.6 mm
Distance mirror–detector	27.7 mm

Table A.2: Parameters of OPC optical system.

OPC detector:	
Detector area (BPX65)	1.0 mm^2
Detector area (OSD5-5T)	5.0 mm^2
Operational amplifier	OPA655P
Feedback resistor R_F	9.4 MΩ
C_1, C_2	1.0 pF
C_3	3 to 40 pF

Table A.3: Components and parameters of OPC detector. The photodiode OSD5-5T (Centronic) was used in calibration.

OPC light source:	
Laser module	LOC-2000 (LasIRvis)
Laser diode	Hitachi, 35 mW
Laser power (in coll. beam)	25 mW
Laser wavelength	650 nm
Focal length of collimating lens	4 mm

Table A.4: Components and parameter of OPC light source.

CPC flow system:	
Capillary tube ID	0.8 mm
Capillary tube OD	1.2 mm
Sample flow rate	10 $ml \cdot min^{-1}$
Saturator volume	77 cm^3
Flow rate through condenser	400 $ml \cdot min^{-1}$
Condenser diameter	5 mm
Condenser length	64 mm
OPC focusing nozzle diameter	1 mm

Table A.5: Dimensions and operating parameters of CPC flow system (as designed for first CPC prototype). ID denotes the inner diameter and OD the outer diameter of the capillary tube.

A.2 Circuit Diagrams

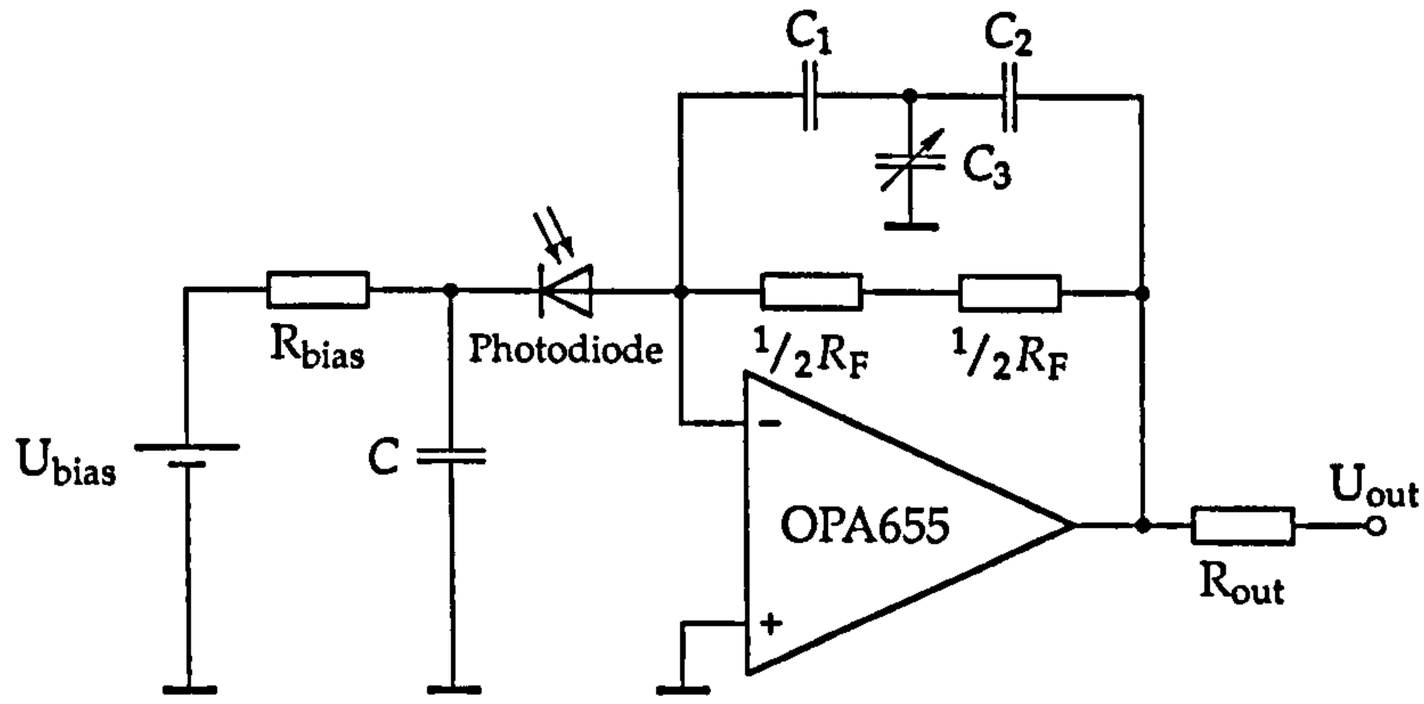

Figure A.1: Transimpedance amplifier circuit of first OPC prototype. Two feedback resistors in series, rather than one, are used to decrease the intrinsic capacitance of the feedback. R_F is 9.4 MΩ, the sum of the two 4.7 MΩ resistors. Adjusting C_3 the effective capacitance $C_{eff} = \frac{C_1 C_2}{C_1+C_2+C_3}$ of the network formed by C_1, C_2, and C_3 can be changed. C_1 and C_2 were 1 pF, C_3 was adjustable 3 to 40 pF; so C_{eff} could be changed in the range 0.03 to 0.20 pF. It was adjusted in order to allow the shortest rise time working under stable conditions (no oscillation as response to a step change at the input). The value of the effective capacitor so adjusted was close to its maximum of 0.20 pF.

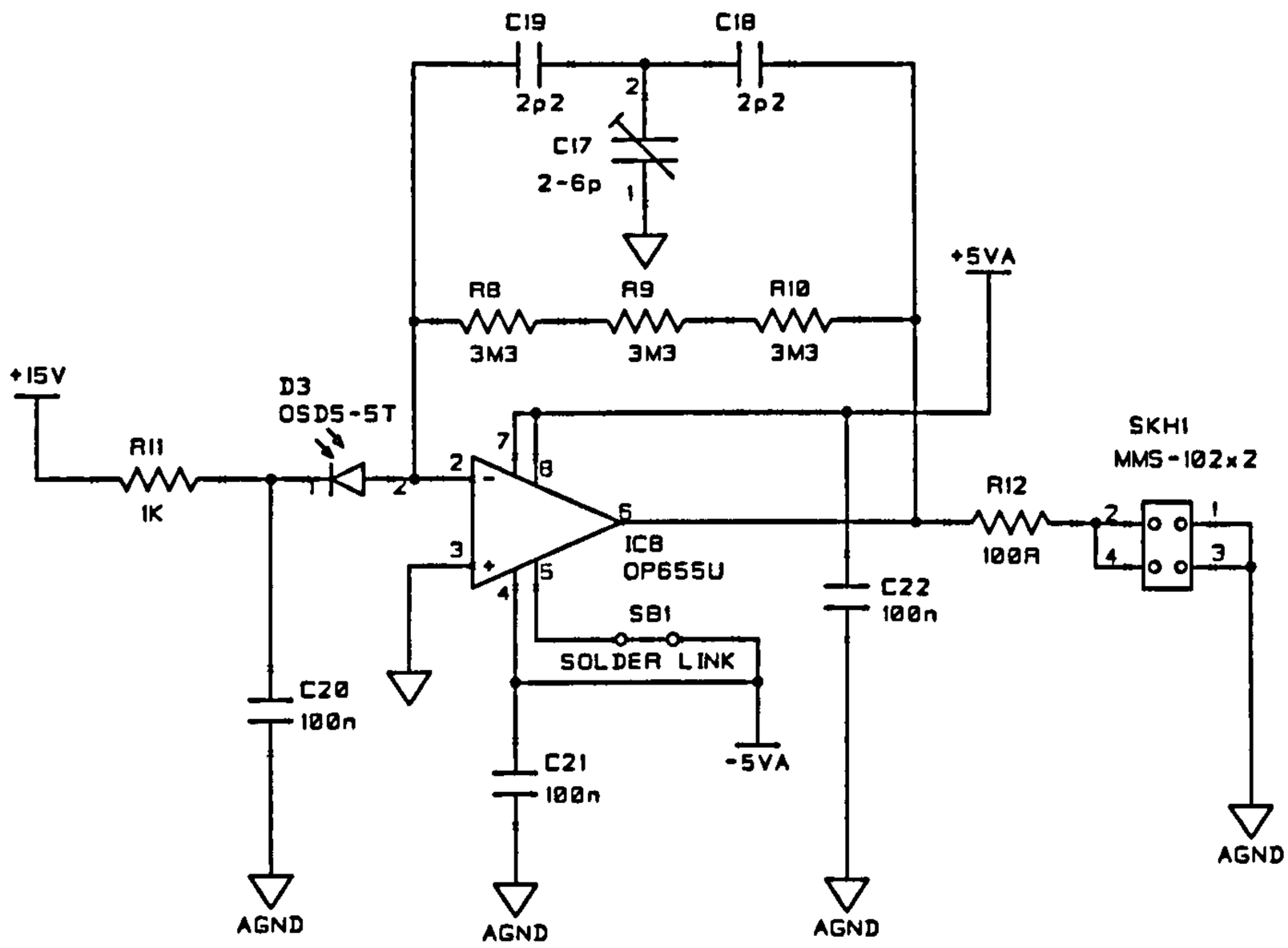

Figure A.2: Transimpedance amplifier circuit as designed to be used with the OPCs of the prototype instrument. Three feedback resistors in series are used to decrease the intrinsic capacitor of the feedback. R_F is 9.9 MΩ, the sum of the three 3.3 MΩ resistors.

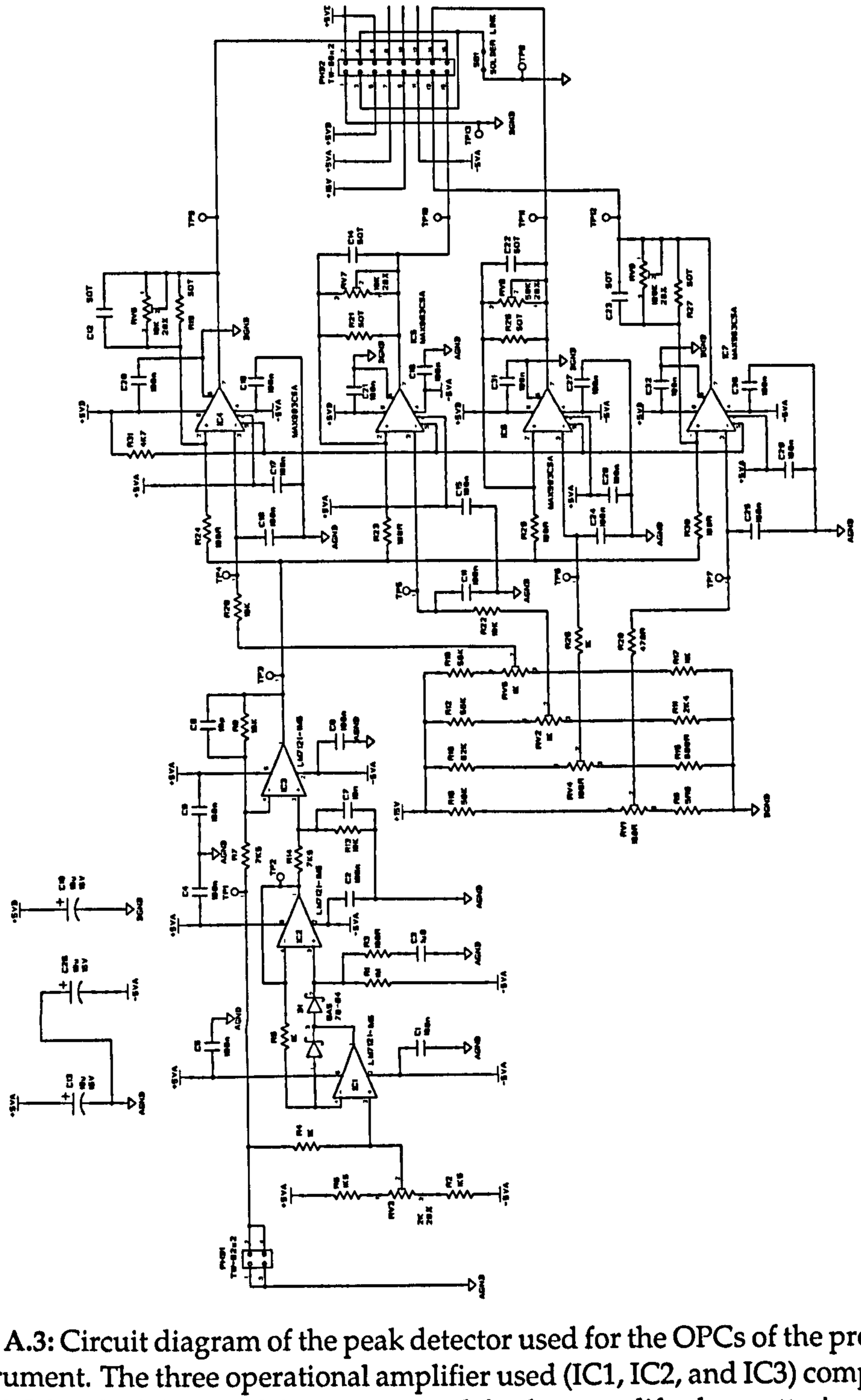

Figure A.3: Circuit diagram of the peak detector used for the OPCs of the prototype instrument. The three operational amplifier used (IC1, IC2, and IC3) compensate the DC level of the amplifier output and further amplify the scattering signal. The four comparators (IC4 to IC7) implement the thresholds whose levels are set by the four variable resistors (RV1, RV2, RV4, RV5). The circuit includes hysteresis for the threshold levels implemented with four variable feedback resistors (RV6 to RV9) for the four comparators. The output signals of the comparators are used to trigger counters (not shown on this circuit diagram). In case the OPC is used with the CPC (as OPC2) only one threshold level is used to detect the CPC droplets without sizing.

B OPC Alignment

B.1 Alignment of First OPC Prototype

The following describes the procedure followed to align the optical system of the first OPC design as described in sections 4.2.1 and 4.2.2.

The laser module was turned so that the longer axis of its elliptical beam shape would be focused by the cylindrical lens and its shorter axis, which was approximately 1.5 mm, would remain unchanged and define the width of the laser beam at the sensing volume. For the adjustments smoke was introduced in the sample air. The mirror in its holder was assembled, while the photodiode was removed. In the first alignment step a glass plate was fixed over the hole for the photodiode holder (sealed with silicone grease). For the further steps the photodiode holder (without the photodiode) was mounted to the chamber and a focusing screen covered the hole for the photodiode (sealed with silicone grease). On this focusing screen the image of the sensing volume (the scattered light from smoke in the sensing volume, collected and reflected by the mirror) can be observed, which is helpful in the alignment process.

The following procedure was used to align the system:

1. First the axis of the laser beam is adjusted so that the laser illuminates the sample air beam symmetrically, i. e. the sample air beam is in the centre of the laser beam. Then the laser beam is moved up and down along sample air column until it illuminates the sample air at the height of the mirror–detector axis. At this point the sensing volume is already defined by the intersection of laser beam and sample air column. The following alignment steps are performed with mirror and detector photodiode, in order to align mirror–detector axis with the sensing volume and to adjust their distances to the sensing volume.

2. The mirror adjustment flange is moved slightly in the two directions

perpendicular to the mirror–detector axis before it is fixed to the body with two screws. This allows minor corrections to the mirror–detector axis so that it is aligned with the sensing volume. This is confirmed by when the light spot (image of sensing volume) will be centred on the focusing screen. If the previous step was performed accurately then only movement of the mirror perpendicular to the sample air beam is necessary here. At this point of alignment mirror–detector axis, the axis of the laser beam, and the centre line of the sample air column intersect in one point—the centre of the sensing volume.

3. The last step is the adjustment of the distances of mirror and photodiode holder to the sensing volume in order to produce a sharp image on the focusing screen. As the image position is more sensitive to changes of the mirror distance (in this OPC configuration), this is adjusted prior to photodiode position. The distance of the photodiode holder is then changed slightly to optimize alignment.

   The optimum alignment can be achieved by putting the photodiode holder in the position where the sharpest image of the sensing volume is produced in the centre of the focusing screen (which was located in place of the photodiode).

4. Finally the focusing screen is removed and photodiode (with the amplifier circuit) put in its place. The photodiode holder is then moved to correct for the different positions of focusing screen and sensitive area of the photodiode. When a thin focusing screen is used on the outside of the photodiode holder covering directly the hole for the photodiode this difference is 0.95 mm (in case of the photodiode OSD5-5T). Therefore the photodiode holder needs to be moved outwards by this amount.

B.2 Alignment of OPC with changed Design

The following describes the procedure followed to align the optical system of the OPC with changed design as described in section 4.2.4 and implemented in the prototype instrument (see section 4.4.3).

The laser module was turned so that the longer axis of its elliptical beam shape would be focused by the cylindrical lens and its shorter axis, which was approximately 1.5 mm, would remain unchanged and define the width of the laser beam at the sensing volume. For the alignment described in the following, the mirror can already be mounted, while the photodiode should not be mounted assembled to leave the hole free for observing the alignment, which is performed according to the following procedure:

1. Laser beam is aligned to illuminate sample air column symmetrically, so that a section of the sample air column would be illuminated completely and the sample air passes through the centre of the laser beam. The laser beam is also to be brought in the plane perpendicular to the sample air column defined by the mirror–detector axis. The beam is therefore adjusted along the axis of the sample air column, always illuminating it symmetrically, until it is in the correct position. This alignment step can be aided, rather than using smoke visualization, by using a little tool which marks the centre of the scattering chamber when introduced through extractor nozzle and fixed in position with a pin exactly fitting in the exit hole of the focusing nozzle. Such a tool can be made out of cardboard or similar material and the centre of the scattering chamber can be marked with cross hairs. While adjusting the laser axis using the two sets of three screws that secure the laser module in its holder to tilt its axis slightly, the position of the beam on the tool can be observed. For safety reasons, this task should be performed either by using a video camera or at a very reduced laser power.

2. To perform the next step of alignment, the mirror should be mounted and the hole for the photodiode should be covered with a clear plastic window securing it airtightly with screws allowing to see inside the chamber for flow visualization tests. Although the laser beam should now be optimally aligned, it is useful to check the alignment, firstly by introducing smoke in the sample air, and secondly by introducing smoke in the sheath air, which should show the sheath air column equally illuminated by the laser beam with leaving a small dark point in the centre marking the position of the sample air column. Should

the sheath air column not be exactly in the centre of the laser beam then the sample air column will not be in the centre as well, and hence not in the position of maximum irradiance. In this case the laser beam should be adjusted to correct this slight misalignment.

3. The final step of alignment checks the position of the image of the sensing volume. It is performed by adding a focusing screen below the plastic window covering the photodiode hole. If this screen is cut round to size to fit below the O-ring seal, then it will be at the position where the sensitive area of the photodiode will be when mounted. The centre of the screen should marked with cross hairs. In case of correct alignment, scattering from smoke in the sensing volume should produce a sharp image on the centre of the focusing screen. Otherwise the alignment can be completed by moving the mirror holder in the mirror adjustment flange adjusting its distance to the sensing volume to produce a sharp image. Finally, the mirror adjustment flange can be moved in the direction perpendicular to the sample air column (and parallel to the laser beam) to bring the image in the centre of the focusing screen. This should be possible if the previous alignment steps were done accurately. If, however it is not possible, indicating that the laser beam is not in the plane perpendicular to the sample air column defined by the mirror–detector axis, the alignment should be repeated (or refined) starting again from the first step.